Carbon-Based Microfluidic Impedance Cytometry

By

Talha Qamar

A thesis presented for the degree of

Doctor of Philosophy

Mathematics, Statics and Physics

Newcastle University

United Kingdom

February 2024

Abstract

Microfluidic Impedance Cytometry (MIC) is a powerful sensing technique for single-cell electrical analysis and discrimination. It involves applying AC voltage to two or more pairs of electrodes to measure the change in impedance as single particles pass by. This method has been used to analyse various micro-organisms, blood cells, and animal and human cell lines. The development of MIC holds promises for the integration of flow cytometry with wearable hardware and mobile processing, paving the way for a user-friendly system for continuous and remote diagnosis.

In this work the traditional coplanar electrode configuration is used, and the electrode material is changed from metal electrodes to carbon-based such as graphene and Pyrolytic carbon. Results are presented for gold, graphene, and Pyrolytic carbon electrodes as part of a complete microfluidic detection system.

a) Experimental investigations on the MIC device with gold coplanar electrodes provide valuable insights into particle detection and behaviour. Controlled experiments with varying channel heights and electrode separations demonstrate the crucial balance between sensitivity and fluid dynamics, with 30µm Au electrode separation emerges as the optimal choice, boasting the highest sensitivity of 4.97×10^{-8}. Subsequently, analysis of 10µm and 20µm particle mixtures highlights the challenges and successes in distinguishing particle sizes.
b) A novel approach to fabrication of the pattern graphene electrodes and a method for integration with a microfluidic channel is presented. A comprehensive study then addresses the challenges in preserving the integrity of graphene electrodes. MIC measurements with graphene electrodes presents unique challenges emphasizing the need for precise optimization in surface treatments and protective coatings.
c) Microstructured Pyrolytic carbon are integrated with an equivalent MIC device to optimization, Study shows that using a modified electrode separation of 50μm leads to a promising sensing result. Optimized Pyrolytic carbon electrodes are shown to provide a sensitivity of 2.29×10^{-8} under testing.

In closely related work, two-photon subtractive manufacturing is explored for use in microfluidic channel fabrication where feature definition of 50$\mu m \times 50\mu m$ was demonstrated for common polymeric materials PMDS, PMMA, PS and PC. Feature fabrication at depths below 1mm were discovered and the ability for versatile subsurface patterning opens up a host of exciting future work.

Acknowledgements

I extend my heartfelt gratitude to my primary supervisor, Dr. Toby Hallam, for his unwavering guidance, encouragement, and invaluable assistance that played a pivotal role in the successful completion of my academic research. His readiness to offer support and advice significantly enriched my learning experience in the research journey.

Special appreciation goes to Dr. Konstantin Vasilevskiy and Dr. Johannes Gausden for dedicating substantial time to train me on the fabrication equipment and assisting in the procurement of necessary chemical materials. The University of Newcastle deserves sincere thanks for providing me with the opportunity to pursue my Ph.D. with funding and support.

I would like to express my thanks to Dr. Elisabetta Arca for her assistance in the XPS measurements. Additionally, I am grateful to Dr. Christian Johnson, Dr. Nathan Hill, Dr. Luke Bradley, and Dr. Abdullah Aladim for their invaluable help and support in the laboratory.

My deepest appreciation extends to my parents and sister for their unwavering moral support throughout my research journey. I am also grateful to my understanding and supportive wife, Raisa Zafar, for her patience during my study period. I thank her for the continuous support and encouragement throughout my Ph.D. and it would not have been possible without her.

COVID-19 Impact

My PhD research, heavily focused on experimental work in physics and engineering, constituted approximately 80% of the project workload of this project is based on experiments, where 10% data analysis of those experiments and the rest of the 10% could be counted as literature reviewing and skill learning. This included a diverse range of experiments across various labs situated in different university buildings.

My experimental work includes a wide variety of very different aspects of fabrication and device operation which must be carried out in person in a laboratory. During my PhD, my experimental work was carried out across a collection of labs across several building in the university: Cleanroom and ETM measurement lab in Merz Court, Nanolab and Perovskite lab in Bedson building and E4.02 in Merz Court.

The significant disruption occurred in 2021 when the lockdown forced the closure of the laboratories for a prolonged six-month period, profoundly affecting my ability to conduct essential experiments. The subsequent challenges upon returning to work, marked by access restrictions, reduced occupancy, limited working hours, and altered lab functions, extended the modified working conditions by at least an additional six months.

To adapt to the new circumstances, my supervisor and I revised experimental protocols, aiming to accommodate single-lab fabrication and reduced measurement capability. Unfortunately, the long-term impact of these modifications revealed inaccuracies and non-reproducibility in the devices fabricated and results obtained.

The uncertainties and lack of control over the situation caused considerable stress, affecting not only my work but also my overall well-being. Isolation and social distancing measures further intensified feelings of anxiety, as the inability to socialize with colleagues and engage in activities outside of work made coping with the situation difficult.

The uncertainty surrounding the future of my project and the pressure to perform within a limited timeframe added to the stress. The lockdown's impact on mental health during this challenging and stressful time required resilience and support to overcome.

Contents

List of Figures

1. Introduction

1.1. Background

Microfluidic Impedance Cytometry (MIC) is an extensively used technique for single–cell electrical analysis and discrimination[1]. When AC voltage is applied to two pairs of electrodes the impedance of single particles is measured via differential current as a cell passes between them. A voltage is supplied at several different frequencies and the change in current is analysed to determine the cell dielectric properties. MIC has been used to analyse micro-organisms[2], erythrocytes[3], leukocytes[4], platelets[5], and animal and human cell lines[6, 7]. Low frequency (e.g., 500 kHz) impedance is used to size particles because at these frequencies (and in high conductivity buffer) the particle volume is related to the real part of the complex impedance signal, in a similar manner to a Coulter volume measurement. At higher frequencies, the electrical impedance is influenced by the cell membrane and the cytoplasmic properties. For the widely used parallel electrode geometry, the measured impedance signal also depends on the position of the particle between the electrodes, i.e., the trajectory of the particle as it flows through the channel. This is because the electric field in the channel is not uniform, and the particle can influence the current in the reference arm of the sensor. This manifests itself as an error in the measured “volume” of the particle for off-centre particles (i.e., close to the top or bottom electrodes).

Flow cytometry, a biomedical procedure which has typically been restricted to the confines of a lab, has the potential to be integrated with wearable hardware and mobile processing to introduce a novel, user-friendly system for continuous and remote diagnosis. Flow cytometry, the gold standard technique for cell counting, is primarily based on optical detection of fluorescently labelled biological cells and particles suspended in a stream of fluid. To date, it requires bulky and costly optical instrumentation and also difficult fluorescent tagging of cells. Impedance cytometry[8], which is based on electrical detection, is advantageous over optical readout because of the potential for developing instrumentation much smaller in size.

The ability to detect single cells and particles at micron scale generally requires a highly sensitive system that can detect at least a 0.1% change in baseline impedance. This typically requires both high-end analogue-to-digital conversion hardware and channel sizes comparable to the particle being detected. Small channel sizes generally result in device failure due to clogging of the microfluidic channels, and high-resolution analogue to digital converters usually require a customized integrated circuit. To be able to detect single particles without clogging channels requires a sensor cross-sectional area five to ten times larger than the largest particle that will be detected[8], which is difficult to achieve with low-resolution off-the-shelf analogue-to-digital converters.

One of the major challenges of electrical impedance detection is detecting low signal-to-noise ratio (SNR) output signals provided by low voltage, low power sensors, which can be an order of magnitude smaller than electrical noise and interference signals from the environment. One of the most common techniques for detecting very small AC signals down to a few nano-volts is lock-in-amplification (LIA), which makes use of the synchronous phase sensitive detection (PSD) technique.

Using the principles of MIC, the aim of this research is to introduce innovations in the coplanar electrode configuration by utilizing carbon-based electrodes instead of the conventional gold electrodes with carbon-based materials, specifically Graphene and Pyrolytic carbon (PyC). This research aims to address several key challenges associated with MIC, specifically the channel dimension and electrode gap optimization to avoid clogging and the need for high sensitivity in detecting micron-scale particles. By utilizing carbon-based electrodes, particularly Graphene and PyC, we aim to overcome limitations inherent in gold electrodes, offering improved performance in terms of reliability and precision.

Furthermore, the overarching aim of this research is to apply the two-photon ablation technique for negative 3D printing in carbon materials. Specifically, the focus is on utilizing this technique to create microfluidic channels for MIC devices.

1.2. Two-photon Ablation (TPA)

Two-photon ablation is a process that utilizes the focused energy, with ultra-short pulse with low photon energy, of a femtosecond laser to selectively remove material through the nonlinear absorption of two photons. While it is not as widely recognized as some other laser processing techniques, research has demonstrated the potential of two-photon ablation for highly selective modifications in various materials, including biological samples[9] and microfabrication processes[10]. Femtosecnod laser with wavelength of 520nm is being used for TPA, which is not a typical wavelength. Few studies have mentioned the usage of wavelength around 780nm to 800nm. The materials being explored in combination with TPA are PDMS, PMMA, Polystyrene and Polycarbonate. A literature review can be found in **section 3.2.2**, whereas the fabrication and results can be found in **section 4.2**.

1.3. Carbon-based Materials for MIC

1.3.1. Graphene

Graphene-based electrochemical impedance sensors have recently gained attention around the world due to its outstanding sensing capability and economic practicability. With its conductive properties and as a tool for electrochemical impedance spectroscopy (EIS), it has been gaining attention with the detection of microplastics [11], endocrine disruptors[12], biomolecular events[13], and supercapacitors[14]. Graphene-based bioelectrical electrodes have significant merits including excellent mechanical properties, flexibility, exceptional and stable electrochemical properties, low contact resistance, and high SNR. These electrodes are being discovered in different applications; one such example is as graphene electronic tattoos (GET). Which are being used to obtain ECG, EEG and EMG. The graphene-based bioelectrodes are attributed to the unique characteristics of graphene's mechanical robustness, biocompatibility[15] and electrochemical stability[16].

The use of graphene in microfluidic devices offers advantages such as high surface area, excellent electrical conductivity, and mechanical compatibility, making it suitable for diverse applications in health monitoring and biomedical analysis[17]. Therefore, graphene holds promise for the advancement of microfluidic technology in biomedical and analytical applications.

1.3.2. Pyrolytic carbon (PyC)

PyC, produced through the pyrolysis of hydrocarbons, holds some similarities with graphite structure with distinct difference. In PyC, there is a mix of sp2 and sp3 hybridized carbon atoms, introducing some covalent bonding within the layers. This covalent bonding contributes to the material's anisotropic properties, meaning it exhibits different physical properties. It has been explored for specifically in the area of supercapacitors[15] and in electrochemical sensors[18]. In case of supercapacitors, PyC is considered as promising electrode material due to its exceptional electrical conductivity and tuneability[19]. The tunability of PyC stems from its flexible synthesis process, allowing for the adjustment of key properties such as electrical conductivity, anisotropic characteristics, and chemical stability. The unique structure enables supercapacitors with Pyrolytic carbon electrodes to deliver high power density and rapid charge/discharge rates, along with its chemical stability contributing to the longevity of supercapacitor cycles. Furthermore, due to its chemical inertness and biocompatibility, it is a preferred choice for electrode fabrication in electrochemical sensors.

The material's exceptional electrical conductivity, combined with its chemical stability, makes it an excellent choice for fabricating electrodes in microfluidic impedance sensors. These sensors are sensitive to variations in impedance resulting from interactions between the medium and the electrode surface[20]. PyC's biocompatibility is particularly advantageous for applications involving biological samples, where it minimizes interference with bio materials and ensures reliable impedance measurements[21]. Therefore, the unique combination of properties exhibited by PyC makes it a desirable material for the fabrication of microfluidic devices.

1.4. Thesis Summary

In this thesis, we explore the MIC devices with optimized electrode configurations for enhanced particle detection. Explored two aspects of MIC devices: Patterning of microfluidic structure, for potential parallel electrode configuration and coplanar electrode configuration. **Chapter 4** reports experiments and findings for the microfluidic structure with conventional laser and two-photon ablation. **Chapter 5** reports the experiments and findings of co-planar electrode configuration in MIC devices.

The first aspect of MIC devices explored was based on the idea of parallel electrode configuration. Parallel electrode configuration has higher sensitivity but its complexity in fabrication has its challenges. The conceptual approach involved the creation of a laser-printed microfluidic channel on a flexible and transparent material, positioned between two glass substrates, each featuring a single electrode. Initially, conventional laser cutting techniques were explored using CO_2 and Fiber lasers, but challenges such as material melting, and insufficient depth hindered the desired results. The project then introduced a novel approach involving two-photon ablation on transparent carbon-based materials, including PDMS, PMMA, polystyrene, and Polycarbonate. The selection of these materials was based on their advantageous properties, such as optical clarity to visible light, non-conductivity, and non-toxicity. **Chapter 4** is dedicated to showcasing the potential of two-photon ablation for intricate 3D patterning and precision material processing. This section will present the experimentation process, focusing on the optimization of ablation parameters and addressing

challenges encountered in fluid flow testing. Despite facing issues during experimentation, the results demonstrated the considerable potential of two-photon ablation in the creation of intricate structures within microfluidic impedance cytometry devices.

Subsequently, in Chapter 5, an exploration of the coplanar electrode configuration of the MIC devices were performed. The chapter holds important information about the fabrication process of the complete MIC device, encompassing crucial steps in the fabrication procedure. It covers novel aspect of sealing of PMDS and glass substrate.

The coplanar electrode configuration was pursued to enhance sensing capabilities by replacing conventional metal electrodes. The investigation considered three distinct materials: gold as a metal, graphene, and PyC as carbon-based materials. The fabrication process for MIC devices included experimenting with different electrode gaps and channel heights, where gold electrodes were fabricated using UV lithography and thermal evaporation, graphene pattering was done with combination of dry and wet etching, while PyC were fabricated by collaborators at Universität der Bundeswehr, München.

The study proceeds into experimental investigations on these MIC devices, incorporating electrical circuit involving LIA technique for particle detection. Controlled experiments with varying channel heights revealed the impact of height on particle detection efficiency, leading to the selection of a 50µm channel height. The most effective electrode separation for particle detection was found to be $30\mu m$ for gold electrodes. The study then focuses on PyC electrodes, conducting a careful analysis of sensitivity based on electrode separation and channel height. Conclusively, a 50µm electrode separation consistently exhibited the highest sensitivity, offering detailed information about particle behaviour. This configuration was identified as the preferred choice for PyC electrodes in microfluidic sensing devices, offering valuable insights for device design and optimization.

Further investigation showed the novel approach of graphene patterning and addressed challenges related to etching of graphene electrodes when exposed to the MIC system. Furthermore, it explored protective measures taken to hold patterned graphene electrodes, like using APTES functionalization and PMMA coating.

2. Theoretical

2.1. Flow Cytometry

Flow cytometry is a technique used to analyse the physical and chemical characteristics of cell suspension. It provides rapid multi-parametric analysis of single cells, which is one of the key advantages of the flow cytometry and it has potential to measures properties such as cell size, total DNA, and fluorescence intensity. A flow cytometer is composed of three main systems: fluidics, optics, and electronics[22]. A schematics of flow cytometry is illustrating in **Figure 1**.

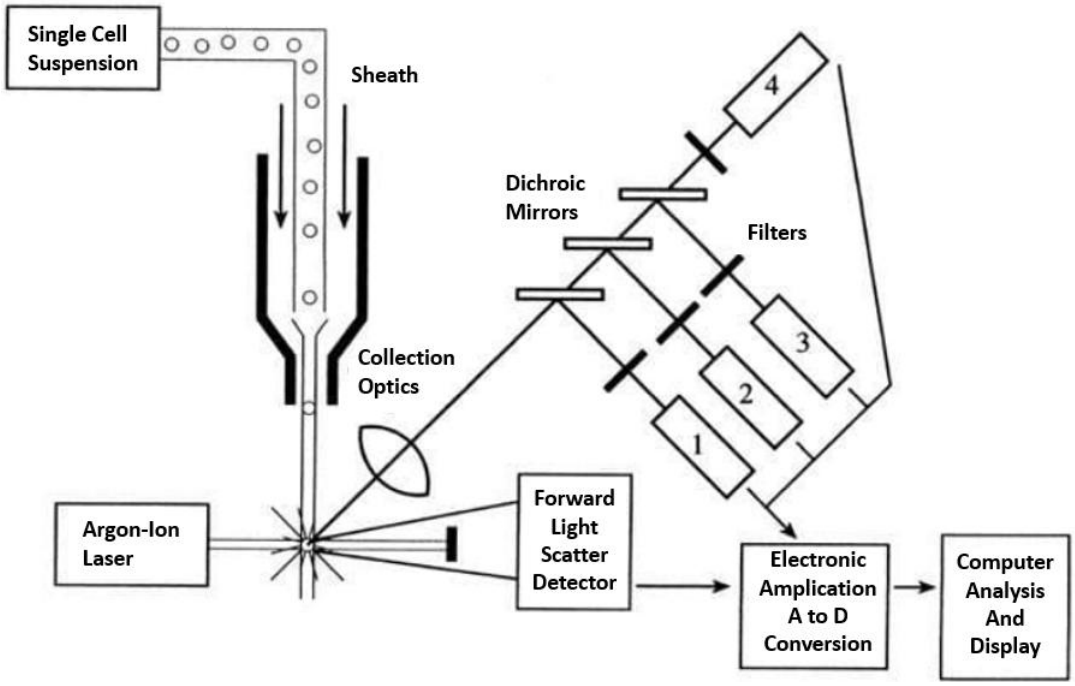

Figure 1: A schematic of a Flow Cytometry, showing all the stages of the technique[23].

The method involves the labelling of cells with fluorescent dyes or antibodies that specifically bind to cellular components of interest, such as proteins or DNA[24]. This allows for the precise identification and quantification of various characteristics at the single-cell level. The process involves suspending cell suspension and injecting it into a flow cytometer through the vibrating mechanism where it is arranged to be separated in relative diameter sizes and form droplets. The system is adjusted to ensure that each droplet contains only a single particle. As the droplet passes through the lasers, they generate scattered and fluorescent light[22]. These signals are then converted into electronic signals and analysed by a computer. Flow cytometry is widely used in various fields such as immunology, virology, molecular biology, and cancer biology for tasks like cell analysis, sorting, and identifying cell types of interest[25].

While flow cytometry remains a powerful technique, it is important to note that the MIC devices try to bring the application into point-of-care, where miniature version could be used in more mobile environments.

2.2. Microfluidics

Microfluidics is a field of research and technology that involves the manipulation and control of small amounts of fluids within microscale devices. It is often referred to as microfluidic chips or lab-on-a-chip systems. This technique allows precise handling of microliter or nanolitre volumes of liquids into very small channel of micro or nanometres[26]. The advantages of such a reduced sample and reagent allows less consumption, faster reaction times, and the integration of multiple functions on a single platform. Microfluidic devices, combines various laboratory processes for fabrication, including sample preparation, mixing, reaction, and detection, onto a compact chip. This approach finds applications in diverse fields, including analytical chemistry[27], biochemistry[28], medicine[29, 30], and materials science[31].

The field of microfluidics is continuously advancing, with ongoing research and development focusing on next-generation systems and their applications in various scientific disciplines[31].

2.2.1. Flow field (Navier Stokes)

The Navier-Stokes equations are named after Claude-Louis Navier and George Gabriel Stokes[32], who made a significant contribution to the formulation of these equations in early 19th century. These equations are fundamental in fluid mechanics and play a crucial role in understanding and predicting the fluid flow behaviour. They are used to model a wide range of phenomena in recent time such as weather patterns, ocean currents, airflow around objects, and blood flow. The Navier-Stokes equations primarily consist of three key components: the Continuity Equation, the Momentum Equations, and the Hagen-Poiseuille Equation [33, 34].

Continuity equation:

$$\nabla . \mathrm{v} = 0 \tag{1}$$

∇ is Nabla operator of divergence, and v is Velocity vector field. The equation essentially states in simpler terms that the fluid cannot suddenly appear or disappear at a point, the amount of fluid entering a region must be equal to the amount leaving, which expresses the principle of conservation of mass.

Momentum equation:

$$\frac{dv}{dt} + (\mathrm{v}.\nabla)v = -\frac{1}{\rho}\nabla p + v\nabla^2 \mathrm{v} \tag{2}$$

Here, the time derivative of velocity, ρ is the fluid density, p is the pressure, v is the kinematic viscosity, and ∇^2 v is the Laplacian of the velocity field. This equation is essentially Newton's second law applied to fluid motion. It states that the change in momentum of a fluid element is equal to the sum of the forces acting on it. Where the left side of the equation represents the acceleration of the fluid, the right side represents the forces influencing this acceleration.

Hagen-Poiseuille equation:

$$Q = \frac{b.h^3}{12\mu L}\Delta P \quad (3)$$

Where, Q is volumetric flow rate, *b* is the width of the channel, *h* is the height of the channel, μ is the dynamic viscosity of the fluid, L is the length of the pipe and ΔP is the pressure drop across the pipe. This equation is important as it provides insight into how factors such as width, height, length, viscosity, and pressure drop influence the rate of fluid flow.

While these equations provide fluid motion accurately, their complexity and computational demands make them challenge to solve for practical cases[35, 36]. These equations are nonlinear and solving them analytically is often challenging, and numerical methods are commonly employed to obtain solutions for specific flow problems.

Laminar flow is key concept in fluid dynamics and is analysed using the Navier-Stokes equations. When considering laminar flow, these equations provide insights into the behaviour of the fluid, emphasizing the dominance of viscous forces over inertial forces[37].

Laminar flow is described by smooth and orderly movement of fluid layers without significant disruption between adjacent layers. This flow pattern is distinguished by low Reynolds numbers, typically below 2,300, where viscous forces dominate over inertial forces[38]. Reynolds number is dimensionless quantity used in fluid mechanics to characterises the flow, indicating whether the flow will be laminar, turbulent or mixture. Reynolds equation is,

$$Re = \frac{\rho V L}{\mu} \quad (4)$$

Where, ρ is density, V is velocity of flow, L is characteristic length and μ is the dynamic viscosity of the fluid.

In laminar flow, fluid particles follow well-defined paths, and the streamlines remain parallel, resulting in a predictable and stable flow. The velocity gradients across the flow are high, indicating gradual changes in velocity between layers with minimal mixing. Examples of laminar flow include the motion of fluids in small-diameter pipes, blood flow in capillaries, and certain viscous fluid systems[39, 40].

2.3. Cyclic Voltammetry

Cyclic Voltammetry (CV) is a powerful tool used in electrochemical techniques to study electrochemical behaviour of the electroactive species in the solution. It typically involves a sweep of potential of working electrodes while measuring the current[41]. The setup consists of 3 electrodes: a working electrode, reference electrode and counter electrode, except in this work where the reference electrode was not used. The sweep is performed forward and reverse in a cyclic manner, resulting in a characteristics voltammogram. This gives information about the presence of intermediates in oxidation-reduction reactions, reversibility of a reaction, electron stoichiometry, diffusion coefficient of an analyte, and formal reduction potential[42]. This technique is well known for its rapid qualitative identification of electrode processes and is employed in many research areas. The cyclic curve can be used to calculate the effective capacitance between the working and counter electrode with the presence of medium. To calculate the capacitance the derivation of the curve is provided subsequently.

The equation for specific capacitance is given by,

$$C_p = \frac{Q}{mV} \tag{5}$$

Where Q is the charge stored in coulombs, m is the mass of active material in grams, V is the potential and C_p is the specific capacitance.

As we know that,

$$I = \frac{Q}{t}$$

Or

$$Q = I \times t \tag{6}$$

By putting (6) in equation (5) we get,

$$C_p = \frac{(I \times t)}{mV}$$

Dividing nominator and dominator by t,

$$C_p = \frac{I}{m\left(\frac{V}{t}\right)}$$

In the equation above, $\frac{V}{t}$ is the scan rate of the cyclic voltammetry and is represented by k.

$$C_p = \frac{I}{m \times k}$$

Or,

$$I = C_p \times m \times k \tag{7}$$

From the curve CV, the current changes during the charging process as the potential varies from V1 to V2.

Therefore, equation (7) can be written is its integral form as,

$$\int_{V_1}^{V_2} I(v)dv = \int_{V_1}^{V_2} \left(C_p \times m \times k\right)dv \tag{8}$$

If we look carefully at the equation above, the integral on the left-hand side represents the area of the CV curve. Therefore, the equation (8) can be written as,

$$Area = \int_{V_1}^{V_2} \left(C_p \times m \times k\right)dv \tag{9}$$

For a specific material, the value C_p, m and k are constant. Therefore, the integral in the equation (9) can be solved as,

$$Area = (V2 - V1)C_p \times m \times k \tag{10}$$

In the curve, we have three areas,

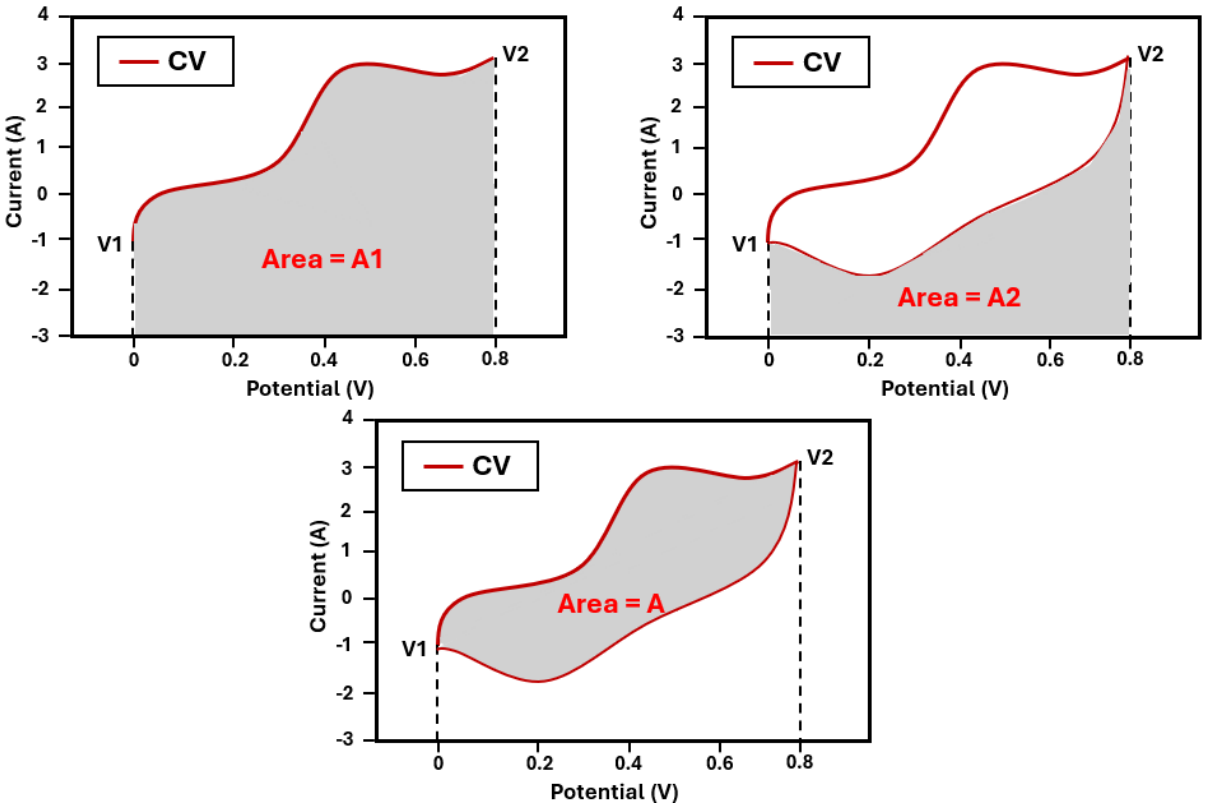

When the capacitor is charging, then Area=A1 and equation (10) can be written as,

$$A1 = (V2 - V1)C_p \times m \times k \tag{11}$$

Similarly, when capacitor is discharging, then the Area = A2 and equation (10) can be written as,

$$A2 = (V1 - V2)C_p \times m \times k \tag{12}$$

For the calculation of the area (A) inside the CV curve, we must subtract equation (12) from equation (11).

$$A = A1 - A2 = \left[(V2 - V1)C_p \times m \times k\right] - \left[(V1 - V2)C_p \times m \times k\right]$$

$$A = \left[(V2 - V1)C_p \times m \times k\right] + \left[(V2 - V1)C_p \times m \times k\right]$$

$$A = 2\left[(V2 - V1)C_p \times m \times k\right]$$

So, it can be rewritten for C_p,

$$Cp = \frac{A}{2mk(V2 - V1)} \tag{13}$$

Where C_p is the specific capacitance in F/g, A is the area inside the CV curve having units AV, m is the mass of active material, k is scan rate of CV in v/s and (V2-V1) is the potential window of CV (total voltage range).

Using capacitance formula,

$$C = C_p \times m \tag{14}$$

m is mass in g. Using **Equation 14**, the capacitance value can be calculated from the CV curve.

2.4. Impedance

One of the most basic concepts of electrical circuits is resistance, known as the ability of a circuit to resist the flow of electrical current. The ratio between voltage and current defines resistance given by Ohm's law.

$$R = \frac{V}{I} \tag{15}$$

Where V is voltage, I is current, and R is the resistance.

Following Ohm's law in ideal condition, resistance is very simple concept. However, real-world experimentation displays behaviour much more complex. At this stage, impedance is introduced as a general parameter. While resistance is a simple opposition to current flow, independent of frequency, impedance accounts for both resistance and reactance, making it more applicable to real-world circuits where frequency-dependent effects play a role. It is derived from simple Ohm's law and is also dependent of frequency depending on the passive element type i.e. resistor, inductor, and capacitor[43].

2.4.1. Component derivation

Impedance (Z) of a circuit component in an electrical circuit is a complex quantity that combines the element of resistance (R), which arises from the collisions of current-carrying particles, and reactance (X), which is the additional opposition to the movement of electric charge[44]. The impedance can be expressed as a complex number in form of equation:

$$Z = R + jX \tag{16}$$

Here j is the imaginary unit ($j^2 = -1$).

Developing I-V equations for the passive components with reference to input **Equation 15**

For a resistor, where,

$$I = e^{j\omega t} \tag{17}$$

Substituting I into equation 15,

$$V = Re^{j\omega t} \tag{18}$$

Taking V/I ratio to get Z,

$$\frac{\mathrm{V}}{\mathrm{I}} = \frac{\mathrm{Re}^{\mathrm{j}\omega\mathrm{t}}}{\mathrm{e}^{\mathrm{j}\omega\mathrm{t}}}$$

Resulting in,

$$\mathrm{Z} = \frac{\mathrm{V}}{\mathrm{I}} = \mathrm{R} \tag{19}$$

So, it means the Impedance of a resistor is equal to the resistance value in Ω as unit.

For an Inductor, we know,

$$\mathrm{V} = \mathrm{L}\left(\frac{\mathrm{di}}{\mathrm{dt}}\right)$$

Using equation 15 where I is complex exponential current which we are forcing through our inductor

$$\mathrm{V} = \mathrm{L}\frac{d}{dt}\mathrm{e}^{\mathrm{j}\omega\mathrm{t}}$$
$$\mathrm{V} = \mathrm{j}\omega\mathrm{L}\mathrm{e}^{\mathrm{j}\omega\mathrm{t}}$$

Taking V/I ratio to get Z.

$$\frac{V}{I} = \frac{\mathrm{j}\omega L e^{\mathrm{j}\omega\mathrm{t}}}{e^{\mathrm{j}\omega\mathrm{t}}}$$

Results in,

$$Z = \frac{V}{I} = \mathrm{j}\omega L \tag{20}$$

This means the impedance across inductor is dependent on value of inductor and directly proportional to frequency.

For a capacitor, we know,

$$I = C\frac{dv}{dt} \tag{21}$$

Where Voltage is

$$v = \omega^{\mathrm{j}\omega\mathrm{t}}$$

Substituting V in equation 16

$$I = C\frac{d}{dt}e^{\mathrm{j}\omega\mathrm{t}}$$

$$I = \mathrm{j}\omega C e^{\mathrm{j}\omega\mathrm{t}}$$

Taking V/I ratio to get Z

$$\frac{V}{I} = \frac{e^{\mathrm{j}\omega\mathrm{t}}}{\mathrm{j}\omega C e^{\mathrm{j}\omega\mathrm{t}}}$$

Resulting in

$$Z = \frac{V}{I} = \frac{1}{\mathrm{j}\omega C} \tag{22}$$

This means the impedance across capacitor is dependent to value of capacitance and inversely proportional to frequency.

2.4.2. Electrochemical impedance spectroscopy (EIS)

Electrochemical impedance spectroscopy (EIS) is a versatile experimental technique, which helps study the properties of electrochemical system at the electrode-electrolyte interface. The principle involves applying a small AC potential across two electrodes at various frequencies and measuring the current response[45]. The data is then analysed using equivalent circuit models, which help extract insights into the electrochemical processes.

The impedance is frequency-dependent and is typically represented by Nyquist and Bode plots. Nyquist plots display the real and imaginary components of the impedance, where important information about resistance, capacitance, charge transfer, frequency dependencies and validity of equivalent circuit model can be extracted[46]. Nyquist plots, presents a semicircle plotted real part of the impedance vs the imaginary part of the impedance. The diameter of the semicircle depicts the sum of resistance of solution resistance (R_s) and charge transfer resistance (R_{ct}), while the radius represents the double-layer capacitance (C_{dl}). On the other hand, a bode plots showcases the magnitude and phase angle of the impedance and can be used to access frequency response and stability of the system[47].

Equivalent circuit analysis, exemplified by the Randles equivalent circuit in the context of electrochemical systems, serves to be a valuable method for simplifying the complex electrical systems. This technique allows researchers to study of electrochemical behaviours with simplified circuits presentation. Furthermore, equivalent circuit models, offer a tool for experimental validation. By adjusting circuit parameters to match experimental data, researchers can refine their models, ensuring a more accurate representation of the electrochemical system.

The technique has found applications in fundamental research as well as practical developments, making it an invaluable tool in electrochemistry.

2.4.3. Conductivity

Electrical conductivity is a property which helps characterize the ability of the material to facilitate the flow of electric current. It is a measure to how easily a substance allows the movement of charged particles in response to the electric current[48]. In metals, conductivity shows the mobility of the free electrons[49], whereas in electrolyte, it expresses the migration of the ions[50]. Materials that exhibit conductivity are known as conductive materials, while materials that do not exhibit conductivity are called insulators. Semiconductor materials occupy an intermediate position, as their conductivity lies between conductors and insulators. The electrical conductivity is denoted as σ, measured in Siemens per meter (S/m) and can be written as,

$$\sigma = n \times e \times \mu \tag{23}$$

Where n is the number of charge carriers per unit volume, e is the elementary charge and μ is the mobility of the charge carrier. Notably there are two factors that can influence the conductivity of the materials, temperature, and concentration of charge carriers.

For Impedance cytometry, electrical conductivity is an important factor to consider. The conductivity of the electrode material plays significant role in determining the impedance

response and sensitivity for the sensor. The choice of electrode materials, such as Au, PyC, and graphene, can significantly influence the performance of the impedance cytometry system due to their respective conductive properties. The electrical conductivity for Au is approximately 4.5×10^7 S/m[51], where graphene exceeds 10^6 S/m[52] and PyC is in between 10^3 to 10^4 S/m[53].

2.5. Impedance cytometry

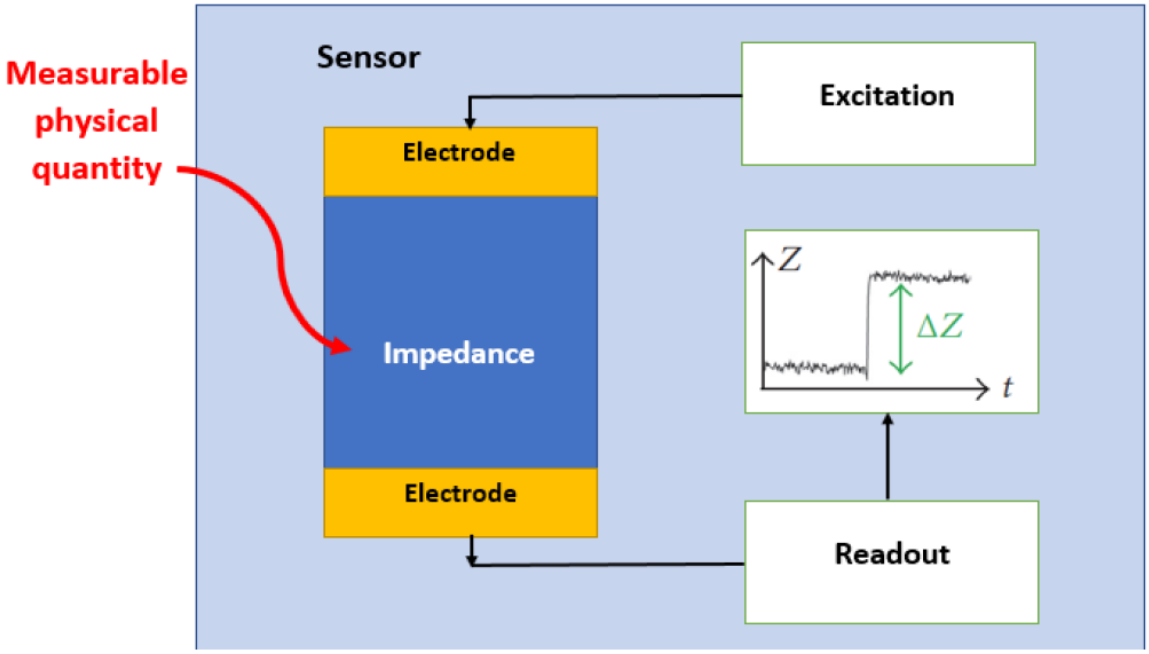

Figure 2: Schematic of an impedance sensor with excitation and readout circuit.

A physical quantity becomes measurable by mean of impedance when a variation of such a quantity reflects into a variation of the impedance. **Figure 2** represents the schematics of such a sensor. A pair of microelectrodes is fabricated and energized with an AC voltage at a discrete frequency, generating a non-uniform sensing region, known as the impedance sensor. One electrode is used to sense electric current fluctuation causes by the event (single cell passing through) and the other measures the current passing through the medium, acting as the counter electrode. Then a lock-in amplifier can be used to subtract the differential current from the 2 signals while rejecting noise. The noise is rejected via demodulation of in-phase and out-phase impedance signal at stimulating frequency from other frequencies. The readout of this impedance sensing is either in form of Voltage or Current. This method is based on the coulter principle.

2.5.1. Coulter counter

Coulter Counter is a technique based on the Coulter Principle, which is used to count and size particles, especially cells, in a liquid. When a particle suspended in an electrolyte (liquid) passes through the sensing region, it displaces the volume equal to the size of particle thus causing the change in electrical impedance[54]. This change is detected via voltage variation and helps in counting and sizing the particles[55]. The impedance change by the passing particle can be related with the equation below,

$$\Delta Z = \frac{R_0 V_p}{A} \quad (24)$$

Where, ΔZ is change in impedance, R_0 is the resistance of the liquid, V_p is the volume of the particle and *A* is the cross-sectional area of the channel.

Coulter counter have various application, including biology, medicine, microfluidic and research industry. Most importantly the principle is independent of the optical and chemical properties of the particle and soes not require fluorescence.

2.5.2. Impedance properties of the cells

A capacitor is formed when two conduction plates are separated by the non-conducting material known as dielectric. The value of capacitance depends on the size of electrodes, distance between the electrodes and the properties of dielectric. The relation is given in **equation 25.**

$$C = \frac{\varepsilon_o \varepsilon_r A}{d} \quad (25)$$

Where, ε_o permittivity of the free space (electric constant) which is 8.85 x 10^{-12} F/m, ε_r is dielectric constant (relative electrical permittivity of the medium/material used), A is the surface of one plate, and d distance between two plates. **Table 1** contains some key materials used in the project along with their respective dielectric constants. A large difference between the dielectric constant of water and air can be noticed**.**

Material	$\boldsymbol{\varepsilon_r}$
Air	1
Polystyrene beads 10um	2.4 [13]
Polystyrene beads 20um	2.7 [13]
DI water	78.5
0.9% concentrated Phosphate Solution	79
9.8% concentrated Phosphate Solution	79

Table 1: Dielectric constant of important materials explored in this project.

2.5.3. Maxwell mixture theory

Impedance sensors, with their various types, can generally be divided into two main categories based on their sensing principle: resistive and capacitive. Resistive based detection is on principle of geometric changes or the arrangement of the cell (the distance between electrodes or sizes etc). Whereas, the capacitance based detection measures the change in capacitance between two electrodes separated by dielectric material. Such adaptation can be due to the change in dielectric constant/material or geometry. The single spherical model from **Figure 3** can be used to describe a cell in suspension, where the impedance of the dilute suspension of particle for a uniform electric field can be calculated via Maxwell's mixture theory. Maxwell's mixture theory aims to approximate the effective permittivity of a particle in a complex electromagnetic medium. Where Complex permittivity $\tilde{\varepsilon}_{mix}$ of the mixture of particles and suspending medium is given as:

$$\tilde{\varepsilon} = \tilde{\varepsilon}_m = \frac{1 + 2\Phi\tilde{f}_{cm}}{1 - \Phi\tilde{f}_{cm}} \quad (26)$$

Where,

$$\tilde{f}_{cm} = \frac{\tilde{\varepsilon}_p - \tilde{\varepsilon}_m}{\tilde{\varepsilon}_p + 2\tilde{\varepsilon}_m} \quad (27)$$

$\tilde{\varepsilon}=\varepsilon - j\sigma/\omega$ is the complex permittivity, $i_2 = -1$, ω the angular frequency, $\tilde{f}_{cm}$ is the Clausius-Mossotti factor and Φ is the volume fraction. This theory helps prove and simulate the change observed in Cytometry for different cell sizes even when the material is same.

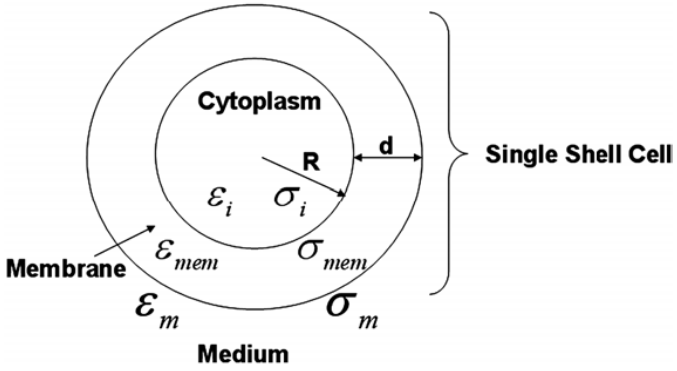

Figure 3: Single electrical model of the spherical cell [12]

2.6. Lock-in-amplifier (LIA)

The invention or LIA is from 1930s. Started being commercially used for detection and recording of small change in AC signals by mid-20th century[56]. Its effectiveness works all the way down to a few nanovolts. An accurate measurement will be recorded even if the noise signal is thousands of times larger than the result[56]. It uses the phase-sensitivity detection method to single out the component of the signal at a certain reference frequency. Any other signal than the reference frequency is then rejected, and measurement does not get any disruption.

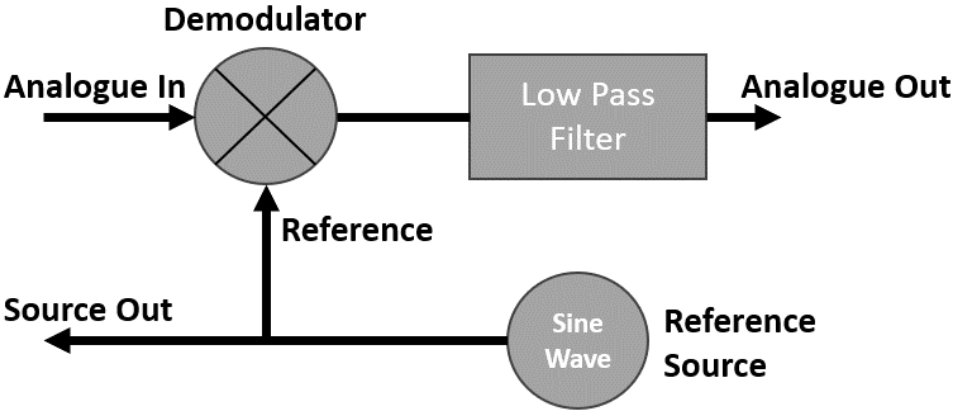

Figure 4: The basic block diagram of a Lock-In Amplifier. The various function blocks may be: analogue, digital or a combination of both[57].

A block diagram is given in **Figure 4** for the Lock-in amplifier working principle. Phase-sensitivity detection depends on the reference frequency. Typically, an experiment is performed at specific frequency and the detection is performed by the lock-in based on to

reference frequency. The LIA magnifies the input with a reference and then applies an adjustable low-pass filter to the result[57, 58].

This method isolates the signal of the frequency of the interest from rest of frequency components[57], Illustrated in **Figure 5**.

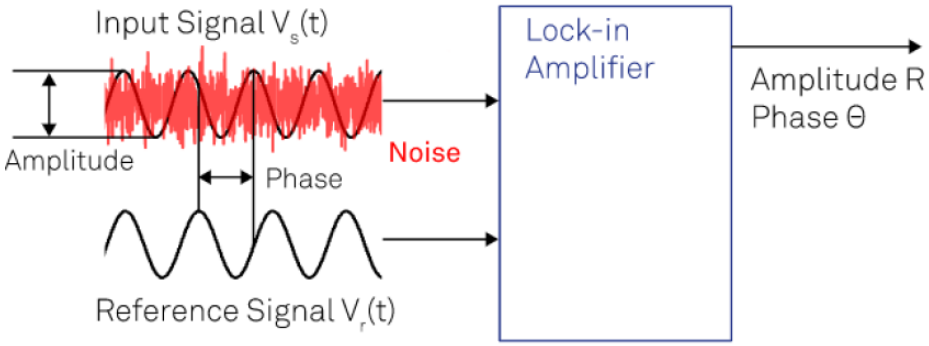

Figure 5: LIA are capable of measuring signal component even if it is entirely buried in noise[56].

2.7. Noise

MIC is a powerful technique, however, it is very susceptible to various sources of noise that can impact its sensitivity and accuracy[59]. The utilization of syringe pumps in microfluidic impedance devices can introduce various sources of noise, potentially impacting the precision and reliability of impedance measurements[60]. One significant concern is the mechanical vibrations generated during the operation of syringe pumps, which may lead to fluctuations in the position of electrodes or microfluidic channels, thereby influencing impedance readings. Additionally, the stability of the flow rate, a critical factor for accurate measurements, can be compromised if the syringe pump exhibits fluctuations or pulsations in its operation[61]. Pressure fluctuations induced by the syringe pump can also affect the electrical properties of the fluid and introduce noise in impedance data.

Electromagnetic interference (EMI) is another consideration, especially with pumps containing electronic components, as it may interfere with the sensitive impedance measurement setup[16]. Regular monitoring and calibration further contribute to ensuring the accuracy and reliability of impedance measurements. To address these issues, careful selection of high-quality pumps, proper calibration, and the implementation of measures to dampen vibrations and shield against EMI are essential for minimizing the impact of syringe pump-related noise in microfluidic impedance experiments.

SNR stands for Signal-to-noise ratio, which is the measure of relative strength of a desired signal compared to the unwanted background noise. It is very crucial in signal processing for MIC devices. The formula for SNR in decibels (dB) is typically represented as

$$SNR_{dB} = 10 \log_{10} \left(\frac{S}{N} \right) \tag{28}$$

Where, S is the amplitude or strength of the signal, and N is the amplitude of the noise.

Higher SNR indicates a stronger and more reliable signal in comparison to the background noise, making it easier to extract meaningful information form the data. In context of MIC, it

is very crucial to have high SNR, otherwise the small variation/detection event will be overshadowed by the background noise.

2.8. Graphene

Carbon (C) is one of the most studied elements in the periodic table[62]. Graphene is an-atom thick sheet of carbon atoms arranged into a honeycomb lattice[63]. Each unit cell consists of two carbon atoms and all atoms are arranged in a hexagonal lattice in a single plane. As shown in **Figure 6** below.

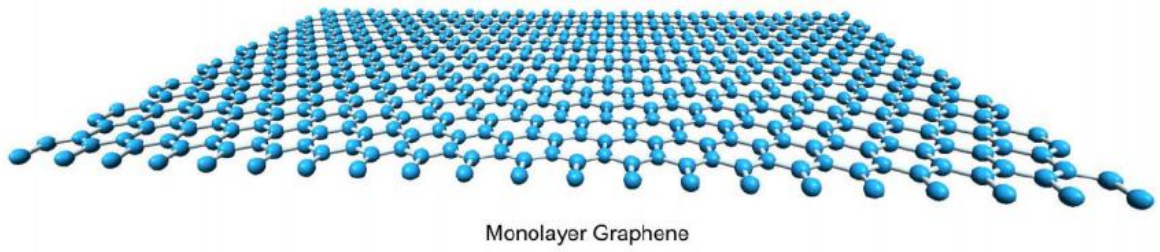

Figure 6: illustration of hexagonal Lattice of monolayer graphene which exists on single plan (2D material)[64].

2.8.1. Structure

The structures of graphene can be perceived as two equivalent atoms of triangular lattice, and the vector displacement to be called a, where a = 1.42Å[63] is the distance between carbon-carbon atoms. **Figure 7a** represent the arrangement of carbon atoms.

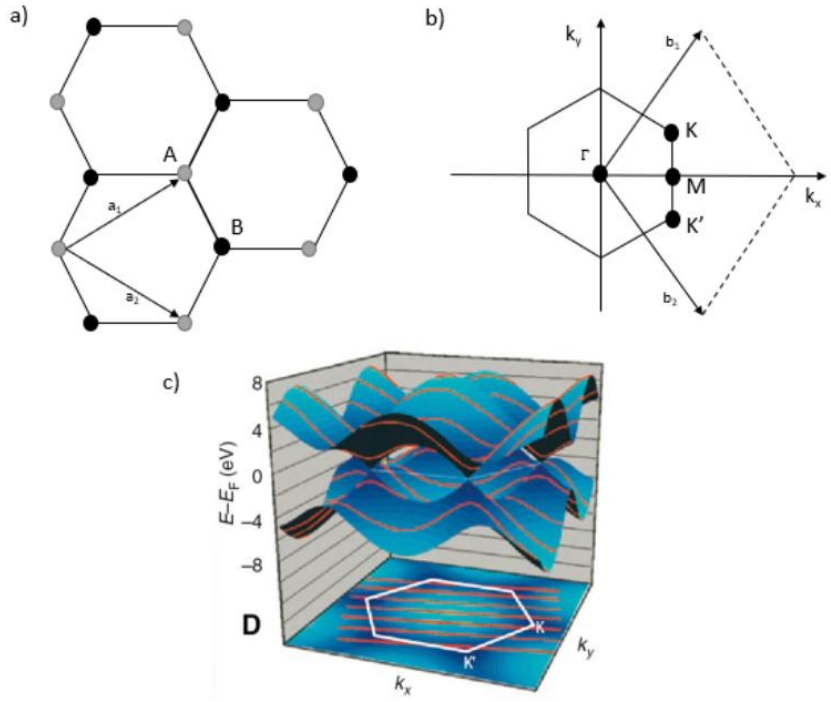

Figure 7: a) Arrangement of carbon atoms in the graphene lattice. Gray and black depicts two carbon atoms A and B. b) illustration of the first Brillouin zone in graphene, with centre, and high-symmetry points: M, K and K'. b1 and b2 are the reciprocal lattice vectors. c) the illustration of band structure (top) and Brillouin zone (bottom) of graphene[65].

The vector of unit cell is given as

$$a_1 = \frac{a}{2}(3, \sqrt{3}) \quad (29)$$

A single layer of graphene has a structure where each C-atom is bonded to two others in the same plane, forming a hexagonal symmetry. The thickness of each sheet of graphene is 0.35 nm[65]. As the band structure of the graphene is found near Fermi level. Fermi level is the term used to describe the top of the collection of electron energy levels at absolute zero temperature[66]. Near Fermi level the conduction band and the valence band intersect at a sole point which is known as Dirac point, this intersection is why graphene is a zero-bandgap semiconductor. Near the Dirac point, the energy and momentum show a linear dispersion relationship[65]. This relationship makes the effective mass of electrons equal to zero, thus electrons in graphene are called massless Dirac Fermion[65]. The massless particles then travel with Femi velocity, $v_f \approx 10^6$ [67] causing an increase to already fast electrons. Compared to the rest of the 2D materials graphene is reported to be the strongest with flexibility and unmatched thermal conductivity[68].

2.8.2. Growth techniques

There are several different methods of fabricating graphene, which of course have their own benefits and downsides. This section describes some of the common methods used for growing graphene.

Adhesion tape exfoliation

Graphite material is made up of stacked layers of graphene which are bonded together with weak van der Waals forces. Utilizing this weakness, one of the earliest methods to separate graphene from within graphite was to cleave it using adhesive tape[69]. Each layer of graphene is stripped off the graphite until a monolayer of graphene is left behind. However, this method has many unpredicted outcomes thus making it highly unreliable. Due to its unreliability this process can't be used in large-scale manufacturing, it is still being used today to obtain a high quality of graphene. The thickness outcome may vary around $10\mu m$[70].

Chemical Vapor Deposition Growth and Transfer

The most profound method of producing graphene on a large scale with high quality is by chemical vapor deposition (CVD). This method is conducted under the presence of different gas precursors (depending on the chosen metal) at high temperature and then deposited on suitable metallic surfaces. Among many metallic surfaces, Nickel (Ni) [71], Cobalt (Co) [72], Platinum (Pt) [73], Iridium (Ir) [74] and Ruthenium (Ru) [75], Copper (Cu) [76]are among the best suited for CVD deposition.

Although there are many different temperatures and gas precursors used for graphene CVD, one of them is where Graphene is deposited on Cu foil at ≈ 1000°N in the presence of methane as precursor [76]. Cu in comparison to other metal has very low carbon solubility at high temperature. This helps bypass any multilayer formation caused by segregation of carbon during cooldown of the substrate. Thus, a high-quality monolayer graphene can be obtained with no limits to covering area expect the size of the substrate itself.

The CVD process is a very versatile way of synthesizing graphene which is used in many other applications as well. With the variation of different material substrates and incorporating various gas precursors, it can be used in a related structure such as graphene-form [77], nanoribbons [78] and 2D-alloys [79].

Epitaxial Growth on Silicon Carbide

Silicon Carbide (SiC) is a semiconductor consisting of covalent bonds between silicon and carbon. It forms crystal types of 4H-SiC and 6H-SiC, which have high bandgaps revealing a great potential for graphene production. When treated in high temperature Si sublimes leaving carbon behind, thus graphene forms on the surface of SiC [80]. This method can be used for the production of high-quality large area graphene. However, temperatures exceeding 1800°C are necessary for the process, and the lack of precise control at such high temperatures makes it challenging to consistently produce graphene layers of the same quality. Additionally, this method requires high-quality SiC, which is expensive and adds to the overall cost of the procedure.

Electrochemical Exfoliation of Graphite

Graphene sheets can be separated from graphite using an electrochemical process. For the process, graphite is used as an anode whereas suitable conducting metals such as Pt and Ni can be used as cathodes. When graphite is inserted in the solution of halide ions such as Cl^-, Br- and I^- [81], which are used as an electrolyte, exfoliation starts when a voltage is applied thus separating graphene layers. These layers are then filtered and dried, resulting in graphene powder. This powder is mixed with 1 methyle-2-pyrrolidinone (NMP) and inserted in the demineralized water where top layer consists of floating ethyl acetate. While ethyl acetate evaporates in the air, a graphene sheet starts to form at the surface of the water which can then be collected on the substrate and dried in an oven.

2.8.3. Conductivity (layer number, doping, crystallinity)

Conductivity of graphene is directly associated with the number of layers it has. A Single-layer graphene, in particular, exhibits exceptional conductivity due to the π-bonding structure inherent in its hexagonal lattice. This unique arrangement allows electrons to move with minimal resistance, resulting in high carrier mobility. However, as additional layers are added, the conductivity starts to decrease[82]. It is vital which technique is used to grow graphene as it impacts the control over the graphene layer. Monolayer graphene can be obtained through methods such as adhesion tape exfoliation or the chemical vapor deposition (CVD) process. In contrast, when aiming for bilayer or multilayer graphene, the CVD process serves as the primary technique for achieving controlled growth.

Crystallinity is another key factor affecting graphene's conductivity. High-quality, defect-free graphene with a well-ordered lattice structure exhibits superior electrical properties[83]. Techniques like CVD on single-crystal metal substrates promote the growth of high-quality graphene with fewer defects, enhancing its conductivity. Conversely, polycrystalline graphene or graphene with imperfections like vacancies and grain boundaries can scatter charge carriers, leading to reduced conductivity. Growth methods, such as liquid-phase exfoliation and the reduction of graphene oxide, can also be employed to produce graphene.

2.8.4. Frequency response

Graphene's frequency response pertains to its characteristics and effectiveness when exposed to different frequencies of electromagnetic signals. The distinctive electronic properties of graphene make it a very interesting material for applications of frequency-dependent responses. The frequency response of graphene has been a subject of research and has shown promising potential for various applications. For instance, graphene-based field-effect transistors (GFETs) have emerged as a notable example of harnessing this property[84, 85]. Moreover, graphene's remarkable carrier mobility and frequency response render it appealing for applications in radio frequency (RF)[86].

2.8.5. Characterization

Graphene can be characterized using various techniques, including Raman spectroscopy and atomic force microscopy (AFM). Raman spectroscopy is a useful tool for characterizing graphene as it can identify the structure of graphene, the number of layers, and the presence of functionalization such as nitrogen or hydrogen. The Raman spectrum of graphene shows distinctive features that can differentiate between single, double, and multi-layer graphene[87]. On the other hand, AFM is used to determine the number of layers and the lateral size of graphene sheets. It can also provide topographic information and is commonly used to determine the thickness of graphene and related 2D materials.

Raman spectroscopy is a simple and effective tool for characterizing graphene. It sheds light on the vibrational modes and crystal structure of graphene through distinctive bands such as G, 2D, and D. The G band signifies the hexagonal lattice, the 2D band reveals layer information, and the D band indicates the presence of defects. This non-destructive technique is crucial for determining graphene layer count and assessing its quality. as it can provide information about the structure and functionalization of graphene. On the other hand, AFM, based on the principle of scanning a sharp tip over the sample surface, provides high-resolution 3D topographical maps. AFM is particularly useful for discerning layer thickness, identifying defects, and offering atomic-scale details of the graphene surface.[88].

2.8.6. PyC

PyC, is a unique form of carbon material renowned for its versatile and adjustable mechanical, electrical, and thermal properties. Also is known for its low density, high impermeability to gases and liquids, excellent chemical stability, and good thermal and electrical conductivities. Unlike graphite, PyC is does not transform into crystalline graphite at any temperature and remains hard and isotropic. The material was first observed in the mid-1950s and has since been the subject of intensive study due to its unique properties and various applications[20]. Wide range of applications has being explored utilizing unique properties of PyC, such as electrodes in supercapacitors, materials for water desalination device electrodes, electrochemical sensors, energy storage devices, tools for precision moulding, and even medical applications like heart valves and neural implants[89, 90].

Production of PyC

The conventional method for producing PyC involves the process of chemical vapor deposition (CVD)[91]. In this process, a precursor gas, typically a hydrocarbon like methane or acetylene, is introduced into a high-temperature reactor chamber. The chamber is heated

to temperatures ranging from 1000° to 2000, leading to the pyrolysis of the precursor gas. During the pyrolysis stage, the gas breaks down into carbon atoms, and these carbon atoms then deposit onto a substrate material through controlled growth. The substrate, often shaped to the desired form, serves as the foundation for the PyC layer. The resulting PyC film, characterized by its structure, finds applications across various fields. One notable application is its suitability as an electrode for supercapacitors[92], capitalizing on its unique properties. The size of the build volume or working area is a pertinent limitation, particularly for large-scale fabrication, requiring specialized equipment and potentially elongating production times. Speed of production is a factor, influencing the feasibility of fabrication methods for applications where high throughput is essential.

3. Literature review

3.1. Contrast MIC designs

3.1.1. Operating Principle

MIC devices contain two electrically excited electrodes which are embedded into the walls of a fluid channel, they are typically made using easy to handle and transparent materials such as PDMS and glass. Interdigitated electrodes are implanted inside the microfluidic channel which carry AC voltage driving an alternating field within the channel. The channel is typically designed to manipulate small volumes of fluids on the micrometre scale such that electrical fields can be applied to a small region to obtain high levels of sensitivity to dielectric changes. The fluid flow is controlled by peristaltic or micro-stepping pumps. Some of the common electrode configurations are con-planar, parallel, and constricted channel electrodes as shown in **Figure 8**. As analyte fluid which contains particles/cells flows through the channel, the moving particles interact with the electric field generated by the AC voltage across electrodes. These interactions can change the electrical properties which are detected as a change in the complex impedance of a circuit containing the MIC.

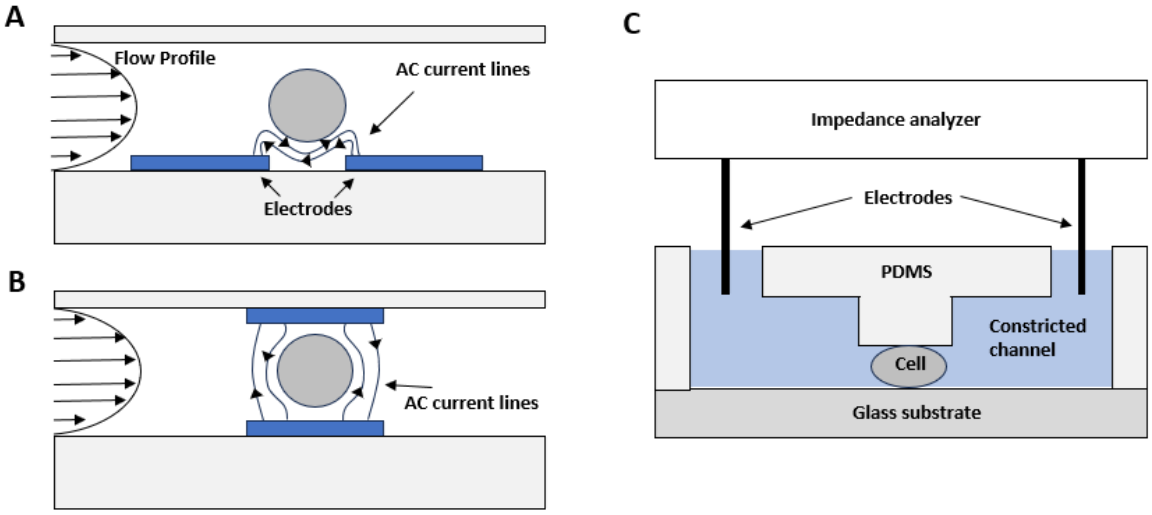

*Figure 8:**A)** illustration of coplanar electrodes design and AC field disruption when a cell flows through the detection region, **B)** Illustration of parallel electrodes design and AC disruption & **C)** Illustration of construction channel design.*

Microfluidic impedance devices most commonly use AC signals to determine a change of impedance in the channel which relates to this displacement of fluid with a high dielectric constant with a cell or particle with a lower dielectric constant. In general, magnitude of the impedance change is used as a measure of particle size. However, different frequencies of the AC voltage can be used to reveal distinct cell properties. **Figure 9** illustrates frequency dependencies, in particular highlighting how lower frequencies indicate the cell size, while higher frequencies could be used for cell membrane characteristics[93]. The impedance in the system can be characterized by the parameters such as resistance (Ω) and capacitance (F). Some of the MIC devices implement multi-electrode arrays, providing spatial information of the cell distribution and enabling the study of heterogeneous cell population. The change in the parameters of resistance (R) and capacitance (C) allows for extracting information about the concentration of particles. The raw impedance data is processed and analysed using

algorithms to extract meaningful information. This may involve comparing impedance profiles, amplitude changes or phase shifts.

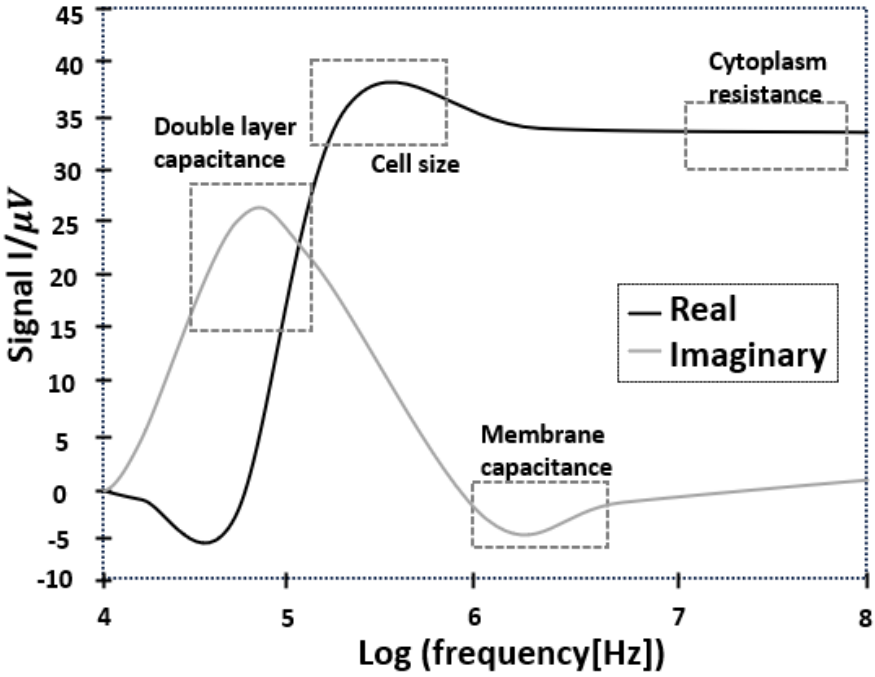

Figure 9: illustrates that the Impedance response at different frequencies carries different information regarding the cell[93]

MIC devices offer advantages like high sensitivity, rapid analysis, and the ability to perform label-free measurements. The requirement of small volume makes them suitable for application in medicine or where the sample availability is limited.

3.1.2. Measurements approaches

Impedance measurement approaches for MIC devices vary depending on the device and its design. However, some of the more common approaches include:

- **Direct Current (DC) impedance measurements:** This technique involves applying constant current to the microfluidic devices and measuring the resulting voltage across the electrodes[2]. The impedance can then be calculated using Ohm's law. These measurements are relatively simple and straightforward, they can provide accurate impedance measurements at low- frequencies and are suitable for steady-state impedance values. However, it does not provide detailed information about the sample's frequency-dependent behaviour and does not capture the dynamic change.
- **Alternative Current (AC) impedance measurements**: In this technique, an AC signal of set frequency is applied across the electrodes and measuring the corresponding voltage response[94]. The impedance can be determined by analysing the amplitude and the phase shift of the voltage response single with comparison to reference input signal. This technique allows for frequency-dependent analysis of the sample, providing information about its electrical properties at different frequencies. Can be used to analyse the electrical properties of cells and enables the detection of changes in impedance over time.

- **Frequency Sweep impedance measurement:** This approach involves sweeping the frequency of applied AC signal over a range of frequency and measuring the corresponding voltage response[95]. By analysing the impedance at different frequencies, Capacitive and resistive properties of the cell can be obtained. This technique helps identify the characteristic frequencies associated with specific cell and differentiates between different cells. Due to the sweep of range of frequencies, longer measurement time is needed, also resulting in complex data for analysis.
- **Time-Domain Impedance measurement:** This technique involves analysing the transient response of the device to a step input signal. By measuring the voltage or current response over time, the impedance can be calculated using a Fourier transform[59]. These measurements can provide information about the dynamic behaviour of the sample, such as its relaxation time, and response to changes in the applied signal. This method can be used to study the transient phenomena, looking into the adhesion or migration of cells. Furthermore, it can provide insight to the kinetics of the cellular processes. However, it requires precise timing and synchronization for the accurate measurements, resulting in sensitivity to noise and alien artifacts in the time-domain signals. Data analyses is complex and more challenging compared to the frequency-based approach.

It is very important to keep in mind the advantages and limitations when selecting an impedance measurement approach for the MIC devices based on the specific requirement and objectives of the application. Considering the cell size and count application, measurement approach chosen for this research was AC impedance.

3.1.3. Design types

There are multiple methods of designing the electrodes in a MIC device to create a sensing region. The most prevalent configurations are now described: coplanar electrodes, parallel electrodes, and constriction channel. Each design is based on a similar detection principle, with excitation electrode and sensing electrodes embedded inside microfluidic channel to establish electrical measurement.

The coplanar electrodes configuration was first proposed by Gawad et al[93] In this design, coplanar metal electrodes were integrated in a microchannel and non-homogeneous electric field was generated. The authors carried out the simulation of cell impedance from equivalent circuit model and their simulation result showed that different parts of impedance spectra contain different information about cell components. The design consists of two patterned electrodes located at the bottom of a microchannel, and it is sensitive to the height of particles in the microchannel due to electric field non-uniformity[96]. The fabrication process of coplanar electrodes design starts with the patterning of electrode layer on glass substrate[97]. The channel is fabricated on PDMS substrate and is combined with electrode substrate to finalize a microfluidic device. The whole process can be easily fabricated since only a single alignment is needed to guide electrodes to the desirable position inside the channel[97].

In a parallel configuration, electrodes are placed at the top and bottom or on opposing sidewalls of the channel. Similar to the previous design, two or more electrodes were used to measure the impedance of cell passing between electrodes and impedance of the medium. With parallel electrodes, electric field distribution was less divergent, leading to better sensitivity as compared to coplanar electrode design[98]. However, this design also suffers from the measured signal dependence on cell position inside detection volume. The fabrication process is more complex as compared to coplanar electrode design[99]. In the top and bottom electrode configuration, two alignment steps are required: one for aligning the channel to the electrode pattern, and another for aligning the two chips with electrodes together. Accurate alignment is needed to make the measurement reproducible. For the sidewall electrodes configuration, sidewall electrodes were fabricated by electroplating followed by SU-8/PMDS channel fabrication on top of the electrodes[100]. This can be done with single alignment. However, there is always a vertical gap between the sidewall electrodes and microchannel, resulting in an inhomogeneity of the electric field. This can possibly lead to a slightly poorer performance as compared to top-bottom configuration.

The lack of direct contact between electrodes and cells in MIC can lead to current leakage issues, where the current tends to pass through the high-conductivity fluid surrounding the cell[101]. In order to solve this problem, the constriction channel design was developed[102]. In the constricted channel configuration, electrodes are placed at the top, bottom, or sidewalls of the microchannel. Similar to the previous design, two or more electrodes are used to measure the impedance as cells pass through the constricted channel. The impedance data collected during cell transit provide valuable information about the specific membrane capacitance and cytoplasmic conductivity of individual cells. This configuration allows for detailed analysis of cellular properties at a single-cell level. In the constricted channel configuration, two main electrode configurations have been proposed: the coplanar and the parallel microelectrodes. The fabrication process is more complex as compared to coplanar electrodes design. This complexity arises from the need for two alignment steps: one for aligning the channel to the electrode pattern and another for aligning two chips with electrodes together[103]. Accurate alignment is needed to make the measurement reproducible. Additionally, for the sidewall electrodes configuration, a single alignment step is needed in the channel fabrication process. However, there is always a vertical gap between the sidewall electrodes and the microchannel, resulting in an inhomogeneity of the electric field[101]. This can possibly lead to a slightly poorer performance as compared to top-bottom configuration.

Table 2 summarises the advantages and disadvantages of each of the electrode configurations.

Design		Advantages	Disadvantages
Coplanar electrodes design	Coplanar electrode	Simple fabrication High throughput	Vertical position dependences Low sensitivity
	Liquid electrodes	Simple fabrication High throughout	Lateral position dependences Low sensitivity
Parallel electrode design	Top-Bottom configuration	High sensitivity High throughput	Vertical position dependences Complex fabrication
	Sidewall configuration	High sensitivity High throughput	Lateral position dependences Complex fabrication
Constriction channel		Simple fabrication High sensitivity Size independent electrical parameters Mechanical Property characteristics	Prone to clogging Low throughput

Table 2:Comparison between different impedance cytometers-based electrode configurations.

3.1.3.1. 2-Electrode Design

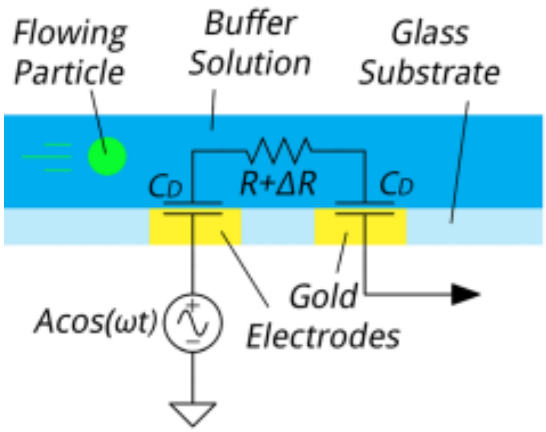

Figure 10: Lateral View) model of particle flow through LIA based biosensor, where R is the base resistance, ΔR is the resistance fluctuation due to particle flow, and CD represents the dielectric capacitance between the electrode and buffer solution[104].

Talukder et al[104], illustrated in **Figure 10**, presents a portable system for personalized blood cell counting, consisting of coplanar electrode based MIC and a portable analogy readout. The novel design of the analogy readout includes a LIA followed by a high-pass filter stage for subtraction of drift and DC offset, and a post-subtraction high gain stage, enabling the detection of particles and cells sizes of $1\mu m$, $3\mu m$ and $8\mu m$ in diameter. 100nm thick gold electrodes were use with $10\mu m$ width and $15\mu m$ apart. Oxygen plasma treatment was used to create addition between the electrode substrate and printed PMDS surface. The frequency of 500KHz was used with 2V input signal. The particle detection was performed with individual particle size solutions but not as a mixture. The system is broadly applicable to assaying a wide range of biomarkers, including proteins, nucleic acids, and various cell types. The research paper describes the implementation of the analogue readout circuit for a portable

battery-powered MIC with smartphone readout, emphasizing its potential for personal health monitoring.

Jason et al[95] presents a notable advancement with micro milled MIC designed for enhanced single-cell analysis. A key feature is the integration of vertical parallel electrodes, achieved through a negative manufacturing process, to improve sensitivity, accuracy, and throughput for cell viability analysis. Using a 75 µm platinum wire embedded in PMMA, the device creates vertically uniform electric fields, addressing challenges seen in coplanar electrode geometries. Jurkat cells, 15μm in diameter, in a low-conductivity buffer were analysed, and an optimal excitation frequency of 2 MHz with 1V was identified for discriminating live and dead cells based on cell membrane disruptions. The study introduces a computational algorithm correlated with video microscopy to determine cell viability status. While acknowledging limitations, such as microelectrode size and data throughput, the micro milled MIC presents a promising and accessible platform for diverse single-cell analyses with potential applications in various biological and diagnostic contexts. Despite its successes, the study acknowledges limitations such as the necessity for microelectrode diameters equal to or larger than the microchannel diameter to prevent undetected cell passage. Data collection throughput was noted to be limited.

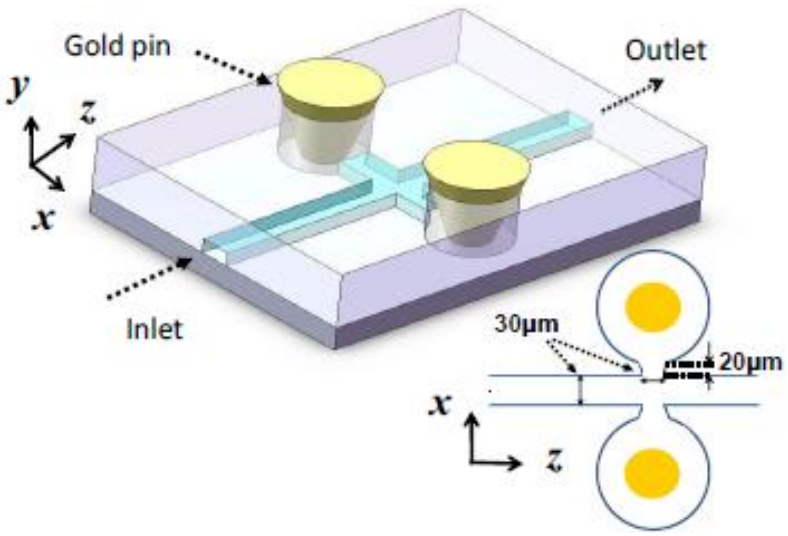

Figure 11: The schematic of device design. Top left: The 3D view of the device. Bottom right: The top view of the device. The dimension of main channel is 30 µm × 30 µm (Width × Height). The opening of sensing area is also 30 µm. Two gold pins are inserted and sealed to both microfluidic electrode chambers[105].

Based on Mei et al[105], a microfluidic cell impedance measurement device designed for point-of-care applications, emphasizing simplicity, compactness, and high sensitivity. The unique design, illustrated in **Figure 11**, utilizes fluidic channels as "liquid electrodes," ensuring a uniform electric field distribution and contributing to the device's simplicity and enhanced sensitivity. 30μm electrode gap was used with 800KHz frequency and 5V input voltage. Notably, the system's cost-effectiveness and compact size are achieved through a sheathless flow design and a single circuit board for cell impedance detection, eliminating the need for costly and bulky equipment such as lock-in amplifiers and additional sheath flow pumps. The device demonstrates its capability to effectively detect and differentiate polystyrene beads

with diameters of 7.66 µm, 10.5 µm, and 14.7 µm in a mixture, achieving low coefficients of variation (CVs) of 13.87%, 7.98%, and 3.74%, respectively. Introducing a novel parameter, impedance ratio, through signal processing enhances the device's cell classification capabilities. In experiments involving lymphocytes and granulocytes detection from whole blood, the impedance ratio proves to be an effective tool. A very low concentration of particle mixture was used with only 150 beads/μL.

3.1.3.2. Multi-Electrode Design

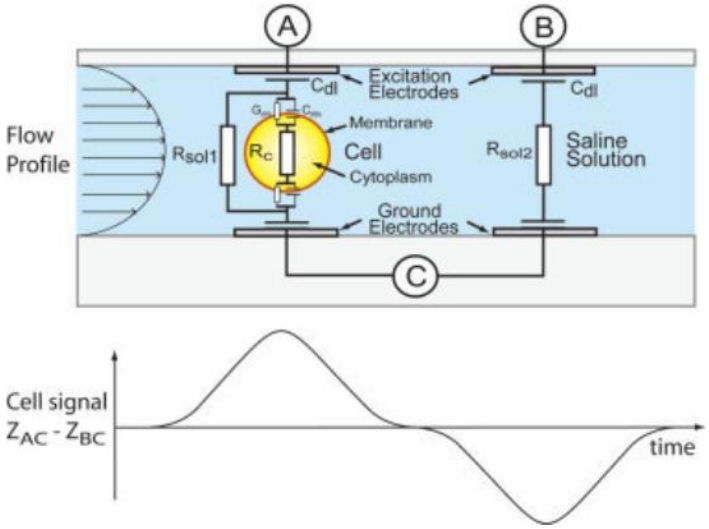

Figure 12: Illustrated in the side view of the microfluidic channel is the transit of a sample cell between the measurement and reference electrodes. Below the schematic, the anticipated waveform of the output from the lock-in amplifier is depicted. This waveform is expected to be observed on an oscilloscope as the cell traverses the detection region within the microchannel[93].

Gawad et al [93] demonstrate that the micromachined impedance spectroscopy flow cytometer is a device used for cell analysis and particle sizing, illustrated in **Figure 12**. It measures the spectral impedance of individual cells or particles, allowing screening rates over 100 samples per second on a single-cell basis. The particles detected were 4, 5.14, 6.0μm. The device is based on a glass-polyimide microfluidic chip with integrated channels and electrodes microfabricated at the laminar liquid flow carries the suspended particles through the measurement area. Each particle's impedance signal is recorded by a differential pair of microelectrodes using the cell surrounding media as the reference. The micromachined chip and processing electronic circuit allow simultaneous impedance measurements at multiple frequencies, ranging from 100 kHz to 15 MHz. This technology is capable of discriminating cells using their electrical parameters as measured by impedance spectroscopy. The device is intended for various applications such as diagnostic cell counting and separation in haematology, oncology, or toxicology.

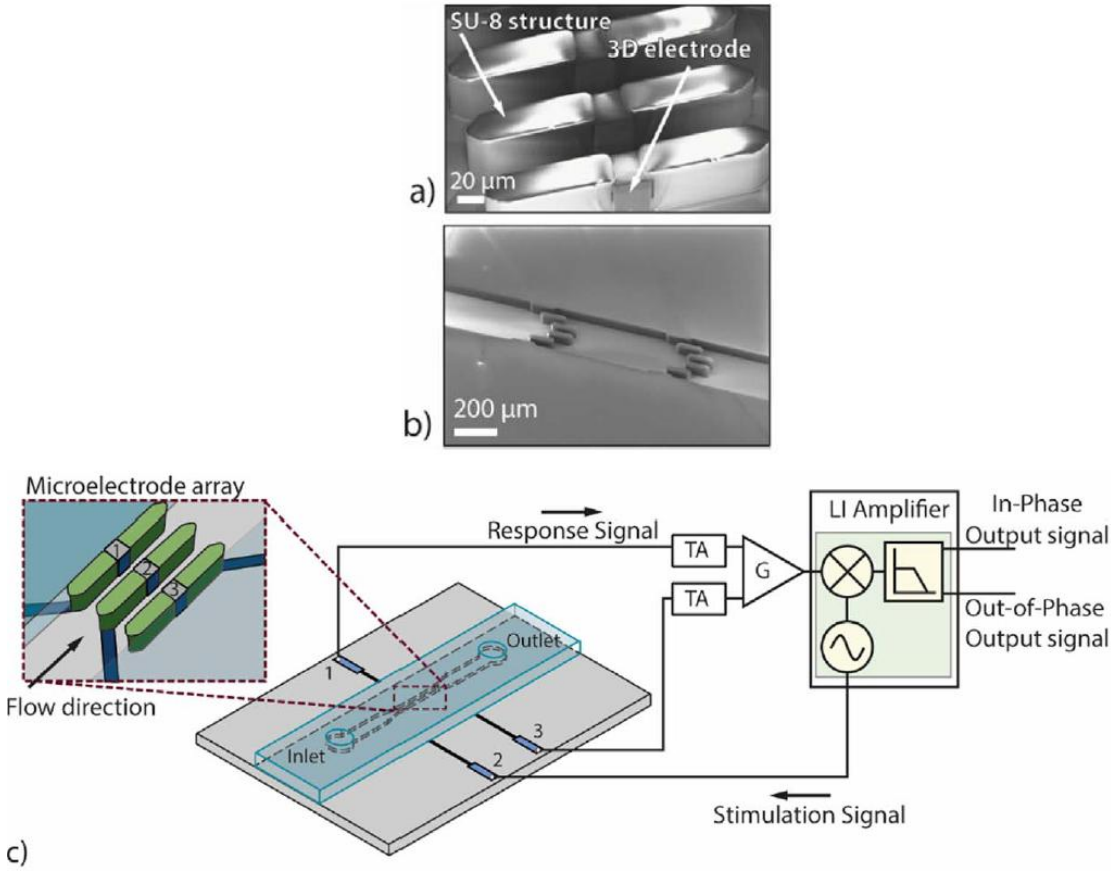

Figure 13: Device configuration diagrams and schematics of the measurement approach. a) SEM picture of 3D microelectrodes and adjacent passive SU-8 elements. b) SEM picture of the filters fabricated in SU-8 to prevent sensor clogging (mostly due to small fibres). c) A sinusoidal voltage is applied using six simultaneous frequencies (ranging from 100 kHz to 27 MHz) to the central microelectrode. The current outputs from the outer microelectrodes are converted to voltage by trans-impedance amplifiers (TA) and then processed differentially by a lock-in amplifier. The zoomed-in detail reports a sketch of the sensor in the microfluidic channel[106].

Based on Rollo et al[106], **Figure 13** illustrates a unique platform featuring Three-dimensional (3D) free-standing microelectrodes integrated into microfluidic channels, allowing for the single-cell detection of in vitro activated T lymphocytes in flow through an electrical impedance-based setup. Six modulated frequencies were applied simultaneously between the range of 100KHz-27MHz to acquire particle flow characteristics. The diameter of 8, 10, and 15μm particles were used with the concentrations of 500,000 beads/ml. The detection was done in the order of 1000 beads per second. The Tri dimensional microsensors on chip, particularly the 3D free-standing microelectrodes and microfabricated channel with vertical platinum electrodes, demonstrate the innovation in the field. The paper not only provides a comprehensive overview of the methodology but also emphasizes the potential applications and advantages of this label-free strategy in the context of adoptive T cell-based immunotherapy.

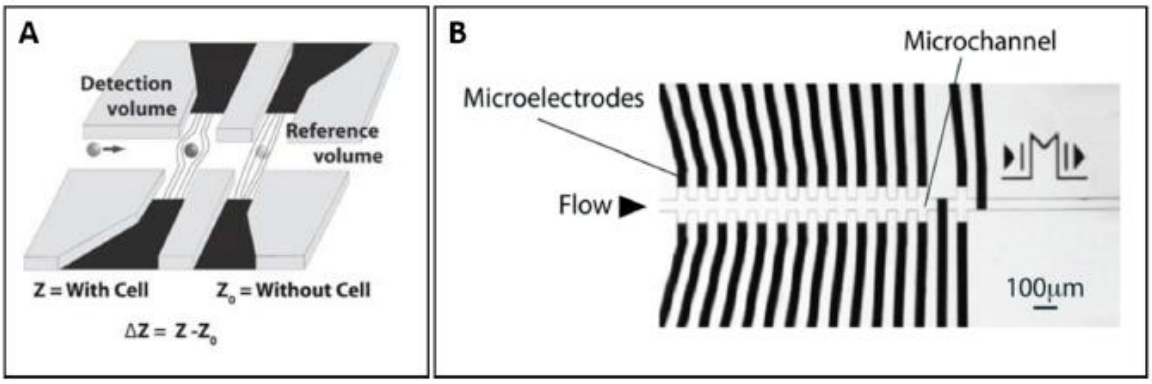

*Figure 14: **A)** Illustration of liquid electrode design. **B)** illustration of combination approach of conventional coplanar electrode design and liquid electrode design[107, 108]*

Based on Valero et al, 2010 [107], due to the non-uniform electric field created by the coplanar electrode configuration, the impedance measurement is significantly influenced by the vertical position of the cell in the detection region. This design, illustrated in **Figure 14**, emphasizes how the positioning of the cell within the electric field affects the impedance measurement, which in turn impacts the accuracy and sensitivity of the analysis. To reduce the effect of vertical position of cell on impedance, another coplanar electrode configuration called liquid electrodes were used [109, 110]. In this case, the electrodes were placed at bottom of lateral channels perpendicular to main channel. As a result, homogeneous electrical field over the channel height was generated. Shaker et al[108] used the combination of conventional and liquid coplanar electrodes configuration shown in **Figure 14B**. Longitudinal measurement and transverse measurement provide different characteristics that can be exploited to detect the shape of particle. The fluid flow was controlled to achieve 100 beads per second on the single cell basis. The frequency used was between 100KHz to 15MHz simultaneously to achieve robust information of the sample. For the cell sorting purposes low frequencies ranging between 50KHz and 150KHz were used. However, this design had several drawbacks. Firstly, the sensitivity is poorer than traditional coplanar electrode design due to the increase in detection volume as the distance between the electrodes pair needs to be placed far enough in order to generate homogenous electrical field across main channel. Secondly, the effect of lateral position rises due to fringing effect at edges of electrodes. In this work, they used di-electrophoresis (DEP) force generated by liquid electrodes to focus the cell at the centre of the channel.

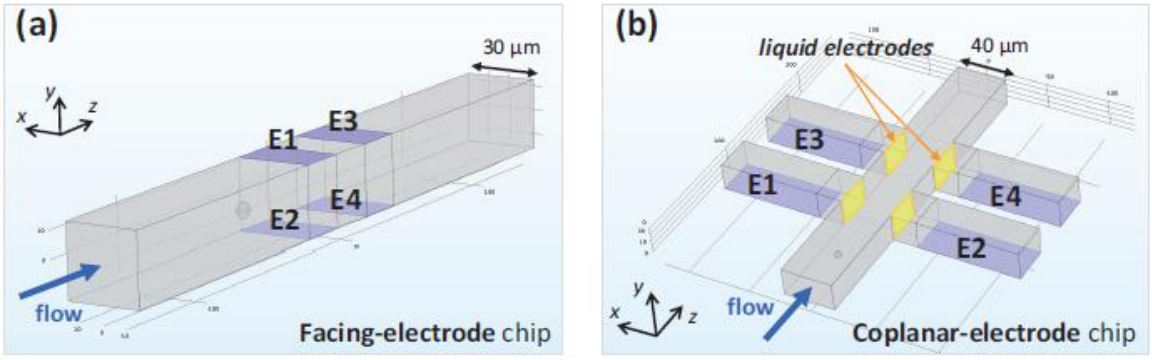

*Figure 15: **a)** Geometric model of a microfluidic impedance chip comprising two pairs of facing electrodes (E1–E2 and E3–E4 pairs). Dimensions are those of a commercial impedance chip by Microunit: 30µm x 28µm cross-section (W x H in xy-plane), 20µm electrode width and spacing; **b)** geometric model of an impedance chip with coplanar electrode configuration: two pairs of liquid electrodes are generated by two pairs of metal electrodes. Dimensions are 40 µm x 21.5µm cross-section (W x H in xy-plane), 30µm lateral channels width and spacing, 20µm electrode recess with respect to the main channel.*

In Caselli et al[111], the geometric model of a standard microfluidic impedance chip with two pairs of facing electrodes is shown in **Figure 15a**. An AC voltage is applied to the top stimulating electrodes (E1 and E3), and the differential current flowing through the bottom measuring electrodes (E2 and E4) is collected. The use of a differential measurement scheme instead of an absolute one increases the signal-to-noise ratio and reduces the effect of electrode polarization. 20μm and 30μm electrode gaps are simulated along with detection of 2 & 6 μm particle sizes. The passage of a flowing particle is recorded as a pair of opposite pulses with the same amplitude. Pulse amplitude measured at low frequency stimulating AC voltage is a measure of particle volume. However, the electric field within the channel is non-uniform, and therefore the magnitude of the measured electrical current depends on particle trajectory height (i.e., y-coordinate of the centre of the flowing particle). A further contribution to pulse amplitude comes from the cross current between the left and right pairs of electrodes (i.e., current flowing through a measuring electrode, E2 or E4, originating from the diagonally opposite stimulating one, respectively E3 or E1). As a consequence of the cross current, pulse amplitude is higher when the particle flows closer to the measuring electrodes than to the stimulating ones. Therefore, the system is asymmetric top to bottom.

3.1.3.3. Constricted Channel

Xie et al [112], describes the design of a sheath-less microfluidic IFC chip with a constriction structure between the detection electrodes to enhance particle sensing performance. The device is designed for rapid label-free cell classification and viability testing. The excitation signal of 1MHz frequency and 0.3V amplitude was applied. The device demonstrates high throughput for single-cell screening, with ability to analyze up to 172 beads per second for statistical analysis. It also shows good performance in distinguishing apoptotic/necrotic cells from live cells, with consistent results compared to traditional flow cytometry. The paper highlights the potential application of the system for novel, compact, and easy operative single-cell analysis systems in the future. The device is based on microfluidic electric impedance flow cytometry (IFC) chips, which have advantages over traditional flow cytometry

systems due to their self-contained, disposable, and economic nature. However, the throughput, sensitivity, and simplicity of these chips are inversely related to each other, and their reported impedance-based cell differentiation capability is generally limited. The sheath-less microfluidic IFC chip described in the paper aims to address these limitations by enhancing particle sensing performance and increasing throughput for single-cell screening.

3.2. Channel Fabrication

3.2.1. Stamp lithography

Stamp lithography, which is also known as soft lithography, has gained prominence in recent years as a most versatile and cost-effective patterning method for micro and nano structures. This technique is inspired by traditional printing processes, where flexible stamps are used to transfer patterns from one sample to the required substrates [113, 114].

The research of Whitesides and Shea in 1996 [115] did pioneering work in this field. They introduced soft lithography as a new approach to microfabrication which opened new avenues for the coming microfabrication researchers. The method involves the use of elastic stamps, typically made of polydimethylsiloxane (PDMS), which can conform to the surface of the substrate and replicate patterns with high precision. This flexibility allows the creation of complex, well-defined structures over large areas.

Stamp lithography includes many different forms, each intended for specific applications. Microcontact printing (μCP) is perhaps the most well-known, as it enables the transfer of functional inks or molecules to substrates, forming patterns with distinct sizes ranging from micrometres to nanometres. This ability has found utility in research areas of biosensing, where accurate profiling of biomolecules is critical [116-118]. Another variant, nanolithography (NIL), takes stamp lithography to the nanoscale. NIL involves pressing a hard stamp with nanoscale properties onto a thermoplastic material onto a substrate, creating patterns with great precision and uniformity. This technique has proven invaluable in fabricating nanostructured surfaces for optical and electronic applications[119-122].

In recent years, researchers have discovered hybrid methods, combining lithography with other techniques to enhance their capabilities. For example, the integration of stamp lithography with inkjet printing has allowed the creation of functional electronic devices with improved performance and complexity[123, 124].

However, stamp lithography is not without challenges. Issues such as master mask (stamp) wear, defects, and limited mask life have been the subject of extensive research to improve the reliability and reproducibility of this technique[125, 126]. Furthermore, advances in materials science have led to the development of new sealing techniques with enhanced durability and performance[127].

Some of the recent application of stamp lithography includes, microelectronics[128], biomaterials patterning[126], microfluidics and optical devices[129].

As further research gets develop, stamp lithography holds the promise of revolutionizing the way micro- and nanostructures are fabricated. The literature reflects a dynamic landscape of innovations and applications, ranging from basic studies illustrating basic principles to practical applications in diverse scientific and technological fields. Stamp lithography's journey into the literature is not just a review of a technology, but rather an account of its transformative impact on the world of nanofabrication.

3.2.2. 3D printing – Two photon Ablation

Two-photon laser ablation is technique involves using a two-photon laser to induce highly focal and precise tissue removal. It has been applied in various research areas, including the study of morphogenetic biomechanics, brain imaging, and targeted cell ablation. Two-photon laser ablation works based on the principles of two-photon excitation. This is a nonlinear process in which the absorption rate depends on the second power of the light intensity[130]. When two photons of near-infrared light are simultaneously absorbed by a molecule, it can lead to the excitation of the molecule to a higher energy state, allowing for precise and localized tissue removal. Two-photon laser ablation works at a wavelength typically in the range between 680 nm and 1300 nm[9, 131]. The technique typically involves using femtosecond laser pulses, which are extremely short pulses of laser light. This enables precise targeting and minimizes the heat generation associated with longer pulses. This process enables the technique to achieve high spatial resolution and minimal damage to surrounding tissue, making it suitable for various biological and biomedical applications.

While two-photon ablation offers many advantages, it also has limitations. The equipment can be expensive, and the technique requires specialized expertise. Additionally, the penetration depth of the laser light is limited, and the effectiveness may vary depending on the tissue type.

Marshall et al[132] describes the use of two-photon laser ablation to infer mechanical tension in cells and tissues, particularly in mouse embryos. The wavelength of 680nm is used with femtosecond pulse laser. The study identifies factors that can affect the interpretation of ablation tests, such as differences in physical properties, viability of cells, and image acquisition rate. The methods have been applied to the closing portion of the mouse spinal neural tube, demonstrating long-range biomechanical coupling of the embryonic structure, and identifying highly contractile cell populations involved in its closure process.

Yamaguchi et al[131] discusses the development of a method for evaluating the focal volume in living mouse brains to increase the two-photon excitation efficiency. The study demonstrates the successful focal laser ablation in deeper brain regions, enabling the dissection of targeted neural processes in living mouse brains. The excitation wavelength used was 910nm.

Hill et al[133] introduces a technique termed two-photon chemical apoptotic targeted ablation (2Phatal) that uses focal illumination with a femtosecond pulse laser to cause highly focal and very brief photobleaching, leading to targeted apoptosis without off-target effects. This method provides a tuneable and reproducible system for single-cell in vivo induction of apoptosis. Two-photon laser was tune to different wavelength for optimal excitation of particular fluorophores, from 775nm to 1030nm.

While the literature results provided some information on two-photon absorption, TPA in general, including its applications in various fields such as laser applications, biological imaging, and material design, there is a lack of specific literature reviews focusing on TPA in the context of 3D printing. Furthermore, TPA at 520nm is not an explored wavelength in ablation regards. The literature mainly discusses two-photon excitation at different

wavelengths, such as between the range of 680-1300nm, for applications like cancer cell ablation and fluorescence imaging.

3.3. Graphene Patterning

Graphene, a two-dimensional carbon material with remarkable electronic and mechanical properties, has gained immense attention for its potential applications in various fields. As researchers try to harness the full potential of graphene, the development of precise patterning techniques has become crucial for tailoring its properties. There are 3 major types of methods used to pattern graphene:

a) **Top-down:** these approaches involve the breakup of large graphene sheets into nano-sized structures with specific shapes using various post-processing techniques. This strategy can be categorized into different types based on the processing characteristics.
b) **Bottom-up:** This technique involves assembling graphene from precursor materials or individual atoms. Bottom-up techniques offer a promising approach, and various methods have been developed to date.
c) **Chemical etching:** This method is defined by selectively binding additives to specific regions of the graphene lattice, not only allows for the adjustment of graphene's electronic properties but also proves advantageous in tailoring its chemical characteristics.

3.3.1. Top-down method

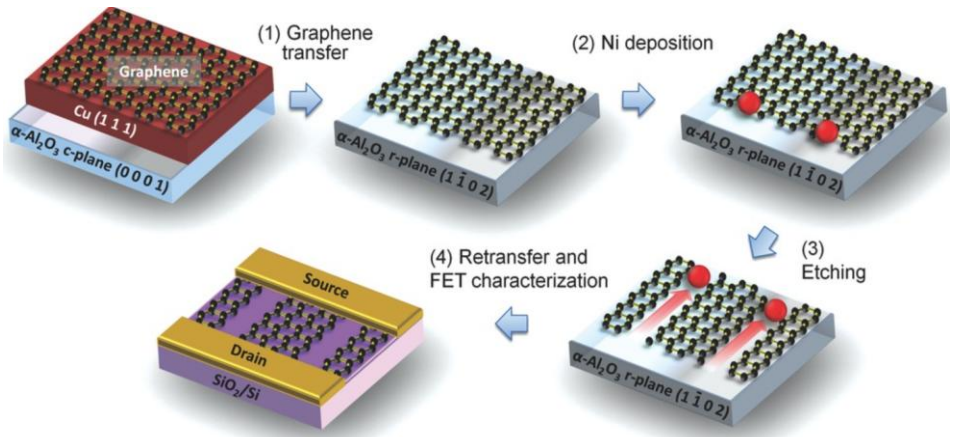

Figure 16: Illustration depicting the substrate-guided etching process of graphene: 1) Transfer of single-layer graphene grown through chemical vapor deposition (CVD) onto r-plane sapphire. 2) Application of catalyst nanoparticles through sputtering. 3) High-temperature metal-assisted etching in the presence of hydrogen. 4) Subsequent transfer back to SiO2/Si and fabrication of field-effect transistor (FET)[134].

Solis et al[134] discusses the fabrication of dense arrays of aligned graphene nanoribbons (GNRs) through substrate-controlled etching of large-area single-layer graphene, shown in **Figure 16**. The research demonstrates the production of these GNR arrays using metal-assisted etching. using nickel (Ni) nanoparticles, graphene monolayer was cut into channels at a temperature around 1100°C in a H2 atmosphere. This process is accompanied by rebound angles of 60° and 120°C. The researcher also have showed the ability to use metal other than Ni, such as Fe[135], Co[136], Ag[137], and Cu[138].

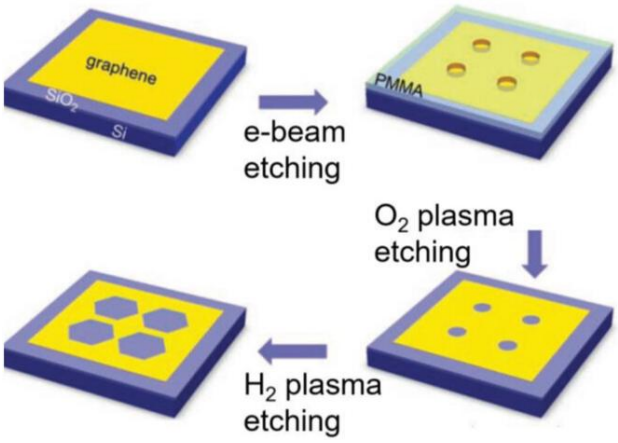

Figure 17: The fabrication process begins with(I) mechanically exfoliated bilayer or multilayer graphene as the starting material. (II) Subsequently, a Poly(methyl methacrylate) (PMMA) resist mask is formed through e-beam lithography. (III) To introduce artificial defects, oxygen-plasma etching is employed. (IV) Finally, anisotropic etching using hydrogen plasma is conducted, leading to the transformation of circular holes into hexagonal shapes [139].

Shi et al[139] presents a top-down approach for controlled tailoring of graphene nanostructures with zigzag edges, represented in **Figure 17**. It consists of two key steps: artificial defect engineering and self-aligned anisotropic etching. The research demonstrates the potential for creating graphene nanostructures with specific edge configurations, which is significant for various applications in nanoelectronics and nanophotonic. PMMA was spin coated with required patterns, acting as protective layer against plasma etching. The process involves creating artificial defects followed by anisotropic etching to produce hexagonal holes with zigzag edges in the graphene material. This approach holds promise for the development of future graphene-based devices.

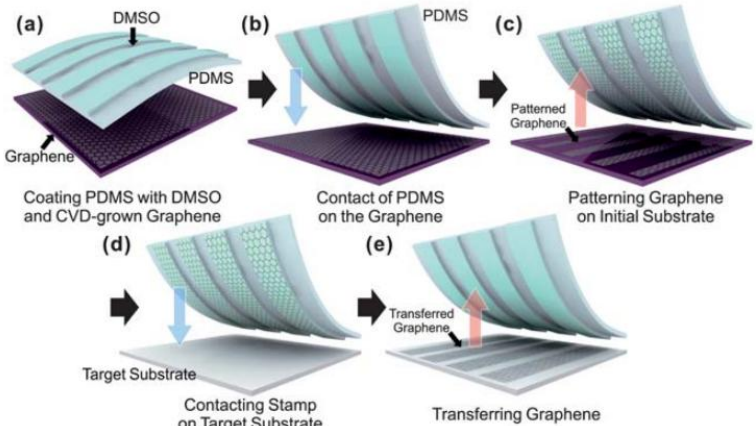

Figure 18: Soft lithographic patterning and transferring processes for CVD-grown graphene sheets involve several key steps. (a) PDMS surface coating with DMSO to enhance the surface energy of PDMS and facilitate the adhesion of CVD-grown graphene on the initial substrate. (b) Bringing the PDMS coated with DMSO into contact with the graphene. (c) Patterning the graphene layer on the initial substrate. (d) Applying the PDMS stamp onto a target substrate. (e) Transferring the graphene from the PDMS stamp to the target substrate[140].

Kim et al[140] demonstrate the synthesis and transfer of graphene sheets, particularly for applications in advanced graphene-based flexible devices such as transistors. Soft lithography is an economical and straightforward technique for patterning graphene using elastomeric stamps, primarily made of polydimethylsiloxane (PDMS), one such technique is illustrated in **Figure 18**. Unlike traditional methods involving photoresists, soft lithography enables direct

application of predesigned PDMS templates onto graphene surfaces, serving as an etching mask. This process is followed by an O_2 plasma etching step to achieve graphene patterning[141]. In another variation, enhanced adhesion between the template and graphene enables direct peeling of graphene from the substrate. To improve adhesive forces by using the hydrophilic substance dimethyl sulfoxide (DMSO)[140]. They modified a PDMS template with micrometre-scale channels by coating it with DMSO through an evaporation method[142]. Upon contact with graphene, the increased interfacial adhesive force allowed graphene to be peeled off from the substrate. The resulting graphene patterns, aligned with the template's channel geometry, could be released from the template through additional heat treatment at 70 °C. Subsequent research demonstrated the application of these graphene patterns as chemical sensors with outstanding performance.

Sing et al[143] shows the ability to focus laser writing on the graphene sheet with required pattern. This method involves inducing a local physical or chemical state transition in graphene using laser-induced heating. For example, a 1064 nm laser was used to selectively oxidize epitaxial graphene films, creating patterns of graphene oxide (GO) lines on a graphene film. Infrared absorption measurements revealed the semiconducting properties of the resulting GO patterns, enabling their application as Schottky junction photodetectors with exceptional photoresponsivity. Additionally, irradiating a suspended graphene sheet with a 517 nm laser caused it to shrink continuously until it ruptured, leading to the preparation of triangular graphene ribbons[144]. Recently, a CO2 laser was utilized to scribe micro-sized trenches into graphene deposited on a flexible substrate. Initially, a graphene film was deposited on a PET film, and after heat treatment, the graphene sample was patterned directly by irradiation with the CO2 laser, resulting in ablation of the irradiated areas[145]. However, the rough edges of the resulting graphene patterns from laser ablation posed challenges.

There are many other techniques that uses this method to get modified pattern graphene, such as nanoimprint Lithography [146], Plasma lithography [147], UV lithography [148], and femtosecond laser writing[149].

The top-down processes, such as lithography and etching, can introduce defects and damage to the graphene structure[150]. This can affect the electronic and mechanical properties of graphene, potentially limiting its performance[151]. While the top-down approach is easier to scale up and less expensive than the bottom-up approach, achieving high-resolution features with top-down techniques can be challenging[152]. The minimum feature size is often limited by the wavelength of the employed lithography method, making it difficult to create extremely fine structures.

3.3.2. Bottom-top method

The technique used in Yan et al[153] is substrate-assisted growth for graphene via chemical vapor deposition (CVD) method. In CVD, a gaseous precursor containing carbon, such as methane, is decomposed on a metal substrate, typically Cu[153], Ni[154], Ge[155], Pt[156], Au[157] or In[158], to grow graphene. The prepatterned substrate provides a catalytic surface for the carbon atoms to assemble into graphene layers.

Some other techniques are known as surface-mediated coupling, and solution synthesis. In surface-mediated coupling, development of atomically precise graphene nanoribbons (GNRs) has been achieved through a surface-mediated coupling procedure[78]. This method involves surface-mediated radical-polymerization and cyclodehydrogenation of aromatic monomers, typically sublimated onto a metal surface like Au (111) or Ag (111). The process begins with the thermal sublimation of aromatic monomers, leading to the cleavage of halogen substituents and the formation of surface-stabilized biradical moieties. These biradicals undergo polymerization on the metal surface, forming linear polymer chains. Subsequent annealing at higher temperatures initiates intramolecular cyclodehydrogenation, resulting in the creation of fully aromatic structures, known as GNRs.

Bottom-up methods may face challenges when it comes to scalability for large-scale production[159]. Achieving uniform and consistent patterns across large areas can be difficult. Some bottom-up methods involve complex chemical processes, which might be challenging to control and reproduce[160].

3.3.3. Chemical etching

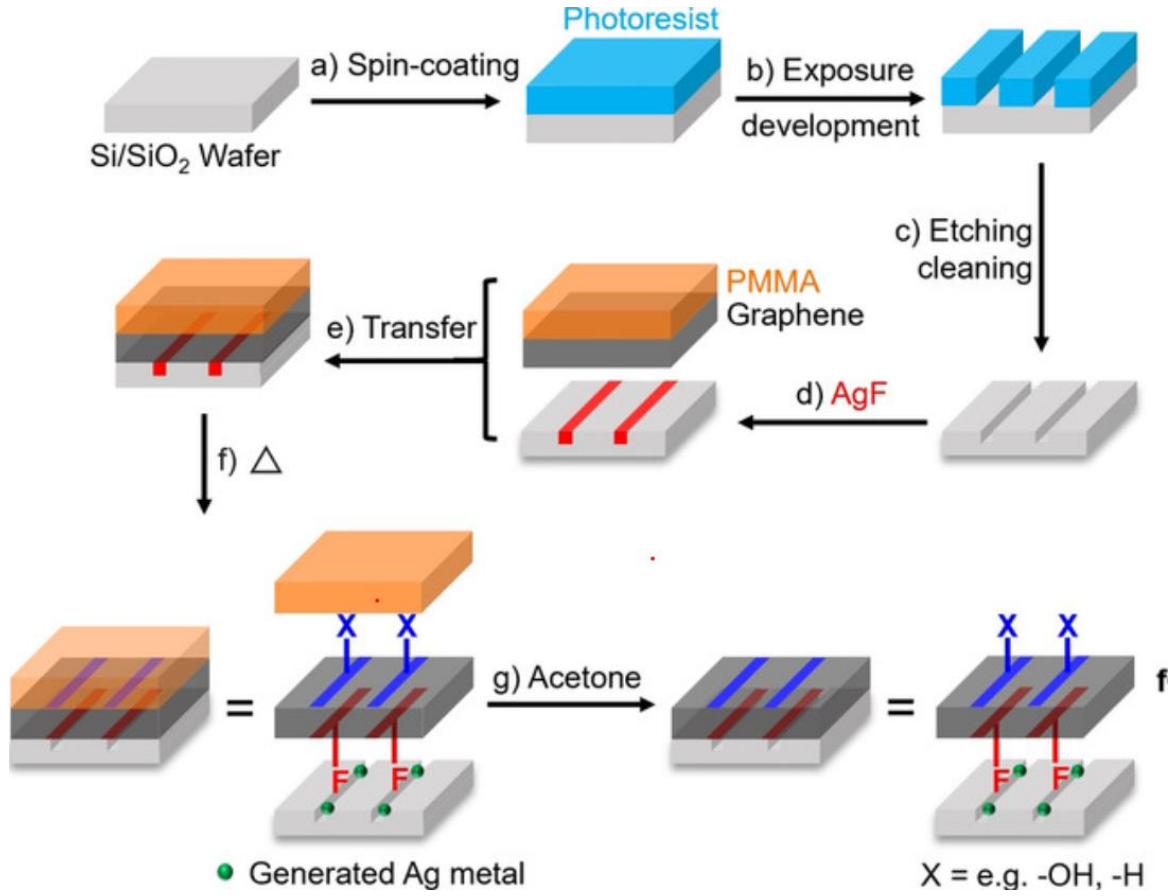

Figure 19: Demonstration of 2D substrate patterning leading to structured bottom-side fluorination on graphene. ***a)*** *A wafer was coated with a positive photoresist layer,* ***b)*** *The desired pattern was created on the photoresist film through exposure UV light via a mask and subsequent development in a diluted solution (NaOH).* ***c)*** *Exposed silicon oxide was etched using buffered ammonium fluoride/hydrofluoric acid, followed by cleaning with acetone, resulting in predefined channels on the wafer.* ***d)*** *An AgF water solution was selectively trapped in these channels using a needle and observed under a microscope.* ***e)*** *Monolayer graphene was transferred onto the wafer.* ***f)*** *The wafer was heated, and* ***g)*** *The PMMA layer was removed using acetone[161].*

Bao et al[161] developed a novel method called "2D substrate patterning" for patterned functionalization of graphene. The approach involved trapping a mild fluorination agent, silver fluoride (AgF), in patterned channels on the substrate to achieve patterned fluorination on the bottom side of graphene, recipe presented in **Figure 19**. The proposed reaction mechanism involves the thermal decomposition of AgF, generating Ag metal and fluorine radicals. These fluorine radicals attack graphene, fluorinating the bottom side and generating dangling bonds on the top side. Reactive carbon radicals on the graphene can then undergo antaratopic reactions with molecules like H_2O or O_2 to form hydroxylation or hydrogenation moieties on the top side. This method offers a facile and efficient way to control the functionalization of graphene and can be extended to other systems using different reactants.

Wei et al[162] planned to enhance graphene's functionalization through successful antaratopic binding of functional entities. The approach involves three main steps: a) activating graphene with alkali metals; b) adopting a strain-free antaratopic addition scenario; and c) structuring using electron beam lithography (EBL) with a poly(methyl methacrylate) (PMMA) mask. Initially, a monolayer of graphene is deposited on a Si/SiO2 wafer, acting as a reactive substrate for strain-free antaratopic backside bonding. A PMMA mask is placed on

the graphene, and EBL creates distinct patterns, selectively exposing specific graphene areas. These exposed regions are activated by reduction with a Na/K alloy, increasing reactivity towards electrophiles. After removing the Na/K alloy, binding of the addend is confined to the uncovered regions via exposure to arylated diazonium salts in degassed/dehydrated ethanol. The final step involves dissolving the PMMA mask with acetone, yielding 2D-functionalized graphene patterns. Remarkably, post-annealing effectively defunctionalizes the graphene, enabling a writing/erasing cycle for chemical information management. Unlike one-step chemical patterning, the current challenge involves creating multiple patterned graphene architectures with distinct functionalities systematically arranged on graphene sheets for advanced high-tech applications.

Chemical etching allows for high precision in creating intricate patterns on graphene surfaces, enabling the fabrication of complex nanostructures[163]. However, it may introduce defects or damage to the graphene lattice[164], affecting its electronic and mechanical properties, among other limitations such as, low resolution, process complexity, chemical waste, and compatibility issues with substrate[165].

3.4. Pyrolytic carbon

PyC is a unique form of carbon that is non-graphitizing and exhibits an graphite like structure[91] but with some covalent bonds. It is typically produced with the help of CVD, with a precursor gas introduced in the high-temperature reactor chamber. It is characterized by high thermal stability, high thermal conductivity, low density, low electrical resistance, and extreme resistance to chemical attack[166]. Unlike graphite, PyC has a fullerene-related microstructure, which gives it unique properties and makes it impermeable to gases and liquids. It is also resistant to crack propagation and has high thermal shock resistance, making it suitable for various industrial applications. It has been explored in different fields such as Electrochemical sensors[167, 168], electrochemical device for water treatment[169], electrochemical device for energy storage[170], biomedical implants[171], and as tool for moulding process[172, 173]. PyC electrodes are commonly used as substrates for the fabrication of electrochemical sensors and biosensors due to their high electrical conductivity and chemical stability.

Zhao et al[174] have highlighted that unmodified GC electrodes serve as simple and cost-effective options for rapid analytical analyses[168, 175]. Additionally, efforts to enhance the reliability, accuracy, and sensitivity of GC sensors involve the incorporation of modifier materials onto GC surfaces[167]. Ideal modifier materials should possess excellent electrical conductivity, chemical and thermal stabilities, strong absorption capacity, good adherence to electrode surfaces, large specific surface areas, non-toxic characteristics, good electrochemical performance, and outstanding catalytic activity. Various approaches have been employed to produce modified GC electrodes for sensing applications. These include decorating with carbon nanoparticles such as carbon nanotubes[176] and reduced graphene oxide (rGO)[177].

Wang et al[178] conducted research on the reaction kinetics of cerium on PyC with in situ electrochemical treatment for cerium-based flow battery. The study investigates the impact of an in situ electrochemical treatment on a PyC electrode, aiming to enhance its activation

and provide guidance for consistent electrochemical measurements. Activated GC exhibits reduced charge transfer resistance and increased double layer capacitance compared to a fresh electrode, attributed to elevated oxygen functional groups. Additionally, carbon oxidation reactions are observed on the bare PyC electrode, emphasizing the importance of considering these effects on electrochemical study accuracy.

Taylor et al[170] systematically explores the impact of oxygen functional groups and carbon microstructure on the activity of the vanadium (V) reduction reaction on a PyC model electrode surface. Various oxygen treatment methods, including thermal, acid, and electrochemical means, are applied to modify the GC surface. Additionally, mechanical polishing on an abrasive surface is utilized to create a rough GC electrode, followed by further electrochemical oxidation. The electrode activity is assessed through cyclic voltammetry (CV), focusing on potential peak separation (ΔEp), which is corroborated by electrochemical impedance spectroscopy (EIS). Surface characterization involves X-ray photoelectron spectroscopy (XPS) to determine oxygen to carbon ratios (O/C) and Raman spectroscopy to probe structural changes. The findings suggest that structural changes, induced by defect introduction and disorder, play a crucial role in improving the catalytic activity of GC for V(V) reduction. The study also posits a limit to the impact of roughness or defect exposure on activity enhancement.

The versatile applications of GC electrodes in electrochemical sensing have been extensively explored. The research has not only emphasized the simplicity and cost-effectiveness of unmodified GC electrodes but has also demonstrated the efficacy of modifying them with various materials, both inorganic and biological, to enhance their sensing capabilities for diverse analytical purposes.

4. Parallel electrode Microfluidic devices

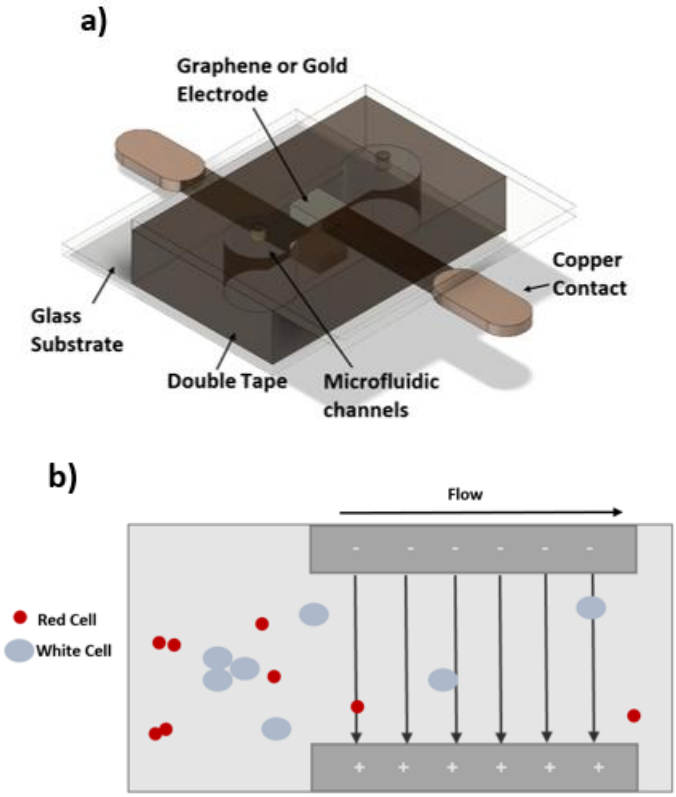

Figure 20: ***a)*** *3D model of the parallel electrode configuration &* ***b)*** *schematic illustrating the particle/blood cells flow & electric field across electrodes.*

In this chapter, we investigate into the challenges associated with fabricating MIC devices featuring a parallel electrode configuration. The primary focus of this research centres around the precision laser machining of channels through various polymer materials. The inspiration for this extensive exploration stems from the microfluidic device depicted in **Figure 20**. The design offers notable advantages, including heightened measurement sensitivity, an improved signal-to-noise ratio, enhanced throughput, and increased resolution. Two primary methods of fabrication were investigated:

- **Double sided tape:** This approach involves the strategic utilization of double-sided tape to construct microfluidic channels. Detailed methodologies regarding the application of the tape and the subsequent channel formation will be explained upon in subsequent sections.
- **3D microfluidic (Two photon ablation) devices:** An alternative avenue of exploration involves the use of two-photon ablation on a Polydimethylsiloxane (PDMS) slab. This technique employs laser-induced processes to intricately create microchannels within the PDMS material. Specifics regarding the two-photon ablation process and its application on the PDMS slab will be thoroughly interpreted in coming sections.

The research analysed and evaluated these two fabrication methods, considering factors such as precision requirements, material compatibility, and overall device performance. The goal is to contribute valuable insights to the field of MIC, advancing the capabilities and

functionality of the devices in question using combination of lasers milling and polymer materials.

4.1. Double-sided tape

When conducting experiments, two types of polymer-based double-sided tapes were utilized: Acrylic Foam Tape 4905F with a thickness of 500 μm and 9460PC Adhesive Transfer Tape with a thickness of 50 μm. Two different laser cutting machines, namely the LS6090 PRO laser cutter (with the wavelength of 10.6μm) and the Fiber Laser (with wavelength of 1.1μm), were employed in combination with these tapes. The goal was to cut the polymer double-sided tape to form channels, sandwiching it between two glass substrates, each equipped with one electrode. The thickness of the double-sided tape determined the channel height, while laser cutting helped achieve the desired channel width. Profilometer was used measure the surface profiles.

The LS6090 PRO laser cutter is continuous wave (CW) and uses a gas mixture, typically composed of carbon dioxide, nitrogen, and other gases, as the laser medium. This gas mixture is contained within a sealed tube[179]. When electrical energy is applied to the gas mixture, it undergoes a process called excitation. Electrons in the CO_2 molecules absorb energy and move to higher energy states. As the excited electrons return to their lower energy states, they release energy in the form of photons[180]. This process results in the emission of laser light. The specific wavelength of the laser light in CO_2 lasers is in the region of 10.6μm, falling within the infrared spectrum[181]. The focused laser beam is directed onto the material being processed. When the laser beam interacts with the material's surface, it is absorbed, and the

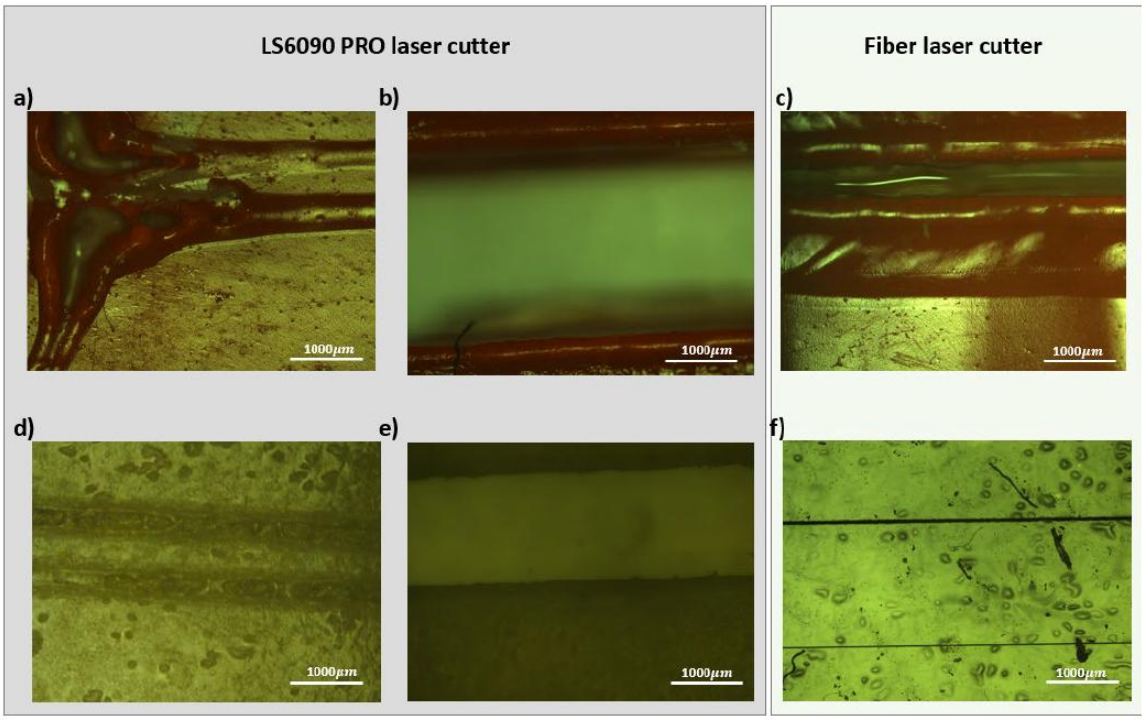

Figure 21: Optical images of patterned double sided tapes with a) & d) are optical images of CO_2 based laser cutter on acrylic and adhesive tape with lowest power and highest speed, b) & e) are optical images of CO_2 based laser cutter on acrylic and adhesive tape with highest power and lowest speed, c) & d) are optical images of Fiber laser cutter on acrylic and adhesive tape.

material heats up rapidly. This localized heating causes the material to melt, vaporize, or undergo a phase change, depending on the laser power and the characteristics of the material[182]. It can cut through wide range of materials including metals, plastics, wood, fabric, paper, and more. It benefits from precision, smooth edges, and non-contact cutting. Some plastics and polymers might exhibit absorption in the power range of 20% to 50%, but this can vary significantly based on the material formulation.

This experiment aims to explore said materials with 2 types of laser printing techniques. Experiments were conducted with varying power (15% to 98%) and speed (15 mm/s to 400 mm/s). Illustrated in **figure 21a)** & **b)** are optical images of acrylic foam tape after laser cut. At **a**) illustrates the used lowest power and highest speed, whereas **b)** was with highest power and lowest speed. In both **a)** and **b)** the thermal laser processing has melted the acrylic tape. Accumulation of material was found around the pattern edges. When laser cutting polymer materials, the laser's heat should ideally instantly evaporate the material. However, that was not the case with acrylic tape. This could be due to low absorption properties of the material, not disclosed by the company. **Figure 21d)** & **e)** shows similar cuts with lowest power and highest speed **d)** and highest power and lowest speed **e)** for Transfer tape. In **d)** it is clear that the laser influence is not sufficient to cut the material resulting in some local melt or polishing of the polymer film, while in **e)**, material has been removed resulting in a cut of 1000μm in width.

it was established that the most optimal setting for the well-defined cuts were at highest power of 98% and lowest speed of 15 mm/s on transfer tape. The transfer tape had the minimum pattern size of 1000μm using CO2 laser cutter, illustrated in e). This was the lowest dimension achieved via these experiments.

The second option for laser cutting for parallel electrode configuration was photon beam-based Fiber Laser. The Fiber Laser is a type of laser that is CW that uses optical Fibers made of a core material doped with rare-earth materials such as erbium or thulium as the gain medium. The Fiber laser is pumped with light from diode lasers or other laser sources. This optical pumping excites the dopant atoms in the Fiber, raising them to higher energy states. As the excited dopant atoms return to their lower energy states, they release photons. When a laser beam is directed at a material, the first step is the absorption of laser energy by the material. The absorbed energy can lead to different outcomes, such as melting or vaporization. In the case of materials like metals, high-intensity laser beams can rapidly heat the surface, causing localized melting. For some materials, especially those with lower melting points, direct vaporization may occur. The intense heat generated by the laser can cause the material to undergo physical changes, leading to its removal. For cutting applications, the material may be vaporized, melted, or ejected as debris, depending on the laser parameters and the material's properties. The benefits of Fiber lasers in cutting applications include precision, speed, versatility, cost-effectiveness, and environmental considerations, making them a preferred choice for many industrial cutting processes. It is capable of handling intensities 100 times higher than CO2. Some plastics and polymers might have absorption in the power range of 20% to 50%, but this can vary based on the material formulation.

Figure **c)** & **f)** illustrates the patterns obtained on both tapes. Using a profilometer, depths were measured 76μm on acrylic tape, which is 500 μm deep, whereas for adhesive tape it were 12μm which is 50μm deep. The laser power settings of 10% to 40% was used, as the setup was still under construction higher power value could not be reached. Although, the accumulation of the melted material around the edges was avoided, the depths of the channel were not accomplished.

Conclusion

The exploration of two distinct laser cutting techniques for fabricating MIC devices using polymer-based double-sided tapes has provided valuable insights into the intricacies of material interactions, laser dynamics, and their impact on device performance. The choice between the CO_2 laser cutter and the Fiber Laser depends on the specific requirements of the channel fabrication. The CO_2 laser cutter showcased simplicity and accessibility, utilizing existing materials and technology. However, challenges such as material accumulation and potential absorption limitations were evident. On the other hand, the Fiber Laser presented advanced capabilities but faced challenges in achieving the desired channel depths, emphasizing the importance of equipment optimization.

4.2. 3D microfluidic (Two photon ablation) devices

TPA is an intriguing process that occurs when two photons, typically from a laser, are absorbed simultaneously by a target material, leading to the removal or alteration of that material.

In traditional laser cutting each individual photon is energetic enough to be absorbed by the material and its energy is transferred into thermal energy causing ablation, typically via vaporization. This means that the laser beam will be absorbed anywhere that it is incident upon the material.

Two-photon ablation is different in that the material may be transparent to the incident irradiation. Only by the simultaneous absorption of the two photons at once will the material absorb the photonic energy that causes the vaporization. Furthermore, TPA is a nonlinear process, the intensity of the light is directly proportional to the amount of material absorbed. This nonlinear nature allows greater precision in the laser applications. Since the likelihood of two-photon absorption increases dramatically with the intensity, when a beam is focused down to a point, the process becomes inherently three-dimensional and localized. This is advantageous in medical applications where surgeons need to target specific tissues or structures without affecting the surrounding areas. This technique is often used in the field of laser surgery and micromachining. A literature review for TPA can be read in **section 3.2.2.**

This section will report upon the development of 3D microfluidic based on TPA. Different carbon-based materials are used to experiment the ablation aspect of the two-photon printing. Subsequently, gold will be integrated as electrodes as parallel electrode configuration is being investigated.

The Fabrication of such a device consists of 2 key stages.

- Metallization
- Two-photon printing

Considering the 2 key stages, a schematic showing the fabrication method can be seen in **figure 22**.

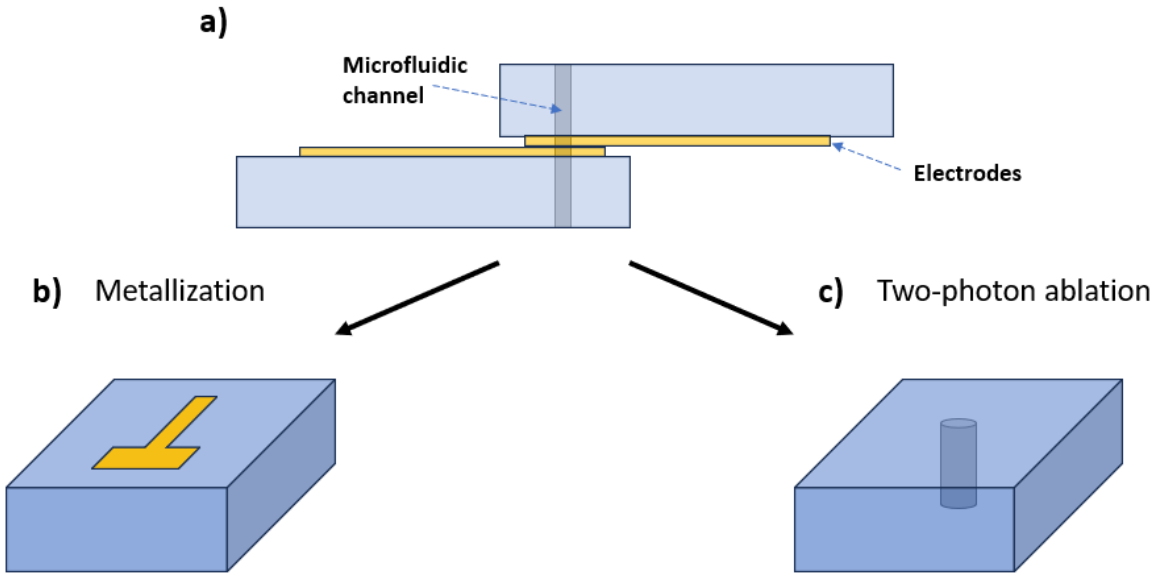

Figure 22: A stack diagram of the steps required for fabrication parallel electrode configuration MIC device.

Where **22a)** presents the diagram of the final MIC device, 2 carbon based substrates are stacked over each other with 1 Au electrode on each side. The Au electrodes are faced towards each other and have a protective layer in between to create a gap which will then lead to capacitance between the electrodes, it is an assembly schematic after **b)** & **c)** are combined. **22b)** presents the substrate with 1 gold electrode printed on it, **22c)** presents the microfluidic channel printed through the material and Au electrode via two-photon printing.

Following fabrication devices are observed using a Nikon Optical microscope, SEM and AFM. For functionality, a fluid flow test is performed.

4.2.1. Two-Photon printing

From **section 3.2.2.** we know how versatile and critical 3D printing have been to research. TPA is a laser-induced process where high-intensity laser pulses are focused on a material, leading to localized vaporization of the material. The TPA has not been explored in context of 3D printing. Nevertheless, this section delves into a novel approach, exploring the application of TPA for printing on carbon-based materials. Four distinct types of carbon-based materials were selected to investigate TPA behaviours. The chosen materials are characterized by being carbon-based, optically clear, cost-effective, and environmentally non-toxic. These four materials include: Polydimethylsiloxane (PDMS), Polymethyl methacrylate (PMMA), Polystyrene and Polycarbonate.

Investigations were performed with different laser powers, repetition rate and xyz stage speeds to obtain patterns on the surface and deep within the material. The femto second

pulse laser is used to perform 2-photon ablation on the samples. Through the utilization of the ablation technique, the material undergoes dissociation as the laser is directed onto a

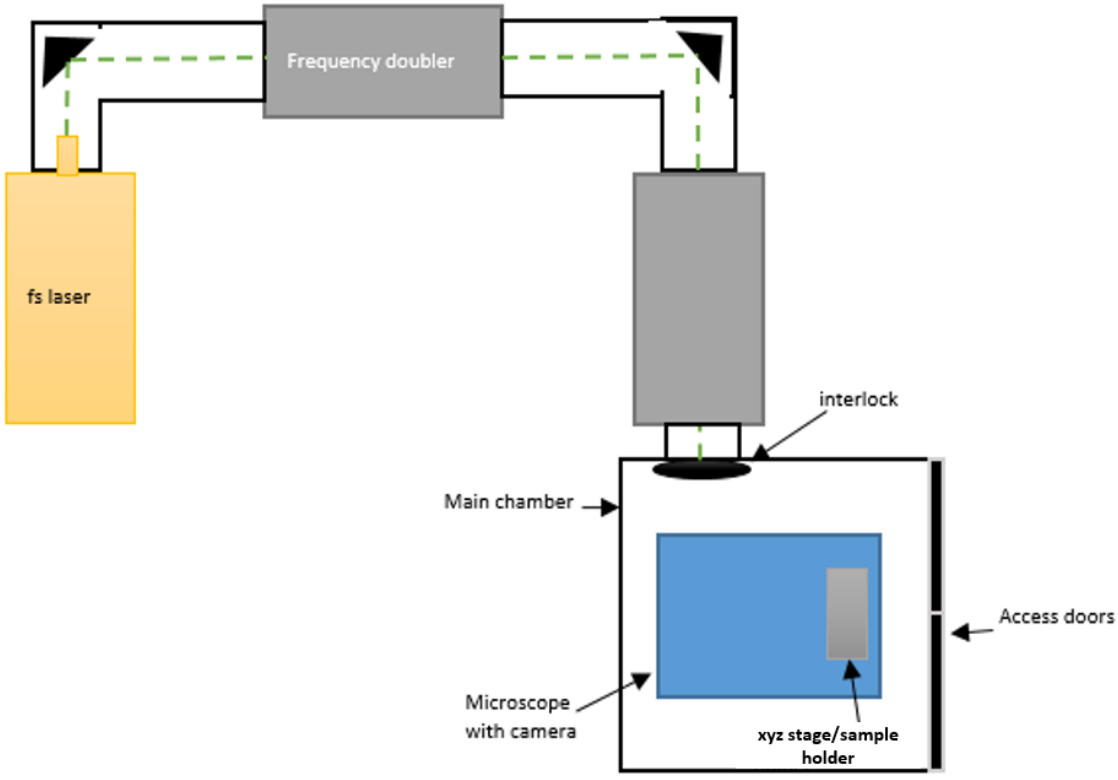

Figure 23: Schematic diagram of the system used for the TPA cutting.

specific point at the focal length of the lens. This process is non-thermal in nature, attributed to the pulsing beam at exceptionally high energy levels[183, 184]. The laser is completely enclosed and at the output it is controlled by interlock. Laser passes through the 5x microscope lens to focus and print on the sample. The Laser instrument used was Spirit One (Femtosecond laser) by Spectra-Physics. Schematics of the laser assembly is provided in **Figure 23**.

The pulse frequncy was 100kHz with laser beam wavelength of 520nm. The energy of the femto pulse laser is between 4W to 1GW. The power of 15%, 20% and 30% were invetigated along with repetitation rate (rep rate) of 1K, 5K and 15KHz, and xyz stage speed of 0.1, 0.17, 0.45 and 0.8 mm/s. As 4 different materials were used to observe the TPA behviour, the results are different, specifically due to the neccesary intensity required for the laser beam to dissociate the material[185].

For experimentation, firstly surface of the materials were investigated with power, rep rate and, stage speed[185]. Once they are optimized, deep cuts within the materials were explored. The process then continues to clean/polish these cuts so they can be used as microfluidic channels.

All the parameters mentioned in the previous section were performed on the PDMS to observe the behaviour of TPA technique on PDMS. The beam was scanned using a microcontroller to obtain the required pattern. Initially, starting with a single line printing at

different speeds moving towards stitch printing of 5-lines. 5-line stitching would have multiple lines next to each other, increasing the size of the trench/channel overall. A smooth surface is required on microfluidic to avoid fluid turbulence[186]. Turbulence can lead to inconsistent flow patterns, which may interfere with precise measurements and analyses, such as in cell detection or particle sizing. A smooth channel surface ensures laminar flow, which is crucial for maintaining stable and predictable fluid dynamics within the microfluidic system, enhancing the accuracy of experiments and diagnostics.

Thus, in 5-line stitch, it is important to overlap most of the area over each other to avoid rough surface. **Figure 24** shows the incorporated method in the stitching technique.

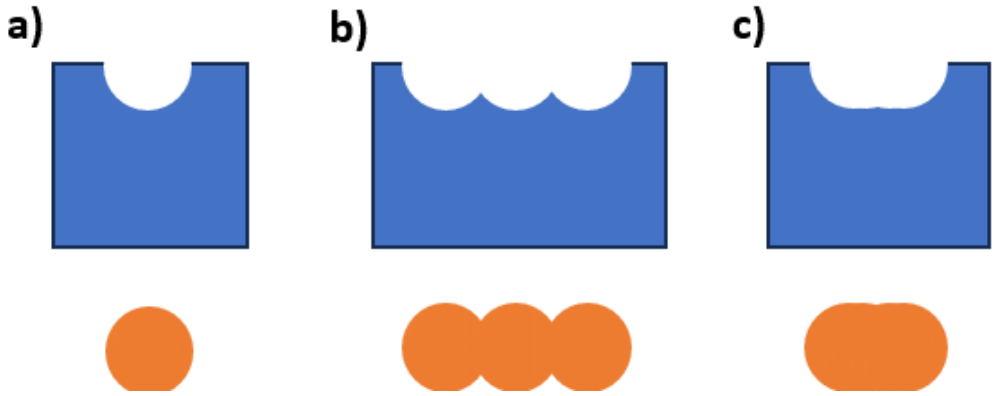

*Figure 24: schematic surface cutting and stitch on the surface. **a)** shows the single line cute, also known to be laser dot, **b)** shows the 3-line cut with some overlapping but not enough to create smooth channel, and **c)** shows the 4-line stitch with proper overlapping cuts so the channel is smooth.*

4.2.1.1. Surface characterization

1. Polydimethylsiloxane (PDMS)

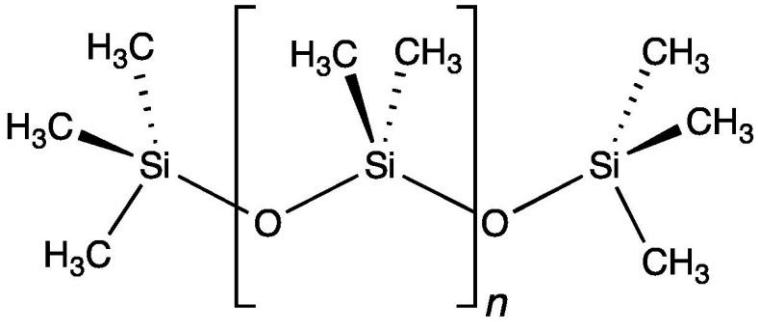

Polydimethylsiloxane (PDMS) is a silicone-based elastomer renowned for its outstanding characteristics. It boasts transparency in the visible and near-infrared spectrum, rendering it well-suited for optical applications. PDMS serves as an effective insulator with commendable electrical insulation properties. Additionally, its flexibility and elasticity enable it to endure significant deformations without incurring permanent damage, making it an optimal material for applications demanding crucial attributes like flexibility and elasticity, such as in soft robotics and microfluidic devices. It is an inexpensive material with biocompatibility[187, 188]. The material is being explored in much current research of different fields, such as bioengineering[188, 189], medicine[190, 191], optical, lab-on-chip[192] and microfluidics.

It is optically clear in the visible and near-infrared spectrum. It typically allows light to pass through with minimal absorption or scattering in the wavelength range of approximately 300nm to 1200nm [193] and is non-toxic[194] thus making it very suitable for TPA printing. This transparency allows the 520nm laser light to penetrate the material with minimal absorption and scattering, ensuring efficient energy delivery to the targeted focal point.

The channel width size also increases with increase in laser power or rep rate. This means, higher powers and rep rates lead to larger trench/channel on the surface when scanned over material. The area of impact increases when these parameters are increased. A single line and 5-line stitching can be seen in **Figure 25**.

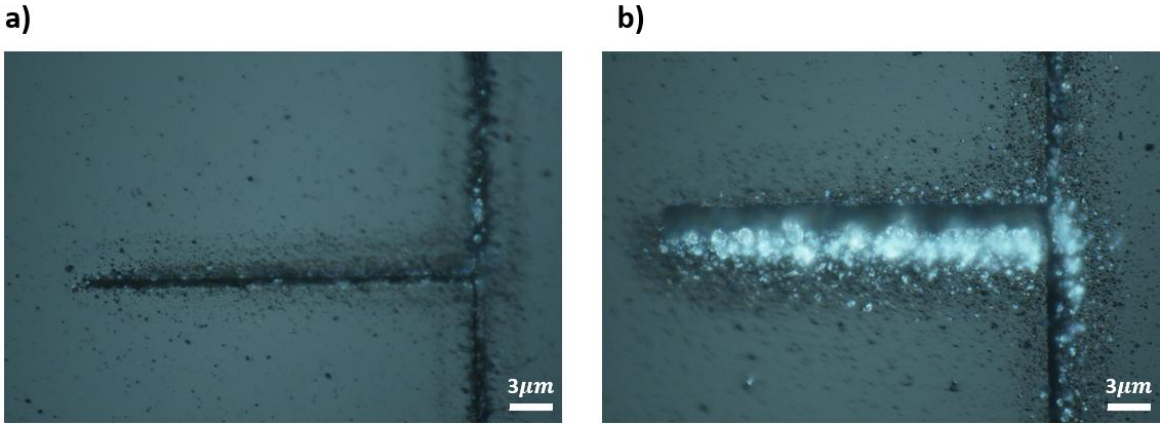

Figure 25: These are the optical images taken from a microscope. The laser power used is 15% and rep rate of 1KHz with the speed of 0.8mm/s. ***a)*** *is the single line cut on the PDMS surface,* ***b)*** *is the 5-line stitch on the PDMS surface.*

Starting with the lowest possible effective settings, we observe the cuts on PDMS. The setting used were 15% power, 1KHz rep rate, and 0.1mm/s speed. The difference in the trench/channel size is visible on the images. A single line is representing the dot size of the laser, is 2.2μm. Where, the 5-line stitched together have given 7.15μm. In **Figure 25a) & b)** we see white particle around the channel mostly, whereas dark material is detected all over the surface. PDMS thermal degradation is typically in the range between 250℃ to 650℃ [195, 196]. When ablation is happening on the surface of PDMS, the material is exposed to very high temperatures ranging from few hundred to thousand degree Celsius. These high temperatures break down the polymer into smaller molecular fragments. The exposed area is decomposed, and structure integrity is compromised, leading to loss of its original mechanical properties[197, 198]. The breakdown composes of Siloxane vapor, ethane, methane, and other gas[197] releases along with carbonaceous residue[199]. The dark material seen on the surface is carbonaceous residue, whereas these white chunks of particles are the unexposed areas of PDMS retaining their original form[200]. These are pushed/blasted away via the release of the gases mentioned above. An important factor to note is the presence of oxygen while material is being exposed to high temperature leading to such outcome of the material[201].

The resulting outcomes from the variation of the control parameters for TPA mentioned earlier are provided in **Figure 26**. These results represent the change of height and width of the debris that was found after TPA measured in distance (μm). As we are to sandwich two

substrates together to form final MIC device, any debris or residues are hindrance to smooth interface.

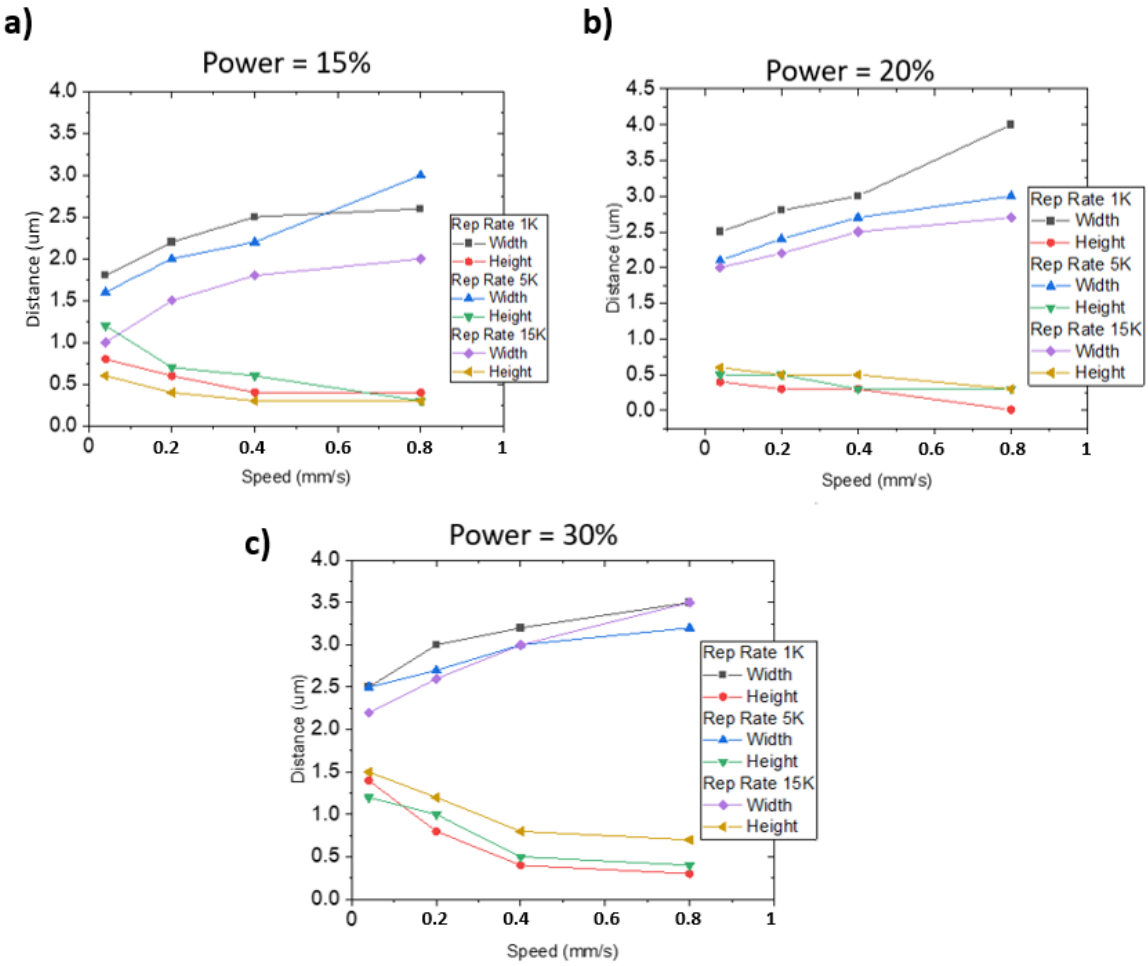

*Figure 26: These are the results of different combinations of laser power, rep rate, and stage speed presenting the impact on width and height of the debris after TPA. **a)** graph shows the experiment fixed at 15% laser power with the rep rate and speed variation. **b)** graph shows the experiment fixed at 20% laser power with the rep rate and speed variation. **c)** graph shows the experiment fixed at 30% laser power with the rep rate and speed variation.*

Each graph presents the fixed laser powers, where **Figure 26a)** are results from 15% power, **b)** are results from 20% power, and **c)** are result from 30% power. From **a)** for 1KHz rep rate at the slowest speed of 0.1mm/s, we can see the width of the debris is 1.80μm on the surface of the PDMS, whereas the height of that debris is 0.75μm. As the stage speed is increased it has impacted on the curve. Taking the maximum speed of 0.8mm/s, the width of the debris has increased to 2.6μm and the height has reduced to 0.4μm. It can be examined, as the stage speed increases the width of how far the debris spread has increased, whereas the height of the debris has decreased.

If we compare the rep rates together at the lowest speed of 0.1mm/s for **a)** we can see 1KHz gives width of the debris is 1.80μm and height of 0.75μm. As for the 15KHz rep rate, the width and height are 1.7μm and 0.6μm, respectively. In conclusion, higher rep rate tends to generate less debris width and height in compared to lower rep rates.

Comparing results depending on powers from **Figure 26a), b)** & **c)**, it can be concluded that the increase in power resulted in increase of debris width and height.

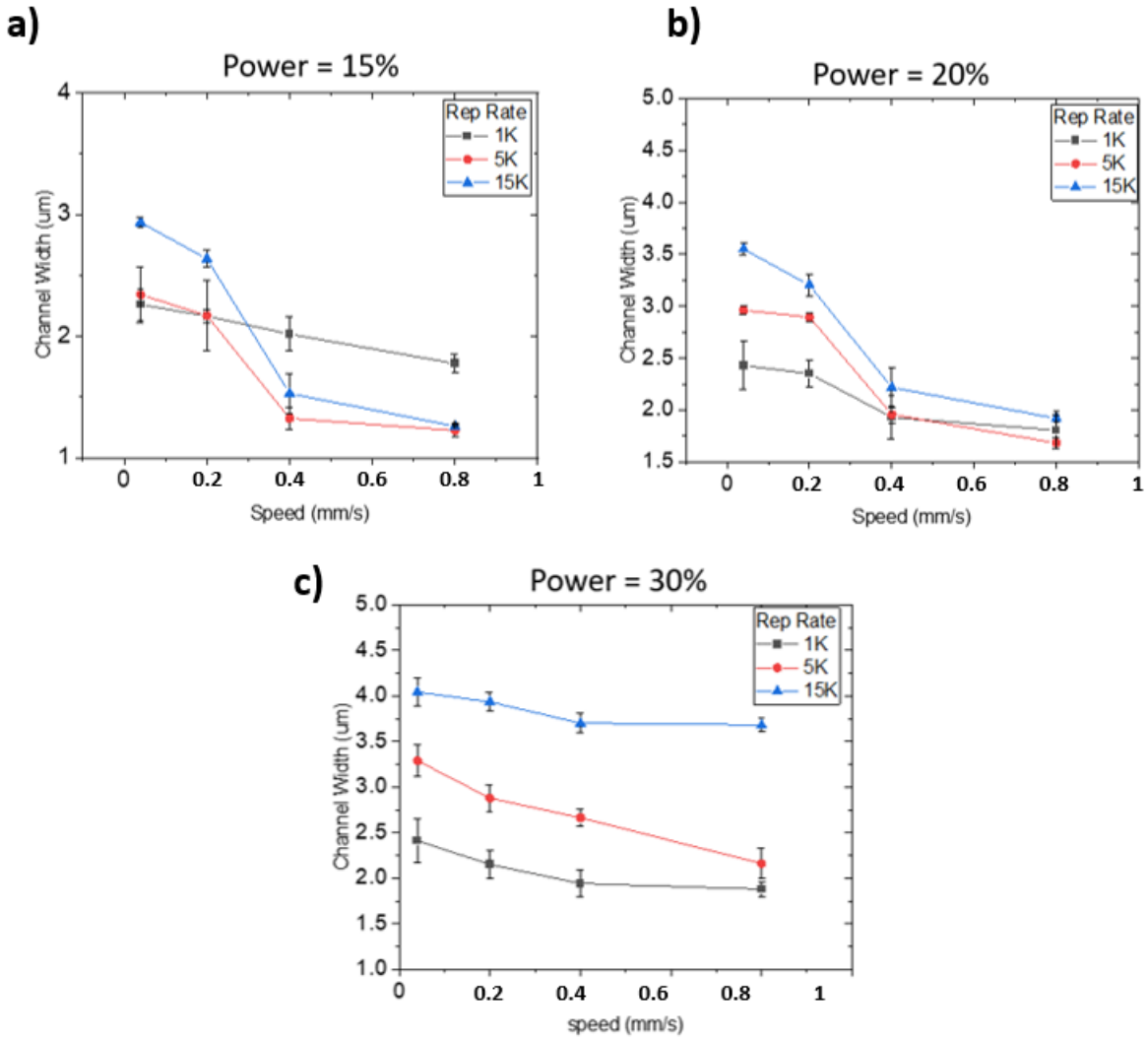

Figure 27: These are the results of different combinations of laser power, rep rate, and stage speed presenting the impact on channel width after TPA. ***a)*** *graph shows the experiment fixed at 15% laser power with the rep rate and speed variation.* ***b)*** *graph shows the experiment fixed at 20% laser power with the rep rate and speed variation.* ***c)*** *graph shows the experiment fixed at 30% laser power with the rep rate and speed variation.*

From **Figure 27**, we can examine the impact of control parameters of TPA on channel width. Channel width represents the single line cut on the PDMS surface. As the speed of the stage increases, we can see the channel width decrease. Whereas, as the power or rep rate increases the channel width starts to increase.

The optimal chosen parameters for multiple line stitching were 30% laser power, 0.8mm/s stage speed and 1KHz rep rate. These parameters were chosen to provide less debris width and height additional to the largest channel width. Larger channel width means less lines required to stitch together, offering larger channel into less time of printing. Distinctly, these debris needed to be cleaned before we would finalize the MIC device.

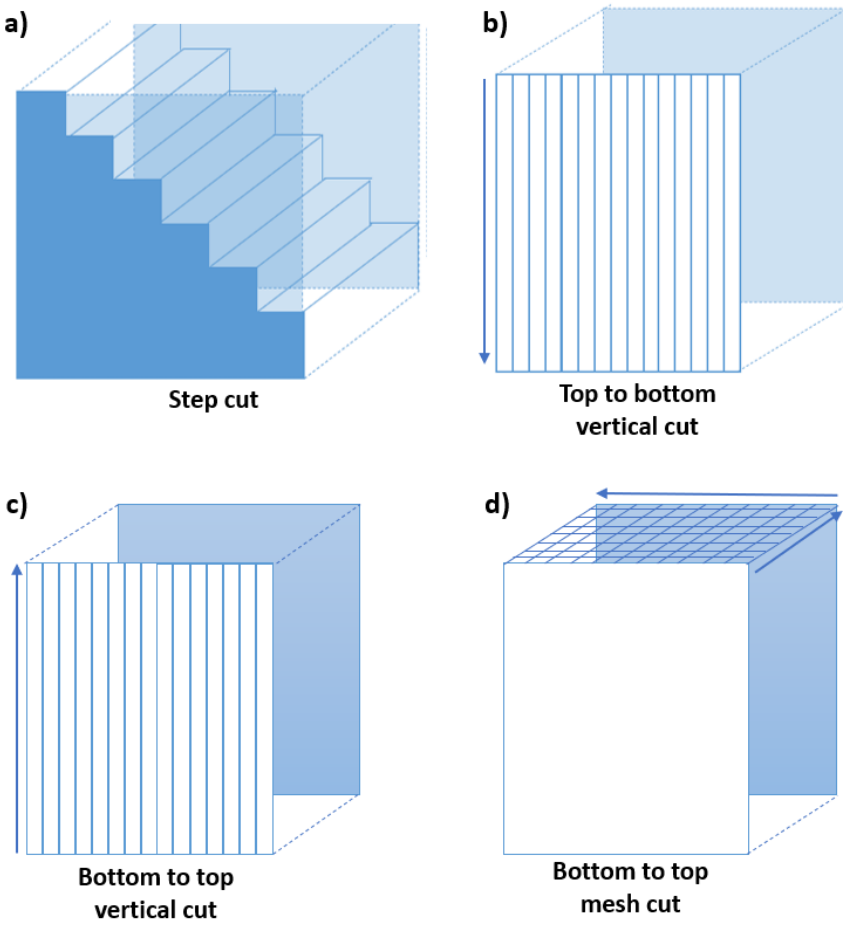

*Figure 28: schematics of the techniques used for vertical in depth cuts, **a)** presents the vertical stepping of the cuts **b)** presents the idea of straight vertical to the sample from surface to bottom, **c)** presents the idea of vertical cuts starting from the middle/bottom of the sample to the top (surface of the sample) and **d)** presents the idea of in-depth mesh cutting.*

Once the optimisation of the parameter was done. Multiple in-depth experiments were performed, Illustrated in **Figure 28**. In **a)** a step cut was performed, this cut was to observe the tidiness of the system on every step and the residual behaviour as it goes deeper into the system. **b)** vertical cuts from surface to in-depth, called top to bottom, was performed to check the ability of the deep cut and its performance. **c)** bottom to top cuts were performed to determine the in-depth cut. In this the cut was started at the middle of the sample and then moved to the surface. This will help determine if the 3D structures can be obtained at the focal point regardless of the surface, also it will help determine the thermal activity. If any thermal activity was to occur, 3D cut in the middle of the sample would not be possible. **d)** bottom to top cut again but this time instead of the vertical movement, a mesh was created. This mesh will smoothen the sample and react to any unexposed debris of PDMS. As the cut is being performed under the surface the material dissociation will be done without the presence of oxygen.

When Step cut from **Figure 28a)** was employed, it was seen that all the debris was either pushed on one side or left within the sample. The side the debris was accumulated was about 5.5μm after a cut of 15μm deep cut, as illustrated in **Figure 29a)**. Debris was not a concern as

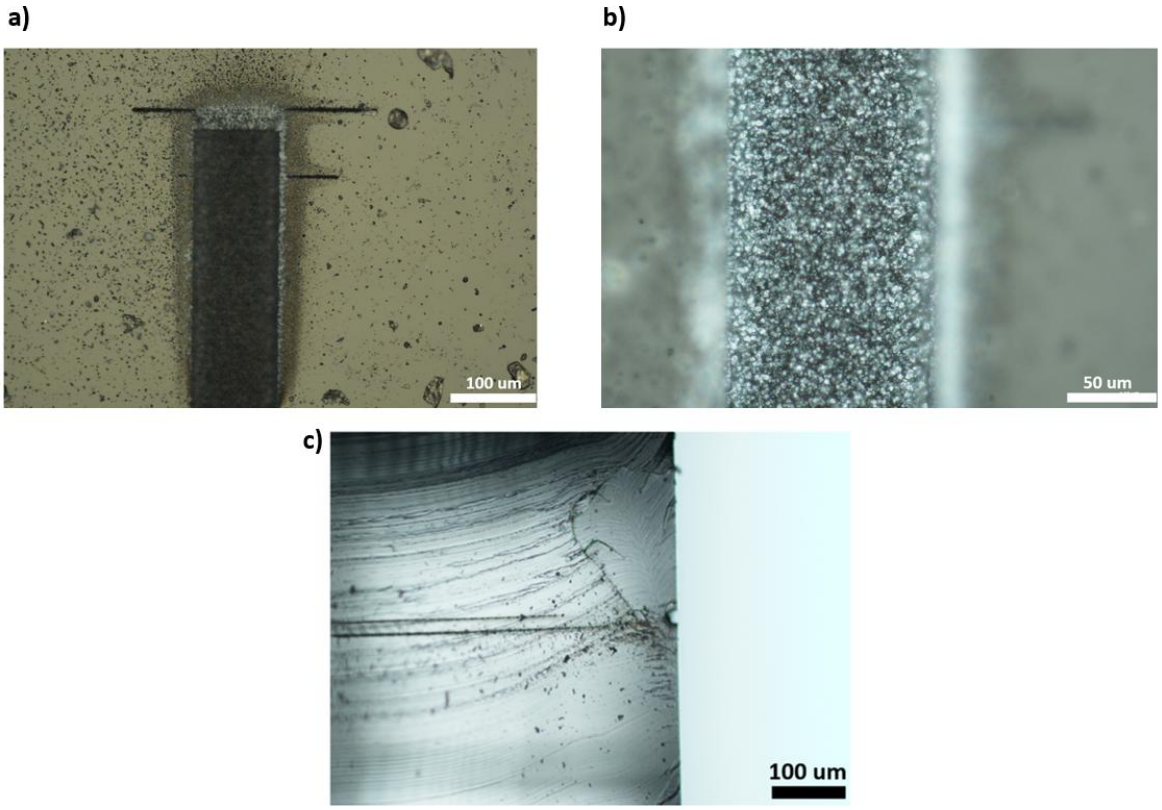

*Figure 29: Optical images to observe the cuts after deep pattern into the material with the method of top to bottom vertical cut **a)** implementing step cut resulted in accumulation of material debris on one side of the cut, **b)** implementing top to bottom vertical cut resulted in debris left inside the channel, and **c)** shows the cross-sectional view of in-deep cut for vertical top to bottom method.*

cleaning was to be performed once the printing was done or optimized. The presence of debris within the channel obstructed deep printing. The debris, randomly sedimented and forming extensive piles, covered a significant portion of the sample. Consequently, it became challenging to focus the laser focal point effectively. The laser was distributed, reflected, and absorbed by the debris resulting in no deep cuts[202]. Same thing was observed when idea in **Figure 28b)** was implemented. After reaching a certain depth of the material, debris starts to accumulate within the channel, resulting in hindering of the deep cutting within the material[203], **Figure 29b)** illustrates the debris on the base of the patterned channel. The deeper the cut, lesser the chance of the debris to explode out of the channel, it rather falls back into the channel and causes obstruction in the focus of the laser beam. The limit of depth observed in top to bottom vertical cut was between 18μm to 23μm. This it obviously not the most viable option, thus vertical cut from bottom to top were performed, methods are illustrated from **Figure 28c)** & **d)**.

In bottom to top mesh cut, the laser is focused deep within the sample and a continuous cut is performed as multi-line stitching forming a square shape. After a single plane is exposed to laser a z step is added on the stage to raise the beam focal point and then it continues the same plane exposure of the beam. This process lasts until the laser beam hits the top surface of the material. This method had worked very well in deep patterning of PDMS. **Figure 30** illustrates microscope images.

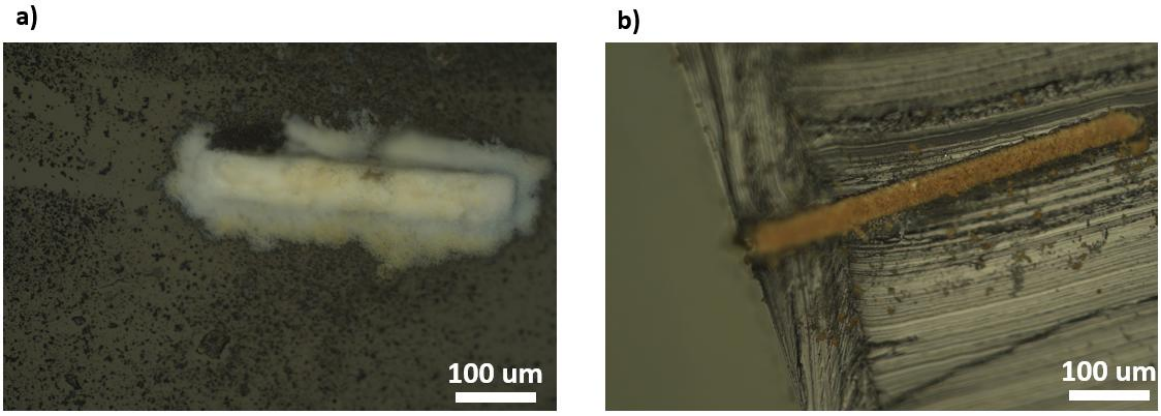

*Figure 30: Microscopic images of bottom to top mesh cut. **a)** is the top view of the patterned area, where a lot of white particles are covering the area in and around the channel, and **b)** is the cross-sectional view of the channel once is having been cut in half. The residual material can be seen in brown colour.*

For the purpose of ease, the channel was patterned wider (rectangular shape instead of square) so a cross-sectional cut can be performed to observe inside of the channel, as illustrating in **Figure 30a)**. The channel depth at this point was set to 600μm, and was effectively achieved.

With success in deep cutting, the residual material was to be removed to progress further. Generally, PDMS is not an ideal material to clean, some of the common solutions include isopropyl alcohol (IPA)[204], ethanol [205], or a mild detergent solution[206]. PDMS is then submerged in the cleaning solution, ensuring that the entire surface is covered. Allowing it to soak for enough time, usually a few minutes to an hour, depending on the level of contamination. This method is used to clean the surface of the PDMS where some impurities are expected from the environment. However, when it is in-depth channel cleaning these methods fail to be of any effective use.

Another method used is swelling of PDMS material. Swelling PDMS involves exposing the material to a suitable solvent, causing it to absorb the solvent and increase in volume[207]. Once the PDMS is removed from the solution and left to dry, it maintains its original size. Expansion and retraction of the PDMS helps remove the particles that are not chemical bonded with the surface. Some of the common solvents for swelling PDMS include hexane, toluene, xylene, heptane, and chloroform[207, 208].

Two methods were investigated to remove the residual material from the PDMS channels after TPA was performed on them.

- **Swelling in Chloroform**:

The desired PDMS slab with deep pattern is placed in the Chloroform and left for 1 hour. Ensuring that the PDMS sample is completely submerged in the solvent. The beaker is than placed on a Sonicator to agitate the reaction. The sonication will help the solvent to reach deep within the sample and have a better surface of reaction. However, the swelling under agitation was not enough to remove the residual debris from deep within the sample.

- **Polishing with Sodium hydroxide (NaOH)**:

NaOH is also known as caustic soda, it is a strong base, and its interaction with PDMS can lead to various effects on the material. It may lead to changes in surface roughness, hydrophilicity, and chemical composition. This modification is often exploited for applications where enhanced surface properties are desired[209]. The treatment with NaOH can make the PDMS surface more hydrophilic. This is often useful in applications where increased wettability is required, such as in microfluidic devices or cell culture substrates[210, 211]. Using the aspect of hydrophilic surface change, a novel approach of using NaOH bath to remove the deep patterned residual material was performed. However, NaOH is known to cleave siloxane (Si-O-Si) bonds. This can lead to the breakdown of the PDMS polymer chains, causing changes in the material's structure and mechanical properties[212, 213]. The extent of siloxane bond cleavage depends on the concentration and duration of exposure to NaOH. Several concentrations were tried, amongst them the optimized recipe was 1M concentration of NaOH in sonication for 3 hours. 40g of NaOH was dissolved in 1 litre of DI water to obtain the 1M concentration. **Figure 31** illustrates the microscope images after cleaning of the sample was done with the chosen recipe. The samples are clean, and no residue is observed.

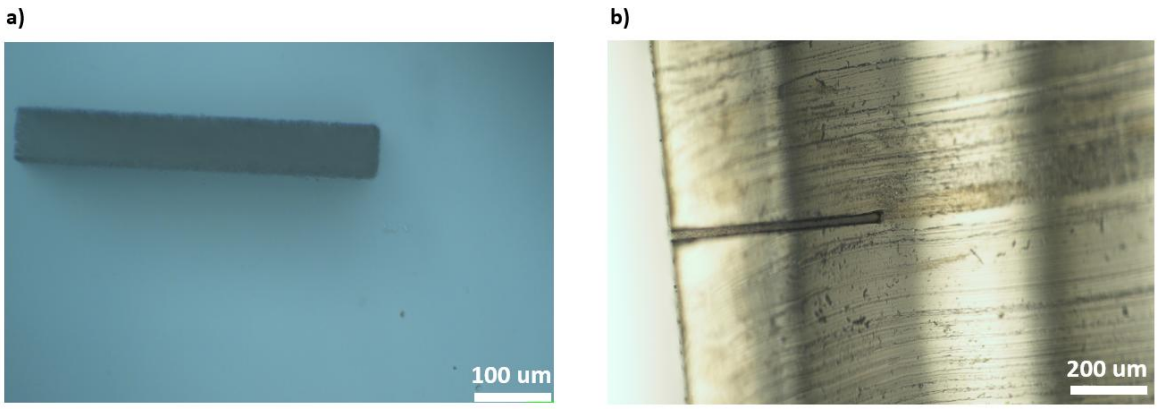

Figure 31: Microscopic images of bottom to top mesh cut after cleaning in NaOH solution for 3 hours under sonication. ***a)*** *is the top view of the patterned area, where no white particles can be see covering the area, and* ***b)*** *is the cross-sectional view of the channel once is having been cut in half. The residual material cannot be seen which was previously very visible in brown colour.*

When using bottom to top cut patterning method, the dissociated material (residue) was not exposed to the oxygen until the surface was hit by the laser beam. As the dissociation reaction lacked the presence of abundance of oxygen, it will hinder the complete combustion of carbon, resulting in the formation of amorphous carbon as a residual material. However, with TPA on PDMS being unknown area of research, a resulting reaction forming SiC was a possibility which needed to be verified.

One of the possible residual materials to the exposure to high energy decomposition of PDMS, without the presence of oxygen, could be Silicon Carbide (SiC). This is a compound of silicon and carbon and is a wide bandgap semiconductor material. It is well-known for its exceptional electrical properties, making it suitable to various electrical applications. Also, it is reported to be nearly impossible to remove as a residue and if it were to be one of the materials found with PMDS dissociation, MIC device of Au parallel configuration would be of no point. The electric field we employ as a detection system, will be disrupted and outcome would be

inadequate. One of the methods employed to check PDMS for SiC was to use Scanning Electron Microscopy (SEM).

SEM is a powerful imaging technique that uses electron beams to visualize the surface of materials at high magnifications and resolutions. It allows for detailed imaging of the surface topography of PDMS. This is particularly useful for studying microstructures, surface roughness, and features at a scale ranging from micrometres to nanometres. SEM can be used to investigate the cross-sectional structure of PDMS samples. This is valuable for understanding the layering or internal structures within PDMS devices or components. SEM can reveal the homogeneity of the material. Differences in composition or structure, if present, can be observed. This is important for quality control and ensuring uniform properties in PDMS samples. It can reveal the presence of contaminants or debris on the PDMS surface. This aspect is important to check for SiC residue.

PDMS is not a conductive material and not very suitable for SEM until proper preparation technique is used like coating it with conductive thin layer material such as gold. Whereas SiC is a very conductive compound[214]. The non-conductive behaviour of PDMS can be advantageous, as it remains less noticeable, while SiC stands out prominently in imaging. [215].

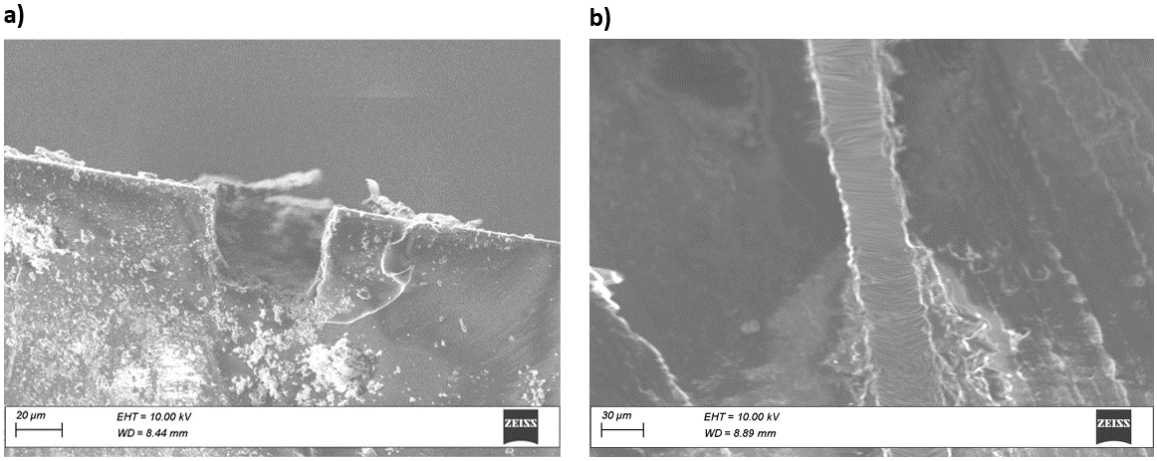

*Figure 32: Cross-sectional SEM images of PDMS after TPA was performed on it, **a)** show the top to bottom cut technique after cleaning with NaOH, and **b)** shows bottom to top cut technique after cleaning with NaOH.*

As illustrating in **Figure 32**, cross-sectional SEM images were taken after PDMS was polished in NaOH for 3 hours under sonication. **Figure 32a)** using top to bottom method, it can be seen the depth of the channel is not very short, and round at the base. While performing TPA, due to the debris, laser beam could not focus and continue deep cutting. This is the limitation of the idea top to bottom cut. **Figure 32b)** presents the bottom to top cut method. The channel can be seen as smooth, and no debris was left after the cleaning process.

PDMS is a nonconductive material, and when exposed to the electron beam in SEM, it can accumulate charge on its surface[216]. This charge can result in distortions, artifacts, or loss of image quality in the SEM images. The low electron conductivity of PDMS can lead to poor electron signal collection. This affects the quality and resolution of SEM images. To address these challenges, lower beam energy was used. It can reduce charging effects on the PDMS

surface. However, this results in lower resolution. Additionally, employing the charge dissipation technique, such as using a low accelerating voltage, can help minimize charging effects.

Due to the conductive nature of SiC, if it were present in channels, the SEM imaging would have been much easier, as SiC material would stand out from the rest of the PDMS. However, from **Figure 32**, it can be deduced that no SiC compound is present in the channels, after TPA and cleaning was done.

To further confirm the material composition in the TPA printed channels, X-ray photoelectron spectroscopy (XPS) was performed, results presented in **Figure 33**. XPS is used to determine the atomic percentage for the Si bond, Si2P bound, and Si-C bond on PDMS.

XPS data was collected at the EPSRC National Facility for XPS ("HarwellXPS"). XPS was acquired using Kratos Axis SUPRA using an X-ray source of monochromated Al kα with an energy of 1486.7 eV. The measurements were collected with a spot size/analysis area of 100 µm × 100µm using Kratos Axis SUPRA. The high-resolution spectra were collected by passing energy of 20 eV with step size and sweep time of 0.1 eV and 60s, respectively. All the data was collected at room temperature with a pressure below 5×10^{-8} Torr. Core-level spectra were recorded around the C1s binding energy. This energy was selected as the Si, Si2P, and Si-C presence is observable due to the bonding between them.

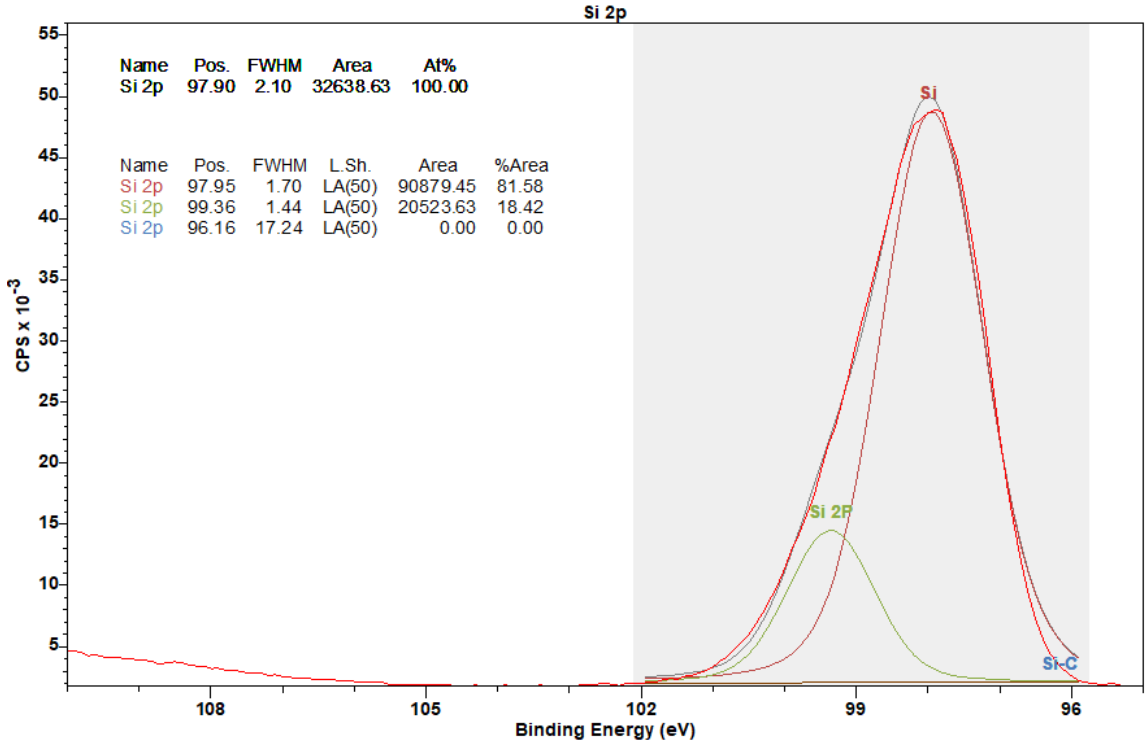

Figure 33: illustrates the XPS spectra on PDMS after TPA and cleaning were performed.

Figure 33 displays the Si core-level spectra collected from the PDMS using Casa XPS Software, used to fit the PDMS XPS spectra for silicon-to-silicon bonding (Si), (Si 2P), and silicon to carbon bonding (Si-C) with peaks at 97.95 eV, 99.36 eV, and 96.16 eV, respectively. The atomic percentage of Si-Si for the sample is 81.58 % and for Si2P is 18.42 %, respectively. In addition,

there is no presence of Si-C on PDMS from Si core-level spectra which indicate that the TPA cutting did not have SiC as a residual element.

Considering all the result from this section, PDMS is a highly suitable material for TPA and creating parallel electrodes MIC devices.

2. Polymethyl methacrylate (PMMA)

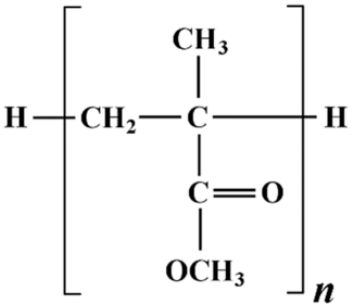

PMMA stands for Polymethyl methacrylate, which is a synthetic polymer of methyl methacrylate. It is a transparent thermoplastic that is commonly known by the trade names Plexiglas, Acrylite, Lucite, and Perspex. It is a transparent thermoplastic that has remarkable optical clarity. It is often used as a lightweight and shatter-resistant alternative to glass[217]. Its transparency, UV resistance, and weathering characteristics make it popular in various applications[218, 219].

It is optically clear in the visible light spectrum; it is transparent to light in the wavelengths ranging from 380nm to 750nm[220] and is non-toxic[221] thus making it very suitable for TPA experiments. At 520nm, PMMA may absorb more energy compared to the near-infrared range. This can affect the efficiency of the TPA process, potentially leading to different results in terms of material removal and precision. The depth of ablation may be affected at 520nm compared to longer wavelengths. Since TPA at 520nm is less common, experimental validation becomes crucial.

An acrylic slab of 0.5 mm thickness was used as printing material. Using multiple line stitching with the chosen parameters of 30% laser power, 0.8mm/s stage speed and 1KHz rep rate, same step by step experiments were executed on PMMA as we did on PDMS. As bottom to top mesh cut method has already been proven to be most effective, only this method is being executed.

The thermal degradation of PMMA occurs at the temperatures above 300℃ [222], which is in TPA temperature range. When PMMA is exposed to high temperatures, it undergoes a transformative process known as thermal degradation. This degradation involves a series of chemical reactions, primarily the cleavage of bonds within the polymer chain[222, 223]. The initiation stage is triggered by external factors like heat, providing the necessary activation energy for the reactions to commence. As the temperature rises, chain scission occurs, resulting in the breaking of polymer chains and the formation of smaller molecular fragments. Concurrently, gaseous byproducts are emitted, such as carbon dioxide and methane[224, 225], contributing to the overall degradation process. Solid residues, often charred or carbonized fragments of the original polymer, are also formed[225].

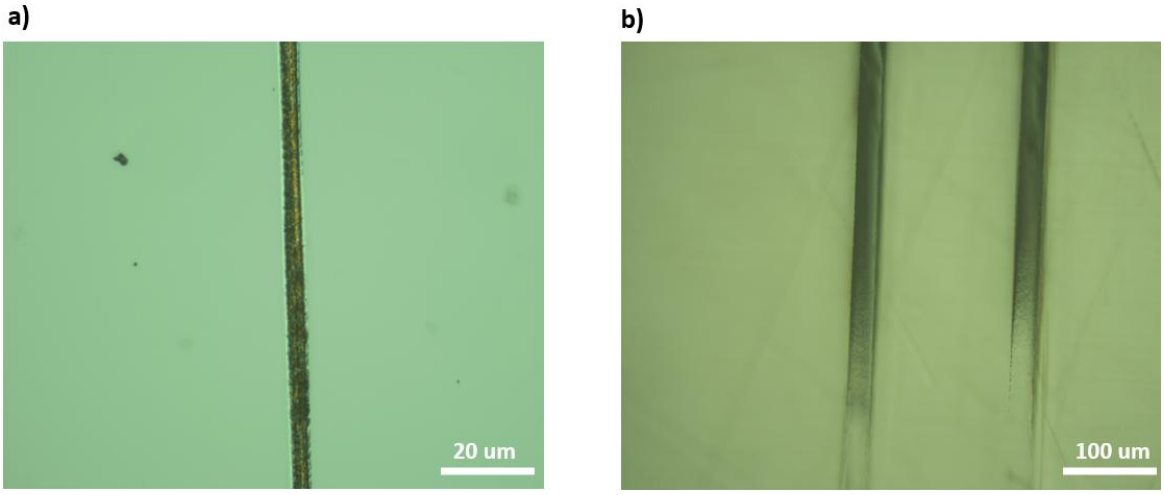

Figure 34: these are the optical images taken from a microscope. The laser power used is 30% and rep rate of 1KHz with the speed of 0.8mm/s. ***a)*** *is the single line cut on the PMMA surface,* ***b)*** *this is a cross-sectional view with in-depth cut using bottom to top mesh cut method.*

A single line cut on the surface, as seen in **Figure 34a**, appears cleaner with minimal debris in or around the channel, in contrast to PDMS printing. However, the residue is of brown in colour, which indicates the carbonized fragments. The channel width is higher than of PDMS, which is $5.6\mu m$. In **Figure 34b)**, it illustrates the cross-sectional view of the in-depth patterning in PMMA. Although a deep cut is feasible, the deeper regions of the pattern do not appear to be thoroughly dissociated. The outline of the cut can be seen but the PMMA is intact within those boundaries. An average of 1.2mm in-depth patterning was achieved via bottom to top mesh cut method. Since each material reacts differently to the TPA technique, multiple factors, known as limiting effects, could be responsible for this occurrence.

- **Absorption and Scattering:** PMMA, like many materials, exhibits absorption and scattering of photons[226]. As the laser penetrates deeper into the material, more photons are absorbed or scattered, reducing the intensity of the laser beam[227]. This diminishing intensity can lead to a decrease in the probability of two-photon absorption events.
- **Nonlinear Effects Saturation:** Two-photon absorption is a nonlinear process, and it can saturate with increasing laser intensity. As you go deeper into the material, the cumulative effects of absorption and scattering can lead to a reduced effective intensity, potentially reaching a point where the 2PA process is no longer efficient[228].
- **Energy Dissipation:** The energy from absorbed photons may be dissipated as heat or other forms of energy, particularly in the case of ablation. This dissipation can affect the energy available for the two-photon absorption process as you move deeper into the material[229].
- **Thermal Effects:** At greater depths, heat generated by the laser can accumulate. This thermal buildup can lead to changes in the material's properties, affecting its response to the laser beam. In some cases, excessive heat can cause thermal damage or alter the ablation dynamics[230, 231].

- **Wavefront Distortion:** PMMA can exhibit variations in refractive index and other optical properties. These variations can lead to wavefront distortion of the laser beam, impacting the precision of the ablation process at depth[232].

Higher Laser power setting was used with decrease in speed to counter the energy dissipation effect, which resulted in no change. The focal length of the 5x lens is 14.5mm which is much higher than the depth of PMMA cut. This rule out the possibility of focal length being too short for TPA to take effect.

The desired length of channel was minimum of 5mm, keeping Reynolds number under 2300 for laminar flow, on each side of the material slab (refer to **section 2.2.1**). As PMMA was only 0.84mm, this is not a viable option to explore further.

3. Polystyrene

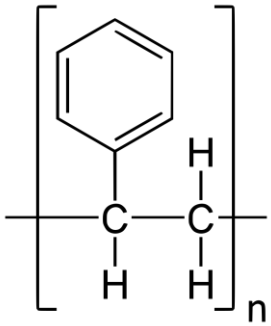

Polystyrene is a versatile plastic polymer, typically used for a variety of applications. It is clear, hard, and brittle[233]. It is an inexpensive material with very low melting point[234]. It's lightweight and has good thermal insulation properties[234]. Due to its cost-effectiveness and transparent nature, it is commonly used in various products like packaging materials, disposable foam products, and insulation.

It is optically clear in the visible and near-infrared regions of the electromagnetic spectrum. It allows light to pass through with minimal absorption in the range of approximately 300nm to 2,500nm[233, 235]. Polystyrene, like many organic materials, can exhibit TPA, making it responsive to the nonlinear optical process involved in TPA. The depth to which the polystyrene is ablated will depend on factors like laser intensity and the specific characteristics of the material.

A normal lab petri dish was used as printing material. Using multiple line stitching with the chosen parameters of 30% laser power, 0.8mm/s stage speed and 1KHz rep rate, no patterns were found. 30% was too low for it to dissociate, thus higher power of 50% was used. The same step-by-step experiments conducted on PDMS were also executed on polystyrene, using the bottom-to-top mesh cut method.

Polystyrene undergoes thermal degradation when exposed to elevated temperatures ranging between 350℃ to 500℃ [236, 237]. Polystyrene is a polymer composed of repeating styrene units, and dissociation typically involves breaking the chemical bonds between these units, giving by-product on styrene monomers, carbon dioxide, carbon monoxide and carbonaceous residue[236, 238, 239].

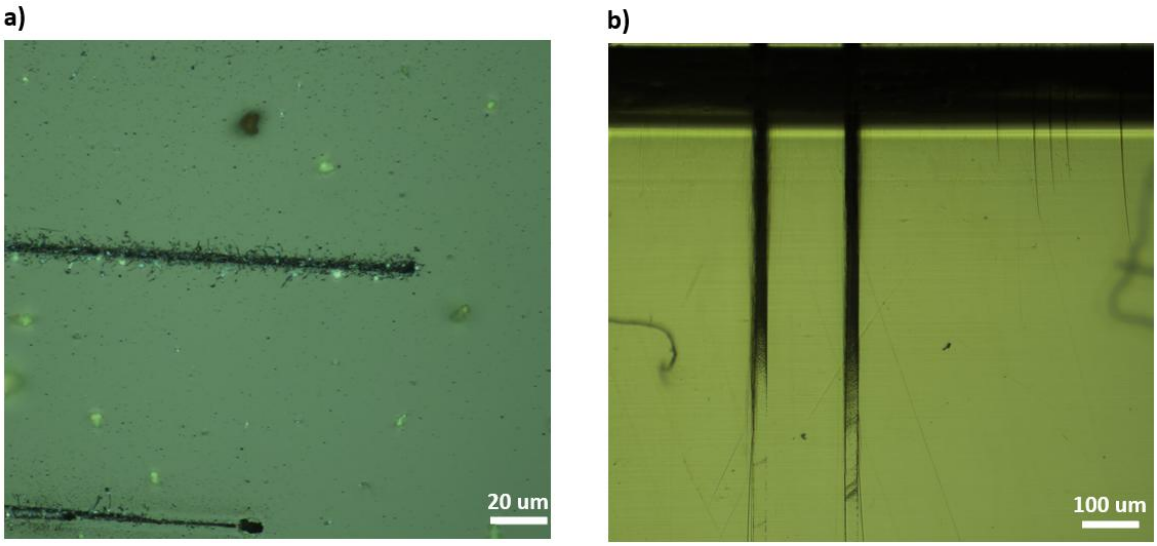

Figure 35: These are the optical images taken from a microscope. The laser power used is 50% and rep rate of 1KHz with the speed of 0.8mm/s. ***a)*** *is the single line cut on the polystyrene surface,* ***b)*** *this is a cross-sectional view with in-depth cut using bottom to top mesh cut method.*

A single line cut on the surface can be seen from **Figure 35a)**, which has some white particles around the surface and in the channel. The debris seems to be more than of PMMA but less than of PDMS printing. However, the residue is of brown in colour[240], which indicate the partial ablation. If the laser energy is not sufficient to fully remove the polystyrene material, partial ablation may occur. The presence of additives or impurities in polystyrene, would also lead to the brown coloration of the residue. The single line channel width is $3\mu m$. In **Figure 35b)**, it illustrates the cross-sectional view of the in-depth patterning in PMMA. Although, deep cut is feasible it appears the deeper part of the pattern is not thoroughly dissociated. The outline of the cut can be seen but the polystyrene is intact within those boundaries. An average of $840\mu m$ in-depth patterning was achieved via bottom to top mesh cut method. As each material reacts differently to TPA technique, the reasons are explained previously with limiting effects.

A higher laser power setting was used with a decrease in speed to counter the energy dissipation effect, which resulted in no change. With the desired length channel of minimum 5mm on each side of the material slab. Polystyrene is not suitable to MIC devices. No further exploration was resolved on this material.

4. Polycarbonate

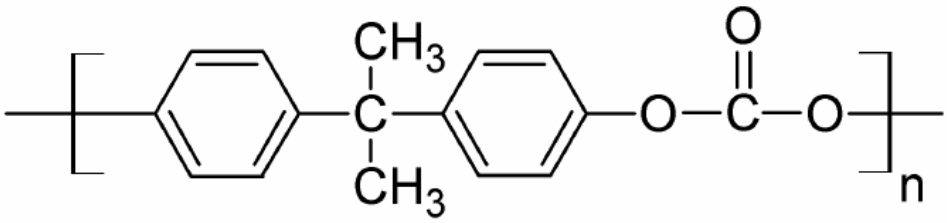

Polycarbonate is a thermoplastic polymer that's known for its exceptional strength, transparency, and heat resistance[241]. It is derived from bisphenol A (BPA) and phosgene,

resulting in a versatile material with a range of applications. It is about 200 times stronger than a regular glass, making it a popular choice for items that need to withstand rough handling[242]. One of its standout features is optical clarity. This makes it ideal for use in eyewear, optical lenses, and even as a substitute for glass in various applications. Polycarbonate has a high heat resistance compared to other plastics. It can withstand temperatures ranging from -40°C to 130°C (-40°F to 266°F) without significant deformation[243]. Despite its toughness, polycarbonate is surprisingly lightweight. This makes it a preferred material in industries where both strength and weight are crucial factors.

It is optically clear in the visible light spectrum and extends into the near-infrared (NIR) range. It allows light to pass through with minimal absorption in the wavelengths from approximately 400 nm to 2,500 nm[244] and is non-toxic thus making it very suitable for TPA experiments. The depth of ablation could be affected at 520nm compared to longer wavelengths.

A normal DVD casing was used as printing material. Using multiple line stitching with the chosen parameters of 30% laser power, 0.8mm/s stage speed and 1KHz rep rate, no patterns were found. 30% was too low for it to dissociate, just like polystyrene, thus higher power of 50% was used. Same step by step experiments were executed on Polystyrene as was done on previous materials, using bottom to top mesh cut.

The thermal degradation of polycarbonate occurs typically between 240℃ to 500℃ [245, 246], which is in range of TPA energy transfer. The dissociation of polycarbonate often leads to the release of gaseous byproducts. This can include compounds such as carbon dioxide (CO2), and carbon monoxide (CO) during the breakdown of polymer chains[247]. Apart from gases, there are solid phase byproducts, such as carbonaceous residues, and monomeric fragments of the original polycarbonate[248].

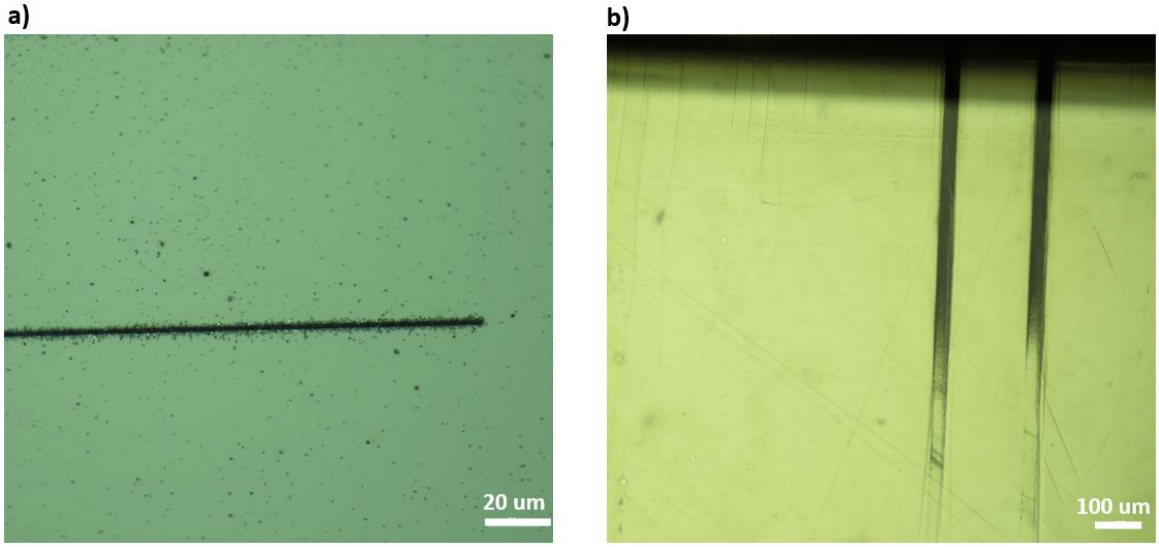

Figure 36: These are the optical images taken from a microscope. The laser power used is 50% and rep rate of 1KHz with the speed of 0.8mm/s. ***a)*** *is the single line cut on the polycarbonate surface,* ***b)*** *this is a cross-sectional view with in-depth cut using bottom to top mesh cut method.*

A single line cut on the surface of polycarbonate can be seen from **Figure 36a)**, which doesn't have any white particle, instead have black reside in and around the channel. The black residue is of black in colour, which indicate the carbonized fragments. The single line channel width is $3.2\mu m$, which is higher than of polystyrene. In **Figure 36b)**, it illustrates the cross-sectional view of the in-depth patterning in polycarbonate. Although, deep cut is feasible it appears the deeper part of the pattern is not thoroughly dissociated. The outline of the cut can be seen but the polystyrene is intact within those boundaries. An average of 1.1mm in-depth patterning was achieved via bottom to top mesh cut method. As each material reacts differently to TPA technique, the reasons for disruption in deep cut are explained previously with limiting affects.

Conclusion

The combination of photonics and carbon-based polymers can not only paves the way for intricate and tailored structures at the microscale but also holds promise for advancements in nanotechnology. This fusion of TPA and carbon-based polymers stands poised to revolutionize manufacturing processes and contribute to the development of innovative technologies across diverse industries.

The study explored the application of TPA for material dissociation in various elastomers and polymers, namely Polydimethylsiloxane (PDMS), Polymethyl methacrylate (PMMA), Polystyrene, and Polycarbonate. Each material exhibited unique responses to TPA, and the study investigated the influence of control parameters such as laser power, repetition rate, and stage speed on the ablation process.

PDMS, a silicone-based elastomer, demonstrated favourable characteristics for TPA, including optical transparency, flexibility, and biocompatibility. Optimizing the TPA parameters for PDMS allowed for successful deep cutting. The study extended its investigation to PMMA, where the material's response to TPA was explored. PMMA exhibited limitations in achieving deep cuts, attributed to factors such as absorption, scattering, nonlinear effects saturation, energy dissipation, thermal effects, and wavefront distortion. The study emphasized the importance of experimental validation due to the less common use of TPA at 520nm.

Polystyrene and Polycarbonate were also subjected to TPA experiments, with varying results. Polystyrene presented challenges with partial ablation and debris generation, making it unsuitable for microfabrication of devices. Polycarbonate showed promise with successful ablation, but limitations in achieving deep cuts were observed.

The Initially optimized parameters for TPA were 30% power, 1KHz rep rate and 0.8mm/s stage speed, which were effective against PMMA and PDMS, However, materials such as polystyrene and polycarbonate required higher laser beam power for them to dissociate. To observe a smooth pattern on the surface or in-depth, 50% Laser power was used with rest of the parameters being the same.

Surface cutting was performed on each material to observe the material reaction. 50% power was used to make a comparison between all four carbon-based materials used in this experiment, results are illustrated in **Figure 37**.

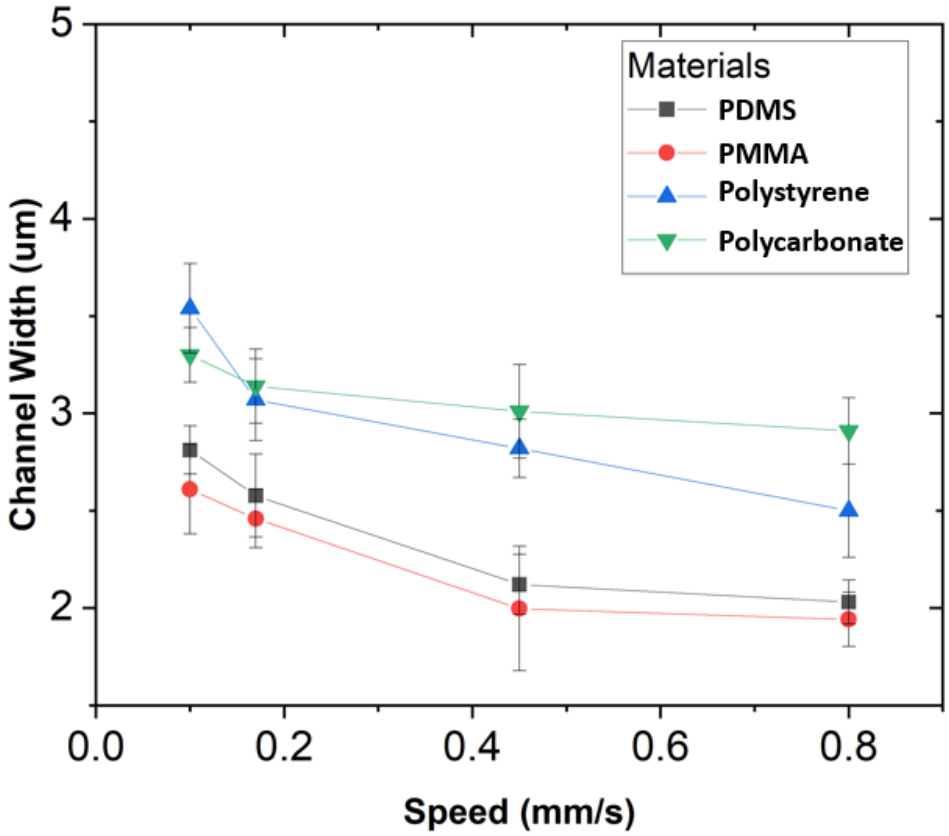

Figure 37: These are the results for 50% laser power, 1KHz rep rate, and variation of stage speed. Presenting the impact on channel width with TPA on different materials.

From **Figure 37**, PDMS and PMMA are at the lower end of the channel width comparison, whereas polystyrene and polycarbonate have high channel width at the same power. The differences in the TPA characteristics, specifically the ablation efficiency and precision, between polycarbonate/polystyrene, and PDMS/PMMA can be attributed to their respective material properties. polycarbonate has a linear, thermoplastic structure with aromatic rings. This structure can facilitate efficient two-photon absorption, allowing for a wider range of photon energies to induce ablation. Where, polystyrene is another thermoplastic polymer with a simpler structure. Furthermore, these materials have lower thermal conductivities compared to PDMS and PMMA. Lower thermal conductivity can contribute to a wider range of effective two-photon absorption, leading to wider TPA structures under the same parameters and condition.

However, PDMS, being a silicone elastomer, has a more complex and branched molecular structure. While it allows for precision, the structural complexity might limit the range of photon energies for efficient TPA. PMMA, though structurally simpler than PDMS, has a more rigid and ordered structure. This may affect the efficiency of TPA, potentially resulting in a narrower range compared to polycarbonate or polystyrene.

In-depth cutting techniques, particularly the bottom-to-top mesh cut, proved to be the most effective in avoiding laser beam absorption and refraction due to leftover debris in the channel. SEM imaging and XPS measurements of the patterned surface of PDMS confirmed the absence of SiC as a residual by-product.

4.2.2. Metallisation

The integration of Au electrodes on PDMS has recently gained significant attention in the field of microfabrication and flexible electronics. PDMS, known for its elastomeric nature, serves as an outstanding substrate for various applications. Au on the other hand, is known for its excellent electrical conductivity, corrosion resistance, and biocompatibility, making it a preferred choice for electrode materials. The fabrication methods for creating gold electrodes on PDMS varies, ranging from conventional photolithography to more innovative techniques such as soft lithography and replica moulding[249-251]. Each method offers its advantages and challenges, influencing the performance and applicability of the resulting devices. Another simpler and effective way metallization, which is used for this project, is via Thermal deposition method. Thermal deposition of gold on PDMS is a common method used to create thin and uniform gold films on the flexible PDMS substrate. This process involves the use of a thermal evaporator, to deposit a layer of gold onto the PDMS surface.

PDMS is prepared by mixing 15:1 of silicone elastomer base with a curing agent. The mixture is then left for degassing in a desiccator for 30 minutes, and further left a glove box for another

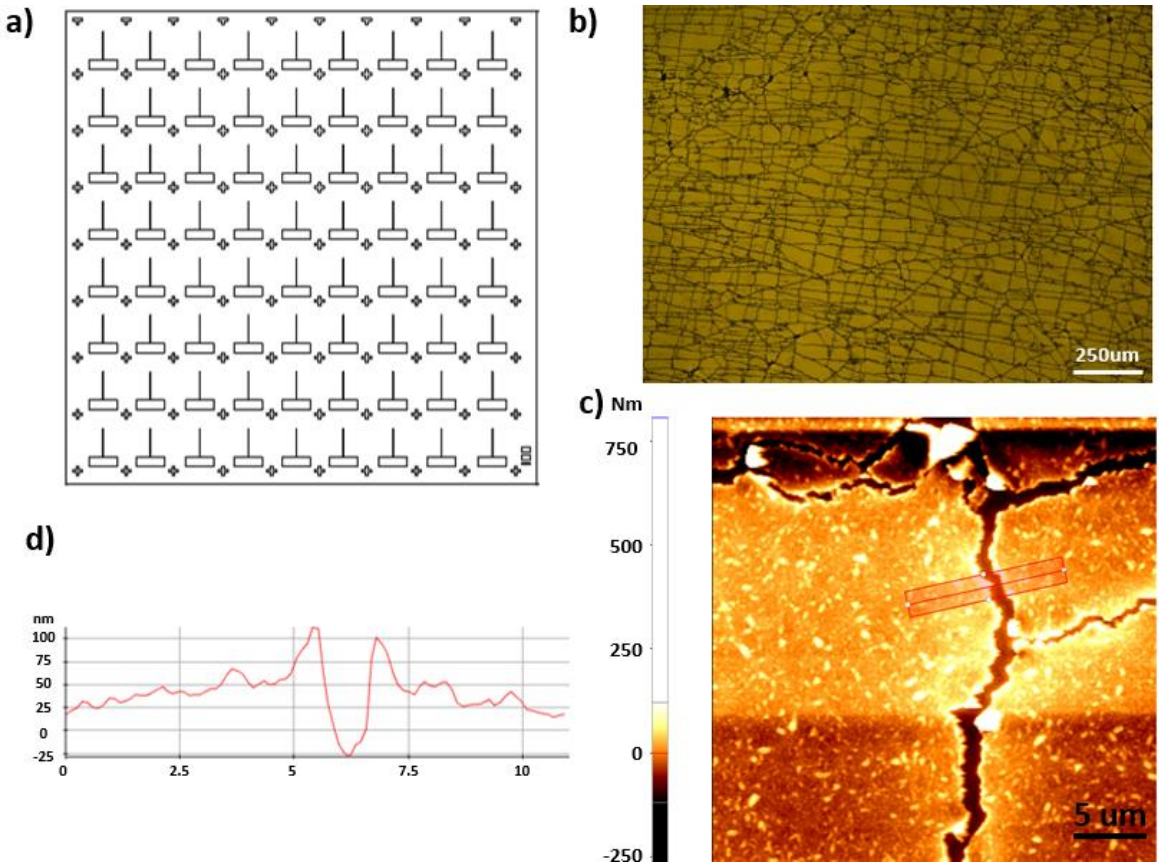

*Figure 38: **a)** is the stencil design used to as a shadow mask, **b)** is a microscope image of Au quality over PDMS after thermal deposition, and **c)** is an AFM image of one the cracks seen in **b)**. **d)** is the average profile scan of the crack, marked as red box in **c)**.*

30 hours to be cured. Before deposition, the PDMS surface needs to be thoroughly cleaned to ensure proper adhesion, and plasma treatment was used for this. The samples are than placed in vacuum chamber with the specifically designed metal stencil-based shadow mask. The design of the mask is illustrated in **Figure 38a)**. Chromium was used to improve the adhesion between gold and the PDMS substrate. The gold material is heated at evaporation temperatures. The thickness of the gold film can be controlled by adjusting the deposition time and rate of deposition. Monitoring the deposition parameters is crucial to achieving the desired film characteristics.

After the thermal deposition, optical microscope and AFM techniques were used to analyse the surface quality of the Au thin film. **Figure 38b)** shows an optical image of the surface after metal deposition. The reflective gold surface shows a loosely ordered network of crossing dark lines. Closer inspection of this surface with AFM, shown in **Figure 38c)** reveals that the dark lines are cracks in the gold film. The depth of the cracks show that the gold film is discontinuous. A line profile extracted from the AFM image shown in **Figure 38d**), the depth to be around 120nm where the Au thin film was around 100nm. When a simple test of continuity, using a multi-meter was performed, it was found that these Au islands were disconnected from each other, which lead to very high resistance across the film. This unwanted resistance cannot integrate to final MIC device. This phenomenon is well known as Mud cracking, schematic illustrated in **Figure 39**.

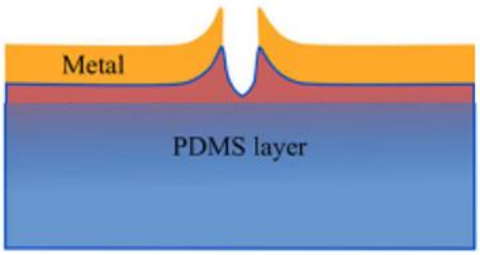

Figure 39: A stack diagram, showing the affect known as mud cracking on PDMS surface.

There are multiple reasons that would lead to such outcome, such as external stress and strain, expansion of PDMS in vacuum, and Thermal absorption. The explanations for each effect and the corresponding countermeasures are detailed below.

- **Stress and Strain:** PDMS, being a highly elastic and flexible material, which exhibits stress and strain behaviour when external forces are applied[252]. Strain (ε), a measure of deformation, allows PDMS to undergo significant elongation and compression. In the linear elastic region, strain is directly proportional to stress, known as Hookean behaviour. However, at higher strains, PDMS may exhibit nonlinear behaviour due to changes in its molecular structure. The Poisson's ratio (v) of the material, which indicates lateral contraction during longitudinal stretching, is usually around 0.5, indicating low lateral contraction. These elastomer behaviour PDMS leads to cracking in Au thin film. The desired PDMS slab was placed on a glass slide to minimize external forces during handling. This approach helped avoid any stress and strain on the PDMS, ensuring its integrity was maintained throughout the process.

- **Expansion of PDMS in vacuum:** PDMS demonstrates distinctive behaviour when subjected to vacuum conditions. One prominent event is degassing, where PDMS releases trapped gases when exposed to low pressure. This degassing can be crucial in a vacuum chamber, impacting the surface environment and potentially affecting the performance of PDMS. Additionally, PDMS face a reversible volume expansion in response to the removal of atmospheric pressure[253]. In a vacuum, the presence of air pockets within PDMS can lead to their expansion, potentially causing deformations or structural changes on the surface of the material. Careful consideration of fabrication processes and material preparation was required to minimize the presence of such imperfections. The curing and cross-linking of PDMS may also be influenced by vacuum conditions, requiring adjustments to optimize the fabrication process. Despite these considerations, PDMS generally maintains its structural integrity in vacuum environments, especially when subjected to minimal mechanical stress. The adhesion and bonding properties of PDMS can be influenced by vacuum conditions, so tailored surface treatments and bonding techniques are required to ensure reliable performance. While the effect of PDMS expansion cannot be completely avoided, the material was properly degassed in a desiccator during the preparation of the PDMS slab to minimize any air bubbles and ensure optimal bonding quality.
- **Thermal absorption:** Temperature variations within vacuum environments can impact PDMS, and understanding its thermal properties, such as the coefficient of thermal expansion, is crucial. One important consideration is the coefficient of thermal expansion (CTE) of PDMS. PDMS has a reasonably high CTE, meaning it can expand or contract significantly to the variation in temperature. In a vacuum, where thermal conduction and convection are limited due to the absence of air, temperature variations can have a more direct impact on the material. Rapid temperature changes can induce thermal stresses on PDMS surface, potentially leading to deformation, dimensional changes, or even structural damage. Sudden cooling after gold deposition induces thermal stress in the PDMS, can lead to cracking in the thin Au film[254]. This effect was avoided by using an E-Beam evaporator instead of a thermal evaporator. In a thermal evaporator, the Au material is heated in a crucible, which can cause the sample to experience indirect heating from the evaporated material. In contrast, E-beam evaporation uses an electron beam to heat the material, preventing the sample from being exposed to high temperatures, thus ensuring more controlled and precise deposition without the risk of thermal damage.

Research has indicated the control of mud cracking using the duration of plasma cleaning and thickness of adhesion layer[254, 255]. To compare the affect and optimize the thin film multiple combinations of settings were used. Plasma cleaning duration of 1, 5, 10 and 15 minutes were explored against adhesion layer thicknesses of 1, 10, and 20μm.

PDMS is a silicone-based elastomer known for its flexibility, low surface energy, and non-reactive nature. However, these properties can make it challenging for certain materials like gold to adhere well directly onto PDMS surfaces. To counter such affect, an additional layer of adhesion is used, in this case, Chromium was chosen. Chromium acts as an adhesion layer that enhances the bonding between PDMS and gold. It promotes better adhesion by forming a strong interface between the PDMS substrate and the subsequent gold layer. Chromium also serves as a barrier layer, preventing diffusion of gold atoms into the PDMS substrate. This is important to avoid any chemical interactions or diffusion that could compromise the properties of the PDMS.

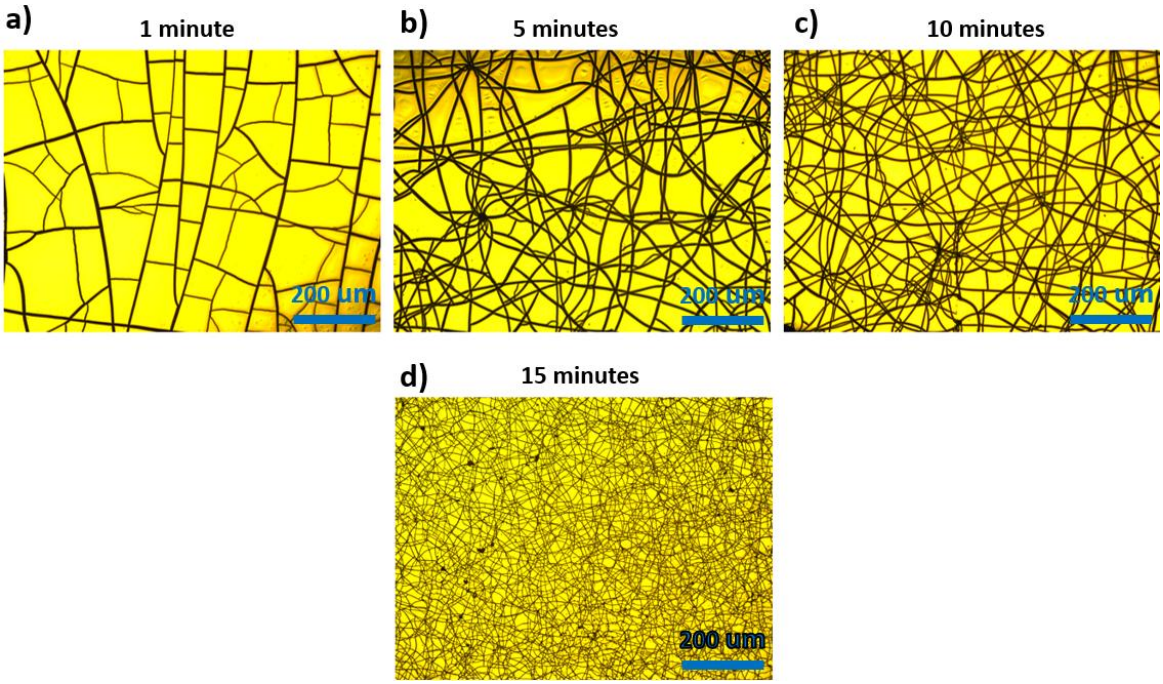

Figure 40: These are the Nikon optical microscope images when 20µm Cr was used as adhesion layer against variating plasma treatment time. ***a)*** *plasma treatment of 1 minute was performed on the sample,* ***b)*** *plasma treatment of 5 minutes was performed on the sample,* ***c)*** *plasma treatment of 10 minutes was performed and* ***d)*** *plasma treatment of 15 minutes was performed on the sample*

It can be observed from **Figure 40**, the increase in plasma time for $20\mu m/100\mu m$ deposition of Cr/Au leads to visible increase in Au Island count, whereas decrease in island areas. For 1 minute of plasma treatments, Au islands were of average $4.7 \times 10^4 \mu m^2$ in area which decreased to $6.2 \times 10^2 \mu m^2$ for 15 minutes of plasma treatment. None of the samples were conductive.

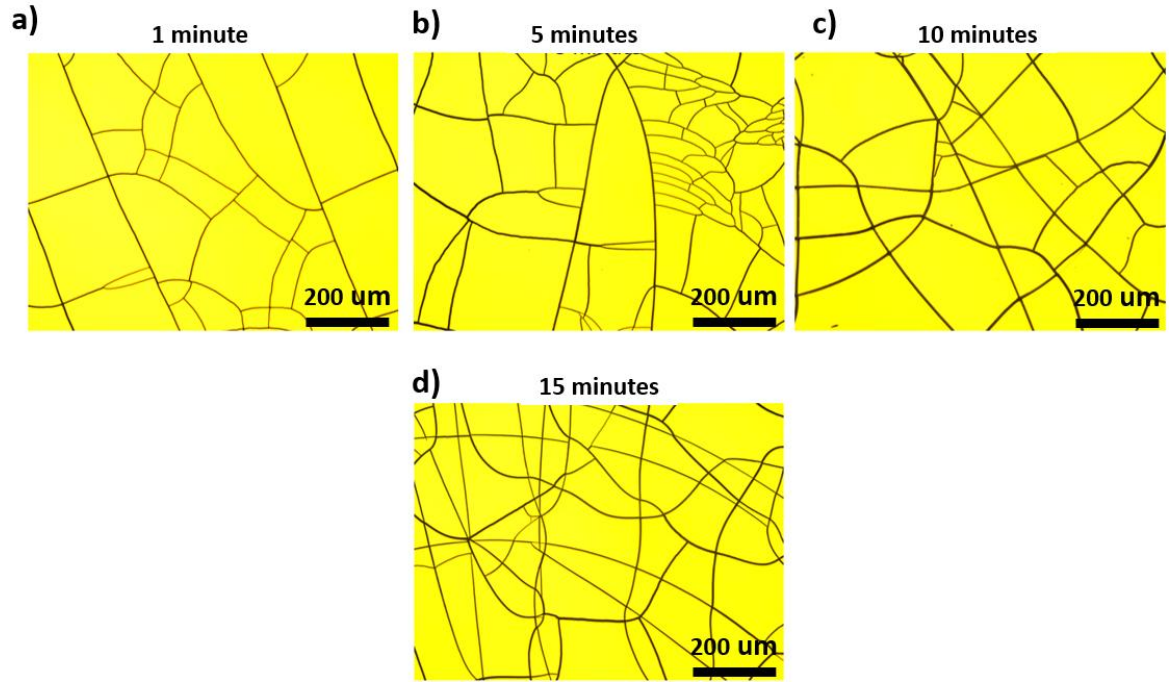

Figure 41: These are the Nikon optical microscope images when 10µm Cr was used as adhesion layer against variating plasma treatment time. ***a)*** *plasma treatment of 1 minute was performed on the sample,* ***b)*** *plasma treatment of 5 minutes was performed on the sample,* ***c)*** *plasma treatment of 10 minutes was performed and* ***d)*** *plasma treatment of 15 minutes was performed on the sample*

A similar trend of island formation can be observed when $10\mu m/100\mu m$ deposition of Cr/Au was implemented, as illustrated in **Figure 41**. The increase in plasma time leads to visible increase in Au Island count, whereas decrease in island areas. For 1 minute of plasma treatments, Au islands were of average $1.2 \times 10^5 \mu m^2$ in area which decreased to $5.6 \times 10^4 \mu m^2$ for 15 minutes of plasma treatment. None the samples were conductive.

A similar trend of island formation can be observed when $1\mu m/100\mu m$ deposition of Cr/Au was implemented, as illustrated in **Figure 42**. The increase in plasma time leads to visible increase in Au Island count, while the island areas decrease. For 1 minute of plasma treatment, no island formation was observed, and as a result, mud cracking of the PDMS was not detected. However, there is formation of ripples or dunes throughout the Au thin film layer. One possible cause is the inherent flexibility of PDMS. During the deposition, the stress generated by the gold layer creates interact with the flexible nature of PDMS, leading to the formation of ripples or dunes. As the Cr layer is just $1\mu m$, which is very thin. The mismatch in thermal expansion coefficients between gold and PDMS can contribute to the development of such surface irregularities. Furthermore, as PDMS expands in vacuum, stress is generated within the material. Under the non-uniform conditions of the shadow mask applied directly on the PDMS surface, could lead to higher localized stress in certain areas. The mechanical interface between the shadow mask and the expanding PDMS may cause additional forces to take effect, such as friction and adhesion, resulting in uneven stretching. This could lead to deformation of the surface to look like ripples or dunes.

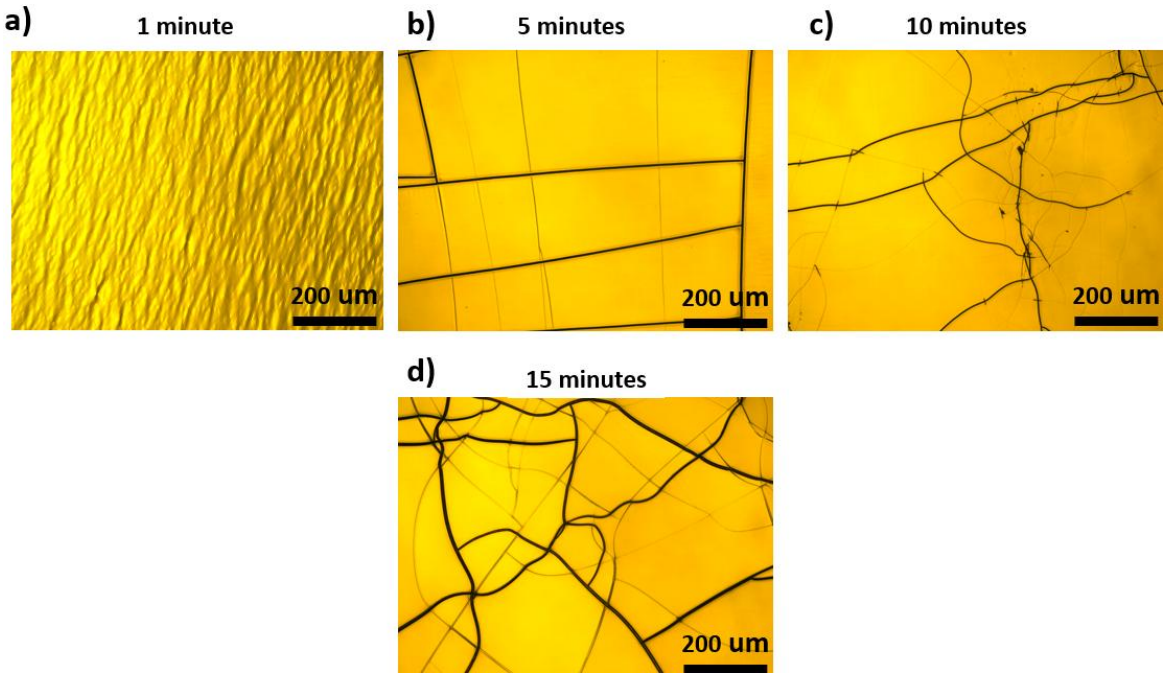

Figure 42: These are the Nikon optical microscope images when 1μm Cr was used as adhesion layer against variating plasma treatment time. ***a)*** *plasma treatment of 1 minute was performed on the sample,* ***b)*** *plasma treatment of 5 minutes was performed on the sample,* ***c)*** *plasma treatment of 10 minutes was performed and* ***d)*** *plasma treatment of 15 minutes was performed on the sample.*

Although sample with 1 minute of plasma treatment displayed ripples, it had good conductivity of 4.47×10^7 S/m and was adhesive to PDMS surface, unlike any of the other samples.

Conclusion

The optimization of thin film deposition on PDMS surfaces, particularly the Cr/Au combination, involves a delicate balance between various parameters. The occurrence of mud cracking in PDMS can be a complex phenomenon influenced by factors such as external stress, strain, vacuum-induced expansion, and thermal absorption. Our approach focused on mitigating these issues through meticulous control of the plasma treatment duration and the thickness of the adhesion layer.

The choice of a glass slide to support the PDMS slab aimed at minimizing external stress and strain during the deposition process. Additionally, the degassing of PDMS in a desiccator during curing was implemented to eliminate air bubbles, thus preventing degassing issues during vacuum-induced expansion. The utilization of E-beam during thermal evaporation allowed for indirect thermal absorption, reducing the risk of mud cracking.

Illustrated in **Figure 43** are the results from the investigation of variation of Cr thickness and plasma treatment. From **Figure 43a)**, for all the Cr thickness observed, if the plasma cleaning is set to zero, the number of islands formed is either zero or low. However, this leads to no adhesion of the Cr/Au thin film. No conductivity was extracted either, as the Au would come off with the slight contact from the pin probs. Same is the case for plasma cleaning variation with 0 Cr thickness. The yellow dot represents the use of optimal values for Plasma cleaning duration and Cr thickness, which are 1 minute and 1μm respectively.

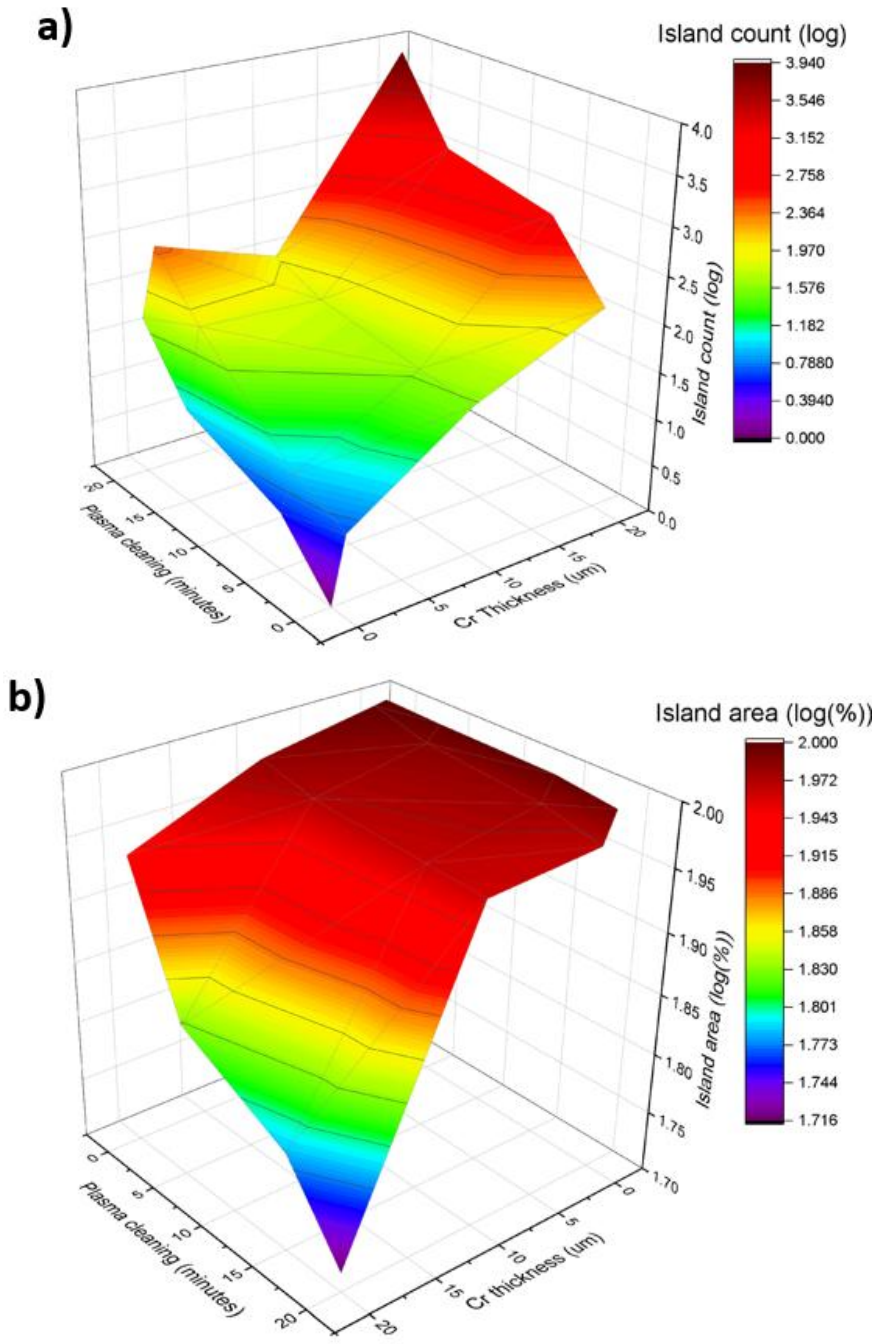

Figure 43: Shows the results of experiments of the change in Cr thickness and variating duration of plasma treatment. ***a)*** *shows the impact of the parameters on the Island counts, and* ***b)*** *shows the impact of the parameters on the island area.*

From **Figure 43 b)**, for all the Plasma cleaning time variations with 0 Cr thickness, island areas have no impact. This means that there is no creation of smaller island, and it is in one smooth surface. However, there was no adhesion and conductivity on the sample. When $20\mu m$ Cr thickness and 20 minutes of plasma cleaning time is used, multiple islands were created with distribution of area.

While this optimized recipe led to ripples on the surface, it proved to be effective in achieving the conductivity and adhesion. The findings underscore the importance of carefully balancing deposition parameters to tailor thin film characteristics on PDMS surfaces, providing valuable insights for researchers and engineers working in the field of microfabrication and device development. Future investigations may delve deeper into the underlying mechanisms and explore additional parameters to further enhance the reliability and performance of thin film depositions on flexible substrates like PDMS.

4.2.3. Parallel MIC devices

Using the optimized parameters found in metallization and 2-photon ablation, both were combined to construct the parallel configuration electrode MIC device. For MIC devices, it is essential to establish a liquid-tight system that ensures seamless fluid flow within the channels without any risk of leaks.

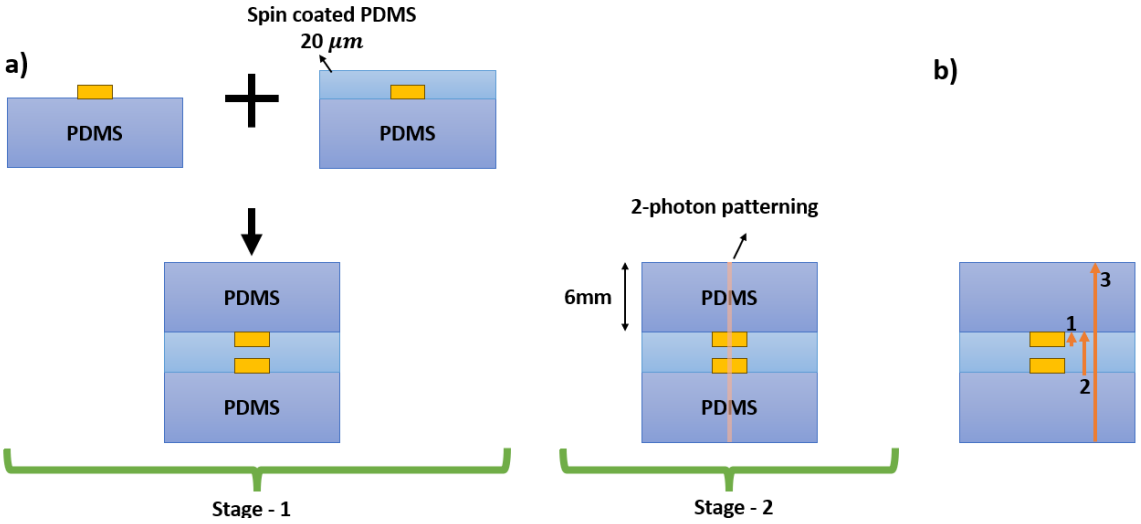

*Figure 44: **a)** A stack diagram of 2 stages used to finalize the parallel configuration of MIC device, and **b)** a stack diagram showing the multistep cut used to obtain 1 single channel through the parallel configuration.*

There were two stages at which Parallel MIC was finished with, illustrated in **Figure 44a)**. In stage 1, two samples of PDMS slab with Au electrodes were secured. One of which was then spin-coated with 15:1 PDMS. With the spin speed of 500 rpm for 30 seconds, 30μm thickness of PDMS was spin coated. The samples were then left on the hotplate at $60°C$ for 2 hours. This will let the spin coated PDMS layer to cure and become solid.

The optimized recipe was obtained after spin-coating PDMS over simple glass substrate with variation of spin speed and time and was testing with profilometer. This PDMS protective layer has two-fold effect, it is used as sealing agent between the two PDMS/Au samples and provide a gap between the electrodes to cause capacitance.

Using the optimized 2-photon patterning recipe, a cut was made through the sample. However, as the Au electrode are not optical clear, the beam would not be focused through them to the base of the device. This meant the simple method of bottom to top mesh cut was not possible. Multistage cuts were used to obtain a pattern through this paradigm, as illustrated in **Figure 44b)**.

The initial cut followed a bottom-to-top approach on the gold electrode of the upper PDMS sample. Subsequently, the second cut employed the same technique on a second gold electrode which also patterned the PDMS sealing layer in between. Lastly, the third cut was focused on the base, executing a bottom to top cut that extended to the upper surface. Once the samples were ready, they were left for cleaning in NaOH for 2 hours under half pulse sonication.

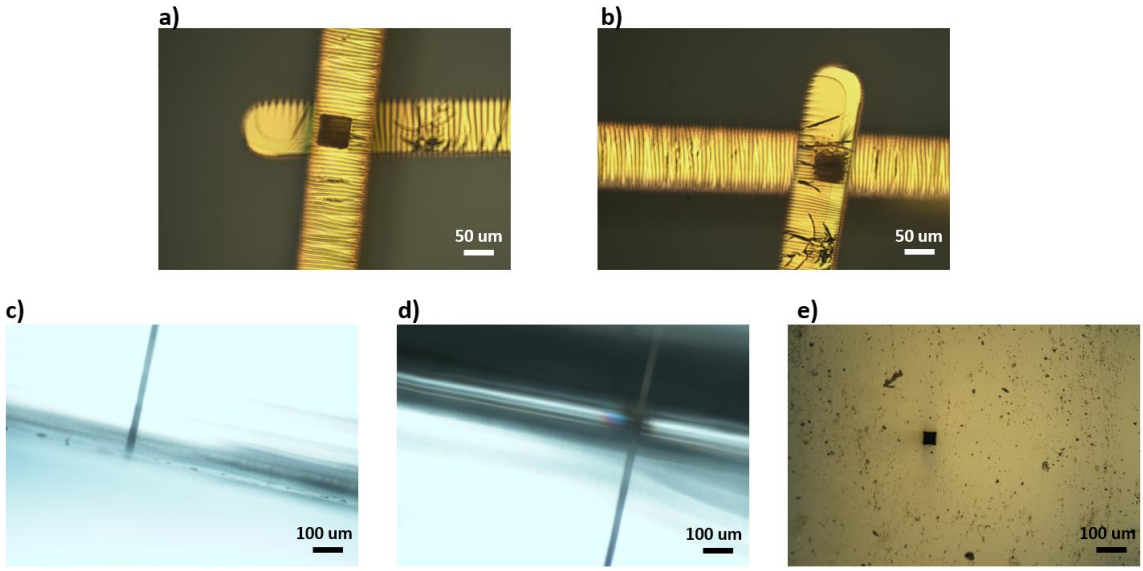

*Figure 45: Optical microscope images for parallel configuration MIC device after cleaning in NaOH. **a)** this shows the 50x50um cut on Au with TPA using bottom to top mesh cut, **b)** shows the second electrode after the cut, **c)** shows the side view of the channel at the base of the device, **d)** shows the side view of the interface between 2 PDMS samples, and **e)** shows the top view of the surface of the top PDMS sample.*

In **Figure 45a)**, a clean cut is evident on the top gold electrode embedded within the PDMS device. Additionally, **Figure 45b)** showcases a successful cut on the second gold electrode situated on the opposite side of the PDMS protective layer, representing step 2 in the patterning process. This indicates the successful patterning of the PDMS protective layer and the two gold electrodes. The interface is clearly depicted in **Figure 45d)**. **Figure 45c)** provides a side view of the device's bottom surface, highlighting the dark line representing the fluid channel. In **Figure 45e)**, the top view of the upper PDMS reveals the through-and-through channel, affirming its readiness for fluid flow testing.

These images collectively demonstrate the successful completion of the patterning process. When the MIC was connected to the fluidic system to observe the fluid flow, no fluid flow was detected. This meant the channel was clogged at some point, or the patterning/ cleaning process did not work. Multiple methods were used to overcome this challenge, such as, flipping the same sample to pattern from the other side, extending the channel pattern to depict a cone diverging towards the surface on both ends, and further cleaning In NaOH bath. None of the methods tried helped with the fluid flow. The problem seems to lie in PDMS protective layer patterning, as it in between 2 Au layer, limiting affects mentioned in **section 4.2.1.** could be the cause. No altering methods were discovered thus the experiment has stop at this point. A classic coplanar electrode configuration was prioritized from the next chapter.

4.3. Conclusion

In conclusion, this study provides valuable insights into the combination of TPA and carbon-based polymers, opening doors to unparalleled possibilities in microscale and nanotechnology. This fusion not only shows potential to intricate and customized structures but also positions itself as a catalyst for advancements in manufacturing processes across diverse industries.

The exploration of TPA in polymers, included PDMS, PMMA, Polystyrene, and Polycarbonate, highlighting the unique responses of each material to TPA. PDMS, with its favourable characteristics, demonstrated successful deep cutting through optimized TPA parameters. PMMA, while presenting challenges due to its characteristics, emphasized the importance of experimental validation, particularly at less common wavelengths. Polystyrene faced difficulties with partial ablation and debris generation, limiting its suitability for microfabrication. Polycarbonate showed promise with successful ablation but encountered limitations in achieving deep cuts.

For in-depth cut techniques, especially bottom-to-top mesh cut, was effective in avoiding absorption and refraction issues during the initial TPA process. However, challenges arose when working with non-optically clear Au electrodes. Multistage cuts were implemented to overcome this obstacle, successfully patterning the PDMS protective layer and two gold electrodes for the final parallel configuration MIC device. However, while the patterning process demonstrated success in creating a through and through channel in PDMS, challenges emerged during fluid flow testing. The inability to detect fluid flow suggested potential channel clogging or issues with the patterning/cleaning process. Multiple attempts were made to address this challenge, double sided patterning, extending channel patterns, and additional cleaning in NaOH, did not yield the desired results. The PDMS protective layer patterning, situated between two Au layers, emerged as a potential bottleneck, warranting further investigation.

Shifting focus to the interplay of deposition parameters for thin film fabrication on flexible substrates like PDMS. The findings are crucial for researchers and engineers in the microfabrication and device development fields, emphasizing the need for precision and balance in the pursuit of tailored thin film characteristics.

This study not only provides some basic understanding of TPA in various materials but also emphasizes the need for tailored optimization based on material characteristics. The fusion of TPA and carbon-based polymers holds immense potential for transformative technological advancements, urging further exploration and experimentation in this dynamic field.

The exploration of a classic coplanar electrode configuration in the subsequent chapters represents a strategic pivot to address the challenges faced in this experiment and advance the understanding of precision material processing techniques.

4.4. Comparison with literature

The literature extensively discusses the superior resolution of two-photon absorption but not much work is found on two-photon absorption (TPA). However, some researchers have use TPA for various medical base ablation processes. In theory of the ablation process it can allow the fabrication of intricate microstructures with sub-micron accuracy. The process enables precise micro dimensions and smooth feature edges, making it ideal for sub surface micro medical procedures. The conclusion supports this by suggesting a under the surface microfluidic channel fabrication of polymer materials with TPA. A microchannel was successfully achieved with high-precision microstructures necessary for impedance-based

cytometry. However, it also points out that while the resolution was optimal, material selection significantly influenced the effectiveness of the printed structures.

Some of the current studies explores the use of various polymers, including SU-8, IP-Dip, and PDMS, in Two photon printing (TPP) based microfabrication but none have explored TPA. The literature acknowledges that material limitation with TPP, such as optical absorption and curing efficiency, affect the final microstructure quality. Certain materials exhibited shrinkage or deformation post-fabrication, requiring process optimization. The conclusion builds on TPA technique based on knowledge from TTP process and outcomes, information from theory and techniques procedure. Conclusion showed details specific to material-related challenges encountered during the study. It highlights that PDMS, despite its flexibility, exhibited issues in achieving stable structures when subjected to TPA only in deep cuts beyond 1000mm. This aligns with the literature's concerns about polymer shrinkage and mechanical instability.

Moreover, TPA at 520 nm remains largely unexplored in the context of ablation. Existing literature primarily focuses on two-photon excitation at wavelengths ranging from 680 to 1300 nm, particularly for applications such as cancer cell ablation and fluorescence imaging.

For metallisation, the literature discusses various methods for depositing Au electrodes on PDMS, highlighting challenges such as adhesion issues, mud cracking, and surface defects. Different fabrication techniques, including photolithography, soft lithography, replica moulding, and thermal deposition, are explored, with thermal deposition being a widely used method. It emphasizes the importance of plasma treatment in improving adhesion and suggests that an additional adhesion layer, like chromium (Cr), is necessary to enhance bonding between Au and PDMS. However, excessive plasma treatment and improper Cr thickness can negatively impact the thin film's integrity. Other factors, such as PDMS expansion in a vacuum and thermal absorption, are also identified as contributors to film defects. Using an E-beam evaporator instead of a thermal evaporator is proposed as a potential solution to minimize thermal stress and cracking.

The conclusion builds on these concepts by presenting experimental findings that confirm and refine the information discussed in the literature. It identifies the optimal deposition conditions—specifically, a 1-minute plasma treatment and a 1µm Cr adhesion layer—as the best parameters for achieving good adhesion and conductivity. The results show that excessive plasma treatment increases Au island formation while reducing island size, leading to non-conductive films. Similarly, varying Cr thickness influences film quality, with thicker layers (10µm or 20µm) contributing to island formation and poor conductivity. The study also confirms that PDMS expansion in a vacuum can introduce defects, but pre-degassing helps mitigate these issues.

5. Conventional coplanar microfluidic devices

5.1. Fabrication

In this chapter, the development of a simple MIC device will be reported. The goal of this work was to replace the traditional metal electrodes with conductive carbon electrodes.

The design is based on an AC lock-in detection principle, where an excitation electrode and sensing electrodes are embedded inside the microfluidic channel[60, 95, 256]. The excitation electrode is driven by a 10^5 Hz sine wave and the detection electrode is measured for its amplitude and phase using a lock in amplifier.

While there are various microfluidic impedance cell designs, we have selected the simplest and well-known device design, which utilizes coplanar electrodes, as shown in schematically in **Figure 46**. As discussed in more details in **Chapter 3**, the coplanar device is preferable for the ease of fabrication but suffers from a non-homogeneous electric field.

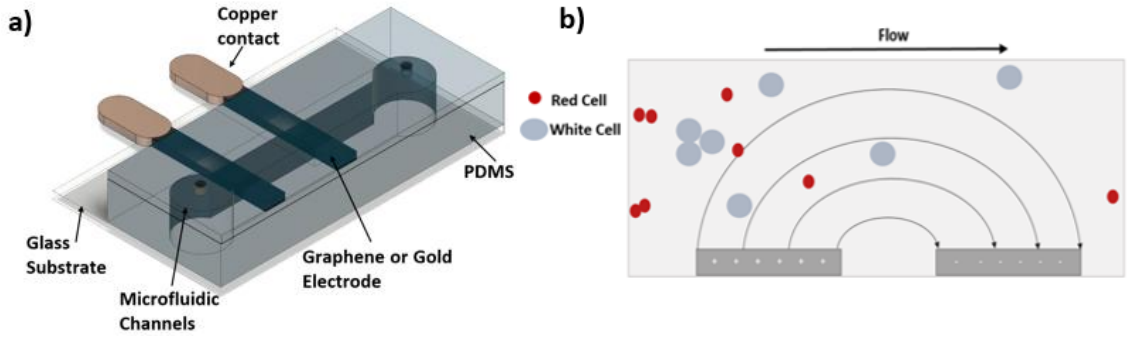

*Figure 46: **a)** 3D model of the co-planar electrode configuration & **b)** schematic illustrating the particle/blood cells flow & electric field across electrodes.*

In **Chapter 5** we will compare the performance of microfluidic impedance cell with gold, graphene, and PyC electrodes. In this chapter we will detail the various processes which were developed to fabricate a coplanar MIC device for both gold and graphene electrodes. Whereas the PyC electrodes were fabricated and shipped from Universität der Bundeswehr, München.

The fabrication of such a device consists of four key stages.

- Design dimensions
- Electrode patterning of gold on glass substrate
- Microfluidic channel pattering with PDMS
- Cell bonding between electrodes and microfluidic channel

Considering the key stages, a schematic showing the fabrication methods can be seen in **figure 47**. Where **47a)** presents the glass substrate with gold electrodes on it, **47b)** presents the block with microfluidic channel and **47c)** presents the MIC device after combining **47a)** & **47b)**.

Following fabrication, devices are tested for functionality through fluid flow testing.

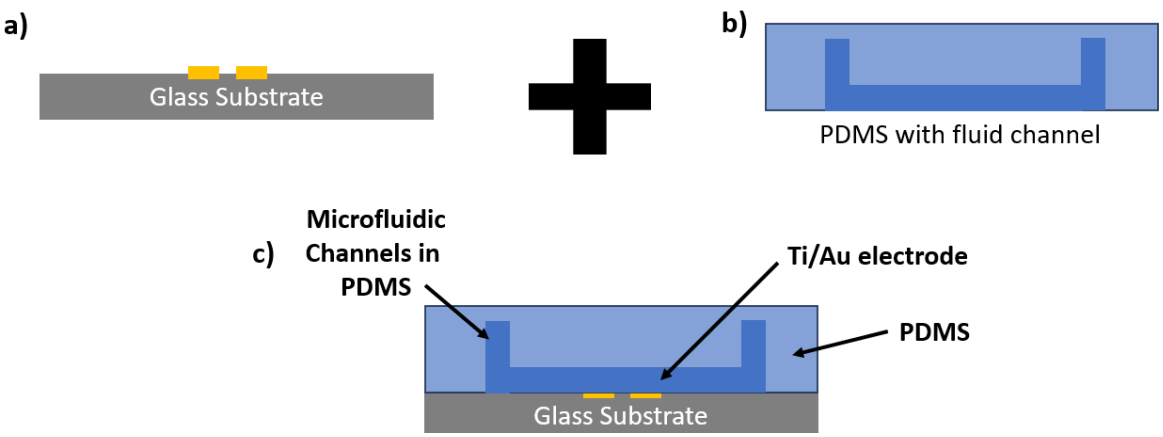

*Figure 47: Schematic of different steps of fabrication for MIC device **a)** electrode pattering on glass substrates, **b)** PDMS microfluidic channel fabricated via tamp lithography, and **c)** MIC device after combining 2 stages.*

For all the three well-known electrode configurations, parallel, coplanar electrode and construction channel configuration, refer to **Chapter 3** for more details, there are two very important dimensional considerations, electrode gap and channel width & height[257]. Due to non-homogenous electric field of coplanar electrode configuration[258, 259], these two elements carry a lot of prominence[256, 260].

The dimensional considerations were based on literature review and simulations run by a Ph.D. colleague, Mickey Warren. The simulation depicts the variation of impedance when a 10μm non-conductive material passes through the well-defined dimensional parameters of the microfluidic channel.

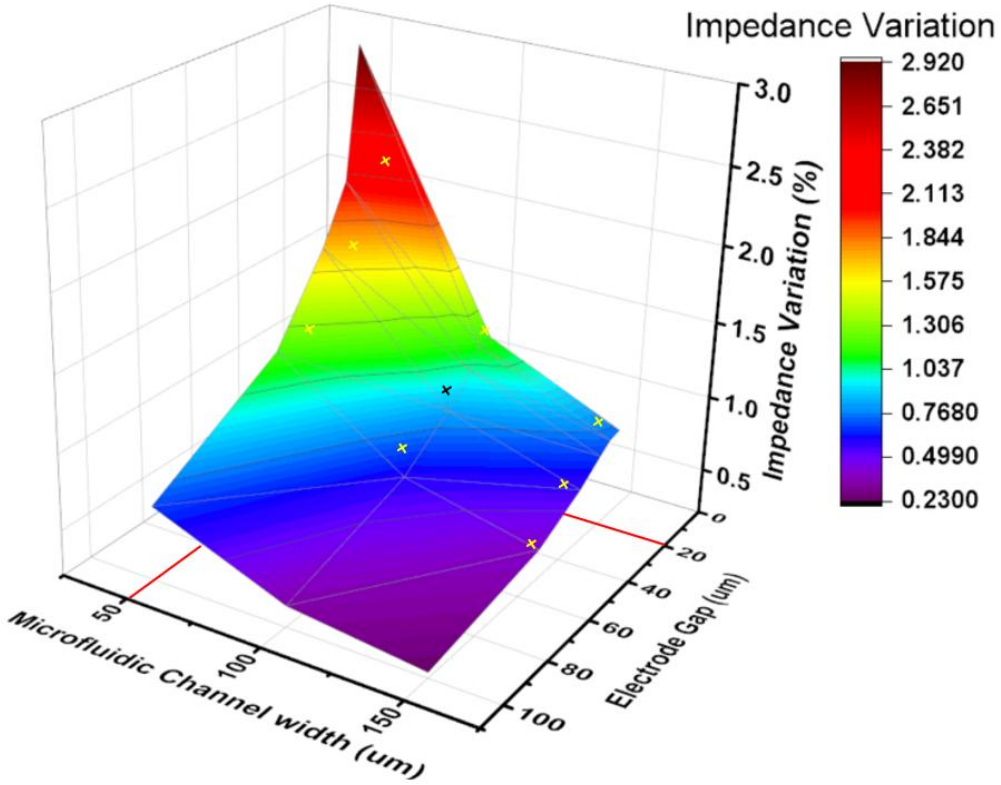

Figure 48: The results of the simulation plotted. Where red lines mark the limitation of the dimensions, yellow cross marks the optional dimensions and black cross marks the chosen dimension.

As illustrated in **Figure 48**, it shows the impact of channel width and electrode gap has on the output signal for impedance variation. The red lines on the axes show the limitation of the specific parameter, such as the distance between electrodes should not be less than 20μm and channel width less than 50μm. The separation is limited to 20μm, as any dimension below will exhibit the dense electric field, becoming more concentrated and saturate quickly which makes it prone to no detection for small variations in the system. The 50µm channel width is found to be the limit due to the risk of clogging. According to Talukder et al, for a microfluidic channel to allow particle flow without clogging, the microfluidic cross-sectional area should be five to ten times larger than the largest particle that will be detected[104]. White blood cells, being the largest particle project aims for, are 18-20μm in diameter. Five time the size of white blood cell proposes the channel width to be 100μm minimum.

When a cell passed through a sensing region (between 2 electrodes) with AC current and sine wave as input, the output amplitude variates due to electric field disruption[60]. The ability to detect that variation is defined where the higher the amplitude of the output signal, the higher the sensitivity and vice versa[261].

To further enhance the sensitivity of the MIC devices, the second important element of channel height was explored. The height of the channel for coplanar electrode configuration also has an impact on the sensitivity. If the channel is reduced to 30μm or lower, it will cause the sensitivity to decrease[262], this is due to the channel compression. The decrease in height will cause compression on the electric field instigating the decline in saturation of current density, leading to fall in sensitivity[263].

Given the range of dimension that the simulation has indicated to have high sensitivity, a selection of electrode gap and microfluidic channel dimensions were explored experimentally and are discussed in later **section 5.2**, **5.3** & **5.4**.

5.1.1. Electrode Patterning

In this section we will explain the steps taken to deposit gold electrodes onto a glass substrate. Electrode gap of 10μm, 30μm & 50μm were fabricated, where generic fabrication process will be explained. The electrode patterning on glass was performed using well known technique of UV lithography[264-266].

UV Lithography

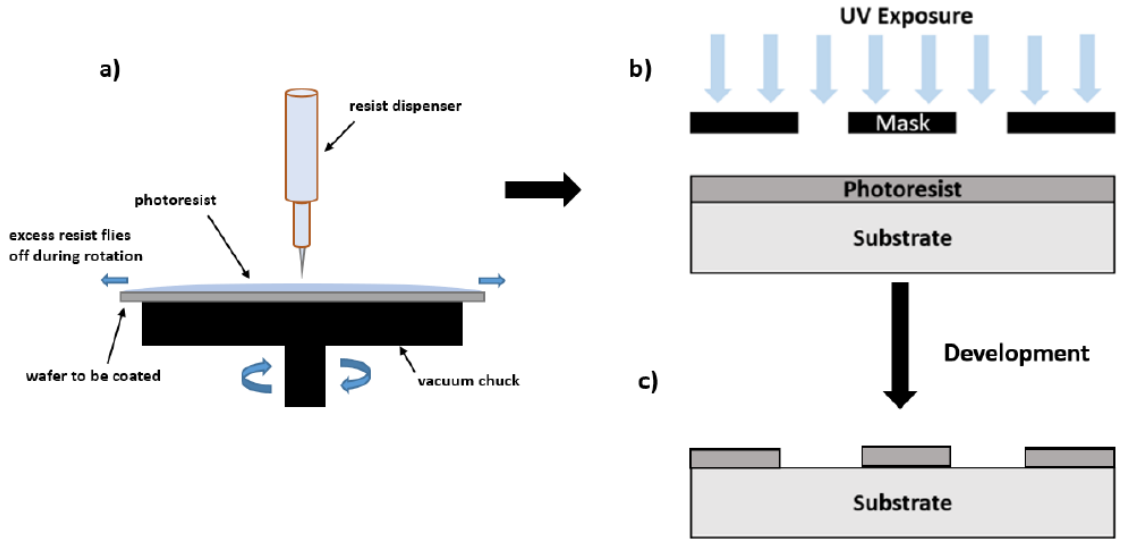

*Figure 49: The schematics of positive UV lithography, **a)** a substrate is spin-coated with photoresist coating, **b)** the substrate with photoresist is exposed to UV exposure with photomask and **c)** when developed the photoresist is removed, leaving behind the patterned substrate.*

In UV Lithography there are several process steps which can be seen in **Figure 49**. The substrate is spin-coated in a thin layer of photoresist. The photoresist is photosensitive material that can be cured with UV light[267]. UV curing is a photochemical process in which high-intensity UV light is used to dry or harden the material. Using the photomask that has the electrode pattern on it, photosensitive material (photoresist) is exposed to UV light. The area that is exposed to UV light becomes very soluble and when placed in developer, it dissolves [268, 269].

For this experiment, glass slides were used as substrates. To improve the adhesion on photoresist and the glass, a dehydration bake at 120° for 30 minutes was performed. AZ-5214 photoresist, which is a reversible positive photoresist (reversal technique used in **section 4.6**), was spin coated on the glass substrates to achieve 1.5μm thickness film. The spin-coated samples were placed in oven for 10 minutes at 90°C. This step is known as soft bake, it helps harden the photoresist layer on the substrate.

The samples were then exposed to UV light through the photomask. The time of exposure is directly in relation between the intensity of the UV light and layer thickness of the photoresist. The under-exposed areas are observed if the duration is too short. The impact of the underexposed photoresist is that these areas are not completely soluble to developer and are not removed during development. Whereas, if exposure time is over than desired time, over-exposure is observed. For over-exposed photoresist, when developed, the pattern will be uneven, expanded and not well defined. Thus, exposure time is very critical and after

experimenting with different exposure times, 15 seconds was chosen with the best outcome. The UV exposed area is then removed when developed in AZ -326 for 25 seconds. Once the development is completed and samples are rinsed in DI water, the patterns are visible on the glass substrate.

Thermal Evaporation

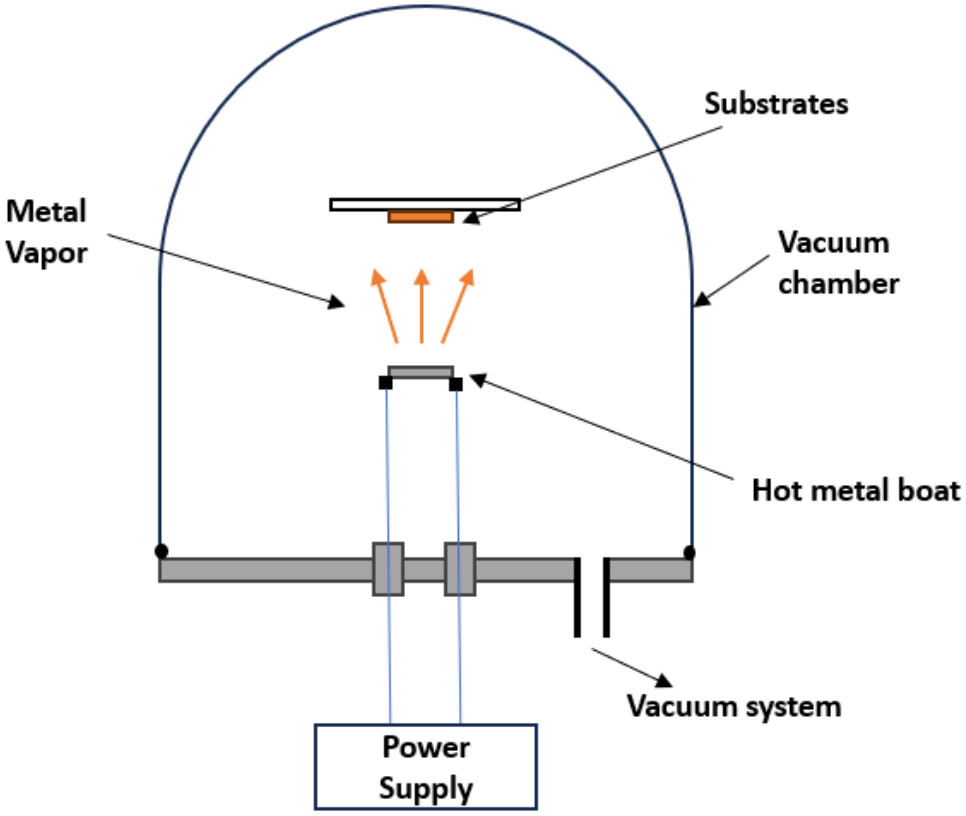

Figure 50: General schematics of a thermal evaporation chamber.

Illustrated in **Figure 50** is the schematic for thermal evaporation chamber. In a thermal evaporation deposition technique, the material is heated until evaporated, this is achieved by high electrical current that passed through a metal boat with desired material in it [270]. The chamber is in vacuum to allow evaporated particles to travel straight to the substrate without colliding with any other particles. The evaporated materials are absorbed back to the solid state at the targeted surface, creating a smooth layer[271, 272]. This technique is a common method for achieving thin-film layers[273] and is very beneficial to deposit numerous layers of different materials with controlled thickness via a deposition sensor.

Using the thermal evaporator at 10^{-5}mbar pressure, 5nm of Titanium at the rate of 2 Å/s and 100nm of Gold at the rate of 3 Å/s, were deposited. Following metal deposit, the photoresist layer is dissolved using a appropriate solvent. The effect of this process is that the metal, which was not deposited directly upon onto the substrate, is removed, leaving only the pattern electrodes. This was done by placing the samples in an acetone bath for 10 minutes[274]. A step-by-step recipe for the electrode patterning is shown in **Figure 51**.

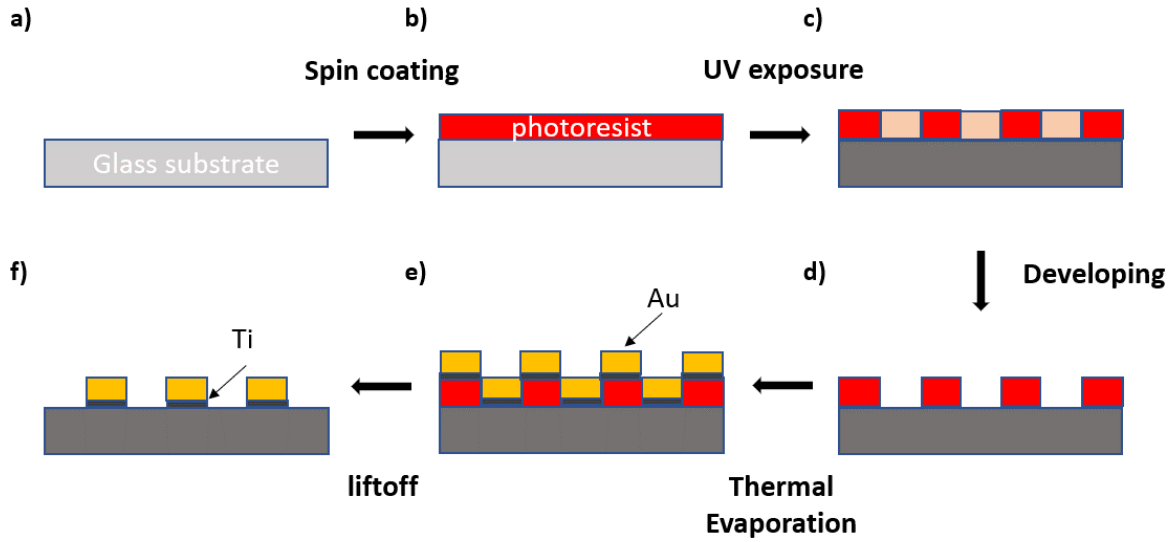

Figure 51: Illustrates the synthesis process of the UV lithography.

Figure 52a) represents the 2D drawing of the setup while **b)** & **c)** illustrates the image taken after liftoff.

Following liftoff, the lithographic pattern is observed under an optical microscope to identify any potential damages and deformations. To further evaluate the quality of the electrodes, each sample is subject to the electrical testing. These measurements are discussed in **Section 5.2.1.**

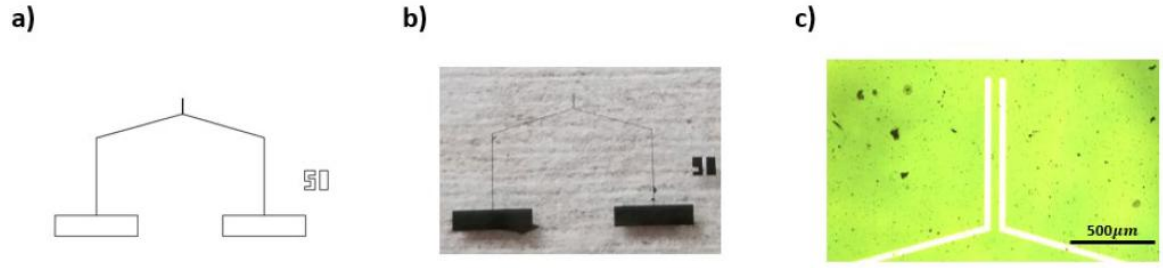

*Figure 52: **a)** the 2D sketch of the 2-pin electrode design for coplanar configuration of 50μm, **b)** the glass substrate with gold electrodes on it, patterned via UV lithography, thermal evaporation, and liftoff and, **c)** an optical image of the gold electrodes in glass substrate.*

5.1.2. Microfluidic channel

A microfluidic channel is a pathway with micrometre dimensions, which helps transport liquid from inlet to outlet of the channel. There are multiple techniques to make microfluidic channels, each leading to different kind of device configuration with different material. This chapter will report the coplanar electrode configuration with channels pattern on PDMS. Soft lithography was used with a master mask made of silicon. The mask was created by etching the silicon wafer to create the wanted pattern[275, 276].

Coplanar electrode on PDMS

The most commonly and well-known method for obtaining patterns is Soft Lithography[277]. In this technique, a lithographically defined 3D 'master' mask is completely covered in polymeric material. The polymer is cross-linked or solidified in some other way and then

removed from the master. The result is a solid polymer 'cast' with the inverse morphology of the master. With appropriate design of the master the cast can be utilised as a microfluidic channel.

Silicon wafer etching facilities in INEX Microtechnology Ltd was used to obtain a silicon-based master mask. Silicon wafer was etched via Bosch process in RIE. Silicon master masks created in this way are very reliable, stable, and surface roughness was down to 50-200 nm.

Using a silicon wafer etched as a master mask and PDMS as the casting material, the microfluidic channels were cast. PDMS was chosen as the best available material for making of microfluidic channel[278] although other materials such as SU-8, PMMA and Hydrogels are also used. One difficulty with PDMS casting on a silicon master is that Si in PDMS reacts and makes covalent bonds with silicon wafer. Such bonding makes it difficult to de-mould the PMDS resulting in damage to the edges of pattern and leaves residue on the master mask[279-281]. To avoid any PDMS residue on the silicon master mask, the process of Silanization was performed.

Silanization

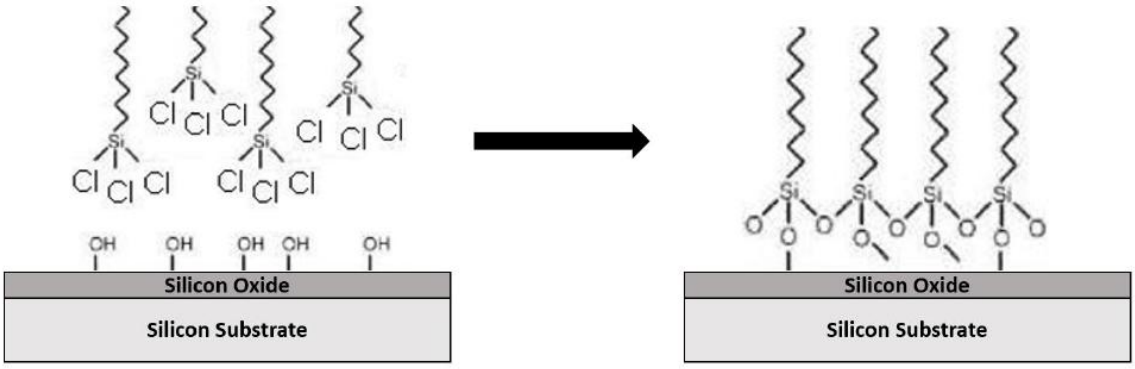

Figure 53: Reaction process of Silanization on Silicon wafer (master mask). OH group on silicon oxide layer reacts with Cl group making the by-product of HCl while the Si group forms covalent bond with silicon oxide layer, creating a hydrophobic anti-stick surface

In Silanization, a self-assembling molecular monolayer (SAM) is created on the surface of the silicon master. **Figure 53** shows a schematic of the process where the SAM is formed of Octadecyl trichlorosilane molecules which are long alkane chain where one end is terminated with a functional group that can bond with hydroxyl groups on the silicon surface. When a silicon surface is suitably treated (as will be discussed) a SAM is produced with a significantly lower surface energy that of the bare silicon. The impact of this is that the treated surface develops a hydrophobic character. A further benefit of this is that when PDMS is cast onto the silicon it is unable to bond with the silicon resulting an effective non-stick treatment.

Using Octadecyl trichlorosilane (OTS) solution in Toluene

For the OTS monolayer a solution of 5mM of Silane in Toluene is prepared. The hydroxyl group on the surface interacts with the hydrolysed OTS molecules through hydrogen bonding. The existence of water is very important for the Silanization process where a small amount is required but excess of the water leads to unwanted polymerization in the silane solution. The solution should not be left in open air, or it will start polymerization. This effect can be seen

as white suspension is formed in the solution[282]. Once the solution is prepared, a special jar with airtight lid and sink-like base is preheated at 80° for 10 minutes for dehydration. The preheating will remove any excess of water inside the jar. Thus, it is critical keep the jar airtight and sealed as soon as possible after placing the substrate and solution. When left over night, the cross-linking in between the OTS molecules on the surface leads to forming of stable network[283].

A contact angle test was performed on the silicon surface to observe the surface energy. For silanization to be successful, the surface should be highly hydrophobic. The droplet should have very high angle, and surface should be water repellent, test showed contact angle of 141°. Once the silicon master mask was non-stick and hydrophobic, the soft lithography process was carried out.

This process is very favourable to counter the PDMS moulding process with Silicon wafer, however there are few limiting factors. This monolayer last about 5 lithography process and wear each time used. The process itself is very tidies and time consuming.

Using Dimethyldimethoxysilane (DMDES) solution in IPA

DMDES is an organosilane compound commonly used to form self-assembly monolayer (SAM) on various surface, particularly on silicon-based substrates[284]. A solution of 0.0005mM of DMDES in IPA is prepared. The Si samples is submerged into the solution for 60s and rinsed with ethanol and DI water. Upon exposure to substrate, the methoxy groups of DMDES reacts with hydroxyl groups ion the surface. The reaction leads to the formation of Siloxane bonds between DMDES and the substrate[285]. This initiates the assembly process of DMDES molecules on the silicone surface. The contact angle measurement showed the angle of 138°.

This process is also very favourable to counter the PDMS liftoff from Silicon wafer, however this monolayer only last 1 stamp lithography process. The solution is easier to mix plus the process time is only 60s.

Soft Lithography on PDMS mould

9 different combinations of microfluidic channel were explored, as illustrated in **Table 3** below, where generic fabrication will be explained.

Electrode Gap	Channel Width [μm]	Channel Height [μm]	Simulated Impedance Variation [%]
$10\mu m$	100	30	0.114
		50	1.14
		150	0.647
$30\mu m$	100	30	0.183
		50	0.829
		150	0.516
$50\mu m$	100	30	0.37
		50	0.593
		150	0.502

Table 3: Presents the explored parameters with simulated Impedance variations for each dimension.

PDMS was cast using ratio of 15:1 Silicone Elastomer in Curing Agent is used. To ensure adequate mixing the PDMS was stirred for 10 minutes continuously. This mixing process leads to formation of a number of air bubbles. Which can disrupt the interface between the mask and PDMS. To remove these air bubbles, the mixture is left for 20 minutes in desiccator before casting. **Figure 54a)** shows the design of the master mask with $100\mu m$ width and $50\mu m$ channel depth. Unfortunately, the silicon master had only a $50\mu m$ prominence at the fluid inlet and outlet which made making external connections very difficult. To provide a large void to connect the microfluidic channel to external pipework a 3D cylinder structure was placed onto the designated inlet and outlet of the device before casting as illustrated in **Figure 54b)** to form cylindrical well (blue). The mixture is transferred slowly onto the master mask and left in glovebox overnight for about 18-24 hours.

After 18-24 hours PDMS is cured about 90%-95%, solid enough to handle yet soft enough to further cure itself when placed on the glass substrate. The process of curing the channel is crucial for bonding with the glass substrate, as discussed in **section 5.1.3**.

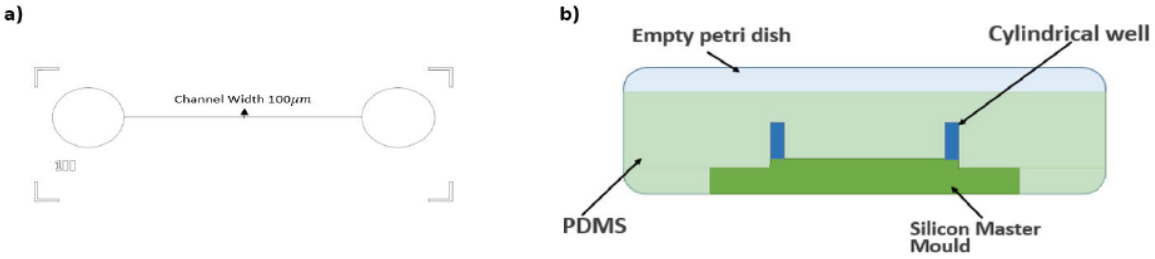

*Figure 54: **a)** is the sketch of the master mask with $100\mu m$ width and $50\mu m$ height. The cylindrical ends mark the inlet and outlet well for the channel and **b)** is the model of the soft lithography process. The inlet and outlet wells are raised higher by the cylindrical well placements. A petri dish is used as the moulding container and silicon mask as master mask.*

5.1.3. Microfluidic Device

The requirements for MIC devices are that it must be a liquid-tight system where the fluid flows in the channel without leakage. To achieve this, glass and PDMS surfaces must be clean and should have an intimate contact together. The adhesion caused between these layers should be able to hold the device together. **Figure 55a** shows the microfluidic channel (blue), placed upon the glass substrate (grey) where the darker blue channel forms a channel that is open only at the ends. **Figure 55b** shows such a completed device viewed from above where the inlet and outlet have been fitted with a syringe needle to allow for solution to be pumped through the microfluidic channel.

Channel dimensions, fluid flowrate, pressure difference, surface energy and liquid viscosity, have an impact on the closed microfluidic system. One important aspect which will be examined in this section is the adhesion of the PDMS block to the substrate and the surface energy of the channel.

Once the glass substrate with electrodes (from **section 5.1.1)** and patterned microfluidic channel on PDMS (from **section 5.1.2)** were prepared, the electrodes were carefully aligned with the channel and PDMS block was laid on the glass substrate. The channel must be able to sustain fluid passing through which requires that fluid can move through (wet) the channel and that the channel remains sealed.

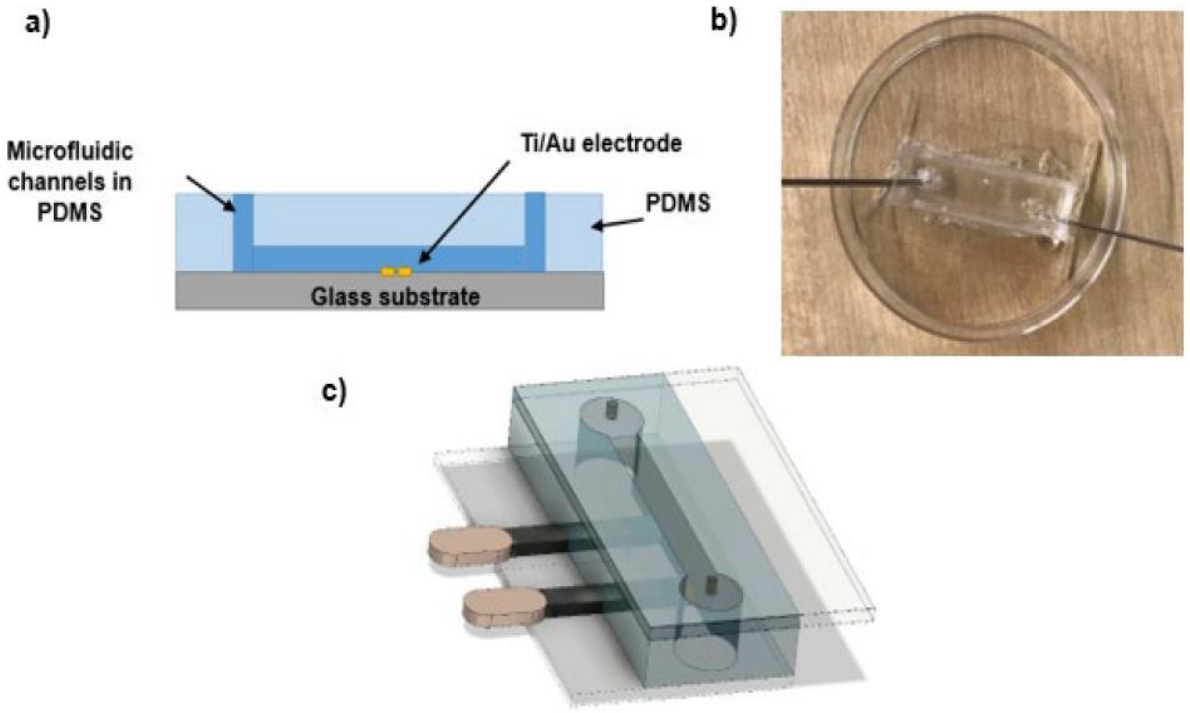

*Figure 55: **a)** the cross-sectional schematic model of glass and PDMS going together, **b)** the top view of the actual device with syringes at the inlet and outlet wells, and **c)** the 3D model of the MIC device.*

When liquid interacts with microscopic channel dimensions, they feel a resistance to the flow due to the relatively high surface area of the channel with respect to its cross section (refer to **section 2.9** for surface energy). When the fluid is pumped this leads to an increase in pressure within the channel[286], until either: the fluid passes through, or a fluid wedge is formed between PDMS and glass. A wedge occurs when PDMS loses its adhesion with the substrate, allowing air or fluid to seep in. This eventually compromises the device seal, leading to leakage and potential failure of the entire system. Fluid flow outside of the defined channel is undesirable for the flow and hence passage of the particle for counting becomes unconstrained. To solve the problem of wetting and wedge formation two approaches to PDMS-glass adhesion were explored:

- Achieving hydrophilic surfaces
- Increasing the adhesive between the PDMS and glass substrate

Achieving a hydrophilic surface

Surface energy is a well-established concept in material science. If the surface is hydrophobic, it has low surface energy. Which causes higher contact angles between glass surface and fluid droplets. Working in μm channel dimensions, such large size droplets cause additional undesirable resistance and to avoid it, substrate needs to be hydrophilic. To achieve the wettability or hydrophilicity in the MIC system, an oxygen plasma treatment was performed on both PDMS and glass surfaces before combining. Plasma treatment is a technique employed to achieve hydrophilicity. It modifies the surface properties of the material by removing contaminants and introducing functional groups, such as hydroxyl groups, that enhances its affinity for water[287].

a)

Exposure Time (Minutes)	Contact Angle (°)	Surface energy (mN/m)
0	118	-34.18
1	56	40.71
2	48	48.71
4	35	59.63
5	29	63.67
10	47	49.65

b)

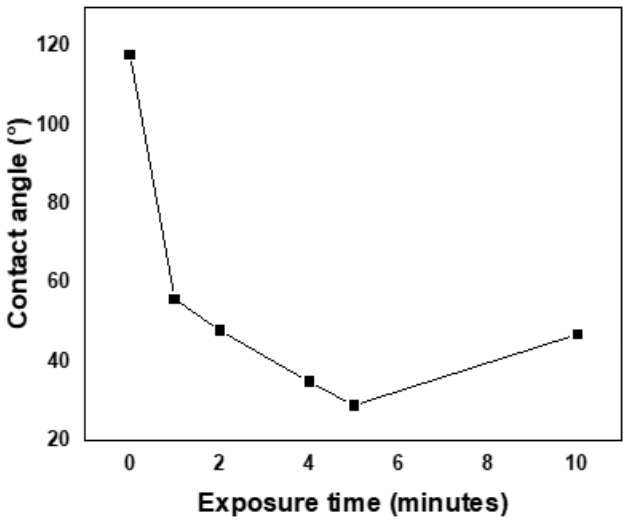

*Figure 56: **a)** is the table which shows the contact angles and surface energy and, **b)** is the contact angle plotted against exposure time.*

To show the modification of surface energy by oxygen plasma on glass we used oxygen plasma with oxygen flow rate of 10 sccm, using approximately 8 mbars of oxygen at the power of 90 watts. The resulting contact angles measured for different durations of oxygen plasma treatment of a glass surface are shown in **Figure 56a)**. Where it can be seen that without any oxygen plasma treatment, the surface contact angle is 118° and as the duration of the plasma treatment increases, the contact angle decreases. **Figure 56b)** shows that this decrease follow a non-linear trend with initial very rapid reduction in contact angle which slows down with extended exposure[288]. The surface energy was calculated using the equation $\gamma_s = \gamma_L \times cos\theta + \gamma_{sL}$[193], where the surface energy increases with the decreasing contact angle, indicating that the surface has become hydrophilic. The surface energy of the glass increases until it reaches a minimum value at 5 minutes of exposure with the contact of 29° and surface energy of $63.67\ \mathrm{mN/m}$. This compare well with the literature where 18° has been observed after 5 minutes of exposure[289]. However, as the exposure time increases, the oxygen species from the plasma starts interacting with the surface, forming new polar functional groups. This leads in increase in surface energy as can be seen in **Figure 56b** at 10-minute exposure.

The effect of plasma treatment on the glass surface diminishes quickly as oxygen from the ambient atmosphere interacts with the surface, leading to the formation of an oxide layer[290]. The channel was sealed by placing treated substrate and PDMS together within 10 minutes of plasma treatment.

According to Amador et al[291], using DI water as fluid, a minimum surface energy of 30mN/m[291] is required for flow through a channel with a width of 100µm and a height of 50µm, which is achieved in this chapter.

Increasing adhesion between PDMS and glass

In principle, PDMS does not form covalent Si-O bonds with glass[292]. As it is an elastomer, PDMS is able to conform to substrates and provided they are sufficiently flat a seal is formed.

However, in practice, the adhesion between PDMS and glass is insufficient to create a reliable seal for the microfluidic channel[293].

The surface interaction between glass and PDMS lacks sufficient covalent bonds, making it unable to withstand the pressure difference. ΔP is the pressure difference across the microfluidic channel and is the sole reason for the liquid to move from inlet to outlet. Without the difference of pressure across the channel, the fluid will not move through the channel. According to Raj et al [294], a PDMS microfluidic channel with the same dimensions to our channel can withhold ΔP of up to 2.23kPa[96, 262, 274].

After the surface treatment from previous section, using Hagen-Poiseuille from **Equation 3** with laminar flow fluid (from **section 2.2**), the ΔP calculated for our channel is 0.067kPa. The Reynolds number, calculated from **Equation 4**, is 0.083, which proves it's a laminar flow.

To address the issue of PDMS adhesion we have applied several techniques such as Plasma cleaning [273, 295], Oxidation in Oven[292] and Piranha Etching[296]. These treatments modify the surface morphology and functionalities. To compare these different treatments three test relevant to microfluidic channel formation were applied,

1. Adhesion (creation of seal for MIC device when PDMS is placed on glass substrate)
2. Stability (shelf life of the device when left for 1 day and it retains its adhesion)
3. Liquid flow (the fluid flow determines the capability of the MIC device to hold against the pressure created by flow rate)

The unfavourable outcome of stability and liquid flow can be seen in **Table 4**. For all the surface treatment techniques, the test for stability and liquid flow resulted in failure. None of the techniques were able to keep the adhesion and prevented leak points.

	Plasma Cleaning			Oxidation in Oven @ 120°			Piranha Etching Sulphuric Acid: Hydroperoxide (3:1)		
Time (minutes) / Features	30	60	90	30	60	90	2	5	10
Adhesive	×	✓	✓	✓	✓	✓	✓	✓	✓
Stability	×	×	×	×	×	×	×	×	×
Liquid flow	×	×	×	×	×	×	×	×	×

Table 4: Results of the MIC devices, where 3 phase system is investigated against different methods of attaining adhesion between glass substrates with electrodes and PDMS block with microfluidic channel.

The low value of ΔP across our channel and the functionalization of the surfaces with the techniques mentioned, created only partial Si bonding which did not keep the adhesion. Obviously, ΔP in fabricated device was less than the breaking limit of the device from Raj et al[294].

To overcome such a critical problem where the well-studied techniques did not function, we developed a novel approach to the channel formation based upon partial curing of the PDMS. Instead of waiting until the PDMS was cured while on mould, the PDMS was peeled when it was about 90% cured and immediately placed on the glass substrate. This allows uncured PDMS mould to cure over the glass substate and have stronger Si-Si bond with glass. To further enhance the adhesion, additional PDMS was mixed at the cross linker to monomer ration of 2:1 and added to the outer edges as a kind of glue. **Figure 57** illustrates the schematic model of the glue placement on MIC device. This would directly create strong bonding force between PDMS and Glass on the outer edges. The device was then placed on the hotplate at 50° for 30 minutes, this would accelerate the curing process of PDMS block and PDMS glue. With self-curing and PDMS curing, adhesion between the two surfaces were very consistent when established against relevant fluid tests. This method was the only technique which held the device together and worked for us.

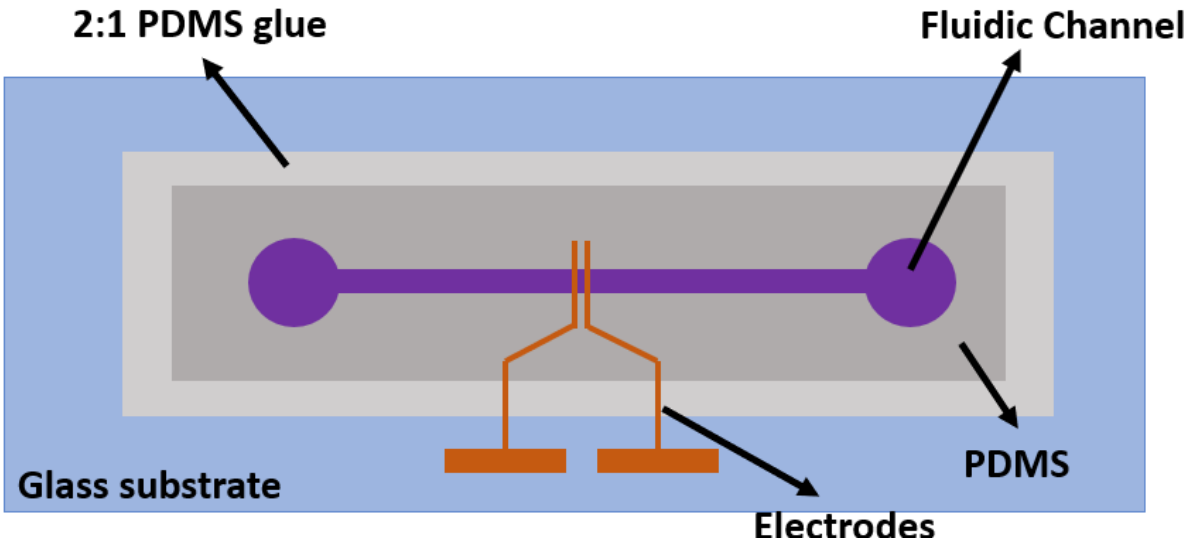

Figure 57: The schematics of the MIC device, where 90% cured PDMS block is placed on the glass substrate with electrodes. The 2:1 PDMS glue is carefully placed around all the edges.

5.1.4. Graphene Growth

There are several methods of growing graphene, each with its advantages and disadvantage. Some of the well-known methods have been explained in detail in **chapter 2.8.2**. The graphene growth type used for this project is CVD graphene. With its advantages in high homogeneity, high purity, fine grain boundaries, and control over layer numbers, a higher charge mobility can be detected.

CVD graphene

Chemical vapor definition is explained in **chapter 2.8**. In this section, we will explain the CVD growth process. Graphene CVD growth was performed by Dr Abdullah Aladim. The recipe is explained in detail below[297].

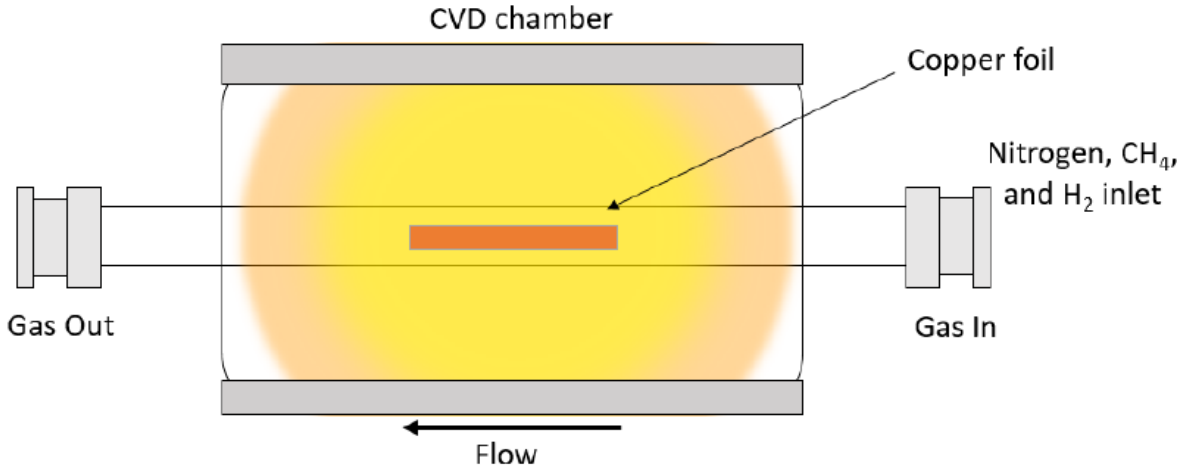

Figure 58: A schematic model of the CVD growth chamber, where copper foil is placed inside the glass tube. A temperature of 1050℃ and pressure of 66mbar is maintained throughout growth process. The Gas inlet is connected to controlled gas flow regulators.

Figure 58 illustrates the schematics model of the CVD chamber. A copper foil of thickness $25\mu m$ was used to synthesize the CVD growth of graphene. The gasses used during the growth were methane (2% CH_4 with nitrogen balance) as carbon source, hydrogen (2% H_2 with nitrogen balance) as growth catalyst/moderator and nitrogen (N_2) as the gas carrier. The copper foil was placed in the quartz tube furnace which was evacuated to a base pressure of 2mbar. N_2 was introduced with a flowrate of 100sccm, and the chamber pressure maintained at 66 mbar. The foil was annealed at $1050°C$ for 30 minutes. After annealing, H_2 and CH_4 are introduced in the tube for 30 minutes at the flowrate of 1000sccm and 20sccm, respectively. As the chamber was at the activation temperature of $1050°C$ for methane in the presence of copper, the carbon atoms will start to dissociate and bond with copper surface. N_2 gas, acting as carrier gas, will carry all the residual gasses to the gas outlet. At this stage called as slow growth, few small islands of graphene structure will start to accumulate. After 30 minutes, CH_4 inflow was increased to 200sccm for 3 minutes at constant temperature. This higher concentration of methane increases the graphene growth rate filling in the gaps between the graphene islands seeded during the slow growth stage. The CVD grown graphene monolayer is approximately 2nm in thickness. Once the growth is complete, the system is left to cool down, while the flow rate is kept same.

Graphene transfer

While graphene is grown on a copper surface it is not so useful for electrical applications in this context. In the case of the electrodes in the coplanar microfluidic device the graphene must be moved to the glass substrate without breakage or crumpling. This process is known as graphene transfer and there are numerous methods available. In this work we have used polymer assisted transfer using the particular details given in Chen et al[298].

Removing the copper foil from graphene sheet is a major part of the graphene transfer. A well-known method of doing so is to chemically etch away the copper foil, leaving graphene behind[299]. Monolayer graphene at around 0.7nm thick, is very fragile to the effects of any stress or strain. Given the fragile nature of a graphene monolayer once the copper is removed it must be stabilized until it is relocated. To protect it from any external forces, a supporting polymer layer was used throughout the process of copper removal. Following the work of Cui et al[300]. Cellulose nitrate was spin-coated over graphene as supporting layer[301, 302].

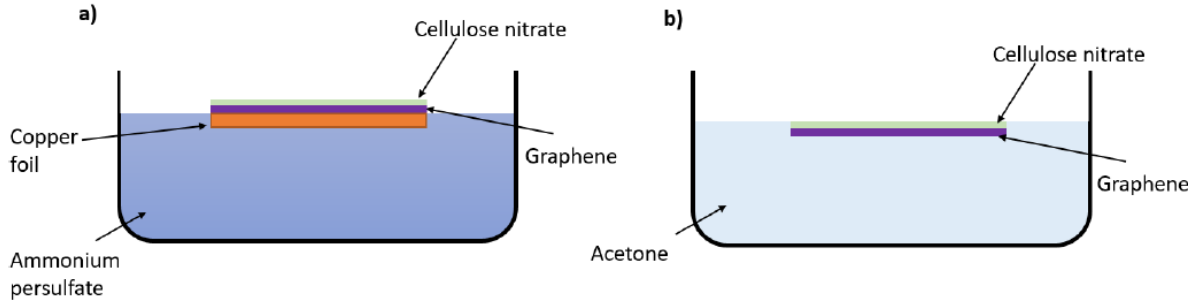

*Figure 59: **a)** a schematic of etching copper. Copper foil with graphene/cellulose nitrate is placed in etching solution for 2 hours, **b)** the schematic of acetone bath for removing supporting layer from graphene sheet. Once the removal is completed, graphene floats on the surface of acetone and transferred on glass slide.*

The copper foil with graphene/cellulose layer was placed in ammonium persulfate ($(NH_4)_2S_2O_8$) as shown in **Figure 59a)**. The etching process can be explained by following chemical reaction:

$$S_2O_8^{2-} - + \mathrm{Cu} = \mathrm{C}u^{2} + + 2SO_4^{2-} \qquad (30)$$

After 2 hours the 0.5M of ammonium persulfate solution completely etches the copper from graphene/cellulose nitrate film[300]. **Figure 59b)** shows the remaining polymer and graphene layer which is carefully removed from the etchant and rinsed in DI water before being placed upon a glass substrate and dried in air. The polymer film is then removed by immersion in an acetone bath for 2 hours.

5.1.5. Graphene Patterning

In the past ten years, a multitude of different techniques have developed for graphene patterning[303]. Some of the techniques used for graphene patterning are top-down, bottom-up, and chemical etching, refer to **section 3.3**. In this chapter, we will discuss the use of chemical wet etching and dry etching for achieving graphene electrodes in the context of a microfluidic devices. In particular a novel mix approach will be presented.

Figure 61 shows a process schematic for the formation of patterned graphene layer following graphene transfer as described above. Initially the un-patterned graphene on a glass substrate is mounted in a thermal evaporator. Under the chamber pressure of 10^{-5}, when the

boat temperature reached 1020°C, a deposition rate of 3Å/s was used. A thin film layer of 50nm copper was deposited.

The Graphene/Cu substrate was than spin-coated with AZ-5214 photoresist, achieving 1.5μm film thickness. The sample was placed in an oven for 10 minutes at 90°C for soft bake to drive off the remaining solvent.

In this process the photoresist is developed and exposed for use in a negative tone process.

The samples were exposed to UV light through the patterned photomask for 15 seconds. This will make the exposed area soft. The samples were placed on hotplate for 30 seconds at 120°C. This process is known as post bake, which will harden the UV exposed area. The samples are then again exposed to UV light for 25 seconds but with no mask, this is known as flood exposure. This will instigate the reversal of resist, causing cross linking to occur on the unexposed area of the first exposure. The photoresist is then developed in AZ -326.

Once patterned electrodes of photoresist over copper/graphene layers were prepared, the exposed copper layer was etched for 10 seconds using ammonium persulfate ($(NH_4)_2S_2O_8$) revealing the underlying graphene sheet. As the etchant solution is very robust, the control of exposure time is very crucial. If the samples were to be left for over desired time, a process known as over etching occurs. This means that the copper will start to get etched from the sides even under protective layer of photoresist. In some cause, etches through the pinholes of the photoresist were also seen. Optical images in **Figure 60a) & b)** shows the over etching and etching through pinholes, respectively.

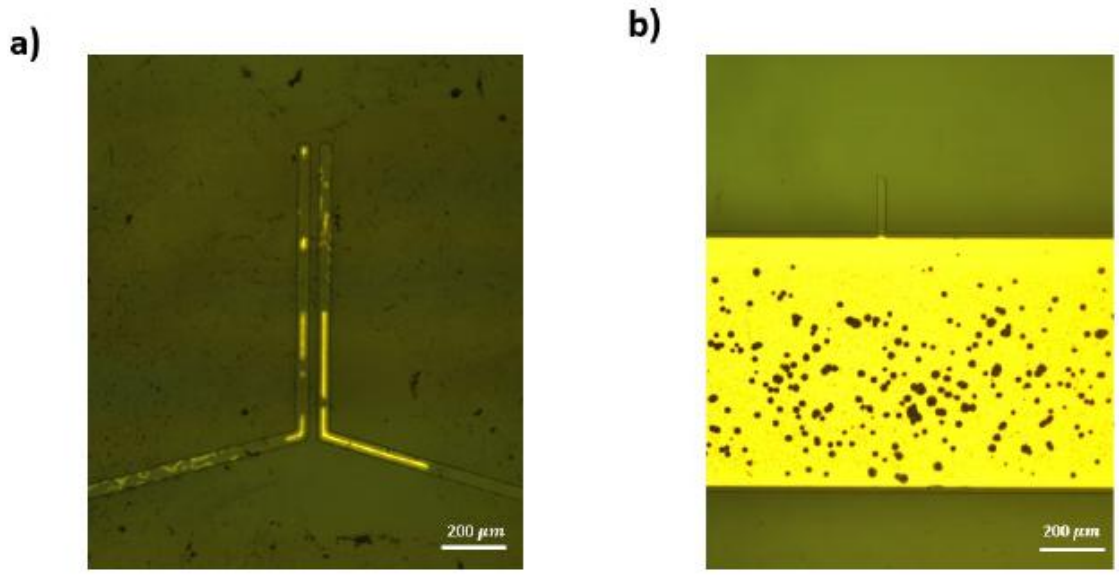

*Figure 60: **a)** an optical microscope image showing the effect of over etching. The yellow parts are the remaining copper while the well-defined borders are photoresist patterns, and **b)** an optical microscope image showing the etched holes in copper layer through the pinholes of photoresist.*

Following the copper etching, the photoresist is removed by placing the sample in acetone bath for 5 seconds. As can be seen in **Figure 61**, the remaining copper is now used as a protective layer for graphene sheet during oxygen plasma etching. The sample was placed in

a plasma cleaner for 20 minutes. During this time, any exposed regions of the graphene sheet is removed, leaving the graphene only under the patterned copper layer. The final step of the graphene patterning process involved removing the thin copper film, which was done through wet etching in Ammonium sulphate.

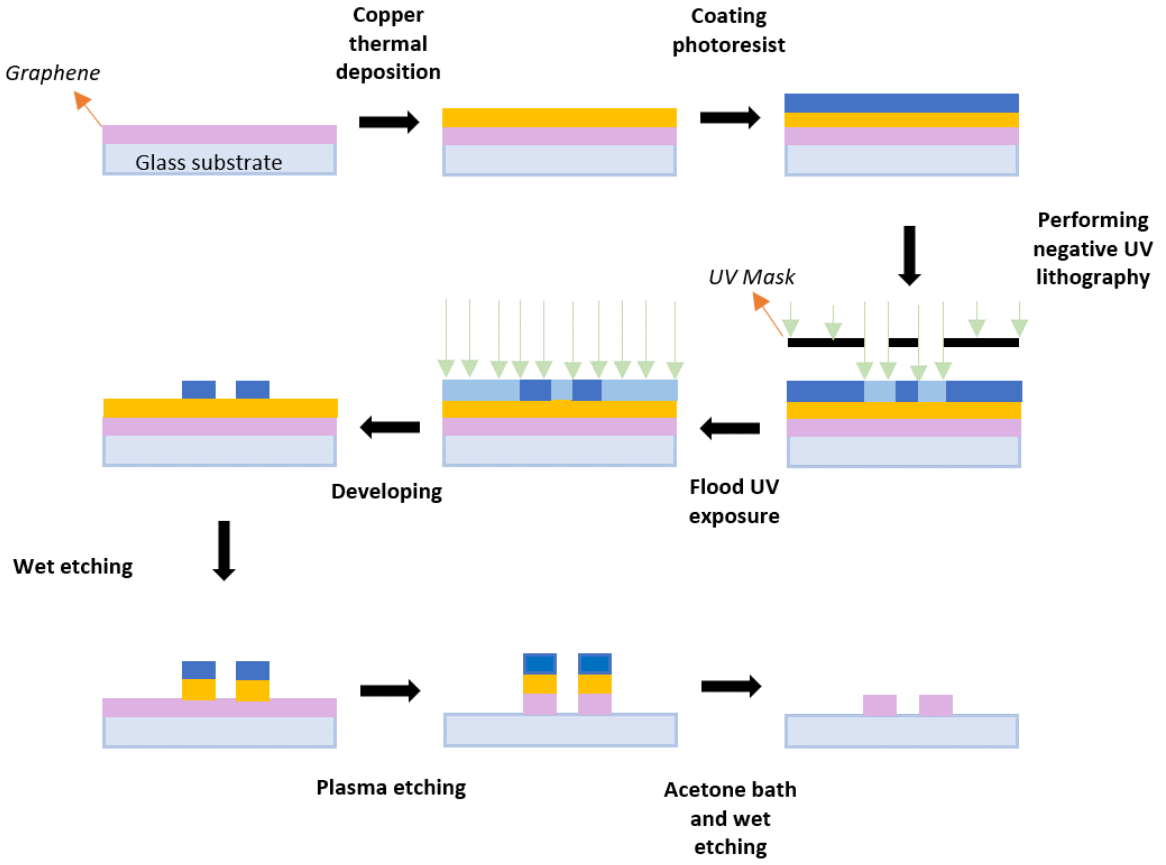

Figure 61: Illustrates the synthesis process of the Graphene patterning.

After each step of the graphene transfer process, an optical microscope was used to inspect the channel quality and pinpoint any disorientation around the sample. As graphene is invisible to naked eye and very hard to spot even through microscope, copper electrodes were only removed from the sensing region of the electrodes. The connection pads were covered with thin film copper layer for the stability. **Figure 62** illustrates the images.

In **Figure 62a)**, as graphene is almost transparent, you can see water marks on the back of the glass substrate through graphene sheet. In **b)**, after copper layer has been deposited via thermal evaporation no surface features can be distinguished beyond some particulate contamination in the lower right. In **c)**, after UV lithography, patterned resist can be seen where occasional marks around the sample are from dust but mostly water marks from previous step involving DI water rinsing and drying. In **d)**, the removal of the exposed copper reveals the electrodes in high contrast with the graphene sheet appearing faintly against the glass. Subsequently, in **e)**, after the plasma exposure is perform, any unprotected region of graphene sheet is etched away leaving only the electrodes visible. Lastly in **f)**, the image is not showing graphene but an after image of patterned copper. To verify the presence of patterned graphene, AFM & Raman mapping analysis were conducted in this region. AFM

offers insights into the thickness and topographical details, while Raman mapping not only illustrates the pattern where graphene is present but also provides a comprehensive assessment of the quality of the graphene at every individual point on that map.

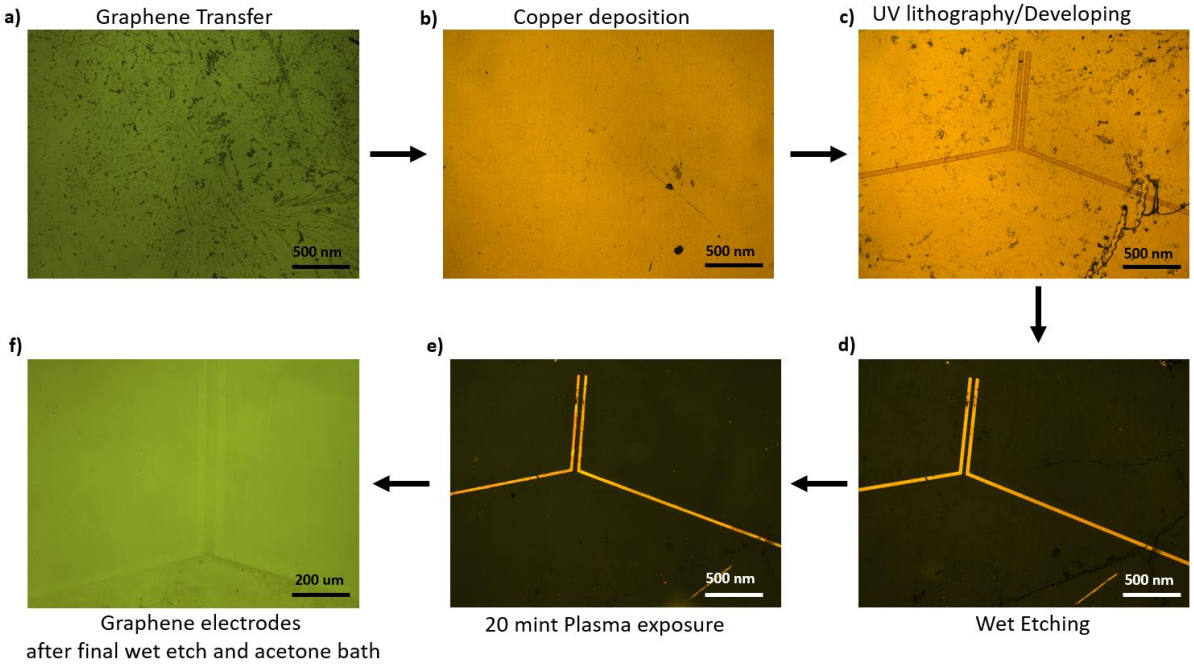

Figure 62: optical microscope image during graphene patterning, where copper is removed from the sensing region of the device on the last step.

In **Figure 63a)**, an optical microscope image of two graphene electrodes on glass is shown, white square shows the area of AFM scan. **Figure 63b)** shows an AFM image taken from the square indicted in **a)**. This AFM shows the edge of the graphene covered region highlighted the clear and well-defined distinction between the two regions. However, noteworthy observation is the presence of contamination, presumably deposited subsequent to the wet etching process. These residual entities could potentially be either dust particles, watermarks,

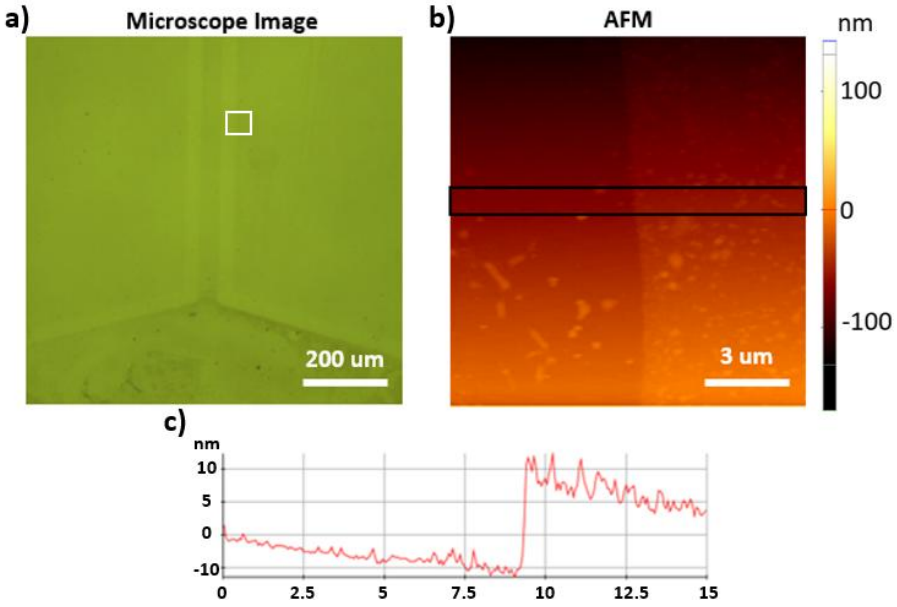

*Figure 63: **a)** is the optical microscope image of the patterned graphene electrode, **b)** is the AFM done at the edge of graphene-glass substrate, and **c)** is the scan profile of the AFM.*

or remnants of the copper from the etching process. A line profile, presented in **c)** shows, the topography at the edge of the graphene sheet. The profile reveals a noticeable step height of 20nm, which is significantly higher than would be expected for graphene alone, indicating the existence of some other material in addition to graphene or due to etching of the substrate by the oxygen plasma. Moreover, the graphene layer exhibits a rougher texture compared to the glass substrate due to corrugation and wrinkles associated with the transfer of CVD graphene[304].

Raman spectroscopy is a useful tool to characterise atomic-scale structural and chemical modification of graphene. To evaluate the presence of graphene and the number of graphene layers, the Raman spectrum is used. It has three major peaks used to study the graphene quality: G, D, and 2D. The intensity of the G peak is increased relative to 2D with an increasing number of graphene layers. Also, the shape and intensity of G and 2D peaks change with the graphene layers [305, 306]. The ratio of IG/I2D can be used to estimate the number of layers of graphene[307, 308]. The D peak is generated from the breathing mode of the hexagonal ring and requires a defect to be activated, meaning that the intensity ratio of ID/IG can be used to evaluate the defect density of the graphene[309].

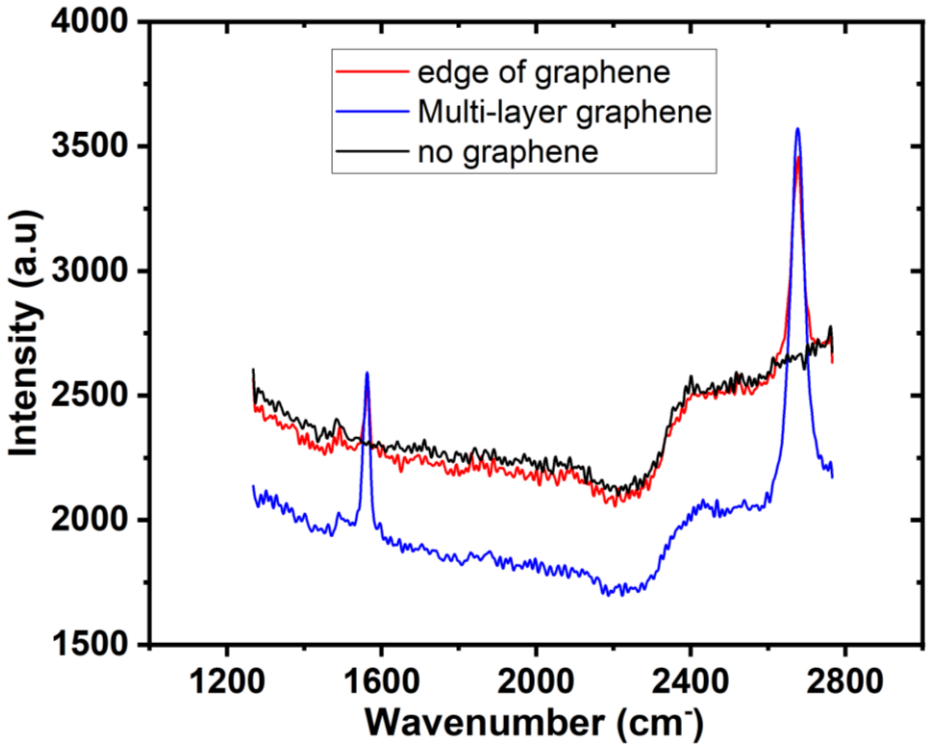

Figure 64: Raman spectroscopy of the patterned graphene sample, showing the quality of graphene at multiple points of the electrode.

Raman spectroscopy measurements were collected using a Horiba Jobin Yvon HR800. The incident laser power was 4 mW at room temperature, and the laser beam diameter was 0.70 µm. An acquisition time was set to 5 second per measurement for spectral windows. Raman measurements have been taken for devices to evaluate the presence of graphene. Raman spectra are presented in **Figure 64** for all peaks G, D, and 2D. Both G and 2D peaks are visible for sample with graphene and absent for sample without graphene presence. In addition, the I2D/IG ratio for the multi-layer and edge of graphene is 1.37 & 1.36, which indicates its

multilayer graphene. If the ratio is between 1.90 to 3 graphene is monolayer and if it's between 1 to 1.88 it is multilayer graphene[307, 310, 311]. Moreover, there is no presence of a D peak on graphene, which indicates that graphene is clean of defect. It is evident from the Raman results that the monolayer graphene is present throughout the pattern region and shows no detectable defects caused by the transfer and patterned process.

5.1.6. Conclusion

The fabrication process for the MIC devices involved several key steps, including the fabrication of gold electrode patterns on a glass substrate using UV lithography, the formation of a microfluidic channel using soft lithography on PDMS, and the utilization of a coplanar electrode configuration. The deliberate selection of electrode separation (10μm, 30μm, and 50μm) and channel heights (30μm, 50μm, and 150μm) were choose following the results from literature and simulation. The calculated value of the pressure range indicated that the device should not experience excessive pressure buildup, minimizing the risk of system leakages. Additionally, oxygen plasma cleaning was performed on glass surface of the device to lower surface energy, and a novel approach involving the transfer of uncured PDMS was employed to enhance bonding between the two surfaces.

Furthermore, the fabrication process involved the utilization of chemical CVD growth technique for graphene synthesis and transfer onto a glass substrate, as well as the development of a process for fabricating graphene electrodes using wet and dry etching processes.

The fabrication process for the MIC devices involved a combination of advanced techniques such as UV lithography, soft lithography, and graphene synthesis. These techniques were carefully chosen to ensure the successful fabrication of well-defined gold electrodes, patterned graphene and a microfluidic channel with optimized bonding and surface properties. The use of these techniques demonstrates a comprehensive approach to device fabrication, taking into account factors such as material properties and device performance.

5.2. Gold devices

5.2.1. Electrodes Measurements

Within this section of the report, two methodologies are employed to enhance our understanding of the electrodes before finalizing our MIC device. Specifically, Cyclic Voltammetry (CV) and Electrochemical Impedance Spectroscopy (EIS) are deployed as crucial techniques to delve deeper into the intricacies of the electrodes and gain a more comprehensive understanding of its behaviour and performance. A 9.8% concentration of phosphate solution from Sigma Aldrich was used as the fluid electrolyte medium, due to its higher ionic concentration, which is equivalent to biological systems. This was used as the standard medium for all the experiments.

The CV technique involved the cyclic variation of the applied voltage to the electrodes, accompanied by the measurement of resulting currents. This dynamic approach proved instrumental in revealing the redox behaviour of the samples, providing crucial insights into their electrochemical reactions and stability, particularly under fluctuating voltage conditions. For background details to understand CV, refer to **section 2.3**.

The electrochemical stability of an electrode in electrolyte is of great practical significance for potential applications. The electrochemical stability window is set by the reactivity of the electrolyte and thus, by the redox reactions of the electrolyte and the solvent at the electrode surface. The onset potential refers to the potential at which a particular electrochemical reaction begins. It is the potential at which the analyte oxidizes at the surface of the working electrode, causing the current to increase exponentially on the cyclic voltammogram until it reaches the anodic peak current[312]. In the case of the oxygen evolution reaction, the onset potential is the voltage at which the applied potential overcomes the activation energy for the electrochemical reaction, leading to a significant increase in current.

Performing CV on gold electrodes spaced 10, 30, & 50 micrometres apart can yield valuable information about the electrochemical behaviour and interactions in this confined system. A Voltage sweep ranged from -500mV to 500mV with the scan rate of 10mV/s in a phosphate solution as an electrolyte was conducted. The interaction area of the Au was 0.5 cm^2. The experimental setup utilized for this investigation was the Gamry Reference 620.

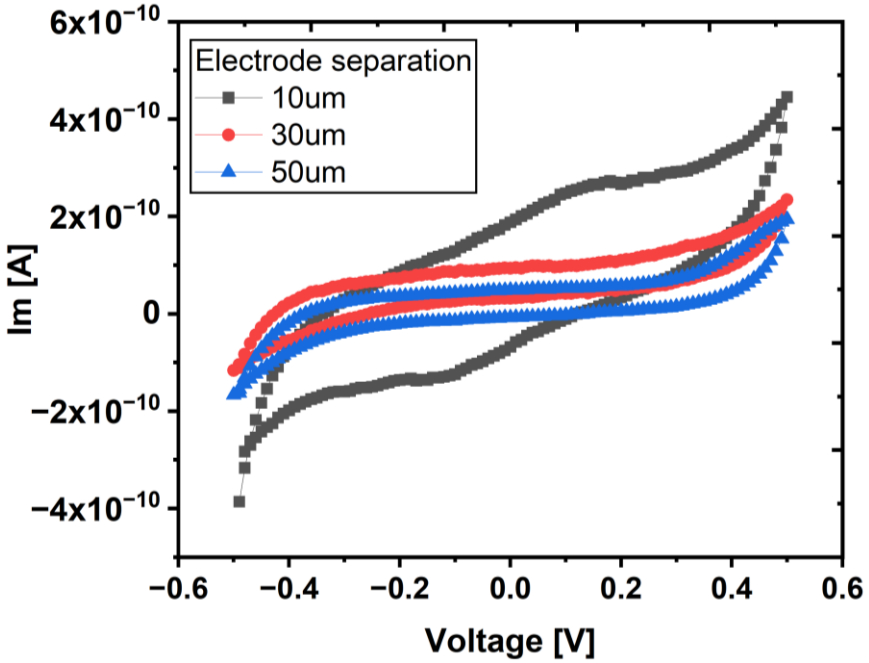

Figure 65: These are the results of a CV curve performed on Au electrodes with 10, 30, & 50um electrodes spacing.

Examining the cyclic voltammogram, presented in **Figure 65**, it can be observed that the redox and oxide peaks are not visible for 30μm and 50μm separations, this is caused due to the electric double layer (EDL) effect. The double layer effect is a fundamental aspect of electrochemistry and refers to the formation of the EDL at the interface between an electrode and an electrolyte solution. In electrochemical sensors and biosensors, the double layer capacitance plays a role in the detection of analytes, contributing to the sensitivity and selectivity of the sensor[313].

For 10μm electrode separation, around 150mV and -150mV the redox peak and oxide peaks can be observed. When the electrode distance is decreased the transfer kinetic and mass transport have a higher impact[314, 315], causing the peaks to be visible in only 10μm electrode separation. This comes to show that the redox and oxide peaks have been overshadowed by the double layer effect for all the separations.

Moreover, the difference on separation of Au electrodes has a significant change in the area under the curve, specifically between 10μm from the rest. The area under the curve for 10, 30 and 50μm is 1.95×10^{-10}, 6.01×10^{-11} and 5.65×10^{-11}AV. This trend shows that there is a difference in between electrochemical behaviour between 10μm from the rest of the separation. Whereas a very negligible difference between 30μm and 50μm.

As there is not a well-defined, sharp and high onset peak, it is associated with the initiation of a redox process, it can be said that no significant shift in the onset potential of the oxygen evolution reaction is found or either its very low, which means the electrodes are electrochemically stable[316].

Using **equation 13**, the specific capacitance can be calculated and using these values in **equation 14**, capacitance of these electrode separation can be determined. The capacitance values for 10, 30 & 50μm electrode separations are calculated to be 9.6nF, 2.8nF & 2.7nF,

respectively. These values also conclude the same change, where 10μm has the highest capacitance in comparison between 30μm and 50μm.

In **Figure 65**, At the range of 400mV to 500mV, the curve is experiencing a stretch towards the top. This is due to the polarization of the electrode, where polymer starts to deposit on the surface of electrode[317]. Polarization of the CV curve at 500mV signifies the removal of the electrode protentional from its thermodynamic equilibrium value during the electrochemical experiment[318]. This phenomenon could be due to various reasons,

- **Activation polarization**: If the potential of 500 mV corresponds to a region where electrochemical reactions are activation-controlled, activation polarization may be prominent. This leads to deviations from ideal behaviour.
- **Concentration polarization:** Changes in the concentration of electroactive species near the electrode surface at 500 mV can contribute to concentration polarization. This can impact the observed currents and influence the overall CV response.
- **Mass transport limitation:** Diffusion-controlled processes may contribute to polarization effects at 500 mV, where the rate of electrochemical reactions is influenced by the transport of species to and from the electrode surface.
- **Double layer charging:** Diffusion-controlled processes may contribute to polarization effects at 500 mV, where the rate of electrochemical reactions is influenced by the transport of species to and from the electrode surface.

Along with CV measurements, impedance spectra were also recorded. EIS measurements, combined with the capacitance model fit, enhances our understanding of the gold electrodes' electrical properties of the electrochemical system under varying gap distances. These insights are invaluable for optimizing electrode designs, evaluating the impact of gap distances on charge storage, sensitivity, and response time.

In the EIS procedure, the impedance of the electrodes was systematically measured across a range of frequencies. This approach facilitated an exploration of the electrical properties of the system. By observing the resistance and capacitance components, EIS offered a comprehensive understanding of the overall electrical behaviour exhibited by the samples. Refer to **section 2.4** for more details.

EIS technique was conducted on gold electrode spaced at 10, 30, & 50μm. A frequency sweep from 0.1 to 10KHz was performed at AC voltage of 10mV rms in phosphate solution as electrolyte. The experimental instrument used was the Gamry Reference 620. Gamry Echem Analyst software was used to do a capacitance (C) model-fit on the resulted output data.

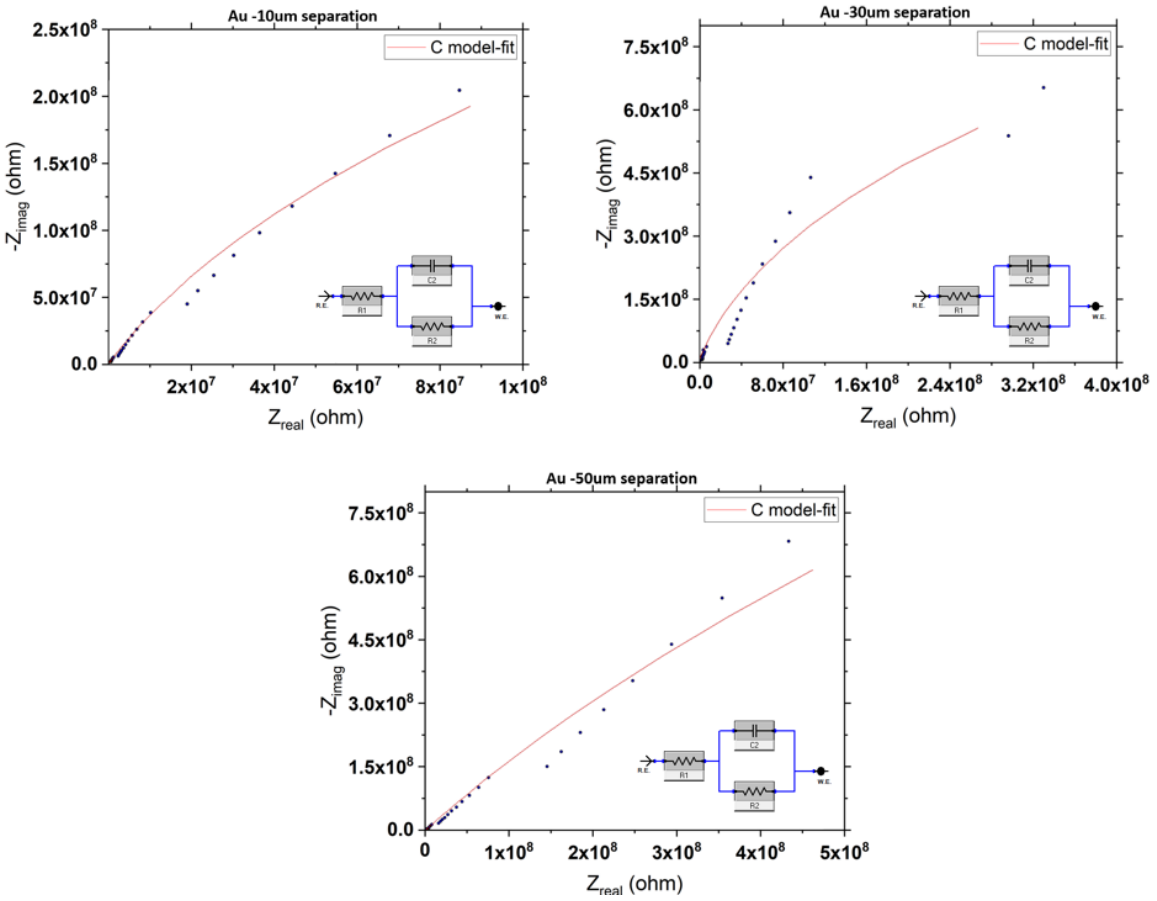

Figure 66: These are the results of an EIS (dotted), and model fit (red line) done on Au electrodes at 10, 30, & 50um electrodes spacing. The Randels equivalent circuit can be seen under the curve.

Figure 66 shows the output of the EIS measurements for gold electrodes, represented by the black dots. Whereas the red line is the fitted capacitance model fit from Echem Analyst software. The model is R in series with RC in parallel, as can be seen in **Figure 66** under the curve. This model is a Randel equivalent circuit model for coplanar electrode configuration with EDL effect[319]. The presence EDL effect was evident from analysis of CV curve from **Figure 65**.

This fitted capacitance model allows for the quantification of capacitance values derived from the impedance curve. In this specific analysis, the calculated capacitance at values for electrode gaps of 10, 30, and 50μm at 10kHz are calculated as 2.2 nF, 0.8 nF, and 1.47 nF, respectively. As stated by Andelman et al[320], the trend of decreasing capacitance with an increase in the electrode separation is a well-established principle. However, the capacitance value for the 30 µm electrodes is very low and does not follow the expected trend. This could be due to damage to the electrodes.

The capacitance values obtained from the analysis are indicative of the capacitive behaviour observed at the Au electrode-electrolyte interface. Lower capacitance values suggest a reduced capacity for faster response times, and higher sensitivity to small changes[321]. From **equation 20**, it is revealed that the impedance exhibits an inverse relationship with capacitance. That implies that opting for lower capacitance values, specifically for electrode separation of 30μm and 50μm in MIC devices, could enhance sensitivity. The reduced capacitance not only facilitates faster response times but also enhances the device's ability to detect subtle changes more effectively. **Section 5.2.2** contains all the results based on particles detection.

The difference in capacitance values between CV and EIS can be attributed to the fact that CV typically assumes a single capacitive element, while EIS analysis involves fitting the data to an Randles equivalent circuit, which is more nuanced and can account for non-ideal behaviours of the electrochemical systems[322]. Additionally, the variance may also stem from differences in the applied amplitude during the experiments. While CV operated with a 500mV AC amplitude, EIS measurements utilized a 10mV rms amplitude. Even when considering an equivalent value for the CV amplitude (353.55mV), it remains significantly higher than the 10mV rms employed in EIS, potentially contributing to the observed differences in capacitance values.

Conclusion

The comprehensive investigation of gold electrodes through Cyclic Voltammetry (CV) and Electrochemical Impedance Spectroscopy (EIS) within this study has provided invaluable insights into their electrochemical behaviour, stability, and capacitance under varying gap distances. The choice of a 9.8% Concentration of Phosphate solution as the electrolyte medium, mirroring biological ionic concentrations, ensured a relevant and standardized environment for the experiments.

CV analysis revealed nuanced redox behaviour, with visible redox and oxide peaks for the 10µm electrode separation, overshadowed by the electric double layer (EDL) effect for the 30µm and 50µm separations. The area under the curve indicated a distinctive electrochemical behaviour for the 10µm separation compared to the larger separations, suggesting a notable impact on charge transfer kinetics and mass transport. Calculated capacitance values further supported this trend, with 10µm exhibiting the highest capacitance, emphasizing its distinct electrochemical characteristics.

The EIS measurements complemented the CV findings, offering a detailed exploration of the electrical properties of the gold electrodes. The fitted capacitance model from Echem Analyst software aligned with the observed EDL effect, providing a quantitative understanding of capacitance values. The decrease in capacitance with increasing electrode separation, as per the Randles equivalent circuit model, adhered to established principles. Notably, the capacitance value for the 30µm separation deviated, potentially indicating damage to the electrodes.

5.2.2. Measurement setup for MIC

Impedance measurement in the MIC devices while under fluid flow are made using a custom setup that combined a precision syringe pump, a high precision lock-in amplifier with additional signal conditioning with pre and post amplification.

The microfluidic channel is held in place using a 2-axis manual micrometre positioning system which combined with a Dino-Lite AM7115 camera was placed under the sample with optical magnification of 220x. With Dino 2.0 Software, this camera would show real-time recording of the channel. The camera has 5MP sensor and operates at a frame rate of 60 fps.

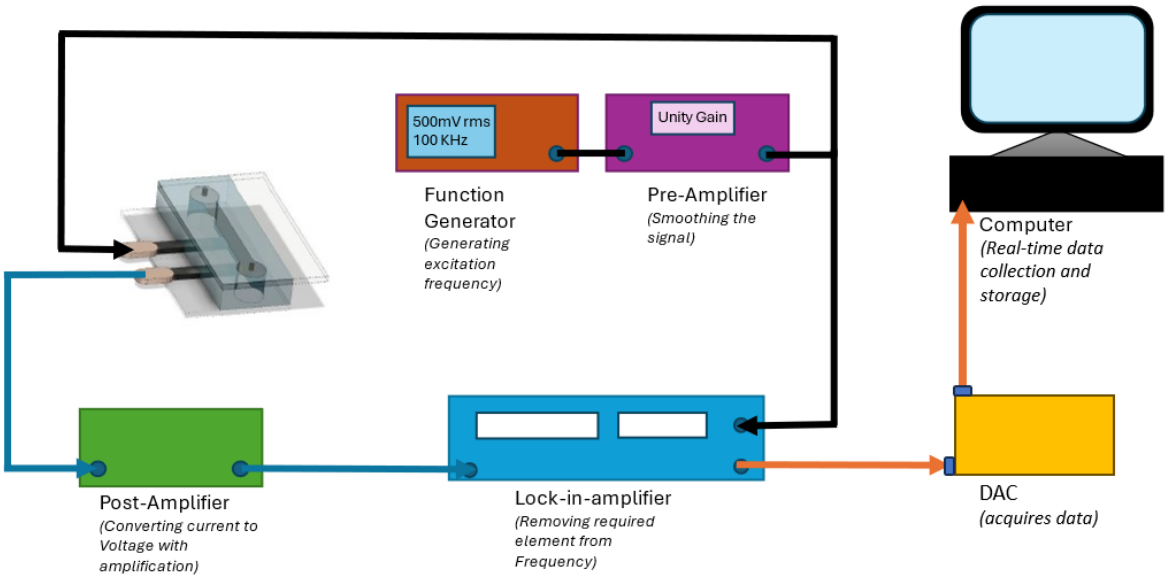

Figure 67: A schematic of complex electrical system employed to record, see real-time changes, and save data files from MIC device.

Figure 67 presents the electrical setup used for MIC devices for particle detection. The LIA, Stanford SR 830 lock-in-amplifier, can use an internal or external reference frequency which is then removed from its input signal received to gain the ability to detect the smallest of variations. More details on how the LIA works can be seen in **section 2.6**. However, to minimise the noise in the signal generated interally, an external function generator was used.

TTi TG4001 Function Generator was used to generate a signal at a frequency of 100 KHz with an amplitude of 200 mV. This signal is then fed into the SRS SR560 Low Noise Preamplifier, configured for unity gain and equipped with a bandpass filter to eliminate background noise. The signal is split, with one branch serving as the external reference frequency for the Lock-in Amplifier, and the other connected to one of the pads of the MIC device.

The second pad of the MIC device is connected to the SRS SR570 Low-Noise preamplifier, referred to as the post-amplifier in the figure above. This post-amplifier will add amplification to the signal and convert the input current to an output voltage. The output from the postamplifier is then fed to the input port of the LIA, where it undergoes frequency element removal based on the reference frequency. The results are collected by the DAC and transmitted to the computer. Real-time observation of the results is possible, with continuous background saving.

The significance of the transition from current to voltage output is particularly meaningful in this context. Voltage, being directly proportional to impedance changes, is expected to exhibit greater variations according to the impedance formula. This modification allows for a more sensitive and distinguishing measurement of the impedance characteristics within the MIC device. A new complex electrical setup was build to enhance the signal strength and reduce unwanted background signal, as illustrated in the schematic in **Figure 63**.

The voltage variation (ΔV) can also be compared to distinguish the particle sizes. For the small particle (P_S) particles the ΔV is in the range of 5mV-18mV, whereas for large particle (P_L) particle the ΔV is between 11mV-85mV. From the ΔV for P_S & P_L, there is a region of overlapping values. This can easily be analysed using the analysis code. The code considers additional parameter, the duration of interaction with the electrodes. The time-based voltage change in the LIA output results plays a pivotal role in this process. With each interaction between the sensing region and a particle, a peak is formed in the voltage signal. The ΔV, which defines the magnitude of the voltage change, is determined by the height of the peak in the signal. Importantly, the width of this peak corresponds to the duration of the particle's interaction with the sensing region.

The analysis Python code imports the file saved by the LIA, then identifies peaks in the voltage signal based on the specified prominences, filters common peaks between two sets, and plots the original signal with identified peaks. Prominence in signal processing serves as a crucial metric for identifying and characterising peaks within a signal. It determines the minimum vertical distance a peak must have above its surrounding baseline to be considered significant. The prominence of a peak is calculated by measuring its height relative to a horizontal line drawn between the two nearest troughs or valleys on either side. Peaks with prominence values below the specified thresholds are filtered out, ensuring that only peaks with a substantial impact on the signal are retained for further analysis. This helps detect the P_S and P_L particles. A function is employed to make a dataset for common peaks region between both and that is filtered using the time element (x-axis) from the original dataset, helping identifiy the peak.

5.2.3. Python code

This section will explain the python code, which is provided in the **Appendix**.

The function is designed to analyse voltage signal data by identifying peaks of different prominence levels and categorizing them into small peaks (peaksS), large peaks (peaksL), and peaks within a common area (common_area_peaks). The data is first imported from a specified file, and the voltage values are inverted to ensure peak detection works correctly. The find_peaks function from the SciPy library is used to identify peaksS based on a lower prominence threshold (pS) and peaksL using a higher threshold (pL). Additionally, peaks with prominence values between half of pL and pL are classified as common_area_peaks, excluding those already in peaksL. These peaks are then analyzed for their full width at half maximum (FWHM) using the peak_widths function to determine their widths and corresponding voltage changes. The results are visualized using Matplotlib, where peaksS, peaksL, and common_area_peaks are plotted in different colours for clarity. Finally, the peak characteristics, including width and voltage change, are saved to a CSV file for further analysis.

This approach ensures a comprehensive peak analysis, accounting for a transition zone between small and large peaks and refining the categorization based on peak width measurements. A flowchart of the function is given below.

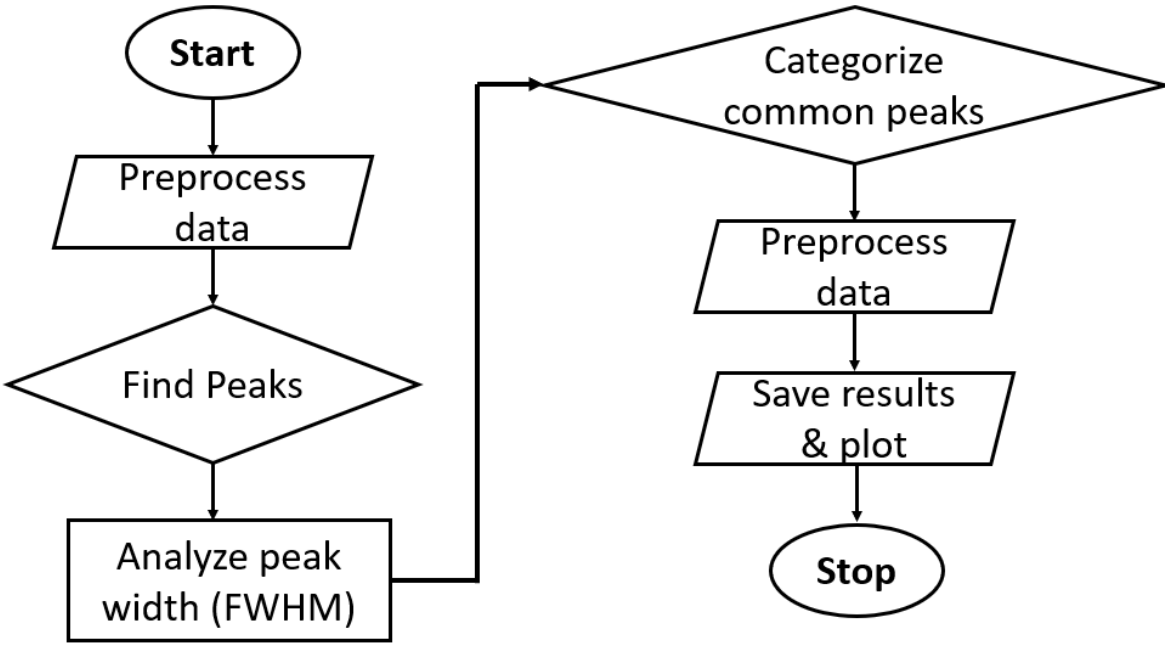

5.2.4. MIC device

For the intial meaurement only the lock-in-amplifer was used with 3V Voltage and 100KHz frequency. The lock in amplifier was initially set to the excitation frequency and was then allowed to automatically optimize phase and integration time to provide highest signal on the R channel. The DC R signal was then further cleaned by a unity gain amplifier with an additional low pass filter, before being converted by an 8 bit ADC which was collected by DAC and presented real-time readings.

During operation the DI water was passed through the device using a home built high precision syringe pump that used a screwdriver PI linear driver with a 2nm step size to minimize start-stop motion of the fluid flow.

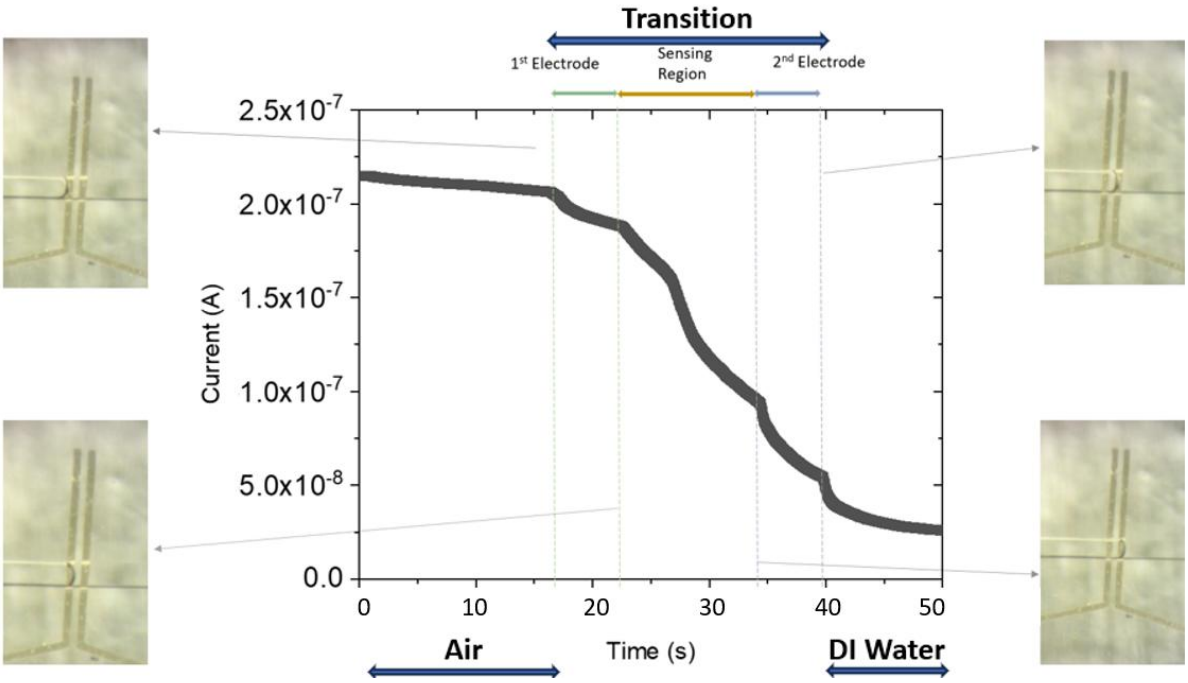

Figure 68: Change of current is seen as water passes through 1st and 2nd gold electrodes in relation to optical view.

The initial experiment explored the process of wetting the microfluidic channel and a characteristic result for gold electrodes are shown in **Figure 68** which shows the evolution of device current as the fluid sensing region (between the electrodes) is wetted by phosphate buffer. During this experiment no amplification or current to voltage conversion was carried out and so the sensing signal is given in terms of current which is proportional to impedance.

Using the video feed, it is possible to associate signal variation with the various stages of wetting. Initially a constant lock in signal is observed during which the channel is dry, As the fluid meniscus pushes past the first electrode a drop in current can be observed. This can be explained by a change in capacitance for the electrodes where lower current implies higher capacitance. Then the meniscus moves through the sensing regions where the current drops more rapidly (due to the electrolyte interacting with the high field concentration in the sensing region). Then, as the meniscus passes the second electrode the rate of change reduces and finally becomes static once the entire sensing region has been fully wetted. Other

more fine-grained changes in rate can be seen due to figure structure of the electric field and the curved shape of the meniscus.

Observing these sections along with the respective optical images allows us to collorate the small changes occuring at each individual electrode. The slight rise at the each end of the subsection indicates the stablility of the electrode until a subsequent change is observed as DI water flows through the region. This behavoiur indicates that the transition from the air to DI water is not uniform across the sensing region, highlighting variations in dielectric properties at different points. The detailed analysis of **Figure 68** reveals the system's responsiveness to changes in the dielectric medium, offering valuable insights into the dynamic behavior of the MIC device under different environmental conditions.

Once the effect of wetting the channel had been confirmed a steady state measurement was made to show that the devices were consistent over time. The results are shown in **Figure 69**. For these measurements the electrical measurement setup includes pre and post amplification and IV conversion as initially described. The results here show largely consistent baseline across 2000 seconds for the 30um gold electrodes. Different signal levels for various electrolytes are shown. DI and air shows a similar signal due to only dielectric contribution to the capacitance whereas the two phosphate buffer connections are significantly increased due to the pressence of free ions in phosphate solution which are able to form an electric double layer at the electrodes. The phosphate solution with a higher concentration of free ions, as indicated by the 9.8% phosphate solution, exhibits a higher baseline signal. This is primarily due to the increased availability of free ions, enabling more easy travel of electrons.

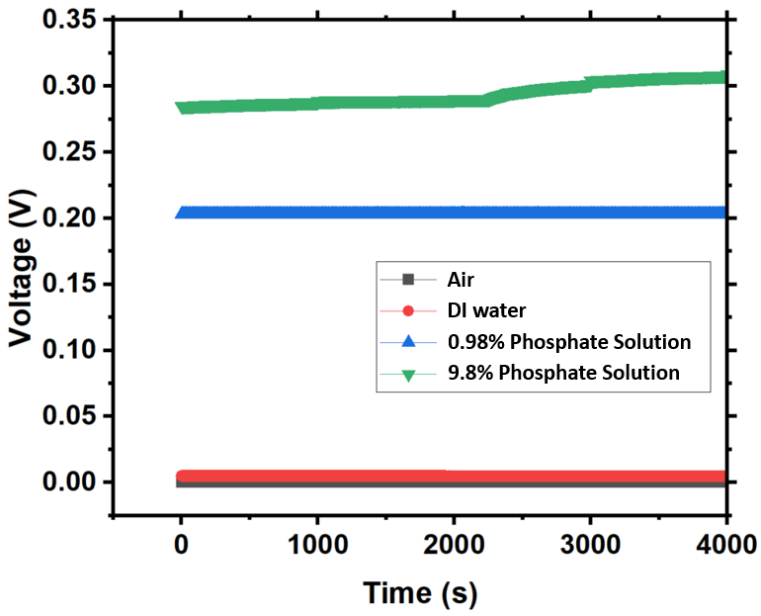

Figure 69:illustrates the medium comparison of the 4 different mediums between Au 30µm electrode separation.

In the case of 9.8% Phostpohate solution, a drift in the baseline signal is seen. this drift is attributed to the dynamic setting of the microfluidic channel, leading to the polarization of the medium. As explained by Feng et al[323], polarization refers to the separation of charges within a material. In the case of the microfluidic channel and the phosphate solution, the continuous flow and interaction of the solution with the channel surfaces can lead to the

polarization of the medium. This observation not only shows the sensitivity of the system but also emphasizes its responsiveness to the dynamic characteristics of the medium. Considering all resulting outputs, 9.8% phosphate solution is the most optimal solution and will be used as medium for further experiments.

Examining the baseline data from **Figures 68 & 69**, a noticeable presence of undesired variation is evident. This unwanted signal noise can be characterized by the signal-to-noise ratio (SNR).

From **Section 2.7**, using the SNR equation, the SNR is calculated to be 6dB. An SNR value of 6dB is relativtly low, a lower SNR implies that the signal is closer in magnitude to the noise, making it more challenging to distinguish the signal from the noise. In experimental settings, a low SNR could mean that the measurement system is susceptible to interference or that the signal of interest is relatively weak compared to the noise present in the system.

In MIC devices where the variation for particle of 10μm & 20μm size are inherently small, a higher SNR is preferable. A higher SNR provides a clearer distiction betwean the signal and the noise, making it feasible to extract meagingful information. Given that the device aims to detect subtle variations in particle sizes, an enhanced SNR becomes crucial for accurate and reliable measurements. Therefore, efforts to improve the SNR in the MIC devices are warranted to ensure the sensitivity required for precise particle detection and characterization.

There are multiple reasons that could contribute to this effect on the required signal, which are presented in **section 2.7**. Implementing solutions to all mentioned problems from that section, no desired yeild was obtaioned. However, some techniques proved effective in reducing the noise. Strategies included replacing the syringe pump with a nano stepper motor to minimize flow variations, optimizing flow rate and syringe diameter to reduce oscillations, and upgrading the data acquisition system to PicoLog 1216 hardware and software for improved resolution and noise reduction.

Despite these optimizations, residual parasitic noise persisted, indicating limitations in the data acquisition system. Nevertheless, the measured signal deviation was significantly reduced from 50mV to 10mV, leading to a noteworthy improvement in Signal-to-Noise Ratio (SNR) from 6dB to 54.16dB.

The sensitivity of selected electrode materials, along with their corresponding electrode gap, has been a focal point for all the measurements. Both CV and EIS results also state the impact of electrode gap on systems sensitivity. To quantify this value, variations in signal strength were measured under different fluid flow settings, and sensitivity was calculated. The sensitivity of each electrode can be calculated using the gradient of the curves obtained from the measurements. The formula for determining sensitivity is as follows[324]:

$$Senstivity = \frac{Change\ in\ Signal\ Strength}{Change\ in\ Fluid\ Flow} \tag{31}$$

Here, the observed variations in the measured signal for different electrode separations reflect changes in signal strength. Simultaneously, adjustments in fluid flow contribute to alterations in signal strength. By examining the slopes of the curves, we gain a numerical measure of the sensitivity of each electrode material. This analysis helps us understand the influence of changes in electrode separation on the overall sensitivity of the system.

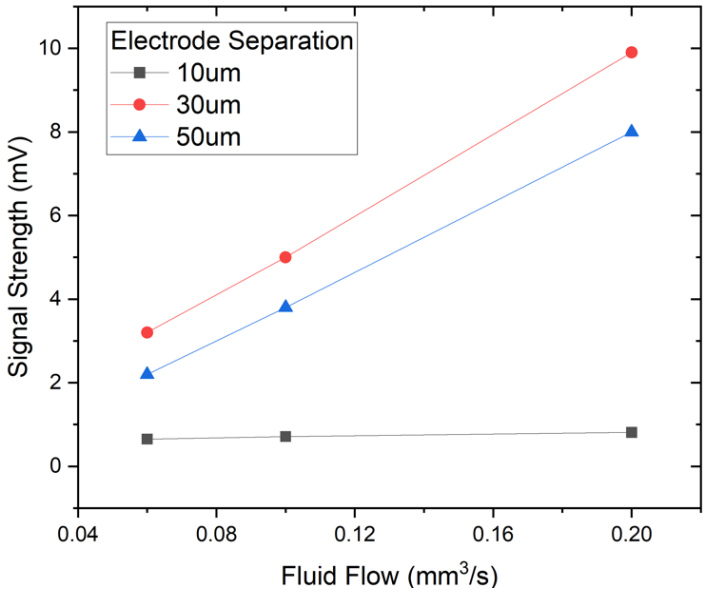

Figure 70: The graph shows the change in signal strength when fluid flow rate is changed. This is be used to calculate the sensitivity of each individual electrode separations labelled on each line.

Upon observing the sensitivity from **Figure 70**, it is evident that the electrode separation 30μm exhibits the highest sensitivity, while 10μm shows the least sensitivity. The variation in Au electrodes separation is showing a notable impact on sensitivity.

5.2.5. Particle analysis

The main goal of the MIC is for particle counting and sizing in this section we carry out tests to examine the capability for MIC devices with gold electrode to measure dielectric particles passing through the sensing region of the microfluidic device. The particles are polystyrene beads with size 10μm and 20μm mixed with the buffer solution.

For initial measurements we used two solutions of a single diameter of particles, with the concentration of 0.0001% in phosphate solution and passed them through as a flow rate of 0.5$\mu l/s$. These distinct mixtures allowed for controlled experimentation, ensuring the detection of approximately one particle per second. This provided a base for observing and analysing the behaviour of particles in the microfluidic channel, complemented by visual aid and peak identification in the dataset. The experimental setup involved utilizing the previously mentioned electrical system, incorporating Picolog data acquisition, and employing Python code for subsequent analysis. The results are extracted from the computer in form of data files. These files are then processed using Python code designed to automatically identify and categorize peak heights and particle speed, associating them to their corresponding particle sizes. The code is programmed to generate results presented

graphically, depicting the relationship between velocity and voltage. The results for the signal acquisition can be seen in **Figure 71**.

The microfluidic (MIC) device employed featured gold (Au) electrodes with a separation of 30µm, and the channel dimensions were 100µm in width and 50µm in height.

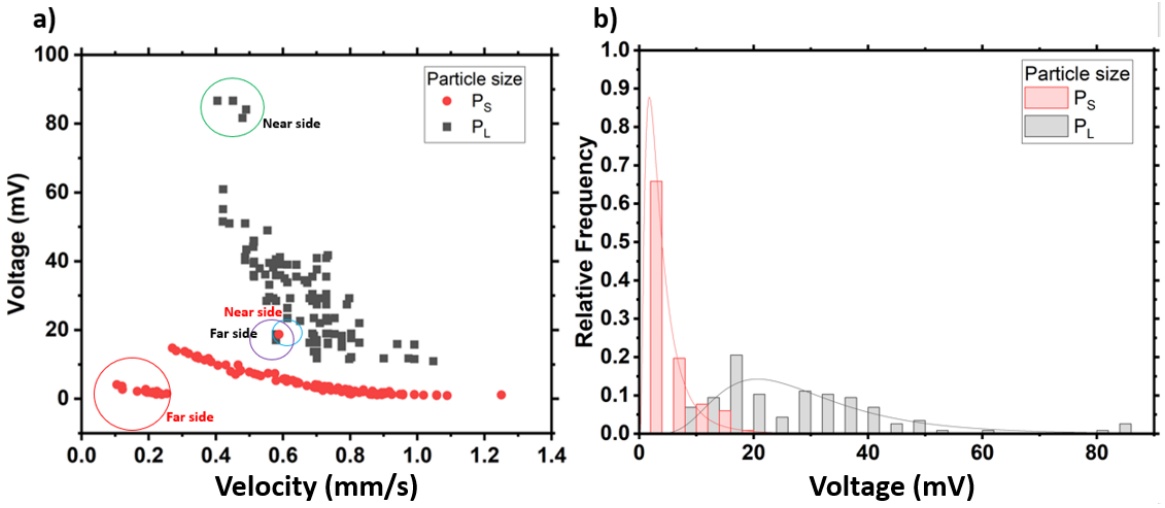

*Figure 71: Particle detection result for two low concentration solutions using 30µm Au electrodes, **a)** scatter plots showing the particle detection events for P_S and P_L particle, and **b)** displays the distribution peak for particle detection.*

Figure 71a) shows a plot of the particle counting data obtained for 2 minutes of acquisition of a 30um electrode device. For each particle signal analysis has extracted velocity (mm/s) and signal magnitude (mV). These are shown as the axis velocity and voltage respectively. Additional, peak distribution in **Figure 71b)** shows frequency data for particle voltage. In the **Figure 71a)**, a trend can be seen in the unmarked points which relate to particles at the highest velocity in the centre of the channel and lowest velocity at the edge of the channel. The tail of this plot shows low velocity particles with high signal and a disconnected cluster of datapoints showing low velocity and low signal. Interestingly, the majority of the particle distribution appears to concentrate in the middle of the fluid system. This can be understood by **Figure 72**, which aids the understanding of the particle voltage to location in the channel.

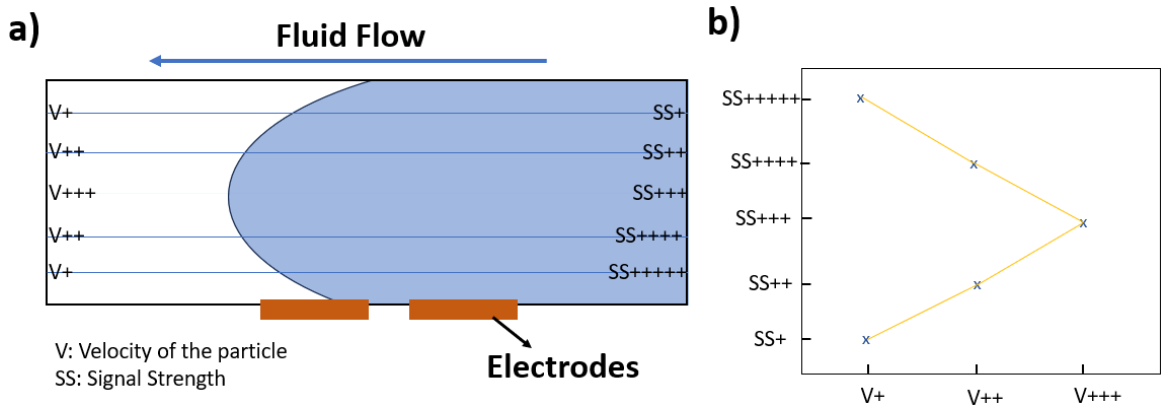

*Figure 72:**a)** is the schematic of the microfluidic channel where fluid is being injected in the presence of coplanar electrodes at base + is used to show the strength, **b)** it is a graphical representation of the expected particle locations depending on SS and V.*

Before progressing further to particle detection, it is crucial to gasp mechanisms that will help understand how particle velocity and signal strength relates to the particle's location within the specified channel. Particle velocity denotes the speed of particle movement within the channel. Meanwhile, signal strength, representing the intensity of a detection signal, fluctuates based on the proximity of particles to the detection point.

In **Figure 72a)**, the microfluidic channel is segmented into five sections, each illustrating the relationship between Signal Strength (SS) and velocity (V) concerning the particle's location, particularly when coplanar electrodes are positioned at the base This analysis is particularly relevant when coplanar electrodes are situated at the channel's base. Notably, particles positioned at the farthest end from the electrodes exhibit the lowest Signal Strength (SS), indicated by the addition of the (+) sign in the figure. Conversely, particles near the electrodes demonstrate the highest SS. In fluid flow, the centre of the fluid experiences the highest velocity, while the velocity gradually decreases towards the boundary.

This comprehension enhances our insight into how Signal Strength and particle velocity correlate with specific locations within the microfluidic channel, especially in the context of coplanar electrodes positioned at the channel's base, illustrated in **Figure 72b)**. When a particle is situated on the opposite side to the electrode, both its velocity and SS are observed to be lower. Conversely, when the particle is near the electrode, its velocity is low, but SS is at their highest levels. **Figure 72b)** gives an approximation of the location based on these understandings.

From **Figure 71a)**, where 20μm (P_L) particle are being detected, similar trend is observed. One noticeable distinct observation is that the major cluster formed by these particles do not exhibit an extensive stretch, like the P_s particles. This phenomenon suggests that larger size of the P_L particle is sufficient to cover a substantial portion of the 50μm height of the channel. In the context of laminar flow, it becomes apparent that most of these larger particles tend to stay concentrated in the middle of the channel. This correspondence between experimental results and the theoretical model suggests a consistent relationship between particle detection, location, and the dynamics within the microfluidic channel.

The voltage variation (ΔV) can also be compared to distinguish the particle sizes. For the P_s particles the ΔV is in the range of 5mV-18mV, whereas for P_L particle the ΔV is between 11mV-85mV. From the ΔV for P_s & P_L, there is a region of overlapping values. This can easily be analysed using the analysis code.

In essence, the duration of interaction has very vital role in allowing the code to discriminate between particles of different sizes based not only on their impact on voltage magnitude but also on the duration of their presence in the sensing region. This refined approach contributes to a more accurate and nuanced differentiation of particle sizes, especially within the overlapping range of ΔV values for P_s & P_L particles.

With an understanding of the coplanar electrode configuration and its limitations **section 5.1**, specific dimensions have been carefully chosen for further experiments. The selected parameters include electrode gap dimensions 30μm & 50μm, channel heights of 50 μm, 100 μm & 150 μm with fixed channel width of 100 μm.

With 0.1% concertation of P_s particle in phosphate solution as medium with the flow rate of $0.5\mu l/s$, the following experiment involved the impact of channel height on electrode separation of $30\mu m$ & $50\mu m$. A 3ml solution was pumped through the MIC device with 1600 particles/ml. The $10\mu m$ electrode separation was excluded from consideration due to its inadequate performance in terms of sensitivity. The detection was performed at 200mV rms drive voltage with 100KHz frequency. All the experiments are under laminar flow due to low Reynolds number, calculated from **equation 4**, 0.083.

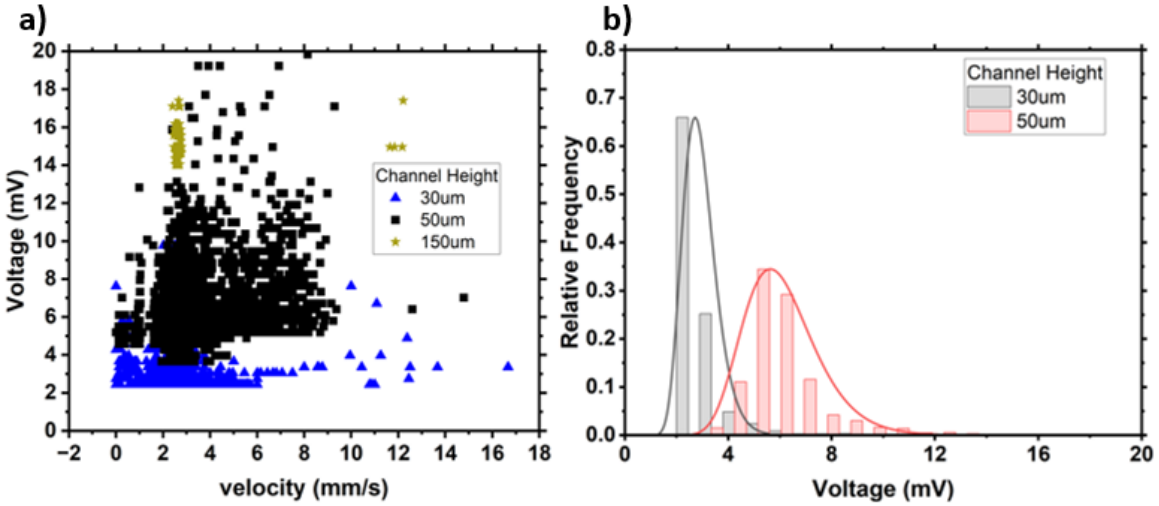

*Figure 73:**a)** illustrates the detection of 10µm particles with Au 30µm electrode separation. It presents a comparison of the detection limit and sensitivity across various channel heights. **b)** displays the distribution peak for particle detection.*

In **Figure 73**, the MIC device in the experiment features an Au electrode separation of $30\mu m$. A comparative scatter plot is employed to analyse the particle behaviour with variation in channel height. As the channel height increases, a greater volume of liquid flows through the sensing region, consequently impacting the ΔV. This is clearly observed from the **Figure 70a)**, where the $150\mu m$ channel height exhibits the highest ΔV. However, despite this, it demonstrates poor efficiency and sensitivity. This is due to the dilution effect, reducing the concentration of particles per unit volume. Consequently, the probability of particle-electrode interaction interactions diminishes, affecting the overall sensitivity of the detection mechanism. Additionally, in larger channels, the electrical field distribution across the width of the channel becomes more diffuse, this diffusion reduces the intensity of the electric field experience by the particles, impacting the efficiency of detection. The $150\mu m$ channel was only able to detect 18.8% of the particles. This observation aligns with the concept explained earlier in **Figure 72a)**, where signal strength weakens as particles move further away from the electrodes. The detection events in this case are probably associated with particles that were in proximity to the electrodes. Conversely, particles within the middle of the fluid flow and those on the far side are beyond the effective detection range.

A $30\mu m$ channel height tends to exhibit a lower number of detection events, only 47.2%, compared to the $50\mu m$, 85% particle detection. The restricted space leads to increased particle congestion and hindered particle-electrode interaction. Additionally, the narrow channel results in a more concentrated electric field, potentially enhancing the sensitivity but also increase in particle trapping and clogging. For $50\mu m$ however, is suggests a balance

between particle concentration and channel height. the higher channel facilitates better fluid flow and particle distribution while maintaining sufficient electrode field strength for effective detection.

Overall, the choice of channel height significantly impacts the performance of the MIC device. While narrower channels may offer higher sensitivity but suffer from particle congestion, wider channels provide better fluid dynamics but may dilute particle concentration. Balancing these factors is crucial to optimizing the detection efficiency and sensitivity of the system.

Analysing **Figure 73b)**, it is seen that the distribution of particles for 50μm channel height is more uniformly distributed, highlighting the sensitivity to the location of the particle. On the other hand, the 30μm height channel is concentrated to specific region with larger peak. As the primary focus of the particle distribution analysis was on regions with optimal sensitivity, the 150μm channel height has been excluded to avoid complicating the interpretation of the data.

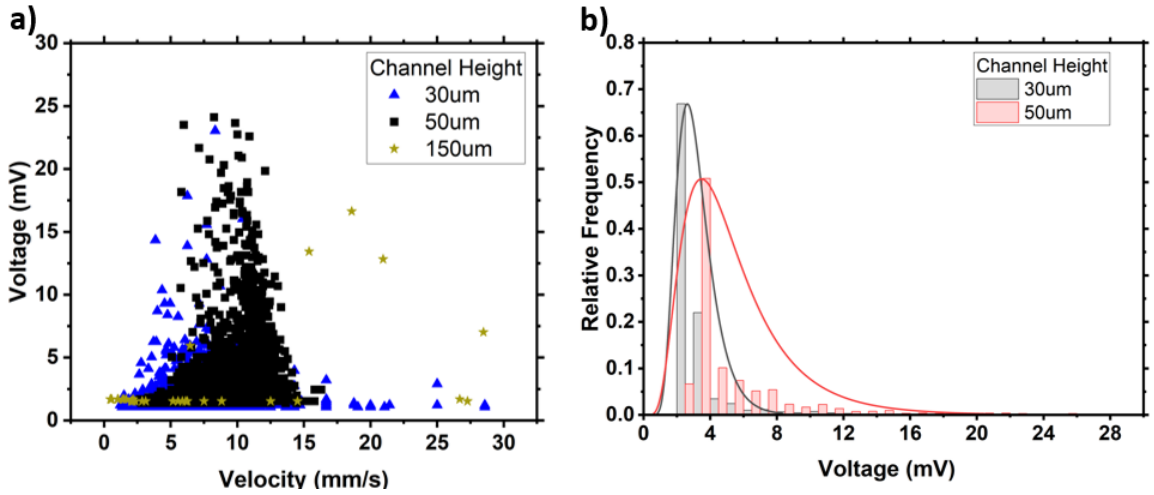

*Figure 74: **a)** This plot shows the detection of 10µm particles with Au 50µm electrode separation. It provides a comparative analysis of the detection limit and sensitivity across different channel heights. In **b)**, the figure showcases the distribution peak for particle detection, offering a frequency distribution of the detected particles.*

Figure 74 presents the results of the experiment conducted with the MIC device, featuring 50μm electrode separation for Au. The general trend is the same as of 30μm electrode gap, albeit with slight changes. One notable change is the increased scattering of data points, especially evident in the higher values of ΔV. The larger electrode separation of 50μm have larger electric field distribution compared to the 30μm electrode gap. The altered interaction between the fluid and the electrodes at this increased gap size could contribute to the observed changes in the output. The detection events of particles for 30, 50 & 150μm channel heights are 34.4%, 70.5%, & 18.2%.

Additionally, contrary to expectation, a higher channel height allows more medium to flow, potentially resulting an increase in ΔV. However, this change in not obvious from the **Figure 74a)**. This means 50μm electrode spacing demonstrates less sensitivity in contrast to 30μm electrode spacing. This reaffirms the previous observation from **Figure 70**, where the 30μm electrode spacing exhibited higher sensitivity.

To further verify this contrast, a comparison of particle distributions was conducted using the previous data for the two electrode separations at specific heights, as illustrated in **Figure 75**.

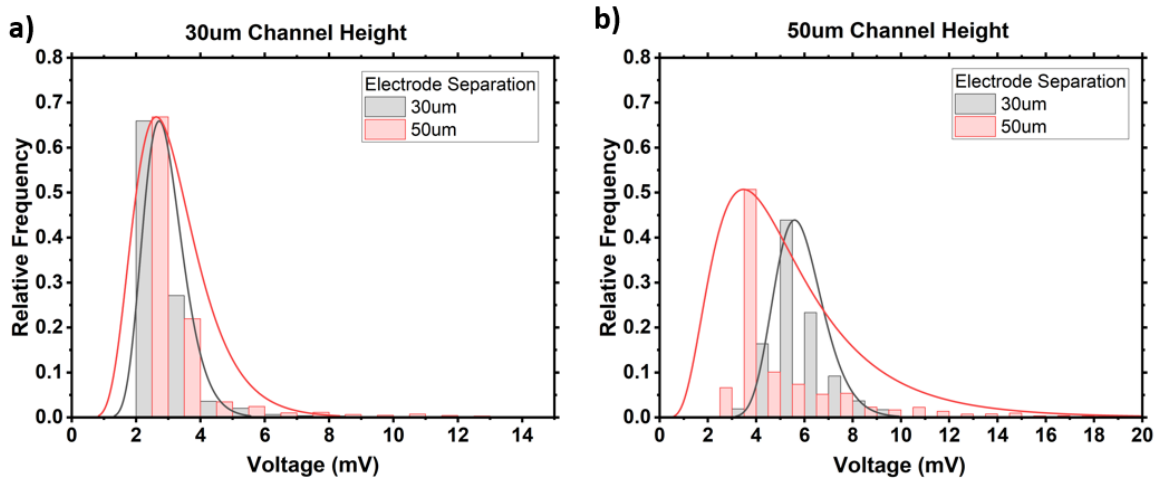

*Figure 75: In **a)**, the frequency distribution graph depicts the detection of 10µm particles at a 30µm channel height. This graph facilitates a comparative distribution analysis between the 30µm and 50µm electrode separations. In **b)**, the figure highlights the distribution peak for particle detection at a 50µm channel height, presenting another comparison of frequency distribution.*

For 30μm channel height, **Figure 75a)** does not reveal significant differences between the two electrode separations. However, upon closer examination of **Figure 75b)**, it becomes apparent that the 30μm separation results in a more even distribution of particles. While both separations exhibit sensitivity, the data suggests that the 30µm separation performs slightly better than the of 50µm separation in achieving better sensitivity in detection.

Mixture of 10μm & 20μm particle analysis

In this experiment, the goal is to demonstrate an effective distinction between different particles sizes in a mixed solution. A solution of 0.1% particle concertation of P_S & P_L (0.05% for each size) particles was made in phosphate solution. Using the nano-stepper, 3ml solution was pumped through the system at 0.5$\mu L/s$ flow rate, 1600 particle/ml. Using electrode separation of 30μm and channel of height of 50μm for further experiments. The detection was performed at 200mV rms drive voltage with 100KHz frequency.

Figure 76 is an example of particle detection through Python for one dataset. In the visual representation, blue crosses are the peaks marked for P_S where the red circles mark P_L. The definition of these peaks is determined by the prominence, and to enable the differentiation of peaks sizes in the overlapping ΔV region, FWHM is used on those peaks. Wider peaks are written to belong to larger particle whereas the narrower peaks are set to be identified as smaller particles. In the graph the red dote presents the P_L and blue cross presents the P_S.

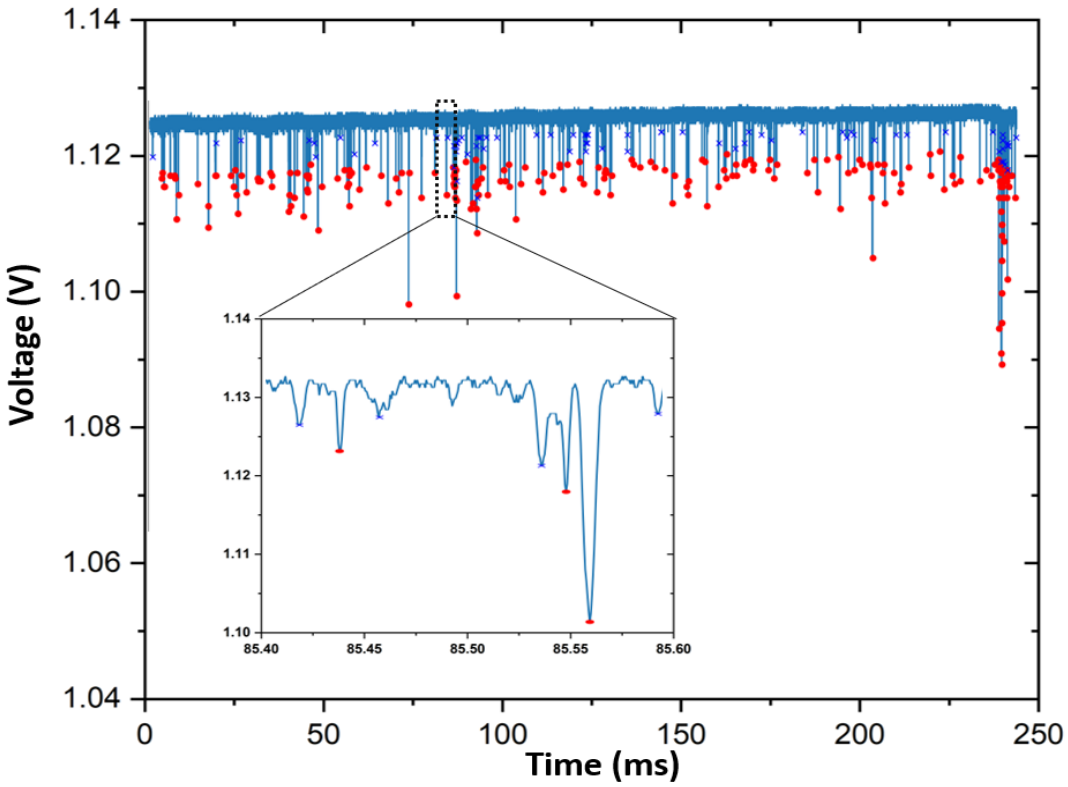

Figure 76: This is Python spit out for one dataset of the mix particle experimentation.

In **Figure 76a)**, a comprehensive scatter plot can be seen, encompassing scatter data files for mixture of P_S & P_L particles. Using FWHM and ΔV, frequency distribution graph is obtained which is able to distinction between P_S & P_L, illustrated in **Figure 72b)**.

In **Figure 77a)**, sensing signal scatter plot is shown, featuring detection events from a 100-minute duration measurement flow of a mixture of P_S & P_L particles as described above. Using FWHM and ΔV, a frequency distribution graph is obtained which is able to distinction

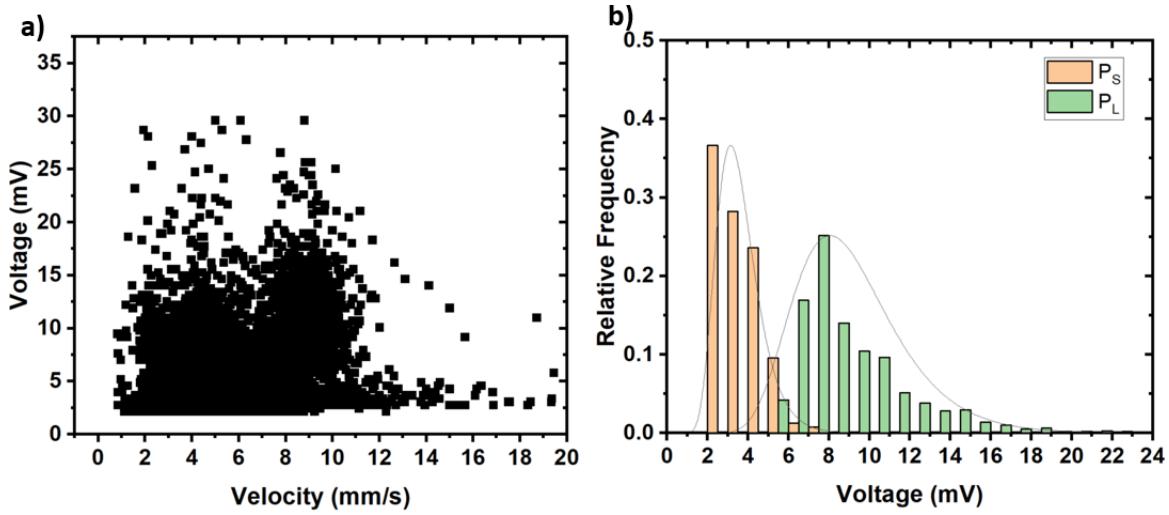

*Figure 77: **a)** This plot shows the scatter plot for the detection of mix particle solution with Au 30μm electrode separation & 50μm ×100μm height and width of the channel. In **b)**, the figure showcases the distribution peaks for particle detection. This provides a frequency distribution of the detected particles, offering insights into the abundance or occurrence of different particle types in the solution.*

between P_s & P_L, as illustrated in **Figure 77b)**. The P_S particles, with 82.9% detection event, exhibits a concentrated peak with some distribution, while the P_L, with 85.1%, demonstrates a more even distribution. This observation suggests that the 30μm electrode gap exhibits reliable sensitivity to the smaller particle sizes, rendering it to precisely locate them in the system. On the other hand, the larger impact of P_L on the impedance of the system allows the electrodes to more accurately capture a substantial amount of information about it.

5.2.6. Conclusion

The experimental investigations conducted on the MIC device with Au coplanar electrode configuration have provided valuable insights into particle detection and behaviour within the microfluidic channel. The MIC device, featuring gold electrodes with a separation of 30μm & 50μm along with channel heights of 50, 100 & 150μm, facilitated controlled experiments with varying channel heights. Observations from the experiments revealed a significant impact of channel height on particle detection efficiency. While narrower channels exhibited higher sensitivity, they also experienced issues like particle congestion. In contrast, higher channels provided better fluid dynamics but risked diluting particle concentration. Achieving a balance between sensitivity and fluid dynamics is crucial for optimizing the performance of the MIC device, ultimately leading to the selection of a 50μm height for the channel. The comparison of electrode separations, 30μm and 50μm, further emphasized the importance of this balance. The 30μm separation showed slightly better sensitivity, as evidenced by a more even distribution of particles and successful particle detection events. The larger electrode separation of 50μm exhibited less sensitivity, confirming the significance of optimizing these dimensions for efficient particle detection. The solution containing a mixture of 10μm and 20μm particles, along with a 30 μm electrode spacing and 50µm channel height, demonstrated the highest sensitivity, leading to the detection of 82.9% and 85.1% of the particle count. The analysis of a mix solution was performed using Python code with FWHM and ΔV parameters allowed for the successful distinction between particle sizes. The duration of particle interaction with the electrodes had a very crucial role in refining this discrimination, contributing to a more refined differentiation of sizes, especially in the overlapping ΔV region.

5.2.7. Comparison with literature

The literature extensively discusses Au as an ideal electrode material due to its high conductivity, chemical stability, and biocompatibility, making it well-suited for MIC applications. Various deposition methods, including sputtering, thermal evaporation, and electroplating, are explored, each offering distinct advantages in terms of adhesion, pattern resolution, and cost. However, limitations such as adhesion issues on polymeric substrates, fabrication complexity, and potential electrochemical degradation are noted. The conclusion aligns with these findings, emphasizing practical challenges encountered during device implementation, such as electrode delamination and variability in impedance measurements due to inconsistencies in gold layer thickness. While the literature suggests surface treatments and adhesion layers like titanium or chromium to improve bonding, the conclusion points out the need for further optimization to ensure long-term electrode stability. Both sources agree that despite Au having superior properties, ongoing improvements in deposition techniques and material integration strategies are essential to enhance the reliability and scalability of gold-based MIC devices. The experimental findings in

the conclusion confirm these theoretical insights but also provide critical refinements. The qualitative value of detection count for particle is not provided in the literature and nor do they confirm 100% detection, but literature do agree alternative materials should be used to enhance the sensitivity of the devices. The conclusion reports 85.1% particle detection as for the most optimised Au electrode MIC device.

5.3. Graphene devices

Following the procedure discussed in **section 5.1.5** above, graphene electrodes were fabricated and integrated with a microfluidic channel. Typically following wetting of these devices no signal was observed. Inspection of the devices following wetting shows that the graphene was not present in the channel. This is in contrast to before the fabrication where optical microscopy and Raman spectroscopy were used to confirm the presence of the electrodes. Explanations for this device failure could be either delamination of the graphene due to fluid flow or small amounts of electrolysis driving the lifting of the graphene from the substrate.

As a first attempt to address this issue was to implement a modified approach. The patterned graphene MIC device was assembled with the protective copper layer covering the graphene electrode. This design aimed to prevent the electrochemical activation and subsequent etching of the graphene layer.

The controlled experiment involved the deliberate etching away of the copper layer from the graphene surface, and the variations in the system impedance were recorded using the external lock in and amplification circuit, mentioned in **section 5.2.2**, with the drive voltage of 100mV. To facilitate this selective etching process a copper etchant was passed through the microfluidic system, specifically ammonium persulfate (APS).

The results in **Figure 78** reveal the impact of the controlled etching process of the copper from the electrodes and subsequent response of the graphene.

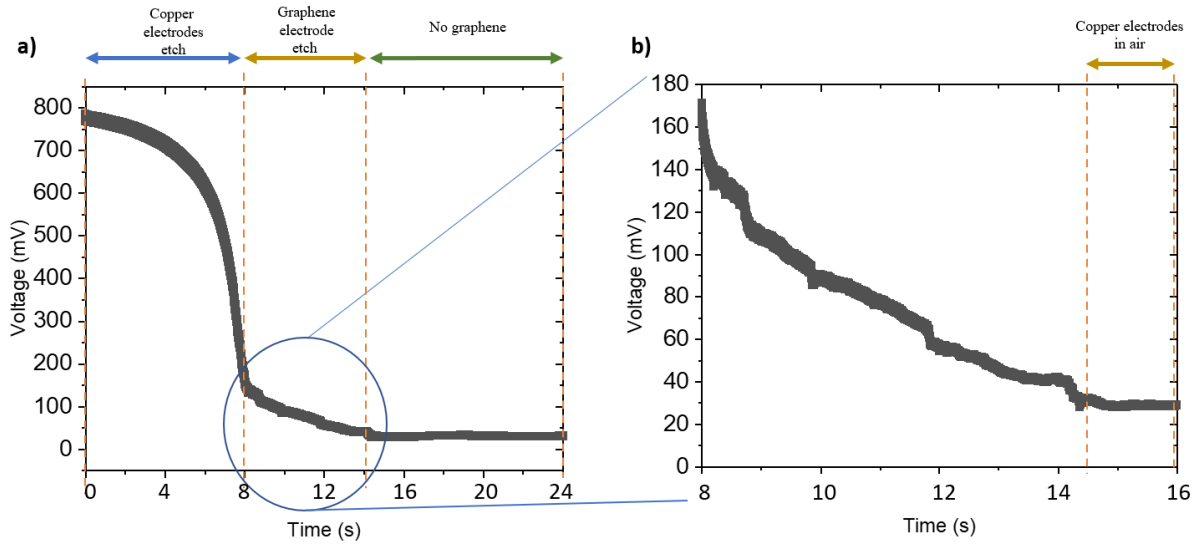

Figure 78: Illustrates the change of potential across the sensing region, depicting the etching of Cu electrode and graphene electrodes.

An initial decrease in signal follows the solution of the copper and the reduction of the conductivity of the electrodes. When the copper is dissolved the signal continues to reduce in a more gradual fashion. A close inspection of this region in **b)** shows that the reduction occurs as a series of step-like features before levelling out with a signal level of 30mV. We interpret this region in three different segments: the first part shows etching of the Cu electrode in the presence of APS, second part depicts the etching of graphene, and the third part showcases the potential for the region outside the channel of the Cu electrodes, where air serves as the medium. Although no graphene is left within the channel, the system still registers some potential across the electrode. This is attributed to the presence of copper electrodes outside the channel, now exposed to air as the medium. Since air possesses a low dielectric constant, the anticipated result is very low potential values.

Given that the removal of the graphene appeared to be unavoidable for an electrolyte fluid flow and that delamination of the graphene was presumable the issue, several adhesion-enhancing strategies were employed.

The experimental methodology comprised two primary surface modification techniques to enhance the adhesion of graphene on a glass substrate: oxygen plasma treatment and surface functionalization with aminopropyltriethoxysilane (APTES). Prior to treatment, the glass substrate underwent a meticulous cleaning process involving Acetone, isopropyl alcohol (IPA), and deionized (DI) water. Subsequently, the substrate was exposed to an Asher plasma cleaner for 5 minutes during the oxygen plasma treatment to induce hydrophilic characteristics and facilitate improved adhesion.

Following the oxygen plasma treatment, a graphene sheet was transferred onto the glass substrate, and the subsequent steps of the graphene patterning process were executed. Contact angle measurements were conducted to assess the success of the plasma treatment, confirming a highly hydrophilic surface with the contact angle of 28°. However, patterned graphene did not maintain adhesion when introduced to the microfluidic system, necessitating further optimization for electrode stability.

The second surface modification technique involved functionalizing the substrate with APTES, a silane coupling agent. The glass substrate was rigorously cleaned with Acetone, IPA, and DI water to eliminate contaminants. Oxygen plasma was then applied to generate hydroxyl groups on the surface, facilitating the attachment of APTES. The APTES solution was applied, leading to the formation of covalent bonds between amino groups on APTES and surface hydroxyl groups, resulting in a stable APTES-functionalized surface. Graphene was subsequently transferred onto the APTES-functionalized substrate, with subsequent steps completing the graphene patterning process.

Despite successful APTES functionalization, as evidenced by the contact angle of 16°, the challenges persisted, particularly in the face of electrochemical etching within the microfluidic device. Potential contributing factors were investigated, including unsuccessful APTES functionalization, potential incompatibility of the graphene patterning process with APTES, and the sensitivity of APTES to high temperatures during the thermal evaporation step. Additionally, attempts to mitigate these challenges involved coating the APTES-functionalized

graphene with a protective 2µm-thick layer of PMMA A11. This protective layer aimed to act as a barrier against direct contact with the medium during device operation, yet results were inconclusive, emphasizing the intricacies associated with electrochemical etching. Challenges included the suboptimal thickness and uniformity of the PMMA layer, potentially leading to inadequate protection or the introduction of defects during spin coating. These defects could compromise the integrity of the graphene and its stability within the microfluidic system.

5.3.1. Conclusion

In conclusion, this study illuminates the intricate challenges involved in safeguarding graphene electrodes within microfluidic devices against electrochemical etching. The modified approach, incorporating a protective copper layer and employing various safeguarding techniques, has unveiled the complexities inherent in preserving graphene integrity under controlled electrochemical conditions. Notable issues, including unsuccessful APTES functionalization, incompatibility with the graphene patterning process, and the stability of APTES under elevated temperatures, underscore the intricate nature of this task.

Furthermore, the exploration of a polymer film as a protective barrier has highlighted challenges concerning thickness, uniformity, and the formation of defects during the coating process. These findings underscore the crucial need for precise optimization of surface functionalization, patterning processes, and protective coatings to effectively counter the impact of electrochemical etching on graphene electrodes.

The study's results provide a compelling argument for the necessity of further investigations and refinements in experimental techniques to overcome the challenges associated with electrochemical etching.

5.3.2. Comparison with literature

The literature talks about the advantages of graphene for sensitivity-based applications. Its currently being used as gas sensors, bio sensors, chemical sensor, and electrochemical sensors, particularly due to its exceptional electrical conductivity, mechanical strength, and flexibility. These properties make it an ideal material to be used in microfluidic devices.. Additionally, some of the literature discusses the challenges related to the integration of graphene into devices, including the difficulty in achieving precise control over material properties during fabrication and the need to optimize surface functionalization for enhanced detection performance.

The experimental findings also provide some notes that are not extensively covered in the literature. While graphene's inherent properties offer significant advantages in sensitivity of the sensor, the conclusion indicates that challenges related to material integration and channel configuration were more pronounced than initially anticipated. The results also emphasize the need for further optimization of electrode positioning and channel dimensions to mitigate issues such as signal distortion or reduced sensitivity due to particle aggregation. Moreover, the conclusion reveals that, while graphene's surface area could be beneficial for detection, fine-tuning the functionalization and ensuring a stable and reproducible fabrication process is critical to performance. Furthermore, the graphene behaviour in the dynamic setting with low AC voltage have some underlying issues that needs to be addressed.

5.4. Pyrolytic carbon

PyC is one of the carbon-based materials explored as electrode material for MIC devices. It possesses several properties and benefits that make them suitable option for microfluidic coplanar electrodes, i.e. high electrical conductivity[325], high mechanical tolerance, high thermal stability and biocompatibility[326]. By leveraging the unique properties of PyC, the transition from metal electrodes to PyC in MIC can lead to improved stability, sensitivity, and versatility.

5.4.1. Electrode Measurements

CV was conducted on PyC using the same parameters and systems mentioned in Au electrodes.

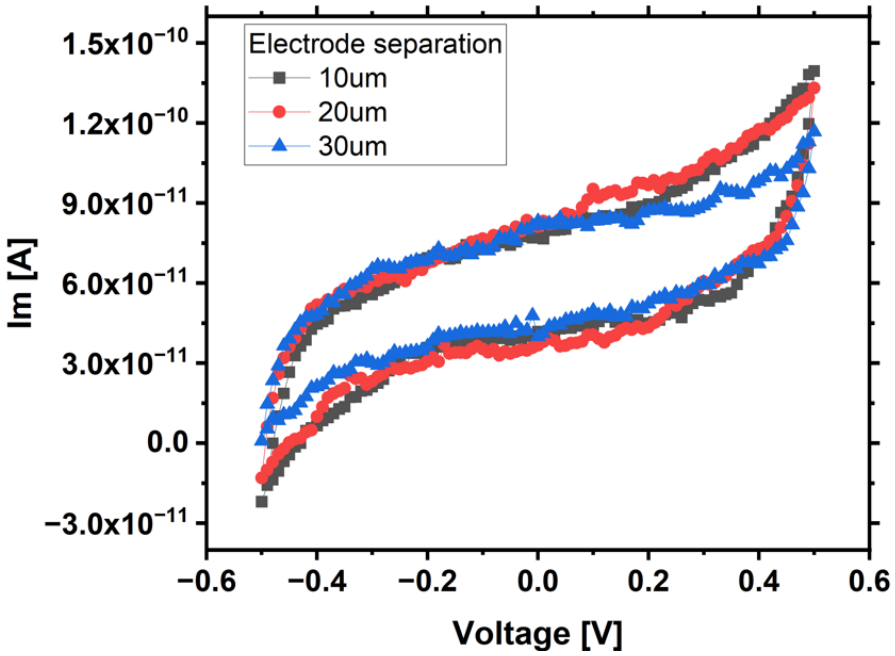

Figure 79: These are the results of CV and shows IV curve for Pyrolytic carbon performed on electrode gap of 10, 30, &

Examining cyclic voltammogram, presented in **Figure 79,** we can see that the difference in separations of PyC electrodes do not have any significant change in the area under the curve. For $10\mu m$, $30\mu m$ and $50\mu m$ the area is 4.13×10^{-11}, 3.7×10^{-11}, 3.07×10^{-11}AV. This suggests that there may be some influence of the electrode's separation on the electrochemical behaviour. Additionally, the redox and oxide peaks are not visible, this is due to double layer effect. Double layer effect is a fundamental aspect of electrochemistry and refers to the formation of electric double layer at the interface between an electrode and an electrolyte solution. In electrochemical sensors and biosensors, the double layer capacitance plays a role in the detection of analytes, contributing to the sensitivity and selectivity of the sensor[313].

By employing **equation 13** to calculate the specific capacitance and using these results to determine the capacitance values using **equation 14**, following values were obtained: 2.1nF, 1.8nF & 1.4nF for electrode separation of 10, 30, & $50\mu m$, respectively. This similarity in capacitance values across different electrode separations suggests that, within the analysed

range, the choice of electrode separation doesn't substantially impact the overall capacitance. As was expected from interpretation of the CV curve.

With its impressive electrical conductivity ranging from 10^3 to 10^4 S/m, PyC emerges as an exceptional candidate for electrode applications in high-performance energy storage devices and energy conversion systems.

Furthermore, the cone-like extensions observed in cyclic voltammograms between 400 to 500mV and -400mV to -500mV can be associated with polymerization processes. The appearance of such features is due to electrochemical reactions involving the formation and deposition of polymers on the electrode surface[327, 328]. This phenomenon is known as electro polymerization and is an irreversible process.

To further evaluate the impact of the electrode spacing, EIS was conducted on PyC electrodes spaced 10, 30, &50 μm. A frequency sweep from 0.1 to 10KHz was performed at AC voltage of 10mV rms in phosphate solution as electrolyte. The area of sensing was 0.5 cm^2, and the experimental instrument was Gamry Reference 620. Gamry Echem Analyst software was used to do a capacitance (C) model-fit on the resulted output data.

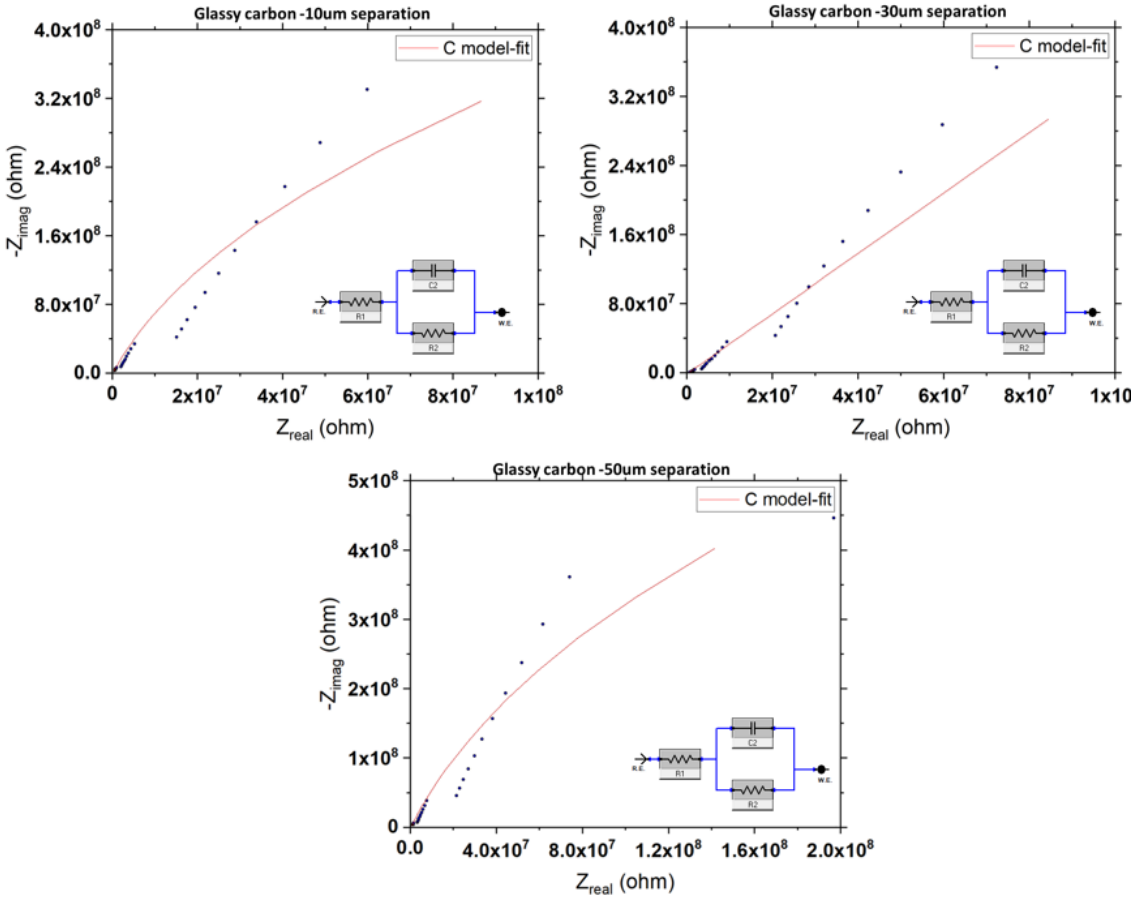

Figure 80: These are the results of an EIS (dotted), and model fit (red line) done on Pyrolytic carbon electrodes at 10, 30, & 50um electrodes spacing. The model fit is based on coplanar electrode capacitance-resistor parallel model.

Figure 80 states the results of EIS measurements for PyC electrodes, represented by black dots. The red line corresponds to the fitted capacitance model generated by Echem Analyst software. The model is R in series with RC in parallel. This module depicts the Randles

equivalent circuit for coplanar electrode configuration with EDL effect, which we have seen from CV curve earlier. This model enables the quantification of capacitance values derived from the impedance curve. From the analysis, the calculated values at electrode gaps of 10, 30 and 50μm at a frequency of 10 KHz are determined to be 2nF, 1.7nF & 1.2nF.

For optimal performance for our microfluidic system, it is crucial to consider the impedance characteristics, as impedance is inversely proportional to capacitance. A lower capacitance signifies higher impedance, and, consequently, higher sensitivity. In the context of achieving a fast response time with minimal noise, it becomes evident that a lower value of capacitance is favourable. Electrode gaps of 50µm consistently demonstrated the most suitable impedance characteristics for our specific needs. This finding aligns with our objective of attaining enhanced sensitivity, ensuring a rapid response time, and minimizing noise levels within the microfluidic system. Considering the results, 50µm is the most suitable to the need of microfluidic system. However, all the electrode gaps were investigated further in **section 5.4.2.**

The focal point of all measurements has been the sensitivity of PyC electrodes, considering their respective electrode gaps. The impact of electrode gap on system sensitivity is also indicated by both CV and EIS results. To quantify this value, measurements of signal strength were taken under various fluid flow settings, as illustrated in **Figure 81**. The sensitivity of each electrode can be determined using **equation 30,** labelled on each line in **Figure 81**.

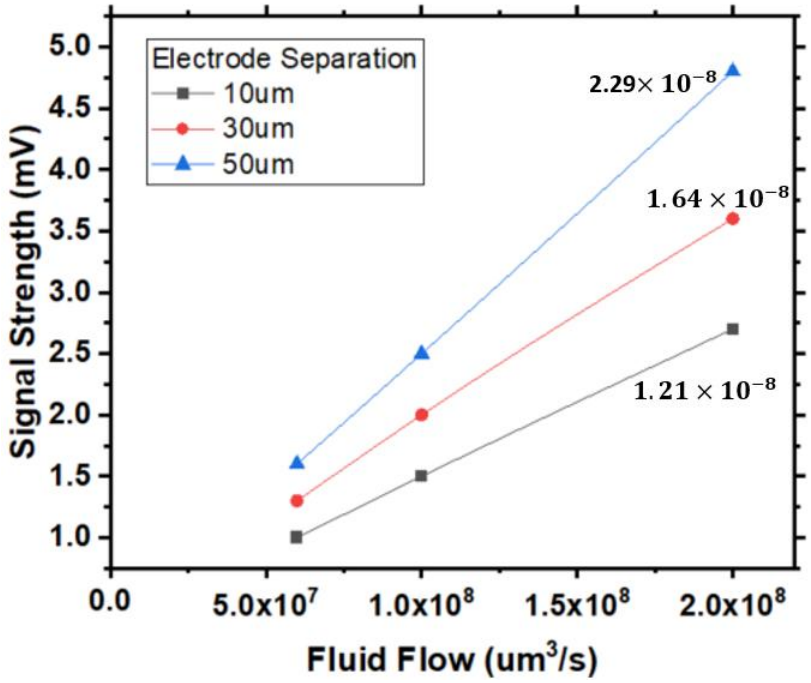

Figure 81: The graph illustrates variations in signal strength corresponding to changes in fluid flow rate. This data is employed to calculate the sensitivity of each individual electrode separation, labelled on each line.

Phosphate solution is used as medium and injected into the microfluidic channel at variating fluid flows. The variation in fluid flow has a direct impact on the ΔV, enabling the calculation of sensitivity for individual gap between electrodes. Upon observing the sensitivity from the **Figure 81**, it is evident that, the electrode separation 50μm exhibits the highest sensitivity,

while 10μm shows the least sensitivity. When compared with the sensitivity of Au electrodes, a notable difference is observed. The sensitivity lines for PyC electrodes concentrate their sensitivity in proximity, exhibiting smaller variation among different electrode separations. In contrast, Au electrodes display a more significant variation in sensitivity across different separations. This suggests that PyC electrodes maintain relatively consistent sensitivity within a specific separation range.

5.4.2. Particle Analysis

A phosphate solution with 0.1% concertation of P_s particle, 1600 partilce/ml, served as medium, with 3ml of solution pumped in at a flow rate of 0.5µL/s. The following experiment involved the impact of channel height on PyC electrode separation of 30μm & 50μm. The detection was performed at 200mV rms drive voltage with 100KHz frequency. The channel width is set parameter at 100μm and will not be change. The 10μm electrode separation was excluded from consideration due to its inadequate performance in terms of sensitivity. All the experiments are under laminar flow due to low Reynolds number, calculated from **equation 4**, 0.083.

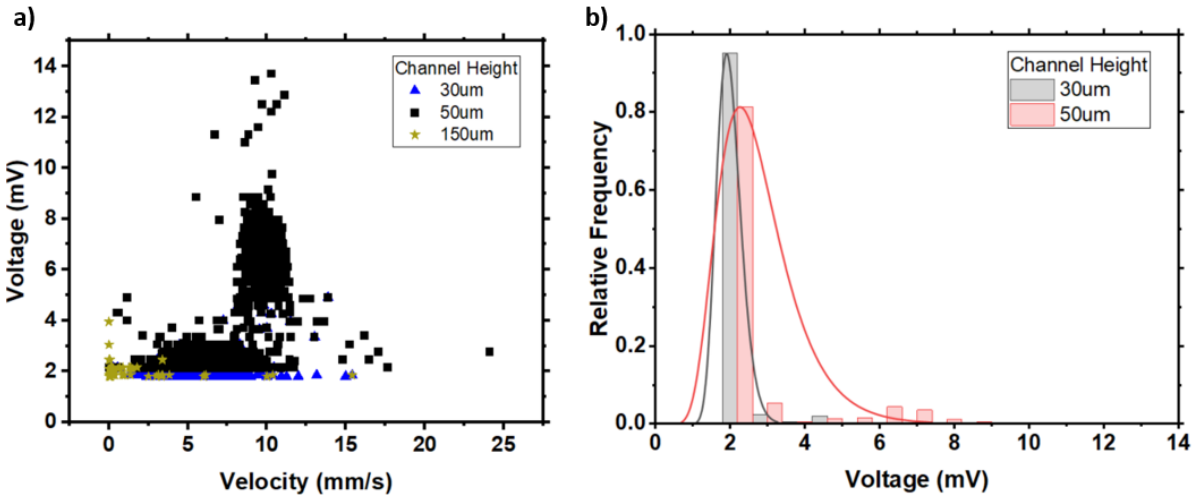

*Figure 82: **a)** illustrates the detection of 10µm particles with Au 30µm electrode separation. It presents a comparison of the detection limit and sensitivity across various channel heights. **b)** displays the distribution peak for particle detection, frequency distribution of detected particles.*

In **Figure 82**, the MIC device used in the experiment features PyC electrodes with a 30μm separation. In **a)** a comparative scatter plot is utilized to analyse the particle behaviour with variation in channel height changing from 30μm to 150μm. Given With an increase in channel height, a larger volume flows through the sensing region, thereby influencing the ΔV. However, the observation in **Figure 82a)** contradicts the expectation that a 150μm channel would result in higher ΔV. This is due to the dilution effect of particles and the diffusion of electrical field across the sensing region. This finding aligns with the concept explained earlier in **Figure 71a)**, where signal strength diminishes as particles move away from the electrodes. The detection events in this scenario are likely associated with particles in proximity to the electrodes, whereas those in the middle of the fluid flow and on the far side fall beyond the effective detection range. Here for a similar integration time (normalized for flow rate) the 150μm channel detects 5.9% of the expected number of particles. For the 30μm and 50μm channels there is a similar distribution in velocity and signal level however, the 30μm channel

appears to detect a smaller 62.7% of expected particles which may be due to the restricted space in the smaller channel leading to congestion resulting in system clogging reducing the number of particles passing the sensing region. The 50μm channel height also shows a more distinct separation of sensing events into the two branches which is discussed earlier for **Figure 72a)**, where signal strength and velocity are related to particles location in the channel in reference to electrodes.

Examining **Figure 82b)** it is evident that the signal strength for the particles of 50μm channel height (3mV) is slightly higher compared to the 30µm (2.5mV). The change in signal strength contributes to the volume in the channel.

50μm channel strikes a balance between particle concertation and channel height, detected 81.75% particle events. The increases channel dimensions enhance fluid flow and particle distribution while maintaining sufficient field strength for effective detection. The 50μm channel does exhibit slightly better sensitivity to particle detection and location. In contrast, the 30μm channel height shows a more concentrated distribution with larger peak.

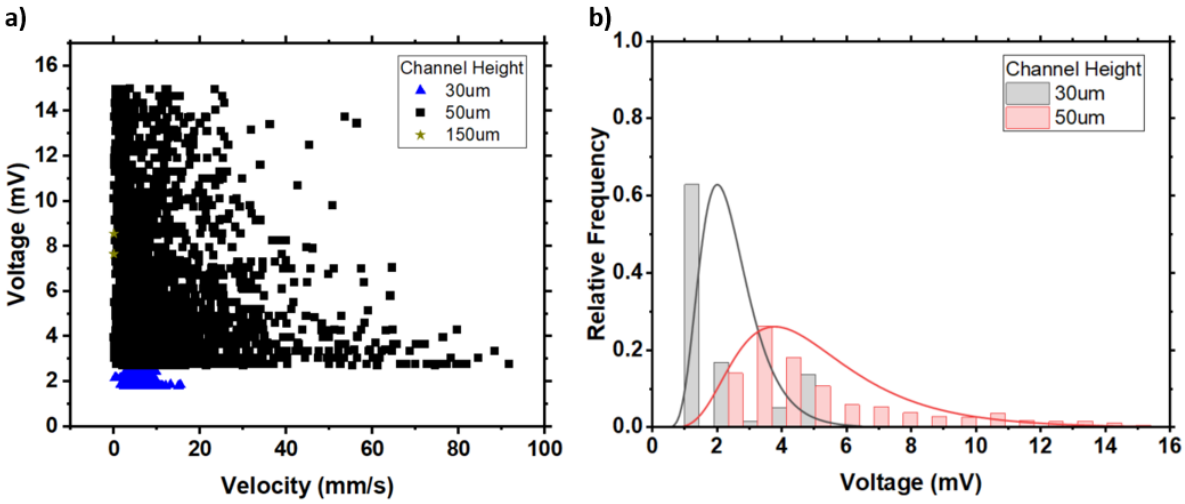

*Figure 83: **a)** This plot shows the detection of 10µm particles with Pyrolytic carbon 50µm electrode separation. It provides a comparative analysis of the detection limit and sensitivity across different channel heights. In **b)**, the figure showcases the distribution peak for particle detection, offering a frequency distribution of the detected particles.*

In **Figure 83**, a similar experiment to the one above is presented, but with the electrode separation of 50μm. In **a)** one notable change is the increased scattering of data points, especially evident for 50μm channel height, with 84.4% event detection. 30μm only 64.2% detection events. Additional, as expected, the 150μm channel height allows more medium to flow, leading to an increase in ΔV. Again, the number of detected particle in the 150μm channel is very low, missing most of the particle detection events, with only 0.6% detected.

Examining **Figure 83b)**, it is apparent that the 50μm channel height displays a more distributed curve, showcasing the higher sensitivity to the location of the particle. In contrast, due to the height constriction, the 30μm channel height exhibits a limited distribution. This aligns with the sensitivity analysis done previously in **Figure 81**, where the 50μm electrode separation exhibited higher sensitivity of 2.29×10^{-8}.

We can consider the improved fidelity of 50μm channel by thinking about the field distribution in the sensing region and in the case of a narrower channel the particle must pass

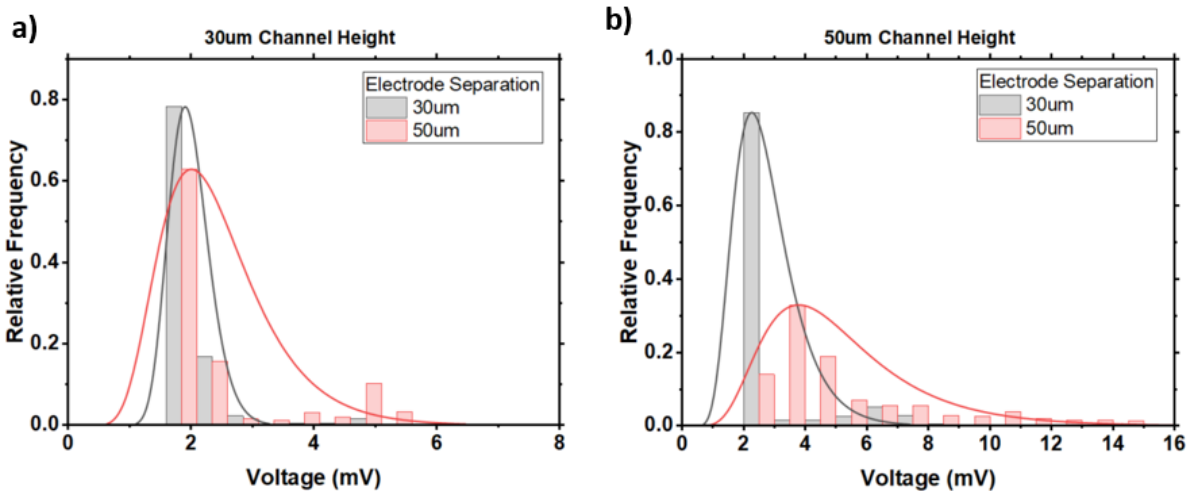

*Figure 84: In **a)**, the frequency distribution graph depicts the detection of 10µm particles at a 30µm channel height. This graph facilitates a comparative distribution analysis between the 30µm and 50µm electrode separations. In **b)**, the figure highlights the distribution peak for particle detection at a 50µm channel height, presenting another comparison of frequency distribution.*

through a region which contains a high field gradient compared with the 50μm channel. These two effects combine to force a narrower signal distribution as 10μm particle will always disturb a larger fraction of the electric field in the sensing region. For the 50μm channel the field is more distributed in the sensing region and the particle distributes less of the field giving a wider possible range in the signals. This when combined by the optimal signal level being for the 50μm electrode separation implies that a combination of 50μm channel height and 50μm electrode separation is ideal.

To validate the contrast between 30μm & 50μm electrode gap, **Figure 84** shows a comparison of the data shown in **Figure 82 & 83**. **Figure 84a)** reveal slight differences between the two electrode separations at 30μm channel height. However, upon closer examination of **Figure 84b)**, it becomes evident that the 50μm separation yields a more evenly distributed pattern of particles. While both separations exhibit sensitivity, the data suggests that the 50µm separation performs better than the of 30µm separation in achieving better sensitivity in particle detection.

Mixture of 10μm & 20μm particle analysis

in this experiment we aim to show effective distinction between different particles sizes in a mixed solution, A solution of 0.1% particle concertation of P_s & P_L (0.05% for each size) particles was made in phosphate solution. Using the nano-stepper, 3ml solution was pumped through the system at 0.5$\mu L/s$ flow rate, 1600 particle/ml. Using electrode separation of 30μm and channel of height of 50μm for further experiments. The detection was performed at 200mV rms drive voltage with 100KHz frequency.

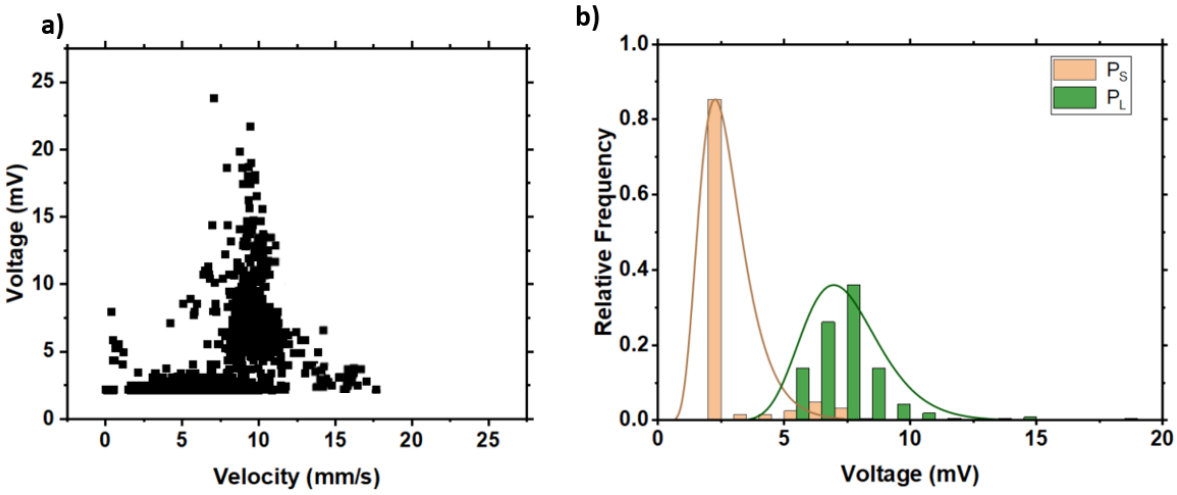

*Figure 85: **a)** This plot shows the scatter plot for the detection of mix particle solution with Pyrolytic carbon 30µm electrode separation & 50µm×100µm height and width of the channel. In **b)**, the figure showcases the distribution peaks for particle detection. This provides a frequency distribution of the detected particles, offering insights into the occurrence of different particle types in the solution.*

In **Figure 85a)**, sensing signal scatter plot is shown, featuring detection events from a 100-minute duration measurement flow of a mixture of P_s & P_L particles as described above. Using FWHM and ΔV, a frequency distribution graph is obtained which is able to distinction between P_s & P_L, as illustrated in **Figure 85b)**. The P_S particles, with 63.3% detection event, exhibits a concentrated peak with some distribution at the higher ΔV, while the P_L, with 76.9%, demonstrates a more even distribution. This observation suggests that the 30μm electrode gap exhibits lower sensitivity to the smaller particle sizes, rendering it unbale to precisely locate them in the system. Consequently, it only shows a detection event for P_S without providing additional details. On the Other hand, the larger impact of P_L on the impedance of the system allows the electrodes to accurately capture a substantial amount of information about it.

The lower sensitivity of the 30µm electrode separation to P_S prompts an exploration of alternative electrode configurations, particularly a 50µm separation. This investigation aims to determine if the larger electrode gap can enhance sensitivity and provide more detailed information about P_S particles in the system.

Employing the previously described experimental setup and mixture, subsequent experiments were conducted with an electrode separation of 50µm. The microfluidic channel dimensions utilized in this experiment is the same as before, height of 50µm and a width of 100µm.

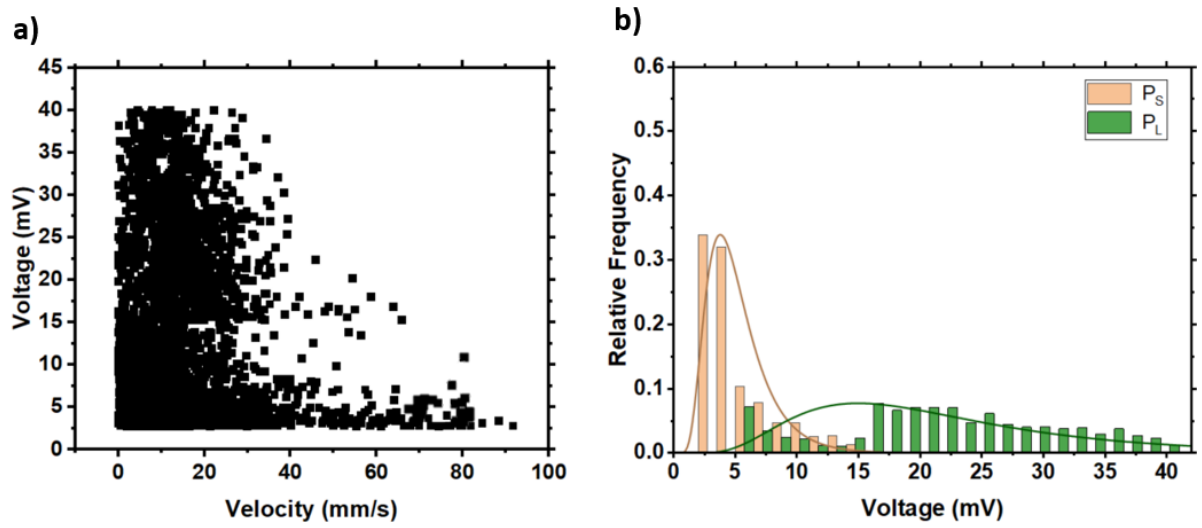

*Figure 86: In **a)**, the plot illustrates a scatter plot depicting the detection of a mixed particle solution with a Pyrolytic carbon electrode separation of 50µm and a channel size of 50µm×100µm in height and width. In **b)**, the figure presents distribution peaks for particle detection, offering a frequency distribution of the detected particles. This insight provides an understanding of the occurrence of different particle types in the solution.*

In **Figure 86a)**, a comprehensive scatter plot is presented, featuring data points from a mixture of P_s & P_L particles utilizing 50μm electrode separation. It can be noted that the scattering of the particles is widely spread out, capturing the detection of high-speed particles, reaching up to 92mm/s. Additionally, the ΔV values are notably higher compared to any of the preceding devices, going up to 40mV.

This observation strongly suggests that the sensitivity of the 50µm electrode separation is optimal for PyC electrodes. The broader scattering and higher ΔV values indicate an enhanced capability to capture detailed information about the particles. The 50µm electrode separation proves to be effective in providing well-defined and comprehensive data on particle behaviour in the system.

A frequency distribution graph capable of distinguishing between P_s & P_L is illustrated in **Figure 86b)**. The P_S particles, with 87.5% event count, exhibits a concentrated peak with broader distribution, while the P_L, with 91.7% event count, demonstrates a more even distribution. An interesting observation is notable for P_L between the ΔV values of 5mV to 16mV, where the distribution decreases before rising again. This observation can be attributed to the far side of the sensing region, where ΔV is the lowest. The drop in distribution indicates that the particle density at the far side is significantly lower, suggesting that particles tend to concentrate towards the centre of the fluid flow.

This insight into the spatial distribution of particles within the microfluidic system offers valuable information regarding particle behaviour and concentration in different regions of the channel. The combined findings underscore the effectiveness of the 50µm electrode separation for enhanced sensitivity and detailed characterization of particle dynamics.

5.4.3. Conclusion

In conclusion, the detailed experimental exploration of MIC devices with varying channel heights and electrode separations offers valuable insights into the optimization of particle detection and characterization. The study began by investigating the impact of channel height, particularly focusing on PyC electrode separations of 30µm and 50µm. The intricate interplay between these parameters was analysed in terms of signal strength, velocity distribution, and sensitivity to particle detection.

The experiments, as depicted in Figures 82 and 83, revealed that the 50µm channel height struck a balance between particle concentration and fluid flow, resulting in the detection of 81.75% and 84.4% of particle events for 30µm and 50µm electrode separations, respectively. The increased channel dimensions enhanced fluid flow and particle distribution while maintaining sufficient field strength for effective detection. The 50µm electrode separation consistently outperformed the 30µm separation in achieving better sensitivity in particle detection.

The exploration extended to a mixed solution containing 10µm and 20µm particles, aiming to demonstrate effective discrimination between different particle sizes. Utilizing a 50µm electrode separation, the experiments provided comprehensive insights into the spatial distribution of particles within the microfluidic system. The 50µm electrode separation exhibited optimal sensitivity, capturing detailed information about particle behaviour and concentration with detecting highest particle events of 87.5% for P_S and 91.7% for P_L. The broader scattering and higher ΔV values indicated enhanced capability, making the 50µm separation ideal for PyC electrodes.

The findings highlight the contribute to the optimization of MIC devices with carbon-based electrode for particle detection. Future research in this field could explore additional parameters and configurations to further refine and expand the capabilities of PyC-based MIC.

5.4.4. Comparison with literature

The literature review talks about the advantages of pyrolytic carbon, especially its excellent electrochemical properties, stability, and biocompatibility, making it a promising material for use in microfluidic channels and devices. PyC has been noted for its ability to support accurate particle detection due to its relatively smooth surface, low electrochemical noise, and high surface area, which enhances the sensitivity and efficiency of the devices. Moreover, many studies point to the ease of fabricating PyC electrodes, particularly when compared to other materials such as gold or platinum, while also highlighting its resistance to corrosion in harsh chemical environments. Recent applications of PyC is being used for different kinds of sensors but have not been explored as MIC detection electrodes.

The conclusion drawn from the experimental studies on PyC microfluidic devices corroborates much of the literature regarding the material's benefits, particularly in terms of its electrochemical stability and ability to support particle detection. The conclusion notes that while PyC electrodes provide a high degree of stability and sensitivity for particle detection, it also has better detection then the typical gold electrode MIC devices.

6. Conclusion

This doctoral thesis represents an exploration into MIC devices with a focus on carbon-based electrode configurations. The study included materials, fabrication techniques, and experimental investigations, aiming to optimize particle detection and characterization within microfluidic channels. The study is mainly divided in two parts: 3D printing of microfluidic channels using TPA, and particle detection of coplanar electrodes configuration.

The fusion of TPA and carbon-based polymers for microfluidic channel printing, offers meaningful possibilities for microscale and nanotechnology. The response of the TPA was investigated on various materials, including PDMS, PMMA, Polystyrene, and Polycarbonate, provided a nuanced understanding of material-specific challenges and opportunities. While PDMS emerged as the optimal material for TPA during the initial assessments, its integration into the MIC configuration revealed unforeseen challenges. Despite its favourable characteristics in TPA, the application of PDMS in the MIC setup presented complexities that resulted in failure of the device.

Coplanar electrode configuration was investigated on gold, PyC, and graphene electrodes. The experimental investigations on the MIC device with Au coplanar electrode configuration illuminated the intricate relationship between channel height, electrode separation, and particle detection efficiency. Achieving a delicate balance between sensitivity and fluid dynamics emerged as a crucial consideration, ultimately leading to the selection of a 50µm channel height. The comparison of electrode separations emphasized the significance of optimizing dimensions for efficient particle detection. Notably, a 30µm electrode separation emerged as particularly noteworthy, displaying superior sensitivity in the MIC system. This configuration demonstrated remarkable detection rates, capturing 85.1% of larger particles and 82.9% of smaller particles.

In the case of PyC electrodes, we found that a 50µm channel height paired with a 50µm electrode separation achieved an optimal balance between particle concentration and fluid flow. This specific configuration not only enhanced sensitivity but also exhibited superior detection capability. The study successfully showcased the device's ability to discriminate between different particle sizes, with the 50µm electrode separation yielding the highest particle detection rates. Remarkably, it detected 90.17% of larger particles and 87.5% of smaller particles within the system. These findings have significant implications for the development of MIC devices with carbon-based electrodes for particle detection.

Using pattern graphene electrodes, the study aimed to leverage the exceptional properties of graphene for enhanced performance in particle detection systems. However, the experimental investigations revealed several critical issues that hindered the success of graphene electrodes in the MIC setup. One of the significant challenges encountered was the susceptibility of graphene to electrochemical etching or electrolysis when subjected to an electrolyte and AC potential. This dynamic behaviour, observed as the movement of particles and debris, indicated potential structural changes in the graphene material. Notably, attempts to mitigate these challenges through protective layers and various safeguarding techniques, including a copper layer, were met with limited or no success.

In Conclusion, it was found that graphene electrodes were unstable under low voltage AC operation, but PyC showed results superior to metal electrodes.

In essence, this research contributes to the optimization of MIC devices with carbon-based electrodes for particle detection, laying the foundation for future research and advancements in the field. The insights gained from this comprehensive study not only advance our understanding of precision material processing techniques but also underscore the potential for transformative technological advancements in microscale and nanotechnology.

6.1. Comparison with literature

The literature on microfluidic impedance cytometry (MIC) devices with carbon-based electrode configurations offers a direct foundation for understanding their potential in particle detection systems but without any quantitative detection values. However, carbon-based electrodes, such as pyrolytic carbon (PyC) and graphene, have been known and used for their excellent electrochemical properties, stability, biocompatibility, and potential to improve sensing capabilities in capacitive applications. Research consistently emphasizes the significant advantages of using carbon-based materials due to their low polluting tendencies, ease of fabrication, and favourable mechanical properties. Specifically, PyC is praised for its robust performance in electrochemical applications, while graphene has been praised for its high surface area and electrical conductivity, promising enhanced detection sensitivity.

Furthermore, the literature also outlines the challenges associated with the electrochemical behaviour of these materials. While graphene's high surface area and conductivity might it an ideal candidate for advanced particle detection systems, it is also noted for being susceptible to electrochemical etching or electrolysis under certain operational conditions, especially under high voltage AC operation. This issue is often cited as a potential drawback when integrating graphene in practical applications. PyC, on the other hand, is noted for its stability in a range of conditions.

The conclusion of this thesis extends and refines these findings through detailed experimental investigations, which highlight both the potential and limitations of carbon-based electrodes in MIC devices. Although the literature doesn’t emphasizes the need for optimizing electrode configurations, it was a necessity based on the MIC understanding, such as electrode separation and channel height, to enhance particle detection performance. The experimental work confirmed the importance of the electrochemical properties of PyC and graphene as outlined in the literature but provided new insights as practical detection sensor and challenges that are not fully discussed in previous studies.

In terms of electrode configuration, the literature supports the notion that electrode separation and channel height are crucial for optimizing particle detection sensitivity and fluid dynamics. The conclusion of this thesis corroborates these findings, demonstrating that a 30µm electrode separation in the gold electrode configuration resulted in higher particle detection efficiency, capturing 85.1% of larger particles and 82.9% of smaller particles. This aligns with the literature’s assertion that smaller electrode separations lead to better detection sensitivity. The PyC-based electrode configuration further validated the literature’s claims about its stability and performance. The experimental results demonstrated that a

50µm channel height combined with a 50µm electrode separation achieved the best performance, capturing 90.17% of larger particles and 87.5% of smaller particles. These results not only confirm PyC's superior performance compared to gold electrodes but also emphasize the significance of fine-tuning electrode configurations to optimize particle detection rates. However, the experimental results of the thesis revealed new challenges regarding the use of graphene electrodes that were not fully addressed in the literature. The thesis found that graphene electrodes were unstable under low-voltage AC operation.

6.2. Future Work

Moving forward, future work of MIC devices with carbon-based electrodes should focus on addressing specific areas identified in the present study to enhance device performance and broaden its applicability. Firstly, an exploration of intermediate electrode separations is warranted, aiming to discern potential trade-offs between sensitivity and other performance metrics. Systematically varying electrode separations within a controlled range could reveal nuanced relationships, guiding the optimization process. Additionally, a detailed investigation into PyC electrode configurations, including variations in dimensions, is essential to further understand the intricate dynamics influencing particle detection efficiency.

The integration of computational modelling and simulations represents another promising avenue for future research. Computational approaches can provide insights into fluid dynamics and electric field distribution within microfluidic channels, aiding in the design of optimized electrode configurations. Furthermore, expanding the scope of particle sizes beyond the current focus on 10µm and 20µm particles will contribute to a more comprehensive understanding of the device's capabilities. This exploration could involve examining the system's performance with a broader range of particle sizes to refine the versatility and applicability of MIC devices.

Exploring advanced materials for electrodes and microfluidic channel construction is paramount for continued improvement. Investigating novel materials with enhanced properties, such as increased conductivity or reduced susceptibility to electrochemical etching, could elevate the overall performance and durability of MIC devices. Integrating real-time data analysis algorithms is another crucial step, enhancing the device's ability to process information efficiently. This could involve the implementation of machine learning or artificial intelligence techniques to improve the accuracy and speed of particle size discrimination.

Moreover, the development of multi-channel MIC systems should be considered to increase throughput and versatility. Such systems would enable simultaneous analysis of multiple samples or different experimental conditions, expanding the device's scope for various applications. In summary, these proposed directions for future work aim to refine and expand the capabilities of MIC devices with carbon-based electrodes. Carbon electrodes offer exciting possibilities for flexible and biologically compatible sensing systems and future work would include 3 electrode configurations to put into competition with the best reported MIC devices. Other nanocarbons such as carbon black and conductive nanoparticles in copolymer composites might also be explored.

Despite the setbacks, this study lays the groundwork for future research and development in the realm of graphene electrodes for MIC applications. Understanding the reasons behind the challenges faced by graphene electrodes prompts avenues for further investigation and refinement of experimental techniques. Future work in this field should focus on tailored optimization approaches to address specific issues such as electrochemical etching, with an emphasis on improving surface functionalization, patterning processes, and protective coatings. The quest for overcoming these challenges will not only enhance the performance of graphene electrodes in microfluidic impedance cytometry but also contribute to advancing the broader applications of graphene in various electrochemical sensing platforms.

Integrating TPA with advanced fabrication methods like 3D printing or micro-milling presents a promising avenue for the creation of intricate and tailored structures. When applying TPA to PDMS for microfluidic applications, it is imperative to adopt a targeted approach to overcome challenges associated with PDMS cleaning and fluid flow. Exploring higher TPA wavelengths offers a potential solution to the difficulties encountered in achieving deep cuts, thereby facilitating fluid flow within the microchannels. Higher wavelength might be favourable considering multiple aspect, such as, better, and more uniform two-photon absorption in thicker materials, less scattering due to material, longer wavelength will have even lower photon energy, and could potentially improve the resolution. More polishing/cleaning methods should be explored to remove the debris from PMDS deep cuts, such as the use of surfactant solutions which aid in removing debris and implementing a secondary laser ablation with different wavelength and intensity to selectively ablate and clean the cut. One such example would be to use the Triton x-100, which is a non-ionic surfactant that is widely used for cleaning, considered very effective in removing debris and residues from the surface. This strategic combination of TPA with tailored fabrication techniques and wavelength optimization holds the key to advancing microfluidic device fabrication for enhanced performance and versatility.

7. Bibliography

1. M. Shaker, L.C., F. Caselli, P. Bisegna, P. Renaud, *Lab Chip*. 2014. 124-32.
2. Cheung, K.C., et al., *Microfluidic impedance-based flow cytometry.* Cytometry Part A, 2010. **77A**(7): p. 648-666.
3. Cheung, K., S. Gawad, and P. Renaud, *Impedance spectroscopy flow cytometry: On-chip label-free cell differentiation.* Cytometry Part A, 2005. **65A**(2): p. 124-132.
4. D. Holmes, D.P., C. H. Reccius, J. D. Gwyer, C. van Berkel, J. Holloway, D. E. Davies, H. Morgan, *Lab Chip*. 2009. 2881-2889.
5. Evander, M., et al., *Microfluidic impedance cytometer for platelet analysis.* Lab on a Chip, 2013. **13**(4): p. 722.
6. H. L. Gou, X.B.Z., N. Bao, J. J. Xu, X. H. Xia, H. Y. Chen, *J. Chromatogr. A*. Vol. 1218. 2011. 5725-9.
7. Hong, J.-L., Lan, K.-C., & Jang, L.-S, *Electrical characteristics analysis of various cancer cells using a microfluidic device based on single-cell impedance measurement.* 2012. **173**: p. 927–934.
8. Emaminejad, S., Talebi, S., Davis, R. W., & Javanmard, M, *Multielectrode Sensing for Extraction of Signal From Noise in Impedance Cytometry.* IEEE Sensor Journal, 2015. **15**: p. 2715-2716.
9. Balena, A., et al., *Two-photon fluorescence-assisted laser ablation of non-planar metal surfaces: fabrication of optical apertures on tapered fibers for optical neural interfaces.* Optics Express, 2020. **28**(15): p. 21368.
10. Ha, C.W. and Y. Son, *Development of the multi-directional ablation process using the femtosecond laser to create a pattern on the lateral side of a 3D microstructure.* Scientific Reports, 2023. **13**(1).
11. Du, H., G. Chen, and J. Wang, *Highly selective electrochemical impedance spectroscopy-based graphene electrode for rapid detection of microplastics.* Science of The Total Environment, 2023. **862**: p. 160873.
12. Zamfir, L.-G., M. Puiu, and C. Bala, *Advances in Electrochemical Impedance Spectroscopy Detection of Endocrine Disruptors.* Sensors, 2020. **20**(22): p. 6443.
13. Magar, H.S., R.Y.A. Hassan, and A. Mulchandani, *Electrochemical Impedance Spectroscopy (EIS): Principles, Construction, and Biosensing Applications.* Sensors, 2021. **21**(19): p. 6578.
14. Gong, Y., Li, D., Fu, Q., & Pan, C. , *Influence of graphene microstructures on electrochemical performance for Supercapacitors.* Progress in Natural Science: Materials International, 2015. **25(5)**: p. 379–385.
15. Zhai, Z., et al., *A review of carbon materials for supercapacitors.* Materials & Design, 2022. **221**: p. 111017.
16. Huang, H., et al., *Graphene-Based Sensors for Human Health Monitoring.* Frontiers in Chemistry, 2019. **7**.
17. Musile, G., et al., *Application of Paper-Based Microfluidic Analytical Devices (µPAD) in Forensic and Clinical Toxicology: A Review.* Biosensors, 2023. **13**(7): p. 743.
18. Pramanick, B., et al., *C-MEMS Derived Glassy Carbon Electrodes-Based Sensitive Electrochemical Biosensors.* IEEE Sensors Journal, 2020. **20**(21): p. 12472-12478.
19. Quang, L.N., et al., *Electrochemical pyrolytic carbon resonators for mass sensing on electrodeposited polymers.* Micro and Nano Engineering, 2019. **2**: p. 64-69.
20. Uskoković, V., *A historical review of glassy carbon: Synthesis, structure, properties and applications.* Carbon Trends, 2021. **5**: p. 100116.
21. Song, K., et al., *The Fabrication and Application Mechanism of Microfluidic Systems for High Throughput Biomedical Screening: A Review.* Micromachines, 2020. **11**(3): p. 297.
22. Drescher, H., S. Weiskirchen, and R. Weiskirchen, *Flow Cytometry: A Blessing and a Curse.* Biomedicines, 2021. **9**(11): p. 1613.

23. adminNC. *How does flow cytometry work?* 2023, March; Available from: https://nanocellect.com/blog/how-does-flow-cytometry-work/
24. Pitsillides, C.M., et al., *Cell labeling approaches for fluorescence-based in vivo flow cytometry.* Cytometry Part A, 2011. **79A**(10): p. 758-765.
25. McKinnon, K.M., *Flow Cytometry: An Overview.* Current Protocols in Immunology, 2018. **120**(1).
26. Pattanayak, P., et al., *Microfluidic chips: recent advances, critical strategies in design, applications and future perspectives.* Microfluidics and Nanofluidics, 2021. **25**(12).
27. Cui, P. and S. Wang, *Application of microfluidic chip technology in pharmaceutical analysis: A review.* Journal of Pharmaceutical Analysis, 2019. **9**(4): p. 238-247.
28. Niculescu, A.-G., et al., *Fabrication and Applications of Microfluidic Devices: A Review.* International Journal of Molecular Sciences, 2021. **22**(4): p. 2011.
29. Nunes, J.K. and H.A. Stone, *Introduction: Microfluidics.* Chemical Reviews, 2022. **122**(7): p. 6919-6920.
30. Deliorman, M., D.S. Ali, and M.A. Qasaimeh, *Next-Generation Microfluidics for Biomedical Research and Healthcare Applications.* Biomedical Engineering and Computational Biology, 2023. **14**.
31. Convery, N. and N. Gadegaard, *30 years of microfluidics.* Micro and Nano Engineering, 2019. **2**: p. 76-91.
32. Amer, A.M., N.I. Ghoneim, and A.M. Megahed, *Investigation of dissipation phenomenon of non-Newtonian nanofluid due to a horizontal stretching rough sheet through a Darcy porous medium.* Applications in Engineering Science, 2024. **17**: p. 100171.
33. Batchelor, G.K., *An Introduction to Fluid Dynamics.* 2000.
34. Kundu, P.K., Cohen, I. M., Dowling, D. R., & Tryggvason, G, *Fluid mechanics.* 2016: Academic Press.
35. Bistafa, S.R., *On the development of the Navier-Stokes equation by Navier.* Revista Brasileira de Ensino de Física, 2017. **40**(2).
36. Sheng, W., *A revisit of Navier–Stokes equation.* European Journal of Mechanics - B/Fluids, 2020. **80**: p. 60-71.
37. Rahman, M., & Brebbia, C. A, *Advances in fluid mechanics VII*. 2008: WIT.
38. Zdravkovich, M.M., *Conceptual overview of laminar and turbulent flows past smooth and rough circular cylinders.* Journal of Wind Engineering and Industrial Aerodynamics, 1990. **33**(1-2): p. 53-62.
39. Gerhart, P.M., Gerhart, A. L., & Hochstein, J. I., *Munson's Fluid Mechanics*. 2017: John Wiley & Sons, Inc.
40. Cimbala, J.M., & Cengel, Y. A., *Essentials of Fluid Mechanics: Fundamentals and Applications*. 2008: McGraw-Hill Higher Education.
41. Libretexts. *Cyclic voltammetry*. 2023; Available from: https://chem.libretexts.org/Bookshelves/Analytical_Chemistry/Supplemental_Modules_(Analytical_Chemistry)/Instrumentation_and_Analysis/Cyclic_Voltammetry
42. Elgrishi, N., et al., *A Practical Beginner's Guide to Cyclic Voltammetry.* Journal of Chemical Education, 2018. **95**(2): p. 197-206.
43. Nilsson, J.W., & Riedel, S. A., *Electric Circuits*. 2019: Pearson Education, Inc.
44. Sedra, A.S., Smith, K. C., Carusone, T. C., & Gaudet, V. C., *Microelectronic circuits*. 2020: Oxford University Press.
45. Bard, A.J., Stratmann, M., Gileadi, E., & Urbakh, M., *Encyclopedia of electrochemistry*. 2002: Wiley-VCH.
46. *Impedance Spectroscopy.* 2005.
47. Zoski, C.G., Leddy, J., Dunwoody, D., & Bard, A. J., *To accompany Electrochemical Methods: Fundamentals and Applications*. second ed. 2002.
48. Daněk, V., *Electrical Conductivity*. 2006, Elsevier. p. 327-357.

49. Kittel, C., & McEuen, P., *Introduction to solid state physics*. 2022: Wiley.
50. Atkins, P.W., Paula, D. J., & Keeler, J. , *Atkins' physical chemistry*. 2022: Oxford University Press.
51. *Electrical conductivity of the elements*. Electrical Conductivity for all the elements in the Periodic Table; Available from: https://periodictable.com/Properties/A/ElectricalConductivity.v.log.html
52. Feng, C., et al., *Electromechanical Behaviors of Graphene Reinforced Polymer Composites: A Review.* Materials, 2020. **13**(3): p. 528.
53. Baker, D.F. and R.H. Bragg, *The electrical conductivity and Hall effect of glassy carbon.* Journal of Non-Crystalline Solids, 1983. **58**(1): p. 57-69.
54. Graham, M.D., *The Coulter Principle: A history.* Cytometry Part A, 2022. **101**(1): p. 8-11.
55. Vembadi, A., A. Menachery, and M.A. Qasaimeh, *Cell Cytometry: Review and Perspective on Biotechnological Advances.* Frontiers in Bioengineering and Biotechnology, 2019. **7**.
56. *Principles of lock-in detection. Zurich Instruments.* 2019; Available from: https://www.zhinst.com/americas/en/resources/principles-of-lock-in-detection
57. Hageman, S. *Design a DSP lock-in amplifier, part 1: Background. EDN*. 2020; Available from: https://www.edn.com/design-a-dsp-lock-in-amplifier-part-1-background/.
58. Www.thinksrs.com. *about lock-in amplifiers*. Available from: https://www.thinksrs.com/downloads/pdfs/applicationnotes/AboutLIAs.pdf
59. Ashley, B.K. and U. Hassan, *Time-domain signal averaging to improve microparticles detection and enumeration accuracy in a microfluidic impedance cytometer.* Biotechnology and Bioengineering, 2021. **118**(11): p. 4428-4440.
60. Honrado, C., et al., *Single-cell microfluidic impedance cytometry: from raw signals to cell phenotypes using data analytics.* Lab on a Chip, 2021. **21**(1): p. 22-54.
61. Xiang, N., et al., *Flow stabilizer on a syringe tip for hand-powered microfluidic sample injection.* Lab on a Chip, 2019. **19**(2): p. 214-222.
62. X. Wang and Y. Shi, *Chapter 1. Fabrication Techniques of Graphene Nanostructure*. 2018.
63. Rozhkov, A.V., et al., *Electronic properties of mesoscopic graphene structures: Charge confinement and control of spin and charge transport.* Physics Reports, 2011. **503**(2-3): p. 77-114.
64. Lloyd-Hughes, J. and T.-I. Jeon, *A Review of the Terahertz Conductivity of Bulk and Nano-Materials.* Journal of Infrared, Millimeter, and Terahertz Waves, 2012. **33**(9): p. 871-925.
65. Wang, J., et al., *Optical, photonic and optoelectronic properties of graphene, h-BN and their hybrid materials.* Nanophotonics, 2017. **6**(5): p. 943-976.
66. *Fermi level in semiconductors. Nuclear Power.* (2022, July 11); Available from: https://www.nuclear-power.com/nuclear-engineering/radiation-detection/semiconductor-detectors/what-are-semiconductors-properties-of-semiconductors/fermi-level/
67. Castro Neto, A.H., et al., *The electronic properties of graphene.* Reviews of Modern Physics, 2009. **81**(1): p. 109-162.
68. Balandin, A.A., et al., *Superior Thermal Conductivity of Single-Layer Graphene.* Nano Letters, 2008. **8**(3): p. 902-907.
69. Novoselov, K.S., et al., *Electric Field Effect in Atomically Thin Carbon Films.* Science, 2004. **306**(5696): p. 666-669.
70. Jensen, B.B.E., *A study of graphene from scientific curiosity towards real sensor application*. 2017, Faculty of Science and Technology of Aarhus University.
71. Gamo, Y., et al., *Atomic structure of monolayer graphite formed on Ni(111).* Surface Science, 1997. **374**(1-3): p. 61-64.
72. Vaari, J., J. Lahtinen, and P. Hautojärvi, Catalysis Letters, 1997. **44**(1/2): p. 43-49.
73. Ueta, H., et al., *Highly oriented monolayer graphite formation on Pt(111) by a supersonic methane beam.* Surface Science, 2004. **560**(1-3): p. 183-190.

74. Coraux, J., et al., *Structural Coherency of Graphene on Ir(111).* Nano Letters, 2008. **8**(2): p. 565-570.
75. Marchini, S., S. Günther, and J. Wintterlin, *Scanning tunneling microscopy of graphene on Ru(0001).* Physical Review B, 2007. **76**(7).
76. Li, X., et al., *Large-Area Synthesis of High-Quality and Uniform Graphene Films on Copper Foils.* Science, 2009. **324**(5932): p. 1312-1314.
77. Chen, Z., et al., *Three-dimensional flexible and conductive interconnected graphene networks grown by chemical vapour deposition.* Nature Materials, 2011. **10**(6): p. 424-428.
78. Cai, J., et al., *Atomically precise bottom-up fabrication of graphene nanoribbons.* Nature, 2010. **466**(7305): p. 470-473.
79. Ci, L., et al., *Atomic layers of hybridized boron nitride and graphene domains.* Nature Materials, 2010. **9**(5): p. 430-435.
80. Berger, C., et al., *Ultrathin Epitaxial Graphite: 2D Electron Gas Properties and a Route toward Graphene-based Nanoelectronics.* The Journal of Physical Chemistry B, 2004. **108**(52): p. 19912-19916.
81. Munuera, J.M., et al., *Electrochemical Exfoliation of Graphite in Aqueous Sodium Halide Electrolytes toward Low Oxygen Content Graphene for Energy and Environmental Applications.* ACS Applied Materials & Interfaces, 2017. **9**(28): p. 24085-24099.
82. Tiwari, S.K., et al., *Graphene research and their outputs: Status and prospect.* Journal of Science: Advanced Materials and Devices, 2020. **5**(1): p. 10-29.
83. Muñoz-Ferreiro, C., et al., *Unravelling the optimization of few-layer graphene crystallinity and electrical conductivity in ceramic composites by Raman spectroscopy.* Journal of the European Ceramic Society, 2021. **41**(16): p. 290-298.
84. Mackin, C., E. McVay, and T. Palacios, *Frequency Response of Graphene Electrolyte-Gated Field-Effect Transistors.* Sensors, 2018. **18**(2): p. 494.
85. Drieschner, S., et al., *Frequency response of electrolyte-gated graphene electrodes and transistors.* Journal of Physics D: Applied Physics, 2017. **50**(9): p. 095304.
86. Colmiais, I., et al., *Towards RF graphene devices: A review.* FlatChem, 2022. **35**: p. 100409.
87. Liu, Z., et al., *Lateral Size of Graphene Characterized by Atomic Force Microscope.* IOP Conference Series: Earth and Environmental Science, 2019. **252**: p. 022022.
88. De Silva, K.K.H., et al., *Nanoscale electrical characterization of graphene-based materials by atomic force microscopy.* Journal of Materials Research, 2022. **37**(20): p. 3319-3339.
89. Sharma, S., *Glassy Carbon: A Promising Material for Micro- and Nanomanufacturing.* Materials, 2018. **11**(10): p. 1857.
90. Vieira, L.D.S., *A review on the use of glassy carbon in advanced technological applications.* Carbon, 2022. **186**: p. 282-302.
91. Marsh, H. and F. Rodríguez-Reinoso, *Production and Reference Material*. 2006, Elsevier. p. 454-508.
92. Jiang, G., et al., *Pyrolytic carbon black-derived porous carbon with spherical skeleton as recovered and enduring electrode material for supercapacitor.* Journal of Energy Storage, 2021. **44**: p. 103372.
93. Gawad, S., L. Schild, and P. Renaud, *Micromachined impedance spectroscopy flow cytometer for cell analysis and particle sizing.* Lab on a Chip, 2001. **1**(1): p. 76.
94. Sun, T. and H. Morgan, *Single-cell microfluidic impedance cytometry: a review.* Microfluidics and Nanofluidics, 2010. **8**(4): p. 423-443.
95. Eades, J., et al., *A Simple Micromilled Microfluidic Impedance Cytometer with Vertical Parallel Electrodes for Cell Viability Analysis.* Micromachines, 2023. **14**(2): p. 283.
96. Cottet, J., et al., *How to improve the sensitivity of coplanar electrodes and micro channel design in electrical impedance flow cytometry: a study.* Microfluidics and Nanofluidics, 2019. **23**(1).

97. Clausen, C., et al., *Coplanar Electrode Layout Optimized for Increased Sensitivity for Electrical Impedance Spectroscopy.* Micromachines, 2014. **6**(1): p. 110-120.
98. Alves De Araujo, A.L., et al., *Influence of Electrode Connection Tracks on Biological Cell Measurements by Impedance Spectroscopy.* Sensors, 2019. **19**(13): p. 2839.
99. Bounik, R., et al., *Impedance Imaging of Cells and Tissues: Design and Applications.* BME Frontiers, 2022. **2022**: p. 1-21.
100. Li, Q., et al., *Precision enhanced alignment bonding technique with sacrificial strategy.* Frontiers in Bioengineering and Biotechnology, 2023. **11**.
101. Petchakup, C., K. Li, and H. Hou, *Advances in Single Cell Impedance Cytometry for Biomedical Applications.* Micromachines, 2017. **8**(3): p. 87.
102. Liu, Y., et al., *Advance of microfluidic constriction channel system of measuring <scp>single-cell</scp> cortical tension/specific capacitance of membrane and conductivity of cytoplasm.* Cytometry Part A, 2022. **101**(5): p. 434-447.
103. Yang, G., et al. *Bioimpedance Measurement: Modeling of Coplanar Electrodes and Impedance Characterization*. IEEE.
104. Talukder, N., et al., *A portable battery powered microfluidic impedance cytometer with smartphone readout: towards personal health monitoring.* Biomedical Microdevices, 2017. **19**(2).
105. Mei, Z., Liu, Z., & Zhou, Z, *A compact and low cost microfluidic cell impedance detection system.* AIMS Biophysics, 2016. **3(4)**: p. 596-608.
106. Rollo, E., Tenaglia, E., Genolet, R., Bianchi, E., Harari, A., Coukos, G., & Guiducci, C, *Label-free identification of activated T lymphocytes through tridimensional microsensors on chip.* Biosensors and Bioelectronics, 2017. **94**: p. 193-199.
107. Valero, A., T. Braschler, and P. Renaud, *A unified approach to dielectric single cell analysis: Impedance and dielectrophoretic force spectroscopy.* Lab on a Chip, 2010. **10**(17): p. 2216.
108. Shaker, M., Colella, L., Caselli, F., Bisegna, P., & Renaud, P., *An impedance-based flow microcytometer for single cell morphology discrimination.* Lab on a Chip, 2014. **14(14)**: p. 2548.
109. Mernier, G., E. Duqi, and P. Renaud, *Characterization of a novel impedance cytometer design and its integration with lateral focusing by dielectrophoresis.* Lab on a Chip, 2012. **12**(21): p. 4344.
110. Demierre, N., et al., *Characterization and optimization of liquid electrodes for lateral dielectrophoresis.* Lab Chip, 2007. **7**(3): p. 355-365.
111. Caselli, F., et al., *Numerical Investigation of a Novel Wiring Scheme Enabling Simple and Accurate Impedance Cytometry.* Micromachines, 2017. **8**(9): p. 283.
112. Xie, X., et al., *A sheath-less electric impedance micro-flow cytometry device for rapid label-free cell classification and viability testing.* Analytical Methods, 2017. **9**(7): p. 1201-1212.
113. Qin, D., Y. Xia, and G.M. Whitesides, *Soft lithography for micro- and nanoscale patterning.* Nature Protocols, 2010. **5**(3): p. 491-502.
114. Sahin, O., Ashokkumar, M., & Ajayan, P. M., *Micro- and nanopatterning of biomaterial surfaces.* Fundamental Biomaterials: Metals, 2018: p. 67–78. .
115. J.L. Wilbur, A.K., H. A. Biebuyck, E. Kim, and G. M. Whitesides. 1996., *Microcontact Printing of Self-Assembled Monolayers: Applications in Microfabrication.* Nanotechnology, 1996. **7**: p. 452-457.
116. Fernandes, T.G., Diogo, M. M., & Cabral, J. M. S. (2013), *Microscale Technologies for stem cell culture.* Stem Cell Bioprocessing, 2013: p. 143-175.
117. Otsuka, H., *Micropatterning of cell aggregate in three dimension for in vivo mimicking cell culture.* Colloid and Interface Science in Pharmaceutical Research and Development, 2014: p. 223-241.
118. Weghuber, J., Brameshuber, M., Sunzenauer, S., Lehner, M., Paar, C., Haselgrübler, T., Schwarzenbacher, M., Kaltenbrunner, M., Hesch, C., Paster, W., Heise, B., Sonnleitner, A., Stockinger, H., & Schütz, G. J., *Detection of protein–protein interactions in the live cell*

plasma membrane by quantifying prey redistribution upon bait micropatterning. Methods in Enzymology, 2010: p. 133-151.
119. Roodbar Shojaei, T., Soltani, S., & Derakhshani, M., *Synthesis, properties, and biomedical applications of Inorganic bionanomaterials.* Fundamentals of Bionanomaterials, 2022: p. 139-174.
120. Shelke, N.T., & Late, D. J., *Synthesis and characterization of 2D materials.* Fundamentals and Supercapacitor Applications of 2D Materials, 2021: p. 77-104.
121. Tiwari, A.K., Yadav, P. K., Mishra, K., Singh, P. K., & Chourasia, M. K., *Magnetic nanoparticles. .* Multifunctional Nanocarriers, 2022.
122. Amen, R., Mukhtar, A., Saqib, S., Ullah, S., Al-Sehemi, A. G., Mehdi, S. E., Babar, M., & Bustam, M. A., *History and development of Nanomaterials.* Nanomaterials: Synthesis, Characterization, Hazards and Safety, 2021: p. 1–14.
123. Zikulnig, J., et al., *Printed Electronics Technologies for Additive Manufacturing of Hybrid Electronic Sensor Systems.* Advanced Sensor Research, 2023. **2**(7): p. 2200073.
124. Su, W., et al., *Fully inkjet-printed microfluidics: a solution to low-cost rapid three-dimensional microfluidics fabrication with numerous electrical and sensing applications.* Scientific Reports, 2016. **6**(1): p. 35111.
125. Zankovych, S., Hoffmann, T., Seekamp, J., Bruch, J.-U., & Torres, C. M., *Nanoimprint lithography: Challenges and prospects.* Nanotechnology, 2001. **12(2)**: p. 91-95.
126. Khadpekar, A.J., et al., *Low Cost and Lithography-free Stamp fabrication for Microcontact Printing.* Scientific Reports, 2019. **9**(1).
127. Zhou, Y., Asbahi, M., Luo, G., Eriksson, T., Yamada, S., Krishnan, P. V., & Heidari, B. (2010), *High Volume Manufacturing of nanoimprint lithography produced devices: Addressing the stamp supply challenge.* SPIE Proceedings, 2010.
128. Kang, S.-W., *Application of Soft Lithography for Nano Functional Devices*. 2010, InTech.
129. Bowen, A.M., Motala, M. J., Lucas, J. M., Gupta, S., Baca, A. J., Mihi, A., Alivisatos, A. P., Braun, P. V., & Nuzzo, R. G., *Triangular elastomeric stamps for optical applications: Near-field phase shift photolithography, 3D proximity field patterning, embossed antireflective coatings, and SERS sensing.* Advanced Functional Materials, 2012. **22(14)**: p. 2927-2938.
130. Svoboda, K. and R. Yasuda, *Principles of Two-Photon Excitation Microscopy and Its Applications to Neuroscience.* Neuron, 2006. **50**(6): p. 823-839.
131. Yamaguchi, K., et al., *In vivo two-photon microscopic observation and ablation in deeper brain regions realized by modifications of excitation beam diameter and immersion liquid.* PLOS ONE, 2020. **15**(8): p. e0237230.
132. Marshall, A.R., et al., *Two-Photon Cell and Tissue Level Laser Ablation Methods to Study Morphogenetic Biomechanics*. 2022, Springer US. p. 217-230.
133. Hill, R.A., et al., *Targeted two-photon chemical apoptotic ablation of defined cell types in vivo.* Nature Communications, 2017. **8**(1): p. 15837.
134. Solís-Fernández, P., et al., *Dense Arrays of Highly Aligned Graphene Nanoribbons Produced by Substrate-Controlled Metal-Assisted Etching of Graphene.* Advanced Materials, 2013. **25**(45): p. 6562-6568.
135. Cheng, G., et al., *Fe-catalyzed etching of exfoliated graphite through carbon hydrogenation.* Carbon, 2016. **96**: p. 311-315.
136. Díaz-Fernández, D., et al., *Nanopatterning on highly oriented pyrolytic graphite surfaces promoted by cobalt oxides.* Carbon, 2015. **85**: p. 89-98.
137. Severin, N., et al., *Rapid Trench Channeling of Graphenes with Catalytic Silver Nanoparticles.* Nano Letters, 2009. **9**(1): p. 457-461.
138. Cheng, G., I. Calizo, and A.R. Hight Walker, *Metal-catalyzed etching of graphene governed by metal–carbon interactions: A comparison of Fe and Cu.* Carbon, 2015. **81**: p. 678-687.
139. Shi, Z., et al., *Patterning Graphene with Zigzag Edges by Self-Aligned Anisotropic Etching.* Advanced Materials, 2011. **23**(27): p. 3061-3065.

140. Kim, H., et al., *Soft lithography of graphene sheets via surface energy modification.* Journal of Materials Chemistry C, 2013. **1**(6): p. 1076.
141. Wang, L., et al., *Fast Patterned Graphene Ribbons Via Soft–lithography.* Procedia CIRP, 2016. **42**: p. 428-432.
142. George, A., et al., *Large Area Resist-Free Soft Lithographic Patterning of Graphene.* Small, 2013. **9**(5): p. 711-715.
143. Singh, R.S., et al., *Laser Patterning of Epitaxial Graphene for Schottky Junction Photodetectors.* ACS Nano, 2011. **5**(7): p. 5969-5975.
144. Tian, H., et al., *Laser directed lithography of asymmetric graphene ribbons on a polydimethylsiloxane trench structure.* Physical Chemistry Chemical Physics, 2013. **15**(18): p. 6825.
145. Hall, L.S., et al., *All-graphene-based open fluidics for pumpless, small-scale fluid transport via laser-controlled wettability patterning.* Nanoscale Horizons, 2021. **6**(1): p. 24-32.
146. Pak, Y., et al., *Large-Area Fabrication of Periodic Sub-15 nm-Width Single-Layer Graphene Nanorings.* Advanced Materials, 2013. **25**(2): p. 199-204.
147. Geng, D., et al., *Fractal Etching of Graphene.* Journal of the American Chemical Society, 2013. **135**(17): p. 6431-6434.
148. Lee, Y.K., et al., *Charge transport-driven selective oxidation of graphene.* Nanoscale, 2016. **8**(22): p. 11494-11502.
149. Ye, X., et al., *Pattern Directive Sensing Selectivity of Graphene for Wearable Multifunctional Sensors via Femtosecond Laser Fabrication.* Advanced Materials Technologies, 2020. **5**(11): p. 2000446.
150. Bhatt, M.D., H. Kim, and G. Kim, *Various defects in graphene: a review.* RSC Advances, 2022. **12**(33): p. 21520-21547.
151. Liu, W., et al., *Effect of defects on optical and electronic properties of graphene quantum dots: a density functional theory study.* RSC Advances, 2023. **13**(24): p. 16232-16240.
152. Biswas, A., et al., *Advances in top–down and bottom–up surface nanofabrication: Techniques, applications & future prospects.* Advances in Colloid and Interface Science, 2012. **170**(1-2): p. 2-27.
153. Yan, Z., et al., *Hexagonal Graphene Onion Rings.* Journal of the American Chemical Society, 2013. **135**(29): p. 10755-10762.
154. Medina, H., et al., *Ultrafast Graphene Growth on Insulators via Metal-Catalyzed Crystallization by a Laser Irradiation Process: From Laser Selection, Thickness Control to Direct Patterned Graphene Utilizing Controlled Layer Segregation Process.* Small, 2015. **11**(25): p. 3017-3027.
155. Jacobberger, R.M., et al., *Direct oriented growth of armchair graphene nanoribbons on germanium.* Nature Communications, 2015. **6**(1): p. 8006.
156. Choi, J.-K., et al., *Growth of Wrinkle-Free Graphene on Texture-Controlled Platinum Films and Thermal-Assisted Transfer of Large-Scale Patterned Graphene.* ACS Nano, 2015. **9**(1): p. 679-686.
157. Zhou, X., et al., *Modulating the Electronic Properties of Monolayer Graphene Using a Periodic Quasi-One-Dimensional Potential Generated by Hex-Reconstructed Au(001).* ACS Nano, 2016. **10**(8): p. 7550-7557.
158. Ha, J.M., et al., *Freestanding graphene nanosheets and large-area/patterned graphene nanofilms from indium-catalyzed graphite.* RSC Advances, 2016. **6**(50): p. 44788-44793.
159. Cooper, K., *Scalable Nanomanufacturing—A Review.* Micromachines, 2017. **8**(1): p. 20.
160. Tang, L., et al., *Bottom-up synthesis of large-scale graphene oxide nanosheets.* Journal of Materials Chemistry, 2012. **22**(12): p. 5676.
161. Bao, L., et al., *Spatially Resolved Bottom-Side Fluorination of Graphene by Two-Dimensional Substrate Patterning.* Angewandte Chemie International Edition, 2020. **59**(17): p. 6700-6705.

162. Wei, T., et al., *Highly Efficient and Reversible Covalent Patterning of Graphene: 2D-Management of Chemical Information.* Angewandte Chemie International Edition, 2020. **59**(14): p. 5602-5606.
163. V. Pham, P., *The New Etching Technologies of Graphene Surfaces*. 2020, IntechOpen.
164. Kim, J., et al., *Graphene-Assisted Chemical Etching of Silicon Using Anodic Aluminum Oxides as Patterning Templates.* ACS Applied Materials & Interfaces, 2015. **7**(43): p. 24242-24246.
165. Wang, D., et al., *Scalable and controlled creation of nanoholes in graphene by microwave-assisted chemical etching for improved electrochemical properties.* Carbon, 2020. **161**: p. 880-891.
166. Hassler, M., *Other commonly used biomedical coatings: pyrolytic carbon coatings*. 2012, Elsevier. p. 75-105.
167. Pinto, G.F., et al., *Indirect determination of formaldehyde by square-wave voltammetry based on the electrochemical oxidation of 3,5–diacetyl–1,4–dihydrolutidine using an unmodified glassy-carbon electrode.* Talanta, 2019. **198**: p. 237-241.
168. Redivo, L., et al., *Bare carbon electrodes as simple and efficient sensors for the quantification of caffeine in commercial beverages.* Royal Society Open Science, 2018. **5**(5): p. 172146.
169. Vasconcelos, V.M., et al., *Electrochemical Degradation of Reactive Blue 19 Dye by Combining Boron-Doped Diamond and Reticulated Vitreous Carbon Electrodes.* ChemElectroChem, 2019. **6**(13): p. 3516-3524.
170. Taylor, S.M., et al., *Vanadium (V) reduction reaction on modified glassy carbon electrodes – Role of oxygen functionalities and microstructure.* Carbon, 2016. **109**: p. 472-478.
171. Zimmerman, R.L., et al., *Permeability control of GPC drug delivery system.* Nuclear Instruments and Methods in Physics Research Section B: Beam Interactions with Materials and Atoms, 1997. **127-128**: p. 1023-1026.
172. Grunwald, T., et al., *Influence of Glassy Carbon Surface Finishing on Its Wear Behavior during Precision Glass Moulding of Fused Silica.* Materials, 2019. **12**(5): p. 692.
173. Yano, T., H. Sugawara, and J. Taniguchi, *Moth-eye structured mold using sputtered glassy carbon layer for large-scale applications.* Micro and Nano Engineering, 2020. **9**: p. 100077.
174. Zhao, C., et al., *Facile fabrication of dual-ratiometric electrochemical sensors based on a bare electrode for dual-signal sensing of analytes in electrolyte solution.* Sensors and Actuators B: Chemical, 2017. **242**: p. 71-78.
175. Pereyra, J., et al., *Hydrogel-Graphene Oxide Nanocomposites as Electrochemical Platform to Simultaneously Determine Dopamine in Presence of Ascorbic Acid Using an Unmodified Glassy Carbon Electrode.* Journal of Composites Science, 2018. **3**(1): p. 1.
176. Roushani, M., Z. Rahmati, and B.Z. Dizajdizi, *Fabrication of novel metanil yellow/multi wall carbon nanotubes-chitosan/modified glassy carbon electrode and its application for sensitive determination of persulfate.* Journal of Electroanalytical Chemistry, 2019. **847**: p. 113192.
177. Kong, F.-Y., et al., *Voltammetric simultaneous determination of catechol and hydroquinone using a glassy carbon electrode modified with a ternary hybrid material composed of reduced graphene oxide, magnetite nanoparticles and gold nanoparticles.* Microchimica Acta, 2019. **186**(3).
178. Wang, Q. and W.A. Daoud, *Reaction kinetics of cerium on glassy carbon with in situ electrochemical treatment for cerium-based flow battery.* Electrochimica Acta, 2019. **315**: p. 1-8.
179. Omi, T. and K. Numano, *The Role of the CO2 Laser and Fractional CO2 Laser in Dermatology.* LASER THERAPY, 2014. **23**(1): p. 49-60.
180. *Understanding CO2 lasers and the advantages of use*. 2023; Available from: https://www.tuscomfg.com/co2-lasers/
181. Jitsuno, T. and K. Uno, *CO2 Lasers*. 2021, Springer International Publishing. p. 1-23.
182. Peterman, E.J.G., F. Gittes, and C.F. Schmidt, *Laser-Induced Heating in Optical Traps.* Biophysical Journal, 2003. **84**(2): p. 1308-1316.

183. Gera, T., et al., *Application of pulsed laser ablation (PLA) for the size reduction of non-steroidal anti-inflammatory drugs (NSAIDs).* Scientific Reports, 2020. **10**(1).
184. Dally, A., Coat, V., & Hill, A. . *Introduction to pulsed laser deposition (PLD):8 applications. VacCoat.* (2023, December 27); Available from: https://vaccoat.com/blog/what-is-pulsed-laser-deposition-pld/
185. Shepelin, N.A., et al., *A practical guide to pulsed laser deposition.* Chemical Society Reviews, 2023. **52**(7): p. 2294-2321.
186. Wang, G.R., F. Yang, and W. Zhao, *There can be turbulence in microfluidics at low Reynolds number.* Lab Chip, 2014. **14**(8): p. 1452-1458.
187. Team, E. *PDMS: A Review.* (2022, December 8); Available from: https://www.elveflow.com/microfluidic-reviews/general-microfluidics/the-polydimethylsiloxane-pdms-and-microfluidics/#:~:text=The%20Polydimethylsiloxane%20empirical%20formula%20is,the%20number%20of%20monomers%20repetitions. .
188. Miranda, I., et al., *Properties and Applications of PDMS for Biomedical Engineering: A Review.* Journal of Functional Biomaterials, 2021. **13**(1): p. 2.
189. João Ribeiro, L., R. *Applications of polydimethylsiloxane (PDMS) in engineering. Encyclopedia.* (2022, January 12). Available from: https://encyclopedia.pub/entry/18079
190. Victor, A., Ribeiro, J., & F. Araújo, F., *Study of PDMS characterization and its applications in biomedicine: A Review.* Journal of Mechanical Engineering and Biomechanics, (2019). **4(1)**: p. 1–9.
191. *PDMS: A possible solution for biomedical devices biocompatibility. NS Medical Devices.* (2021, July 21). Available from: https://www.nsmedicaldevices.com/analysis/pdms-a-possible-solution-for-biomedical-devices-biocompatibility/
192. Team, E. *Introduction to lab-on-a-chip 2023: Review, History and future.* (2023, August 14). Available from: https://www.elveflow.com/microfluidic-reviews/general-microfluidics/introduction-to-lab-on-a-chip-review-history-and-future/
193. Zahid, A., et al., *Optical properties study of silicone polymer PDMS substrate surfaces modified by plasma treatment.* Materials Research Express, 2017. **4**(10): p. 105301.
194. Gale, B.K., et al., *Low-Cost MEMS Technologies*. 2016, Elsevier.
195. Camino, G., S.M. Lomakin, and M. Lazzari, *Polydimethylsiloxane thermal degradation Part 1. Kinetic aspects.* Polymer, 2001. **42**(6): p. 2395-2402.
196. Deshpande, G. and M.E. Rezac, *Kinetic aspects of the thermal degradation of poly(dimethyl siloxane) and poly(dimethyl diphenyl siloxane).* Polymer Degradation and Stability, 2002. **76**(1): p. 17-24.
197. Kulyk, K., et al., *Chemisorption and thermally induced transformations of polydimethylsiloxane on the surface of nanoscale silica and ceria/silica.* Polymer Degradation and Stability, 2015. **120**: p. 203-211.
198. Elmanovich, I.V., et al., *Chemical Recycling of High-Molecular-Weight Organosilicon Compounds in Supercritical Fluids.* Polymers, 2022. **14**(23): p. 5170.
199. Radhakrishnan, T.S., *Thermal degradation of poly(dimethylsilylene) and poly(tetramethyldisilylene-co-styrene).* Journal of Applied Polymer Science, 2006. **99**(5): p. 2679-2686.
200. Lian, H., et al., *Three-Dimensional Printed Carbon Black/PDMS Composite Flexible Strain Sensor for Human Motion Monitoring.* Micromachines, 2022. **13**(8): p. 1247.
201. Xiao, G., et al., *Evolution of Singlet Oxygen by Activating Peroxydisulfate and Peroxymonosulfate: A Review.* International Journal of Environmental Research and Public Health, 2021. **18**(7): p. 3344.
202. Ravi-Kumar, S., et al., *Laser ablation of polymers: a review.* Polymer International, 2019. **68**(8): p. 1391-1401.

203. Maksimovic, J., et al., *Ablation in Externally Applied Electric and Magnetic Fields.* Nanomaterials, 2020. **10**(2): p. 182.
204. Yilgor, E., et al., *Isopropyl alcohol: an unusual, powerful, 'green' solvent for the preparation of silicone–urea copolymers with high urea contents.* Polymer, 2003. **44**(26): p. 7787-7793.
205. Lee, J.H., et al., *Rapid mold-free fabrication of long functional PDMS fibers.* NPG Asia Materials, 2022. **14**(1).
206. Satpute, S.K., et al., *Inhibition of pathogenic bacterial biofilms on PDMS based implants by L. acidophilus derived biosurfactant.* BMC Microbiology, 2019. **19**(1).
207. Vinothkumar, T., et al., *Influence of different organic solvents on degree of swelling of poly (dimethyl siloxane)-based sealer.* Journal of Conservative Dentistry, 2011. **14**(2): p. 156.
208. Keshmiri, K., H. Huang, and N. Nazemifard, *Compatibility of poly(dimethylsiloxane) microfluidic systems with high viscosity hydrocarbons.* SN Applied Sciences, 2019. **1**(7).
209. Hoek, I., F. Tho, and W.M. Arnold, *Sodium hydroxide treatment of PDMS based microfluidic devices.* Lab on a Chip, 2010. **10**(17): p. 2283.
210. Xu, L., et al., *Fabrication and Polishing Performance of Diamond Self-Sharpening Gel Polishing Disk.* Micromachines, 2023. **15**(1): p. 56.
211. Gross, B.C., et al., *Polymer Coatings in 3D-Printed Fluidic Device Channels for Improved Cellular Adherence Prior to Electrical Lysis.* Analytical Chemistry, 2015. **87**(12): p. 6335-6341.
212. Dupuis, R., et al., *Dissociation Mechanisms of Dissolved Alkali Silicates in Sodium Hydroxide.* The Journal of Physical Chemistry C, 2020. **124**(15): p. 8288-8294.
213. Ducom, G., et al., *Hydrolysis of polydimethylsiloxane fluids in controlled aqueous solutions.* Water Science and Technology, 2013. **68**(4): p. 813-820.
214. Yadhuraj, S.R., et al., *Preparation and Study of PDMS Material.* Materials Today: Proceedings, 2018. **5**(10): p. 21406-21412.
215. Sung, H.-K., et al., *Vertical and bevel-structured SiC etching techniques incorporating different gas mixture plasmas for various microelectronic applications.* Scientific Reports, 2017. **7**(1).
216. Zhang, J., et al., *Charging effect reduction in electron beam lithography with nA beam current.* Microelectronic Engineering, 2011. **88**(8): p. 2196-2199.
217. Rahman, S.S., et al., *Mechanically strong and fully transparent PMMA composite with greatly improved toughness and impact strength incorporating PEBA nanofibrils.* Chemical Engineering Journal, 2024. **480**: p. 148311.
218. Deka, N., et al., *Methyl Methacrylate-Based Copolymers: Recent Developments in the Areas of Transparent and Stretchable Active Matrices.* ACS Omega, 2022. **7**(42): p. 36929-36944.
219. Jamaluddin, N., et al., *Optically Transparent and Toughened Poly(methyl methacrylate) Composite Films with Acylated Cellulose Nanofibers.* ACS Omega, 2021. **6**(16): p. 10752-10758.
220. Mahmood Raouf, R., et al., *Transparent Blend of Poly(Methylmethacrylate)/Cellulose Acetate Butyrate for the Protection from Ultraviolet.* Polymers, 2016. **8**(4): p. 128.
221. Heiba, Z.K., M.B. Mohamed, and N.G. Imam, *Photophysical Parameters of Functional Transparent Polymethyl-Methacrylate/Double-Walled Carbon Nanotubes Nanocomposite Sheet Under UV-Irradiation.* Journal of Inorganic and Organometallic Polymers and Materials, 2016. **26**(4): p. 780-787.
222. Holland, B.J. and J.N. Hay, *The effect of polymerisation conditions on the kinetics and mechanisms of thermal degradation of PMMA.* Polymer Degradation and Stability, 2002. **77**(3): p. 435-439.
223. Ferriol, M., et al., *Thermal degradation of poly(methyl methacrylate) (PMMA): modelling of DTG and TG curves.* Polymer Degradation and Stability, 2003. **79**(2): p. 271-281.
224. Zeng, W.R., S.F. Li, and W.K. Chow, *Review on Chemical Reactions of Burning Poly(methyl methacrylate) PMMA.* Journal of Fire Sciences, 2002. **20**(5): p. 401-433.
225. Johnston, P.K., E. Doyle, and R.A. Orzel, *Acrylics: A Literature Review of Thermal Decomposition Products and Toxicity.* Journal of the American College of Toxicology, 1988. **7**(2): p. 139-200.

226. Thi Hong, P., H.Q. Nguyen, and H.T.M. Nghiem, *Complex refractive index measurements of poly(methyl methacrylate) (PMMA) over the UV-VIS-NIR region.* Optics Continuum, 2023. **2**(11): p. 2280.
227. Md Nawi, I.N., et al., *Nd:YAG Laser Welding for Photonics Devices Packaging*. 2012, InTech.
228. Dudek, M., et al., *Two-photon absorption and two-photon-induced isomerization of azobenzene compounds.* RSC Advances, 2020. **10**(66): p. 40489-40507.
229. Rumi, M. and J.W. Perry, *Two-photon absorption: an overview of measurements and principles.* Advances in Optics and Photonics, 2010. **2**(4): p. 451.
230. Cangueiro, L., J.A. Ramos-De-Campos, and D. Bruneel, *Prediction of Thermal Damage upon Ultrafast Laser Ablation of Metals.* Molecules, 2021. **26**(21): p. 6327.
231. Walsh, J.T., T.J. Flotte, and T.F. Deutsch, *Er:YAG laser ablation of tissue: Effect of pulse duration and tissue type on thermal damage.* Lasers in Surgery and Medicine, 1989. **9**(4): p. 314-326.
232. Roth, G.-L., et al., *Microchannels inside bulk PMMA generated by femtosecond laser using adaptive beam shaping.* Optics Express, 2020. **28**(4): p. 5801.
233. Yousif, E. and R. Haddad, *Photodegradation and photostabilization of polymers, especially polystyrene: review.* SpringerPlus, 2013. **2**(1): p. 398.
234. Maafa, I., *Pyrolysis of Polystyrene Waste: A Review.* Polymers, 2021. **13**(2): p. 225.
235. Faltynkova, A. and M. Wagner, *Developing and testing a workflow to identify microplastics using near infrared hyperspectral imaging.* Chemosphere, 2023. **336**: p. 139186.
236. Seleem, S., et al., *Comparison of Thermal Decomposition of Polystyrene Products vs. Bio-Based Polymer Aerogels.* The Ohio Journal of Science, 2017. **117**(2): p. 50-60.
237. Chauhan, R.S., et al., *Thermal decomposition of expanded polystyrene in a pebble bed reactor to get higher liquid fraction yield at low temperatures.* Waste Management, 2008. **28**(11): p. 2140-2145.
238. Faravelli, T., et al., *Thermal degradation of polystyrene.* Journal of Analytical and Applied Pyrolysis, 2001. **60**(1): p. 103-121.
239. Guaita, M., *Thermal Degradation of Polystyrene.* British Polymer Journal, 1986. **18**(4): p. 226-230.
240. Russo, R.E., X. Mao, and S.S. Mao, *Peer Reviewed: The Physics of Laser Ablation in Microchemical Analysis.* Analytical Chemistry, 2002. **74**(3): p. 70 A-77 A.
241. Swinarew, A.S., et al., *The Evaluation of Simulated Environmental Degradation of Polycarbonate Filled with Inorganic and Organic Reinforcements.* Polymers, 2021. **13**(20): p. 3572.
242. Li, J., P. Cheung, and J.C.M. Li, *Materials removal and energy dissipation during sawing of polycarbonate and glass.* Acta Materialia, 1999. **47**(6): p. 1845-1857.
243. Plastics, A. *Polycarbonate Plastic Products.*; Available from: https://www.alro.com/divplastics/PlasticsProduct_PolycarbonateFamily.aspx
244. Goyal, D.K., R. Yadav, and R. Kant, *An Integrated Hybrid Methodology for Estimation of Absorptivity and Interface Temperature in Laser Transmission Welding*. 2021, Research Square Platform LLC.
245. Uyar, T., A.E. Tonelli, and J. Hacaloğlu, *Thermal degradation of polycarbonate, poly(vinyl acetate) and their blends.* Polymer Degradation and Stability, 2006. **91**(12): p. 2960-2967.
246. Jang, B.N. and C.A. Wilkie, *A TGA/FTIR and mass spectral study on the thermal degradation of bisphenol A polycarbonate.* Polymer Degradation and Stability, 2004. **86**(3): p. 419-430.
247. Siddiqui, M.N., et al., *Pyrolysis mechanism and thermal degradation kinetics of poly(bisphenol A carbonate)-based polymers originating in waste electric and electronic equipment.* Journal of Analytical and Applied Pyrolysis, 2018. **132**: p. 123-133.
248. Clagett, D.C. and S.J. Shafer, *Polycarbonates*. 1989, Elsevier. p. 345-356.
249. Kadilak, A.L., et al., *Selective deposition of chemically-bonded gold electrodes onto PDMS microchannel side walls.* Journal of Electroanalytical Chemistry, 2014. **727**: p. 141-147.

250. Casanova-Moreno, J., et al., *Fabricating devices with improved adhesion between PDMS and gold-patterned glass.* Sensors and Actuators B: Chemical, 2017. **246**: p. 904-909.
251. Koh, D., et al., *Introduction of a Chemical-Free Metal PDMS Thermal Bonding for Fabrication of Flexible Electrode by Metal Transfer onto PDMS.* Micromachines, 2017. **8**(9): p. 280.
252. Akogwu, O., et al., *Large strain deformation and cracking of nano-scale gold films on PDMS substrate.* Materials Science and Engineering: B, 2010. **170**(1-3): p. 32-40.
253. Liang, D.Y., et al., *Systematic characterization of degas-driven flow for poly(dimethylsiloxane) microfluidic devices.* Biomicrofluidics, 2011. **5**(2): p. 024108.
254. Baëtens, T., et al., *Cracking effects in squashable and stretchable thin metal films on PDMS for flexible microsystems and electronics.* Scientific Reports, 2018. **8**(1).
255. Seghir, R. and S. Arscott, *Controlled mud-crack patterning and self-organized cracking of polydimethylsiloxane elastomer surfaces.* Scientific Reports, 2015. **5**(1): p. 14787.
256. Warren, M.A., et al., *Development of a Novel Design of Microfluidic Impedance Cytometry for Improved Sensitivity and Cell Identification.* ACS Omega, 2023. **8**(21): p. 18882-18890.
257. Nguyen, T.H., et al., *Concepts, electrode configuration, characterization, and data analytics of electric and electrochemical microfluidic platforms: a review.* The Analyst, 2023. **148**(9): p. 1912-1929.
258. De Bruijn, D.S., et al., *Determining Particle Size and Position in a Coplanar Electrode Setup Using Measured Opacity for Microfluidic Cytometry.* Biosensors, 2021. **11**(10): p. 353.
259. Yang, B., et al., *Label-Free Sensing of Cell Viability Using a Low-Cost Impedance Cytometry Device.* Micromachines, 2023. **14**(2): p. 407.
260. De Ninno, A., et al., *Coplanar electrode microfluidic chip enabling accurate sheathless impedance cytometry.* Lab on a Chip, 2017. **17**(6): p. 1158-1166.
261. Holmes, D., & Webb, B. L. J. *Electrical impedance cytometry. SpringerLink.* (1970, January 1). Available from: https://link.springer.com/referenceworkentry/10.1007/978-90-481-9751-4_122
262. Carminati, M., et al., *Miniaturized Impedance Flow Cytometer: Design Rules and Integrated Readout.* IEEE Transactions on Biomedical Circuits and Systems, 2017. **11**(6): p. 1438-1449.
263. Sathish, S. and A.Q. Shen, *Toward the Development of Rapid, Specific, and Sensitive Microfluidic Sensors: A Comprehensive Device Blueprint.* JACS Au, 2021. **1**(11): p. 1815-1833.
264. *Optical lithography*. Available from: https://www.sciencedirect.com/topics/materials-science/optical-lithography.
265. Kuech, T., & Kuech, T. , *Handbook of Crystal Growth: Thin films and epitaxy*. Vol. (second edition). 2015: North-Holland.
266. Ishihara, T. and X. Luo, *Nanophotolithography based on surface plasmon interference*. 2006, Elsevier. p. 305-312.
267. Mustafa, F., et al., *Printed paper-based (bio)sensors: Design, fabrication and applications*. 2020, Elsevier. p. 63-89.
268. Quero, J.M., F. Perdigones, and C. Aracil, *Microfabrication technologies used for creating smart devices for industrial applications*. 2018, Elsevier. p. 291-311.
269. Licari, J.J. and L.R. Enlow, *Preface to the Second Edition*. 1998, Elsevier. p. vii-viii.
270. Andy Pearce, O.V.S.n.d. *Thermal evaporation. Thermal evaporation techniques.*; Available from: http://www.oxford-vacuum.com/background/thin_film/evaporation.htm
271. Foundation, W. *Photolithography. Wikipedia.* (2024, January 22). Available from: https://en.wikipedia.org/wiki/Photolithography
272. *PVD coatings: Thermal evaporation & sputtering: Alicat. Alicat Scientific.* (2023, March 9); Available from: https://www.alicat.com/pvd-coatings-thermal-evaporation-and-sputtering/
273. Thompson, C.S. and A.R. Abate, *Adhesive-based bonding technique for PDMS microfluidic devices.* Lab on a Chip, 2013. **13**(4): p. 632.
274. Lee, H.S. and J.-B. Yoon, *A simple and effective lift-off with positive photoresist.* Journal of Micromechanics and Microengineering, 2005. **15**(11): p. 2136-2140.

275. Schmitt, H., et al., *Life time evaluation of PDMS stamps for UV-enhanced substrate conformal imprint lithography.* Microelectronic Engineering, 2012. **98**: p. 275-278.
276. Russell, M.T., et al., *Microscale Features and Surface Chemical Functionality Patterned by Electron Beam Lithography: A Novel Route to Poly(dimethylsiloxane) (PDMS) Stamp Fabrication.* Langmuir, 2006. **22**(15): p. 6712-6718.
277. Sahin, O., Ashokkumar, M., & Ajayan, P. M., *Micro- and nanopatterning of biomaterial surfaces.* Fundamental Biomaterials: Metals, 2018: p. 67–78.
278. Friend, J. and L. Yeo, *Fabrication of microfluidic devices using polydimethylsiloxane.* Biomicrofluidics, 2010. **4**(2): p. 026502.
279. Venzac, B., et al., *PDMS Curing Inhibition on 3D-Printed Molds: Why? Also, How to Avoid It?* Analytical Chemistry, 2021. **93**(19): p. 7180-7187.
280. Gupta, S., A. Vilouras, and R. Dahiya, *Polydimethylsiloxane as polymeric protective coating for fabrication of ultra-thin chips.* Microelectronic Engineering, 2020. **221**: p. 111157.
281. Ansari, A., et al., *Increasing silicone mold longevity: a review of surface modification techniques for PDMS-PDMS double casting.* Soft Materials, 2021. **19**(4): p. 388-399.
282. Hancer, M., *The effect of humidity on the stability of octadecyltrichlorosilane for the self-assembled monolayer coating applications.* Progress in Organic Coatings, 2008. **63**(4): p. 395-398.
283. Tolinski, M., *Crosslinking*. 2009, Elsevier. p. 215-220.
284. Aswal, D.K., et al., *Self assembled monolayers on silicon for molecular electronics.* Analytica Chimica Acta, 2006. **568**(1-2): p. 84-108.
285. Onclin, S., B.J. Ravoo, and D.N. Reinhoudt, *Engineering Silicon Oxide Surfaces Using Self-Assembled Monolayers.* Angewandte Chemie International Edition, 2005. **44**(39): p. 6282-6304.
286. Lee, D. and A.Q. Shen, *Interfacial Tension Measurements in Microfluidic Quasi-Static Extensional Flows.* Micromachines, 2021. **12**(3): p. 272.
287. Luque-Agudo, V., et al., *Effect of plasma treatment on the surface properties of polylactic acid films.* Polymer Testing, 2021. **96**: p. 107097.
288. Jaffer, Z.J., et al., *Synthesis and Surface Characterization of PMMA Polymer Films in Pure Oxygen, Argon, and Nitrogen Glow Discharge Plasma.* Journal of Physics: Conference Series, 2021. **1829**(1): p. 012010.
289. Lim, K.B. and D.C. Lee, *Surface modification of glass and glass fibres by plasma surface treatment.* Surface and Interface Analysis, 2004. **36**(3): p. 254-258.
290. Ortiz-Ortega, E., et al., *Aging of plasma-activated carbon surfaces: Challenges and opportunities.* Applied Surface Science, 2021. **565**: p. 150362.
291. Amador, G.J., et al., *Thermocapillary-Driven Fluid Flow within Microchannels.* 2018.
292. Beh, C.W., W. Zhou, and T.-H. Wang, *PDMS–glass bonding using grafted polymeric adhesive – alternative process flow for compatibility with patterned biological molecules.* Lab on a Chip, 2012. **12**(20): p. 4120.
293. Borók, A., K. Laboda, and A. Bonyár, *PDMS Bonding Technologies for Microfluidic Applications: A Review.* Biosensors, 2021. **11**(8): p. 292.
294. Raj, A., P.P.A. Suthanthiraraj, and A.K. Sen, *Pressure-driven flow through PDMS-based flexible microchannels and their applications in microfluidics.* Microfluidics and Nanofluidics, 2018. **22**(11).
295. Mandolfino, C., et al., *Effect of Laser and Plasma Surface Cleaning on Mechanical Properties of Adhesive Bonded Joints.* Procedia CIRP, 2015. **33**: p. 458-463.
296. Koh, K.-S., et al., *Quantitative Studies on PDMS-PDMS Interface Bonding with Piranha Solution and its Swelling Effect.* Micromachines, 2012. **3**(2): p. 427-441.
297. Gausden, J., et al., *Nitrogen as a Suitable Replacement for Argon within Methane-Based Hot-Wall Graphene Chemical Vapor Deposition.* physica status solidi (b), 2019. **256**(12): p. 1900240.

298. Chen, M., et al., *Large-scale cellulose-assisted transfer of graphene toward industrial applications.* Carbon, 2016. **110**: p. 286-291.
299. Lee, J., S. Lee, and H. Yu, *Contamination-Free Graphene Transfer from Cu-Foil and Cu-Thin-Film/Sapphire.* Coatings, 2017. **7**(12): p. 218.
300. Cui, N., F. Wang, and H. Ding, *Acetic Acid and Ammonium Persulfate Pre-Treated Copper Foil for the Improvement of Graphene Quality, Sensitivity and Specificity of Hall Effect Label-Free DNA Hybridization Detection.* Materials, 2020. **13**(7): p. 1784.
301. Tian, P., et al., *Cellulose-Graphene Bifunctional Paper Conservation Materials: For Reinforcement and UV Aging Protection.* Coatings, 2023. **13**(2): p. 443.
302. Wei, W., et al., *Tunable Graphene/Nitrocellulose Temperature Alarm Sensors.* ACS Applied Materials & Interfaces, 2022. **14**(11): p. 13790-13800.
303. Wei, T., F. Hauke, and A. Hirsch, *Evolution of Graphene Patterning: From Dimension Regulation to Molecular Engineering.* Advanced Materials, 2021. **33**(45): p. 2104060.
304. Zhao, Y., et al., *Large-area transfer of two-dimensional materials free of cracks, contamination and wrinkles via controllable conformal contact.* Nature Communications, 2022. **13**(1).
305. Malard, L.M., et al., *Raman spectroscopy in graphene.* Physics Reports, 2009. **473**(5-6): p. 51-87.
306. Yin, P., Q. Lin, and Y. Duan, *Applications of Raman spectroscopy in two-dimensional materials.* Journal of Innovative Optical Health Sciences, 2020. **13**(05): p. 2030010.
307. Das, A., B. Chakraborty, and A.K. Sood, *Raman spectroscopy of graphene on different substrates and influence of defects.* Bulletin of Materials Science, 2008. **31**(3): p. 579-584.
308. Ferrari, A.C., *Raman spectroscopy of graphene and graphite: Disorder, electron–phonon coupling, doping and nonadiabatic effects.* Solid State Communications, 2007. **143**(1-2): p. 47-57.
309. Cançado, L.G., et al., *Quantifying Defects in Graphene via Raman Spectroscopy at Different Excitation Energies.* Nano Letters, 2011. **11**(8): p. 3190-3196.
310. Kim, M.-S., et al., *Effect of copper surface pre-treatment on the properties of CVD grown graphene.* AIP Advances, 2014. **4**(12): p. 127107.
311. Ferrari, A.C. and D.M. Basko, *Raman spectroscopy as a versatile tool for studying the properties of graphene.* Nature Nanotechnology, 2013. **8**(4): p. 235-246.
312. Marken, F., A. Neudeck, and A.M. Bond, *Cyclic Voltammetry*. 2005, Springer Berlin Heidelberg. p. 51-97.
313. Munje, R.D., et al., *Flexible nanoporous tunable electrical double layer biosensors for sweat diagnostics.* Scientific Reports, 2015. **5**(1): p. 14586.
314. Seeber, R., C. Zanardi, and G. Inzelt, *The inherent coupling of charge transfer and mass transport processes: the curious electrochemical reversibility.* ChemTexts, 2016. **2**(2).
315. Giaccherini, A., et al., *Analysis of mass transport in ionic liquids: a rotating disk electrode approach.* Scientific Reports, 2020. **10**(1).
316. Wang, Z., W.A. Goddard, and H. Xiao, *Potential-dependent transition of reaction mechanisms for oxygen evolution on layered double hydroxides.* Nature Communications, 2023. **14**(1).
317. Varol, H.S., et al., *Electropolymerization of Polydopamine at Electrode-Supported Insulating Mesoporous Films.* Chemistry of Materials, 2023. **35**(21): p. 9192-9207.
318. Morales, D.M. and M. Risch, *Seven steps to reliable cyclic voltammetry measurements for the determination of double layer capacitance.* Journal of Physics: Energy, 2021. **3**(3): p. 034013.
319. De León-Hernández, A., et al., *Effective Capacitance from Equivalent Electrical Circuit as a Tool for Monitoring Non-Adherent Cell Suspensions at Low Frequencies.* Bioengineering, 2022. **9**(11): p. 697.
320. Andelman, M., *Flow Through Capacitor basics.* Separation and Purification Technology, 2011. **80**(2): p. 262-269.
321. Qin, R., et al., *A new strategy for the fabrication of a flexible and highly sensitive capacitive pressure sensor.* Microsystems & Nanoengineering, 2021. **7**(1).

322. Gharbi, O., et al., *Revisiting cyclic voltammetry and electrochemical impedance spectroscopy analysis for capacitance measurements.* Electrochimica Acta, 2020. **343**: p. 136109.
323. Feng Cheow, L., H. Bow, and J. Han, *Continuous-flow biomolecule concentration and detection in a slanted nanofilter array.* Lab on a Chip, 2012. **12**(21): p. 4441.
324. Shrirao, A.B., et al., *Microfluidic flow cytometry: The role of microfabrication methodologies, performance and functional specification.* TECHNOLOGY, 2018. **06**(01): p. 1-23.
325. Privett, B.J., J.H. Shin, and M.H. Schoenfisch, *Electrochemical Sensors.* Analytical Chemistry, 2010. **82**(12): p. 4723-4741.
326. Trouillon, R. and D. O'Hare, *Comparison of glassy carbon and boron doped diamond electrodes: Resistance to biofouling.* Electrochimica Acta, 2010. **55**(22): p. 6586-6595.
327. Kiss, L., et al., *Electrochemical polymerization of phenol on platinum and glassy carbon electrodes in mesityl oxide.* Chemical Physics Letters, 2020. **754**: p. 137642.
328. Abdel-Aziz, A.M., H.H. Hassan, and I.H.A. Badr, *Glassy Carbon Electrode Electromodification in the Presence of Organic Monomers: Electropolymerization versus Activation.* Analytical Chemistry, 2020. **92**(11): p. 7947-7954.

8. Appendix

Python Code

```
import csv

import numpy as np

import matplotlib.pyplot as plt

from scipy.signal import find_peaks, peak_widths


def importData(filename):

    # Define your importData function if it's not already defined

    pass


def myfunction(filename, pS, pL, ax):

    time, v = importData(filename)

    time = time / 1e6

    v = -v  # Corrected the typo in this line


    # Find peaks for small and large particles

    peaksS, _ = find_peaks(v, prominence=pS)

    peaksL, _ = find_peaks(v, prominence=pL)


    # Common area peaks between half value of peaksL prominence and peaksL prominence

    common_area_peaks, _ = find_peaks(v, prominence=(pL/2, pL))

    common_area_peaks = np.setdiff1d(common_area_peaks, peaksL)


    # Combine peaksL, peaksS, and common_area_peaks

    peaks = np.concatenate([peaksL, peaksS, common_area_peaks])


    # Sort the combined peaks array

    peaks = np.sort(peaks)
```

```
# Plotting peaksL, peaksS, and common_area_peaks
fig, ay = plt.subplots(1, 1, figsize=(16, 9))
ay.plot(-v)
ay.plot(peaksL, -v[peaksL], "o", color="red")
ay.plot(peaksS, -v[peaksS], "x", color="blue")
ay.plot(common_area_peaks, -v[common_area_peaks], "s", color="green")

# Counting peaks
print("Count Small = ", len(peaksS))
print("Count Large = ", len(peaksL))
print("Count Common Area = ", len(common_area_peaks))

# Defining peak widths
results_halfs = peak_widths(v, peaksS, rel_height=0.5)
results_halfL = peak_widths(v, peaksL, rel_height=0.5)
results_common = peak_widths(v, common_area_peaks, rel_height=0.5)

# Finding peak widths
dVL = v[peaksL] - results_halfL[1]
dVS = v[peaksS] - results_halfs[1]
dV_common = v[common_area_peaks] - results_common[1]

widthsS = results_halfs[0]
widthsL = results_halfL[0]
widths_common = results_common[0]

# Plotting FWHM for common area peaks
ax.plot(1e3 * (30e-6 / (widthsL * 1e-3)), dVL, "o", color='red')
ax.plot(1e3 * (30e-6 / (widthsS * 1e-3)), dVS, "x", color='blue')
```

```
    ax.plot(1e3 * (30e-6 / (widths_common * 1e-3)), dV_common, "s", color='green')

    # Plotting settings
    plt.xlabel('Time (s)')
    plt.ylabel('Voltage (V)')

    # Save results to CSV
    with open('testSave.csv', 'a', newline='') as csvfile:
        thewriter = csv.writer(csvfile, delimiter=',', quotechar='|', quoting=csv.QUOTE_MINIMAL)
        thewriter.writerow(['width_small', 'dV_small', 'width_Large', 'dV_large', 'width_common', 'dV_common'])
        for i in range(0, len(widthsS)):
            thewriter.writerow([widthsS[i], dVS[i], widthsL[i], dVL[i], widths_common[i], dV_common[i]])

# Example usage:
fig, ax = plt.subplots(1, 1, figsize=(16, 9))
myfunction('Data/15-11-2021/multi 1.csv', 0.0165, 0.02, ax)
plt.show()
```